Ultra-thin Oxide Films



Xiao Hu

Lincoln College

A thesis submitted for the degree of

Doctor of Philosophy

Trinity Term 2016

Acknowledgements

Thinking back to the winter of 2011 when I received the offer from Oxford, I could never have imagined a journey as wonderful as what I had. In the last four years I have not only achieved my D.Phil. degree but also transformed from childishness to maturity. I owe a big thank you to everyone who encouraged and supported me through the whole way.

I am indebted to my supervisor, Prof. Martin R. Castell, for his guidance and trust. I feel lucky to have a supervisor as conscientious and patient as he is. His initiative in science and concern for education establish the role model of an academic. We also enjoy a good personal relationship and he has been a pleasure to work with. I am also grateful to Dr. Chen Wu, who trained me on STM and gave me a lot of advice. People who have also helped me in my work include: Dr. Claudine Noguera and Dr. Jacek Goniakowski who provided DFT calculations to accomplish my experimental results; Dr. Lewys Jones and Dr. Fabien Silly who developed STM image processing software SmartAlign and FabViewer, and being incredibly supportive when I encountered problems; Dr. Susie Speller who proposed the collaboration with Diamond Lightsource and Dr. Moritz Hoesch and Dr. Pavel Dudin who provided technique support in Beamline I05; Chris Spencer who has done an excellent job of maintaining the STM instruments as the technician for JEOL UK. Yakun Gao and Shuqiu Wang are especially thanked for those good times we spent in the lab, office and conferences as well as all the lovely restaurants and bars in Oxford. Their positive attitude helped me through tough times. I would like to express my appreciation to other colleagues in the group: Dr. Jingyu Sun, Dr. Shams ur Rahman, Merel Lefferts, Peiyu Chen, Dr. Jan Seidel, Dr. Krishnan Murugappan and Tabitha Jones. It would have been impossible to complete my degree without their selfless assistance over the years.

I am grateful for the support from Lincoln College and the Department of Materials. The funding from both college and department has provided excellent chances for me to attend academic meetings and communicate with experts in scientific research. The comfortable living and study environments of Lincoln make my life in Oxford so enjoyable. The time I spent in the beautiful historical library will definitely be my sweetest memory of student days. I would also like to acknowledge the Department of Materials and all the staff for establishing a firm foundation for my research.

I have to express my special appreciation to my many friends here. Life in Oxford may just be a small part of the long journey of life, but all the company through those years has built a lot of deep friendships. I believe that those who truly treasure the past will not bemoan the passing of the ‘good old days’, because days enshrined in memory are never lost. I wish all of them the very best for the future.

Last but not least, I would like to thank my parents who have provided financial support for my study in Oxford and encouraged me to explore the world from the very beginning. They always stand by my side and show great confidence in me. I am so lucky and proud to have such a great family.

Preface

The work presented in this thesis was carried out by the author under the supervision of Prof. Martin. R. Castell. Parts of the work reported in this thesis have been presented at scientific conferences and are in preparation for scientific journal submissions. These include:

Oral presentations:

- The International FOXSI (Functional Oxide Surfaces and Interfaces) Conference – May 2016, Vienna, Austria.
- COST Action CM1104 'Reducible Oxide Chemistry, Structure and Functions' Final Meeting – April 2016, Osnabrück, Germany.
- 12th ECSCD (European Conference on Surface Crystallography and Dynamics) Conference – October 2015, Trieste, Italy.
- Imaging Surfaces Meeting – January 2015, London, UK.

Poster presentations:

- 3rd General Meeting of the COST Action CM1104 'Reducible Oxide Chemistry, Structure and Functions' – November 2014. Barcelona, Spain.
- Advanced Experimental Methods for Energy Materials Characterization Training School of the COST Action CM1104 'Reducible Oxide Chemistry, Structure and Functions' – September 2014, Delmenhorst, Germany.
- WG4 Meeting of the COST Action CM1104 'Reducible Oxide Chemistry, Structure and Functions' – April 2014, Riga, Latvia.

Abstract

Oxide ultra-thin film surfaces have properties and structures that are significantly different from the terminations of the corresponding bulk crystals. For example, surface structures of epitaxial ultra-thin oxide films are highly influenced by the crystallinity and electronegativity of the metal substrates they grown on. Some enhanced properties of the novel reconstructions are related to catalysis, sensing and microelectronics, which has resulted in an increasing interest in this field.

Ultra-thin TiO_x films were grown on Au(111) substrates in this work. Two well-ordered structures within monolayer coverage – honeycomb (HC) and pinwheel – were generated and investigated. Special attention has been paid to the uniform (2 × 2) Ti_2O_3 HC phase including its regular structure and imperfections such as domain boundaries (DBs) and point defects. Linear DBs with long-range repeating units have been observed; density functional theory (DFT) modelling has been used to simulate their atomic structures and calculate their formation energies. Rotational DBs/defects show up less frequently, however a six-fold symmetrical 'snowflake' DB loop stands out. Two types of point defects have been discovered and assigned to Ti vacancies and oxygen vacancies/hydroxyl groups. Their diffusion manners and pairing habits have been discussed within an experimental context.

The results of growing NbO_x ultra-thin films on Au(111) are also presented in this thesis. An identical looking (2 × 2) HC structure to the Ti_2O_3 ultra-thin film has been formed; a stoichiometry of Nb_2O_3 is suggested. Another interesting reconstruction is a hollow triangle structure. Various sizes have been found, and sides of these equilateral triangles all show a double-line feature aligned along the $\langle 1\bar{1}0 \rangle$ directions of the Au(111) lattice. Chemical composition characterisations of NbO_x thin films are still required as is DFT modelling.

Experimental techniques used in this thesis include scanning tunnelling microscopy (STM), low energy electron diffraction (LEED), and X-ray photoelectron spectroscopy (XPS). Ultra-thin oxide films were created by physical vapour deposition (PVD) in ultra-high vacuum (UHV) systems.

Contents

1. Introduction 1
1.1 Background 2
1.2 Thesis plan 4

2. Experimental Techniques 6
2.1 Introduction 7
2.2 Low-energy electron diffraction (LEED) 8
2.3 Scanning tunnelling microscopy (STM) 10
2.4 X-ray photoelectron spectroscopy (XPS) 13
2.5 Methods and procedures 16
2.5.1 Equipment 16
2.5.2 Sputtering 18
2.5.3 Annealing 18
2.5.4 Metal deposition 20
2.6 Summary 21

3. Literature Review 22
3.1 Surface reconstructions 23
3.1.1 Introduction 23
3.1.2 Park-Madden matrix notation and Wood's notation 23
3.1.3 Reconstructed Au(111)-(22 × √3) surface 24
3.2 Epitaxial growth of thin films 26
3.2.1 Introduction 26
3.2.2 Epitaxial growth of oxide thin films on metal substrates 28
3.3 TiO_x thin films 29
3.3.1 TiO_2 polymorphs 29
3.3.2 Defects and water dissociation on the rutile TiO_2(110) surface 32
3.3.3 TiO_x ultra-thin films 37
3.4 NbO_x thin films 54
3.4.1 Nb_2O_5 polymorphs 54
3.4.2 NbO_x ultra-thin films 55
3.5 Domain boundaries of 2D honeycomb-lattice films 63
3.5.1 Grain boundaries (GBs) of graphene sheets 64
3.5.2 Domain boundaries of metal-supported 2D silica ultra-thin films 71
3.6 Summary and outlook 75

4. Structures of TiO_x Ultra-thin Films Grown on Au(111) 76
4.1 Background 77
4.1.1 Overview 77
4.1.2 Experimental details 77
4.2 Results 79
4.2.1 STM and DFT of TiO_x ultra-thin films grown on Au(111) 79
4.2.2 LEED of TiO_x ultra-thin films grown on Au(111) 86
4.2.3 XPS of TiO_x ultra-thin films grown on Au(111) 91
4.3 Discussion 94
4.4 Conclusions 96

5. Domain Boundaries in (2 × 2) Ti_2O_3 Honeycomb Ultra-thin Films Grown on Au(111) **98**
5.1 Background 99
5.1.1 Overview 99
5.1.2 Experimental details 99
5.2 Results 100
5.2.1 Structural models of the crystallographically unique linear domain boundaries in HC-Ti_2O_3/Au(111) 100
5.2.2 STM and DFT of linear domain boundaries in HC-Ti_2O_3/Au(111) ... 106
5.2.3 STM of rotational domain boundaries in HC-Ti_2O_3/Au(111) 117
5.3 Discussion 122
5.4 Conclusions 123

6. Point Defects in Honeycomb Ti_2O_3 Thin Films Grown on Au(111) Substrates **125**
6.1 Background 126
6.1.1 Overview 126
6.1.2 Experimental details 127
6.2 Results 127
6.2.1 Titanium vacancies in HC-Ti_2O_3/Au(111) thin films 127
6.2.2 Oxygen vacancies/hydroxyl groups in HC-Ti_2O_3/Au(111) thin films. 133
6.2.3 Point defect pairs in HC-Ti_2O_3/Au(111) thin films 135
6.3 Discussion 136
6.4 Conclusions 138

7. NbO_x Ultra-thin Films Grown on Au(111) Substrates **140**
7.1 Background 141
7.1.1 Overview 141
7.1.2 Experimental details 142
7.2 Results 142
7.2.1 STM of NbO_x ultra-thin films grown on Au(111) 142
7.2.2 Structural models of NbO_x thin films grown on Au(111) 149
7.3 Discussion 153
7.4 Conclusions 155

8. Conclusions **156**
8.1 Overview 157
8.2 TiO_x ultra-thin films grown on Au(111) 157
8.3 NbO_x ultra-thin films grown on Au(111) 159
8.4 Future work 159

References **162**

Chapter 1:

Introduction

1.1 Background

Oxide thin films are layers of oxide materials with a thickness ranging from nanometres to several micrometres. Due to size and surface effects, properties of oxide thin films can be remarkably different from bulk materials (e.g. mechanical, optical and electrical properties). The distinct improvement of using thin films is usually related to the increased surface-to-volume ratio or/and the outstanding surface sensitivity. With the development of technology, oxide thin films have been incorporated into a lot of advanced applications including solar cells, catalysts, gas sensors and microelectronic devices [1-5]. Numerous studies on different aspects of oxide thin films have been performed in the last few decades.

In the initial stage of growing oxide thin films, the ultra-thin layers sometimes exhibit unique morphological structures. In the case of epitaxial growth of ultra-thin oxide films on metal substrates, surface structures of the films are highly influenced by the crystallinity of the substrates; to some extent, the film structures are more controlled by the symmetry of the substrates than the thermodynamic preference of the bulk oxide materials in order to minimise the interfacial and surface free energies. Conditions such as annealing temperature and oxygen pressure also affect the forming structures. Thickness of the ultra-thin oxide films is only a few monolayers, which makes it very sensitive to the environment and difficult to apply in commercial applications at this moment. However, in fundamental research, ultra-thin oxide films provide very valuable model surfaces to study the intrinsic behaviours of the oxide as well as the substrate-film interactions. Also the fabrications of ultra-thin oxide films with structures that are not found in bulk crystal terminations provide opportunities of obtaining novel physical and chemical properties. Due to the technical barriers, there hasn't been much research done on the ultra-thin oxide films before the spread of ultra high vacuum (UHV) chambers and the characterisation techniques of surfaces (e.g. scanning tunneling microscope (STM), X-ray photoelectron spectroscopy (XPS), Low Energy Electron Diffraction (LEED)). Nowadays the topic of ultra-thin oxide films has become one of the

hottest research directions.

In this thesis, studies of ultra-thin oxide films with a thickness up to three monolayers are reported; special attention has been paid to the sub-monolayer thin films as it reveals the interactions between thin films and substrates as well as the growth mechanism. The fabrication is carried out in UHV chambers via metal deposition and oxidation. Reconstructions of surface structures that differ from bulk terminations are built and studied using surface characterisation techniques to identify the chemical composition and surface structures. Different reconstructed structures are found as a result of varying the environment; structural models are proposed for each of them. Mechanisms of how experimental conditions influence the formation of various reconstructions are discussed.

A comprehensive study of TiO_x ultra-thin films grown on reconstructed Au(111) substrates is presented in this thesis. This investigation first comes out from the interest of the widely applicable titanium oxide thin films. Titanium oxide supported Au nanoparticles have been investigated as a highly efficient catalyst [6-7]; by developing the inverse model of TiO_x thin films grown on Au it is possible to gain an insight into the interaction between them. What's more, the chemical inertness of Au makes it an excellent choice for a substrate. Reconstructed Au(111) surface orders itself into a (22 × √3) reconstruction and shows a pairwise arrangement of bright line structure. When oxide thin films form on the Au(111) substrate, a strong substrate-film interaction lifts the Au reconstruction; therefore the hexagonal lattice of normal Au(111) surface is used in the discussion. Recent experiments of growing TiO_x ultra-thin films on Au(111) have reported some notable structures [8-10]; however more in-depth research is needed to complete the study. In this thesis, not only the regular TiO_x reconstructions but also the imperfections including domain boundaries and point defects observed in the reconstructed structures are examined. What's more, with the finding of valuable structures, experimental trials of generating similar reconstructed ultra-thin films are carried out. As a transition metal that shares a lot of similarity with Ti, Nb is used in the

experiments; reports of NbO_x ultra-thin films form part of this thesis.

1.2 Thesis plan

In Chapter 2, the characterisation techniques applied in the study of ultra-thin oxide films such as LEED, STM, XPS are introduced. Then the instruments that the experiments are performed on as well as the experimental procedures to produce TiO_x and NbO_x ultra-thin films are described.

Chapter 3 is a review of the relevant studies found in the literature. This includes a basic introduction of surface reconstructions as well as the explanation of reconstructed Au(111)-(22 × √3) surface that is used as the substrate in this thesis. The chapter also covers mechanisms of epitaxial growth of thin films and reports of TiO_x and NbO_x thin films that are most related to the results presented in this thesis.

The original experimental work carried out by the author is presented from Chapter 4 to Chapter 7. In Chapter 4, TiO_x ultra-thin films grown on Au(111) are reported and two most notable reconstructions – (2 × 2) Ti_2O_3 honeycomb structure and pinwheel structure – are studied via STM, Density functional theory (DFT) calculation, LEED and XPS.

In Chapter 5, domain boundaries that have been found in (2 × 2) Ti_2O_3 honeycomb thin films grown on Au(111) are described and discussed in detail. These include linear domain boundaries that are more commonly observed and rotational boundaries that are less frequently seen in STM images.

Chapter 6 focuses on point defects that are discovered in the regular honeycomb (2 × 2) Ti_2O_3/Au(111) system. Two types of recognisable point defects shown as dark and bright spots in honeycomb thin films are studied as well as their diffusion manner and pairing habit.

Chapter 7 presents the work on NbO_x ultra-thin films grown on reconstructed Au(111)

substrates. Coverage of Nb deposition increases from 0 to 3 monolayers. After oxidation, two novel surface reconstructions are observed in sub-monolayer coverage. One is a (2 × 2) hexagonal lattice that is very similar to Ti_2O_3 honeycomb phase; the other is a hollow triangle phase with double-line sides and various sizes. When the first layer of NbO_x thin film is completed, structural phases do not show up any more; the sample surface is covered by disordered features.

Chapter 8 is a summary of the work. It includes the conclusions of this research and the scope of future work. In general this project covers various aspects of the (2 × 2) Ti_2O_3 honeycomb thin films grown on Au(111) and a in-depth study of pinwheel phase. Investigation of NbO_x ultra-thin films grown on Au(111) helps to extend the regular (2 × 2) honeycomb structure from TiO_x/Au(111) system to other transition metal oxides thin films. In the future, water dissociation on (2 × 2) Ti_2O_3 honeycomb thin films grown on Au(111) will be carried out after solving the problem of identifying and creating oxygen vacancies; a comprehensive study of NbO_x hollow triangles is planned; the generation of regular (2 × 2) honeycomb structures will continue by oxidising transition metals that can readily adopt a +3 oxidation state on three-fold symmetrical metal substrates.

Chapter 2:

Experimental Techniques

2.1 Introduction

Over the years an enormous number of characterisation techniques have been developed to explore different aspects of surfaces. The study of surface structures took a big step forward after Davisson and Germer published their low energy electron diffraction (LEED) experiment result in 1927 [11]. However, LEED did not spread immediately due to the poor quality of the signal. The breakthrough of this technique happened in the early 1960s after two major developments: the ultra high vacuum (UHV) environment which reduced scattering effect and environmental impurities [12], and the post acceleration method which efficiently accelerated the diffracted electrons onto the fluorescent screen to form clear patterns [13]. Today, LEED is very popular as a standard technique to study the surface structures of single-crystalline materials.

The development of scanning tunnelling microscopy (STM) has proved to be one of the most exciting revolutions in the surface science field. In 1982, Gerd Binnig and Heinrich Rohrer invented this technique to investigate structures of conductive surfaces at atomic resolution [14-15]. Only four years later, they were awarded Nobile Prize in Physics. UHV is preferred to obtain high-resolution images, however STM has the ability to operate under multiple environments. The working temperature ranges from near zero Kelvin to a few hundred degrees Celsius [16].

Apart from studying surface structure, techniques to detect surface chemical composition are another issue of focus. One of the widely used techniques is X-ray photoelectron spectroscopy (XPS). It is based on the photoelectron effect discovered by Heinrich Rudolf in 1887. In 1905, Albert Einstein correctly explained this effect [17]. Throughout the 1950s and 1960s, Kai Siegbahn carried out a comprehensive study of XPS and significantly developed it [18]. Nowadays, XPS is the key technique to identify the compositions in the surface (1-10 nm), as well as detecting chemical and electronic states of the surface elements. For the purpose of investigating the electronic structure of solid surfaces, angle-resolved photoemission spectroscopy (ARPES) was invented. Information including band structures, Fermi surfaces, and energy gaps of countless

materials could be measured with high precision by ARPES. In 1964, Gobeli et al. showed momentum conservation in photoemission process of germanium and silicon, and proved that mapping out the band structure of the filled states is possible [19]. In the same year, Berglund and Spicer published their angle-integrated measurements of the electronic density of states of copper and silver, which turned out to have a good agreement with the theoretical predictions [20-21]. With the progress of techniques, in 1974, energy bands were first mapped with angular dependence of photoemission [22]. In recent decades, to fulfill the needs of studying high-temperature superconductors, the energy resolution of ARPES has been significantly improved to meV scales.

The techniques mentioned above are by no means exhaustive, but they are most relevant to this thesis. Their principles and instrumentations are described in the following sections.

2.2 Low-energy electron diffraction (LEED)

LEED is an ideal technique for quickly analysing the surface crystallographic structures. Figure 2.1 illustrates a typical LEED system. A beam of electrons is accelerated to the energy level between 20 and 200 eV and is incident normal to the sample. The energy-filtering grids are situated in front of the fluorescent screen. Only the elastic scattered electrons can successfully overcome the retarding field and pass through. They are then accelerated toward the phosphorescent screen and produce bright spots that reflect the periodicity of the near surface structure. In the low-energy level (10-1000 eV), when electrons strike the sample, they will dramatically lose energy during penetration into the crystal. Therefore only the electrons scattered on the uppermost surface atomic regions (under 20 Å) are considered as elastic scattered electrons that maintain the incident energy. In the case of a periodically arranged surface, the wavelength of electrons λ can be calculated via the de Broglie hypothesis:

$$\lambda = \frac{h}{p} = \frac{h}{\sqrt{2\mathrm{E}m}} \tag{2.1}$$

Where h is Planck's constant, p is the momentum, E is the incident electron energy, and m is the mass of electron. According to Bragg's law, surface periodicity d is defined as:

$$d = \frac{n\lambda}{\sin\theta} \tag{2.2}$$

Where n is the integer (order of diffraction), θ and λ are the diffraction angle and the wavelength of incident wave. Combining Equation 2.1 and 2.2, quantitative information of the surface can be deduced. For example, coexistent periodicities can be calculated by measuring the movements of spots responding to the change of incident beam energy. What needs to be mentioned is that LEED patterns indicate the surface crystallographic structure. It can't provide information of surface defects [23-24].

LEED patterns are usually presented in reciprocal space. Equation 2.3 explains the relationship between real space lattice and reciprocal lattice:

$$\begin{gathered} \boldsymbol{a_1} = 2\pi/\boldsymbol{b_1};\ \boldsymbol{a_2} = 2\pi/\boldsymbol{b_2} \\ \boldsymbol{a_1}\cdot\boldsymbol{b_2} = 0;\ \boldsymbol{a_2}\cdot\boldsymbol{b_1} = 0 \end{gathered} \tag{2.3}$$

$\boldsymbol{a_1}$, $\boldsymbol{a_2}$ are the vectors of real space lattice while $\boldsymbol{b_1}$, $\boldsymbol{b_2}$ are the corresponding vectors of reciprocal lattice. The distance between adjacent bright spots in the LEED patterns is inversely proportional to the distance between points in the corresponding direction of the real surface unit mesh.

LEED patterns included in this thesis were all obtained by the facility in the Diamond LightSource Beamline I05 in Oxfordshire (UK). The LEED Model is BDL800IR. It has a beam energy from 5 eV to 750 eV. Beam current is 2 μA at 100 eV with 0.5 mm beam size. The electron source is thermally emitted tungsten-rhenium filaments, and optional directly heated single crystal LaB_6 filaments. The beam energy applied to the samples in the experiments varied from about 45 eV to 150 eV.

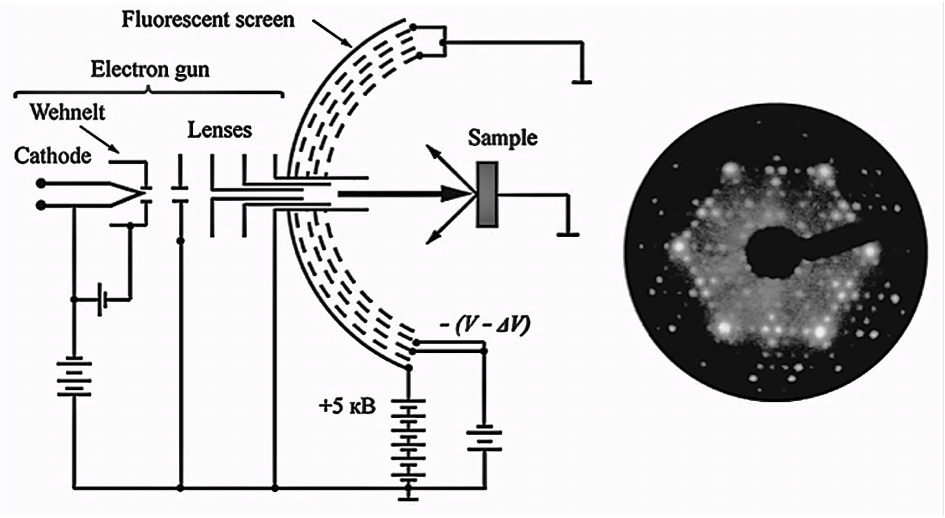


Figure 2.1: A schematic diagram of LEED experiment and LEED image of Si(111) 7×7 surface on fluorescent screen. Image is adapted from reference [25].

2.3 Scanning tunnelling microscopy (STM)

STM is an important technique to investigate structures of conducting surfaces at atomic resolution. In the STM experiments, a bias voltage is applied between an atomically sharp metal tip and the sample surface with a distance less than 10 Å. Electrons tunnel through the vacuum distance to constitute a tunnelling current. The tip is mounted on the piezoelectric scanner that can be accurate controlled in x, y and z dimensions. Information displayed in the image form is acquired by monitoring the feedback when the tip is scanning across the surface [15, 26]. Figure 2.2 shows the STM tip-sample energy band diagrams under various circumstances. When a macroscopic distance separates tip and sample, there is no interaction in terms of energy level (Figure 2.2a). When the tip-sample distance is within the range of tunneling through (typically between 0.3-1 nm), they start interacting with each other. Equilibrium of Fermi level is reached without external applied voltage (Figure 2.2b). When applying a positive voltage to the sample, electrons will tunnel from filled tip states into empty sample states (Figure 2.2c). In the contrast, when a negative sample voltage is applied to the sample, its Fermi level will be raised up, electrons will tunnel from filled sample states to empty tip states

(Figure 2.2d).

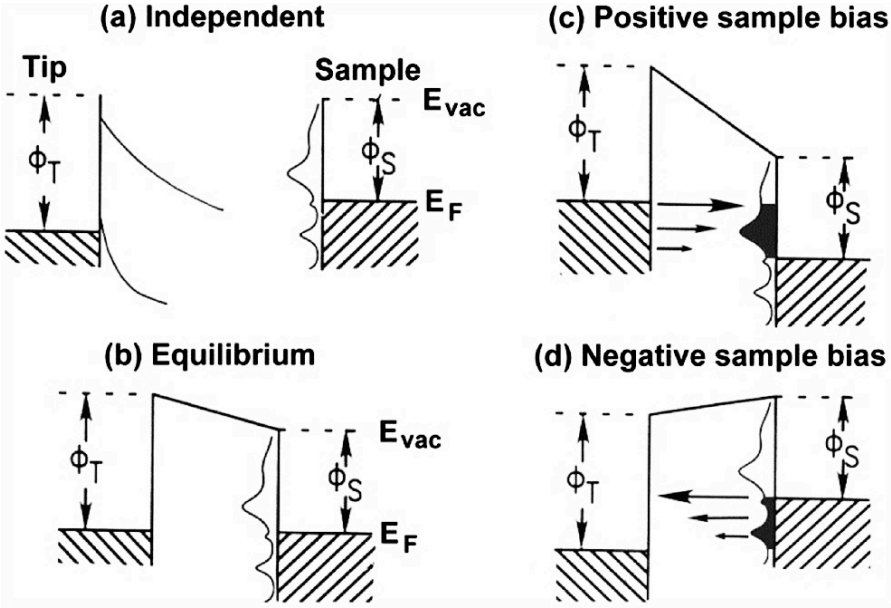


Figure 2.2: Energy level diagrams of sample and tip in STM: (a) when sample and tip are far apart, the Fermi levels of two systems are independent; (b) when sample and tip are under the distance of tunnelling, the Fermi levels of two systems are equal with no external applied bias; (c) when a positive sample bias is applied, electrons flow from occupied states of tip to the unoccupied states of sample surface; (d) when a negative sample bias is applied, electrons tunnel from occupied states of sample surface to the unoccupied states of tip. ϕ_S is the work function of sample; ϕ_T is the work function of tip; E_{vac} is the vacuum-level energy; E_F is the Fermi-level energy. Images are adapted from reference [27].

Equation 2.4 illustrates the tunnelling current during STM imaging. It emerges from the derivation obtained by Tersoff and Hamman [28-29]. With the applied tip-sample bias V, the tunnelling current I_t is proportional to the local density of states (LDOS) between Fermi level and eV:

$$I_t \propto V\, \phi^2\, \rho_t\, \rho_s\, e^{-\kappa z} \tag{2.4}$$

Where ρ_t and ρ_s are the density of states of tip and sample, z is the tip-sample distance in the unit of Å; κ is a constant related to the decay length for the wave funtions in a

vacuum (~ 2 Å^{-1}). ϕ is the average barrier height. It can be calculated by Equation 2.5:

$$\phi = \frac{\phi_t + \phi_s}{2} \tag{2.5}$$

Where ϕ_t and ϕ_s are the work function of tip and sample. According to Equations 2.4, the tunnelling current is very sensitive to the tip-sample distance. When the tip-sample distance increases by about 1 Å, the tunnelling current will drop by nearly an order of magnitude, which makes STM have an extremely high vertical resolution. It also indicates that the majority of the tunnelling current goes through the tip apex and the topmost atomic layer of a sample, therefore the quality of tip is a key factor of obtaining high-resolution STM images [30-31].

There are two modes of STM operation: constant current and constant height (Figure 2.3). In constant current mode, the tunnelling current is fixed. Tip moves forward and backward perpendicular to the sample according to the feedback-controlled system to maintain the constant current value. Information of the sample surface is obtained by plotting the voltage applied to the z-piezoelectric scanner against the x and y displacement of tip. This mode is usually applied on samples with comparatively rough surface. In constant height mode, tip remains a constant distance to the sample surface, the tunnelling current changes as a function of tip position. This mode is very sensitive to the surface roughness so only smooth surface could be scanned. However a relatively high scanning speed could be achieved [32-34].

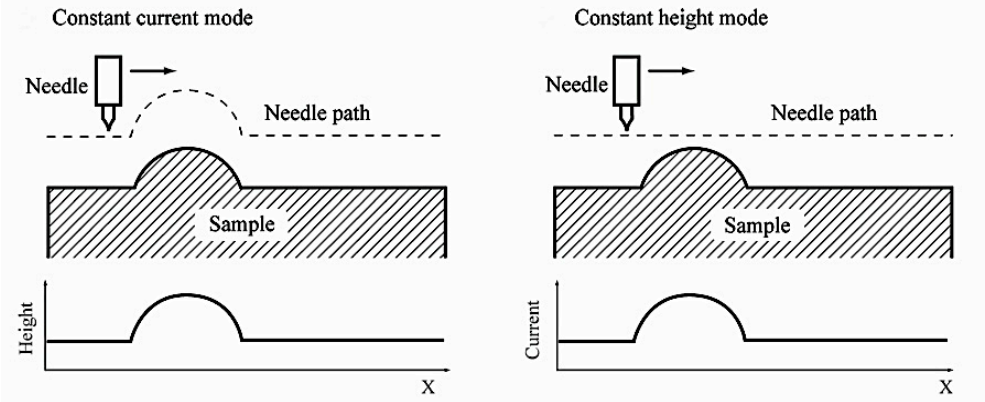


Figure 2.3: Schematic representation of the operating concept of an STM operating in the constant current mode and the constant height mode. Images are adapted from reference [25].

The JSTM-4500XT STM was used to take STM images presented in this thesis. All the samples were cut into size of 2mm × 7mm. Three motors are attached to the sample stage that enable the movement of sample in the x, y and z directions. Tip is made from tungsten (W) wire by chemical etching and examined by an optical microscope before putting into the UHV chamber, and it is attached to three piezoelectric crystals when loaded in the STM chamber. During the procedure of scanning across the sample surface, these piezoelectric crystals expand or contract in directions of x, y and z corresponding to the applied voltage, which ensures a very accurate control of the tip movement. During STM imaging, constant current mode was applied; the bias voltage was in the range of -10 to +10 V; tunnelling current varied from 0.1 nA to 10 nA. The relevant signals are sent to a computer in the image form for subsequent processing.

2.4 X-ray photoelectron spectroscopy (XPS)

As a surface chemical analysis technique, the popularity of XPS is attributed to its high information content and flexibility for a wide variety of samples. The theoretic basis is the photoelectric effect. As shown in Figure 2.4, when a beam of X-rays with sufficient energy irradiates a surface, photoelectrons will emit as the result of energy

transformation. Consider analysing an electrically conductive specimen, electrical equilibrium is achieved between the specimen and the applied material of the spectrometer (equalised Fermi levels in Figure 2.4). Therefore the spectrometer-measured kinetic energy of an emitted electron E_{kin} is give by:

$$E_{kin} = h\nu - E_b - \Phi \tag{2.6}$$

Where $h\nu$ is the energy of incident photon (h: Plank's constant, ν: frequency of incident light), E_b is the binding energy of the electron, and Φ is the work function of the spectrometer material. In XPS experiments, the energy of incident photon can be calculated; work function Φ dependents on the used spectrometer material; and E_{kin} is measured. Therefore E_b is obtained.

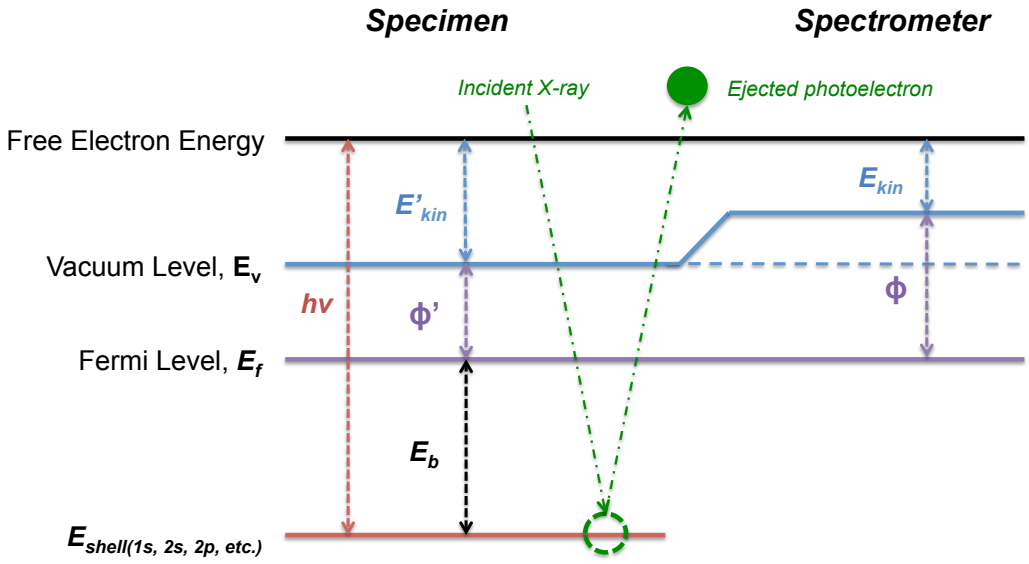


Figure 2.4: Schematic diagram of the interdependence of energy characteristics of conductive specimen and spectrometer. E'_{kin} is the kinetic energy of specimen, and Φ' is the work function of specimen.

Electron binding energy is a measure of the energy required to free electrons from their atomic orbits. Figure 2.5 shows a typical XPS spectrum. The value of electron binding energy is defined by element and electrostatic potential of atom, so the surface

elemental composition can be worked out by comparing with the characteristic binding energy value sets of elements. The amount of element within the irradiated area is analysed by counting the number of detected electrons in characteristic peaks [17, 35-36].

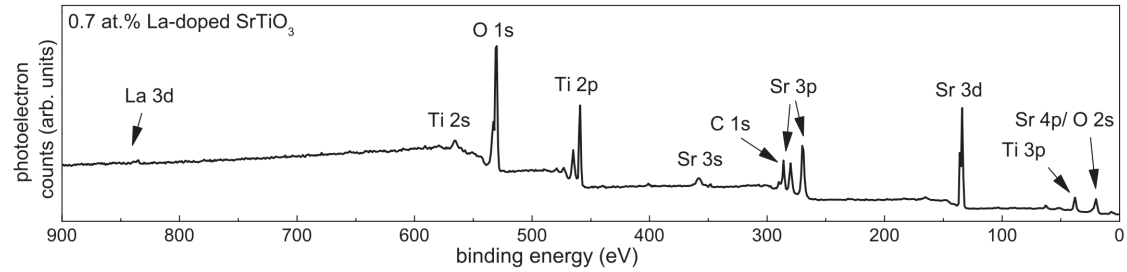


Figure 2.5: The Al K_α core level X-ray photoelectron spectroscopy (XPS) survey for a 0.7 at.% La-doped $SrTiO_3$ sample with all the major peaks indicated. Y-axis is the number of detected electrons; x-axis is the binding energy of detected electron film. Image is adapted from reference [37].

For a typical XPS system, the main components include an X-ray source gun, an electron collection system, a hemispherical electron energy analyser, a detector system, and an UHV system. The facility used in this thesis is a high-resolution X-ray photoemission spectrometer based at the Diamond Light Source Beamline I05 in Oxfordshire (UK). The complete X-ray pack made by SPECS consist of the X-ray source module XR 50, the power supply XRC 1000, the cooling unit CCX 60 and the hemispherical analyser PHOIBOS-HSA3500. The X-ray source employs two anode materials: Al and Mg. It produces $K_{\alpha 1,2}$ radiation lines at energies of 1486.6 eV (Al) and 1253.6 eV (Mg) respectively. The natural line width is less than 1 eV, which is sufficient to determine the binding energies of core levels within 0.2 eV. In the XPS experiments carried out in this work, Al K_α was chosen as the anode. The applied voltage was 12.5 kV, and the power was 250 W. The incident angle was 54°.

2.5 Methods and procedures

2.5.1 Equipment

Two UHV systems are used for the experiments in this thesis. The one used for STM imaging is JSTM-4500XT in the department of Materials at the University of Oxford (Figure 2.6). There are three chambers in this system: an exchange chamber, a treatment chamber and an STM chamber. Two gate valves are installed to separate those chambers. The exchange chamber is a load lock that can be exposed to the air for sample/tip introduction. A turbo molecular pump (TMP) is linked to this chamber, which can pump the pressure down to 10^{-6} Pa. The treatment chamber and the STM chamber both work under the basic pressure of 10^{-8} Pa. This is achieved by the operation of ion pumps as well as titanium sublimation pumps (TSP). Sample degassing, sputtering and annealing are operated in the treatment chamber. STM imaging and e-beam evaporation take place in the STM chamber.

The other UHV system is customised SPECS ESCA in beamline I05 at Diamond Light Source. All the LEED and XPS experiments were carried out in the preparation chamber (Figure 2.7). Similar to the JSTM-4500XT system, the basic pressure is 10^{-8} Pa. A load lock is attached for sample introduction as well. In addition, prepared sample can be UHV transferred into the ARPES chamber to measure electronic structures.

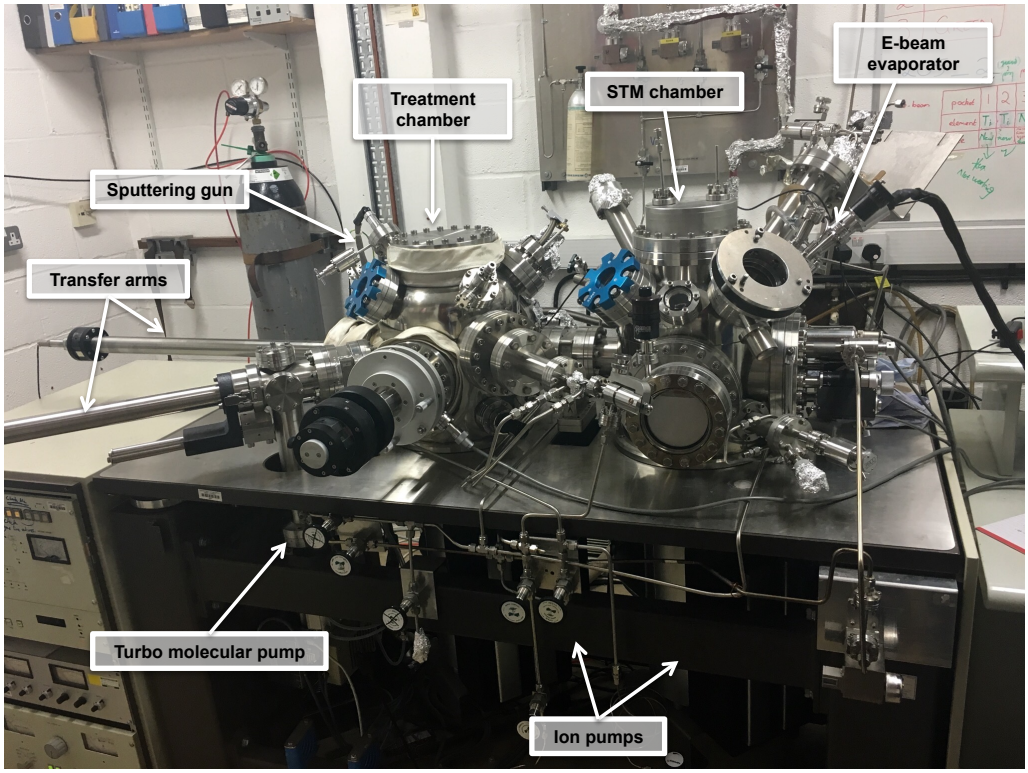


Figure 2.6: Photograph of the JEOL 4500XT microscope. A selection of the facilities is labelled.

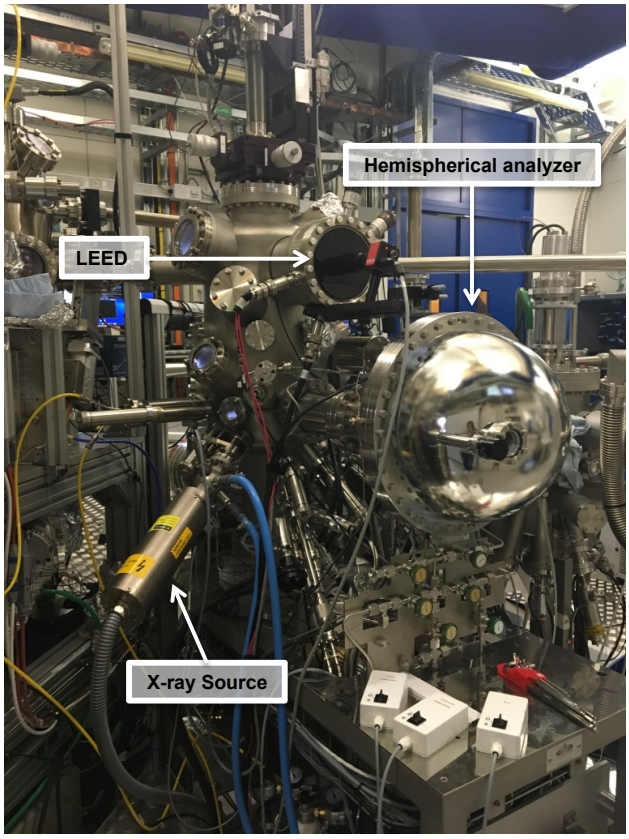


Figure 2.7: Photograph of the preparation chamber of the customised SPECS ESCA. A selection of the facilities is labelled.

2.5.2 Sputtering

Sputtering is the process of cleaning up sample surface by bombarding with energetic ions. Deposited layers can also be removed so that the sample can be reused.

In both UHV systems, an argon gas cylinder is attached to provide source of Ar ions. In JSTM-4500XT, the PSP Vacuum Technology Ion Source ISIS3000 is installed. Argon gas is leaked directly into the discharge chamber where ions are formed at a selected energy between 100 and 3000 eV. The Ar ions are focused into a spot of approximately 10 mm diameter at the sample surface and physically remove surface materials. During sputtering, the required Ar gas pressure is about 2×10^{-3} Pa, so that the ion pump in treatment chamber must be switched off to avoid saturation. The gate valve between exchange chamber and treatment chamber is opened and the TMP in the exchange chamber is turned on to keep the pressure under 10^{-5} Pa.

In the customised SPECS ESCA system, the SPECS Ion Source IQE 11/35 controlled by a digital power supply is installed. An integrated Mini-Conflat Flange directly transfers argon gas in the ionisation. An Ar ion current of 10-15 μA with a Gaussian beam profile is generated. The typical pressure in the preparation chamber is 10^{-3} – 10^{-4} Pa during operation.

2.5.3 Annealing

Two kinds of Au(111) substrates are used in this thesis. For STM imaging, Au(111) film is grown on the nonconductive mica, which makes it impossible to heat the sample directly. In this way, a piece of $SrTiO_3$ with the same size is placed underneath the mica. By applying a direct current through the $SrTiO_3$ plate, it can be heated resistively to a desirable temperature to anneal the Au sample. Temperature below 750 °C is estimated through a best fitting equation:

$$T = 1.4739x^3 - 34.546x^2 + 325.3x + 15.58 \quad (2.7)$$

Where T is the estimated temperature, x is the power (W) applied to the sample [30].

The graph showing this data and the best fitting line is presented in Figure 2.8:

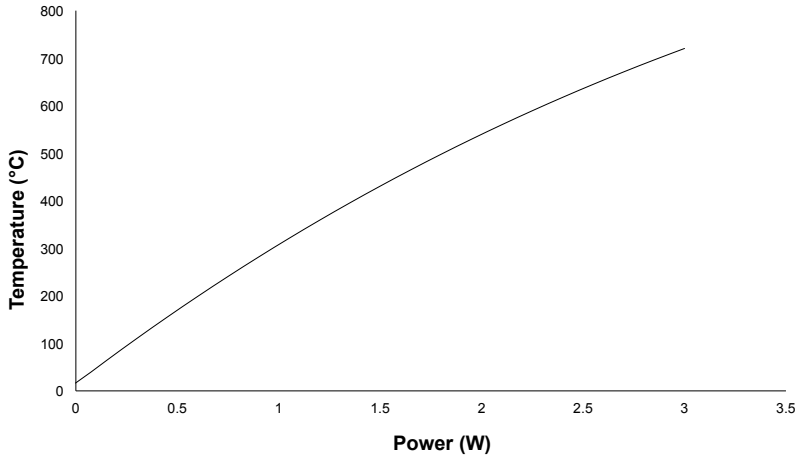


Figure 2.8: Graph showing sample temperature plotted against the power dissipated in the sample for the power supply output in the range of 0-3.5 W.

An analog power supply is used in the experiments. The power P can be calculated through Equation 2.8:

$$P = UI \tag{2.8}$$

U, I is the output voltage and current separately. In STM experiments, mica-supported single crystal Au(111) sample (Agilent Technologies, U.K.) is used, annealing temperature is about 600 °C, so the output power should be about 2.3-2.4 W.

The samples used in LEED and XPS experiments are 99.999% purity Au(111) single crystal cylinders (MaTeck GmbH, Germany) with diameter of 10-20 mm and thickness of 1-2 mm. It is attached to a standard heating plate for annealing. Temperature of the heating plate is controlled by a digital power supply and displayed on the screen. The annealing temperature is about 500 °C.

What needs to be mentioned is that the annealing temperatures described above are the set-point temperatures. The real annealing temperature for both surfaces of Au samples should be the same. A lot of factors cause this large difference in set-point

temperatures between those two systems. For example, when using mica-supported sample, the mica plate works as a heat insulator so that the actual temperature of the Au(111) surface is lower than the temperature of the heated $SrTiO_3$ plate underneath. Also, the Power-Temperature curve in Figure 2.8 is only an estimated fitting. Even with the same power supply, the actual temperature of $SrTiO_3$ plate varies due to the thickness, shape and condition of individuals. For the single crystal Au(111) sample, considering the resistance of the sample cylinders, the temperature of surface layer might be slightly different from the heating plate attached at the bottom of cylinder. The efficient set-point annealing temperature in each system comes from the experimental experience.

2.5.4 Metal deposition

In this thesis, in order to grow metal oxide thin films (titanium oxides and niobium oxides), Ti and Nb atoms need to be deposited onto the substrates in UHV. This is achieved by using E-beam evaporators.

In the JSTM-4500XT system, metal (Ti/Nb) is deposited in the STM chamber by an Oxford Applied Research mini e-beam evaporator ENG4. It has four separated pockets that allow installing different metal rods. In each pocket, a tungsten filament at ground potential is placed close to the top of the metal rod. When current is applied through the filament, electrons will emit and be attracted by the corresponding metal rod with a positive voltage of 1.5-2 kV. At the tip point of the metal rod, electron density is high enough to enable the evaporation of materials including Ti (melting at 1660 °C) and Nb (melting at 2468 °C). During evaporation, only one pocket can be selected to work each time. Water-cooling system is running to protect instruments and metal rods. A shutter is attached to avoid deposition before reaching a stable rate.

In the customised SPECS ESCA system, metal deposition is operated through evaporation from tungsten crucible containing the target metal bar. The crucible is

heated up by an attached power supply. Deposition rate is pre-tested and monitored in real time by XPS.

2.6 Summary

This chapter has introduced a few techniques widely used to study surface structures and chemistry characterisation. All the techniques and experimental procedures mentioned have been used to produce and investigate titanium/niobium oxide ultra-thin thin films in this work. A combined usage of those characterisation techniques is necessary to achieve a complementary understanding of those oxide ultra-thin films, especially for the initial formation stage. At the same time, being produced and tested under different conditions demonstrate the feasibility and stability of those structures.

Chapter 3:

Literature Review

3.1 Surface reconstructions

3.1.1 Introduction

Surface reconstruction and relaxation are two forms of the rearrangement of surface atomic structure. In an ideal infinite crystal, forces that come from all the other atoms determine the equilibrium position of an individual atom. When the bulk material is cut into two, new terminal surfaces will form, and the original force balance will break. In order to minimize the surface free energy, the equilibrium positions of the remaining atoms change, especially for the atoms at or near the surface plane. This imbalance introduces the new surface structure with different spacing and/or symmetry from the bulk atoms, which can be categorised as either a relaxation or a reconstruction.

Relaxation is a subtle rearrangement in the position of entire layers of atoms relative to the bulk positions, either normal or lateral. For most metals, the normal relaxation results in a reduced interlayer spacing between the first and second atomic layers. Neither the periodicity nor the symmetry parallel to the surface becomes different in this case. Reconstruction however changes the periodicity of the surface structure, which involves both the two-dimensional structure of the surface layers and the position of the entire layer. It could result in either a conservative atom number in a layer or having a different number than in bulk materials [38-39].

3.1.2 Park-Madden matrix notation and Wood's notation

Park-Madden matrix notation and Wood's notation are two ways that have been used to describe surface reconstruction in real space.

Park-Madden matrix notation: Define a, b as the basic translation vectors of the two-dimensional structure in the bulk. For the reconstructed plane the basic translation vectors a_r and b_r are:

$$a_r = G_{11}\, a + G_{12}\, b$$

$$b_r = G_{21}\, a + G_{22}\, b \tag{3.1}$$

The matrix defined by G_{11}, G_{12}, G_{21} and G_{22} reflects the relationship between the bulk termination and the reconstructed surface:

$$\begin{pmatrix} G_{11} & G_{12} \\ G_{21} & G_{22} \end{pmatrix} \tag{3.2}$$

What needs to be clarified is that this matrix only describes the individual layer's structure. It is not relative to the relaxation of surface layer.

Wood's notation: Wood's notation is comparatively more commonly used to describe the surface reconstruction. The matrix above is reduced into a more compact notation:

$$X(hkl) - u(m \times n)\, R\varphi \tag{3.3}$$

Where X is the material; (hkl) is given by Miller indices to explain the reconstruction plane; u can be either p (primitive) or c (centred) depending on the type of unit cell; m and n describe the change of interatomic spacing in a, b directions respectively; φ is the rotation angle of the reconstructed plane. Usually if the unit cell is primitive, u will be left out. For a reconstructed surface with no rotation referring to the original plane, $R\varphi$ will be omitted as well. All the reconstructed surfaces in this thesis will be described by Wood's notation.

3.1.3 Reconstructed Au(111)-(22 × √3) surface

The reconstructed Au(111)-(22 × √3) surface is the substrate used in this work. In the case of single crystal Au(111) sample, the reconstruction is achieved by cycles of Ar^+ sputtering and UHV annealing. As shown in Figure 3.1, the reconstructed Au(111) surface has a herringbone structure. Au is a face centred cubic (FCC) crystal, so the ideal (111) plane consists of a hexagonal lattice. In the reconstructed surface layer, 46

atoms 'squeeze' in the uniform lattice sites for 44 bulk atoms in two rows along the $\langle 1\bar{1}0 \rangle$ direction by periodically occupying both regular FCC and faulted hexagonal close-packed (HCP) sites (Figure 3.2) [40-41]. Bright lines in the STM image separate alternating domains of FCC-like and HCP-like structures, which are identified as transition regions. Atoms in the transition regions are packed closer together, so they are raised up with respect to the surface plane and brighter in STM images. Due to the energy difference, more FCC than HCP sites are populated, which ends up with a pairwise arrangement of the $\langle 11\bar{2} \rangle$-oriented domain walls. As illustrated in Figure 3.1, compression in short range is unidirectional, while a 120° bending of domain walls with a period about 250 Å exists [40, 42]. This superposition of three 120° rotated domains is confirmed by LEED, and each domain consists of rectangular (22 × √3) unit cells. A model consisting of a 4.55% uniaxially contracted hexagonal top layer along the $[1\bar{1}0]$ direction is deduced [43-44]. This result fits the STM results that a contraction of about 4.5% along $\langle 1\bar{1}0 \rangle$ can be derived from the atomic model.

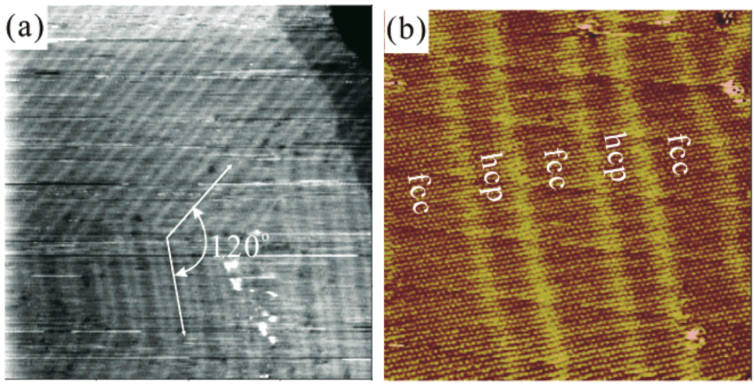


Figure 3.1: In situ STM images acquired with Au(111) at -1.0 V in pH11, 0.1 M KF. The large scan in (a) reveals the general morphology and the herringbone structure of the reconstructed (22 × √3). Two of three possible domains intersecting at 120° are seen (Image size: 100 nm × 100 nm). The high-resolution scan in (b) shows the atomic details of the reconstructed phase, where Au atoms could reside at FCC, HCP and between sites (Image size: 20 nm × 20 nm). These images were collected with 100 mV bias and 2 nA feedback current. Image is adapted from reference [45].

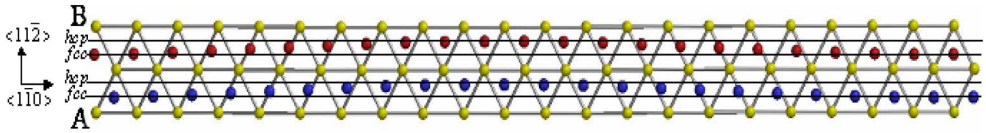


Figure 3.2: Top view of the reconstructed Au(111)-(22 × √3) surface unit cell, highlighting the prevalent ⟨11$\bar{2}$⟩ and ⟨1$\bar{1}$0⟩ directions as well as the surface atoms in row A (blue) and row B (red) above the subsurface layer (yellow). The locations along the ⟨11$\bar{2}$⟩ direction of the HCP and FCC sites above the sub-surface layer are also indicated; the atoms in the surface layer are located near or between these high-symmetry locations. Image is adapted from reference [41].

Even though Au is not one of the most chemically active metals, it has very high electronegativity, which tend to trigger strong interactions with the oxide films via charge transfer processes [44]. Experimental trials of growing oxide thin films on reconstructed Au(111) templates include TiO_x [8-10, 44, 46-47], BaO_x [48], FeO_x [49-50], VO_x [51-53] and CeO_x [54]. When the thin film is within monolayer thickness, the interaction between films and substrates can already be strong enough to lift the herringbone structures. In those cases the herringbone lines wind around the oxide islands instead of being underneath. The formed oxide-Au interface releases the herringbone reconstruction of top-layer Au atoms, therefore the bulk terminated Au(111) hexagonal lattice should be used for modelling [44].

3.2 Epitaxial growth of thin films

3.2.1 Introduction

Epitaxy is the natural or artificial growth of crystals on a crystalline substrate that determines their orientations. To be defined as ‘epitaxial growth’, films must be single or multi-crystallographic orientations with respect to the substrate crystal. Thin films are generated in processes: small clusters forming from individual atoms or molecules; the

continuing nucleation, coalescent and grow; the final formation of thin films [55].

The epitaxial layer is either 'homoepitaxial' – grown onto a substrate with same composition, or 'heteroepitaxial' – grown onto a substrate with different composition or different crystal structures. Heteroepitaxial growth mode is more common. The change of free energy can be simplified into Equation 3.4:

$$\Delta G = \gamma_{fv} - \gamma_{sv} + \gamma_{fs} \tag{3.4}$$

Where ΔG represents the change in total energy during the film growth, γ_{fv}, γ_{sv} and γ_{fs} are the surface or interface free energies of the film-vapour, substrate-vapour and film-substrate interfaces respectively. Heteroepitaxy can be divided into three categories (Figure 3.3): Frank-van der Merwe (FM) growth mode, Volmer-Weber (VW) growth mode and Stranski-Krastanov (SK) growth mode.

Frank-van der Merwe (FM) growth mode: also called layer-by-layer growth mode. It will happen when Equation 3.5 is satisfied:

$$\gamma_{sv} > \gamma_{fv} + \gamma_{fs} \tag{3.5}$$

Consider Equation 3.4, $\Delta G < 0$, a decrease in the overall free energy happens. The clusters of epitaxial layer bond more strongly to the substrate than to each other and grow in a two-dimension (2D) manner. It results in the formation of a smooth, planar surface layer (Figure 3.3a).

Volmer-Weber (VW) growth mode: known as island growth mode as well. It will happen when Equation 3.6 is satisfied:

$$\gamma_{sv} < \gamma_{fv} + \gamma_{fs} \tag{3.6}$$

Compared with Equation 3.4, $\Delta G > 0$, the growing layer intends to minimize the interface energy and its own surface energy. The deposited atoms have a stronger bonding force with each other than with the substrate. Clusters nucleate in a three-dimension (3D) manner and 'ball-up' at the surface (Figure 3.3b).

Stranski-Krastanov (SK) growth mode: known as layer-plus-island growth mode.

It is a modification of the FV growth mode. During the epitaxial growth process, the energy balance changes as the result of in-situ developed strain. At the first stage of initial nucleation, a sufficient number of atoms condense on the substrate and wet the substrate surface. Due to factors including the lattice mismatch between growing layer and substrate, strain energy is produced. As the growth of the film continues, more strain energy would be developed till a significant amount. Misfit dislocations will occur for strain relief when the thickness of the film reaches a critical point, and islands will start forming (Figure 3.3c) [56-59].

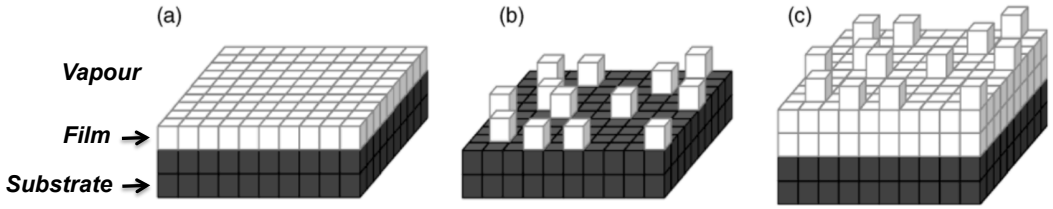


Figure 3.3: Basic models of initial nucleation in the film growth. (a) FM mode; (b) VW mode; (c) SK mode. Images are adapted from reference [59].

3.2.2 Epitaxial growth of oxide thin films on metal substrates

For the purpose of generating epitaxial thin films, the combination of substrates and deposition material is critical because the structure and properties of the thin film can be manipulated by the substrates. Metals and oxides are both used as substrates in the literature. Oxides grown on metal substrates are considered as the inverse model to understand the catalytic mechanism at a fundamental level. The commonly selected metals are relatively noble (e.g. Pd, Pt, Au, Ni, Cu), so the reactions between oxide thin films and the substrates are less likely to happen, which simplifies the study of thin films. At the same time, the preparation procedures of noble metal substrates are relatively simple. What's more, considering a lot of characterisation techniques are electron-based, metal substrates help eliminate surface charging. For the study of ultra-thin oxide films,

metals are more commonly used as substrates [44].

To fabricate monolayer oxide thin films on metal substrates, the Frank-van der Merwe (FM) growth mode is obviously favoured. In most cases of heteroepitaxy, mismatch of lattice between the epitaxial thin film and substrate exist. Stable FM growth mode can only be achieved by either controlling mismatch to a limited extent or by applying 'strong' substrates that impose their lattice constant onto the film atoms [60]. Therefore relieving strain and minimising lattice mismatch are as important as selection of substrates referring to the target thin films, and the control of growth [61].

3.3 TiO_x thin films

Titanium oxides have attracted a great deal of interests due to their remarkable properties in applications of solar cells [62-65], gas sensing [66-69] and photocatalysis [70-73]. Most studies are based on the three common TiO_2 polymorphous – rutile, anatase and brookite. Details of those structures will be introduced in section 3.3.1. For TiO_2 bulk terminations, different faces are distinctive in structure, relaxation and surface energy. Rutile TiO_2(110) is the most studied due to its stability and numerous properties [74]. After the discovery of photo assisted splitting of water on a TiO_2(110) electrode in 1972 [75], water dissociation on the rutile TiO_2(110) has been intensively investigated. This phenomenon plays a key role in using rutile TiO_2 as a photo-catalyst. Section 3.3.2 forms a review of those studies. In recent decades the investigation of TiO_x ultra-thin films has become a new trend because the possibilities of generating different structures with various properties than bulk crystal terminations. Reviews of the ultra-thin TiO_x films produced by epitaxial growth on metal substrates are presented in section 3.3.3.

3.3.1 TiO_2 polymorphs

Titanium dioxide is the only titanium oxide that exists naturally at atmospheric pressure.

It mainly exhibits three polymorphs: rutile, anatase, and brookite. Rutile is a mineral composed primarily of titanium dioxide. It is the most common natural form of TiO_2. Anatase is the phase normally found in the Sol-Gel synthesis of TiO_2. Both rutile and anatase have been well studied and used in laboratory research. Because of the difficulties encountered in order to obtain the pure phase, brookite is the least studied. Among all the three phases, rutile is the most stable form. Both anatase and brookite phases can be converted into rutile irreversibly by heating. The transition temperature varies due to parameters including particle size/shape, heating methods and impurities [76-80].

Both rutile and anatase have tetragonal symmetry but with different dimensions (rutile: $a = b = 4.584$ Å, $c = 2.953$ Å; anatase: $a = b = 3.782$ Å, $c = 9.502$ Å). The building unit can be described as a disordered octahedron with one titanium atom surrounded by six oxygen atoms (TiO_6). In both unit cells, the two bonds between the Ti and O atoms at the apices of the octahedron are slightly longer. As illustrated in Figure 3.4, each octahedron has ten connecting octahedrons in rutile: two sharing-edge oxygen pairs and eight sharing-corner oxygen atoms. While in anatase, each octahedron connects to eight octahedrons: four sharing-edge oxygen pairs and four sharing-corner oxygen atoms. In each tetragonal cell, rutile has two TiO_2 groups while anatase has four. The brookite phase has a more complicated structure and larger cell volume. It belongs to the orthorhombic system ($a = 5.436$ Å, $b = 9.166$ Å, $c = 5.135$ Å) and consists of eight formula units (TiO_2) in one orthorhombic cell. The basic building unit of brookite is also an octahedron (TiO_6) but with stronger disorder – all the Ti-O bond length and O-Ti-O bond angles are different. Referring the crystal structure shown in Figure 3.4, the brookite structure can be described as an octahedra sharing three edges: one determines the crystal distribution along the [100] direction, while the other two are along [001] [81-83].

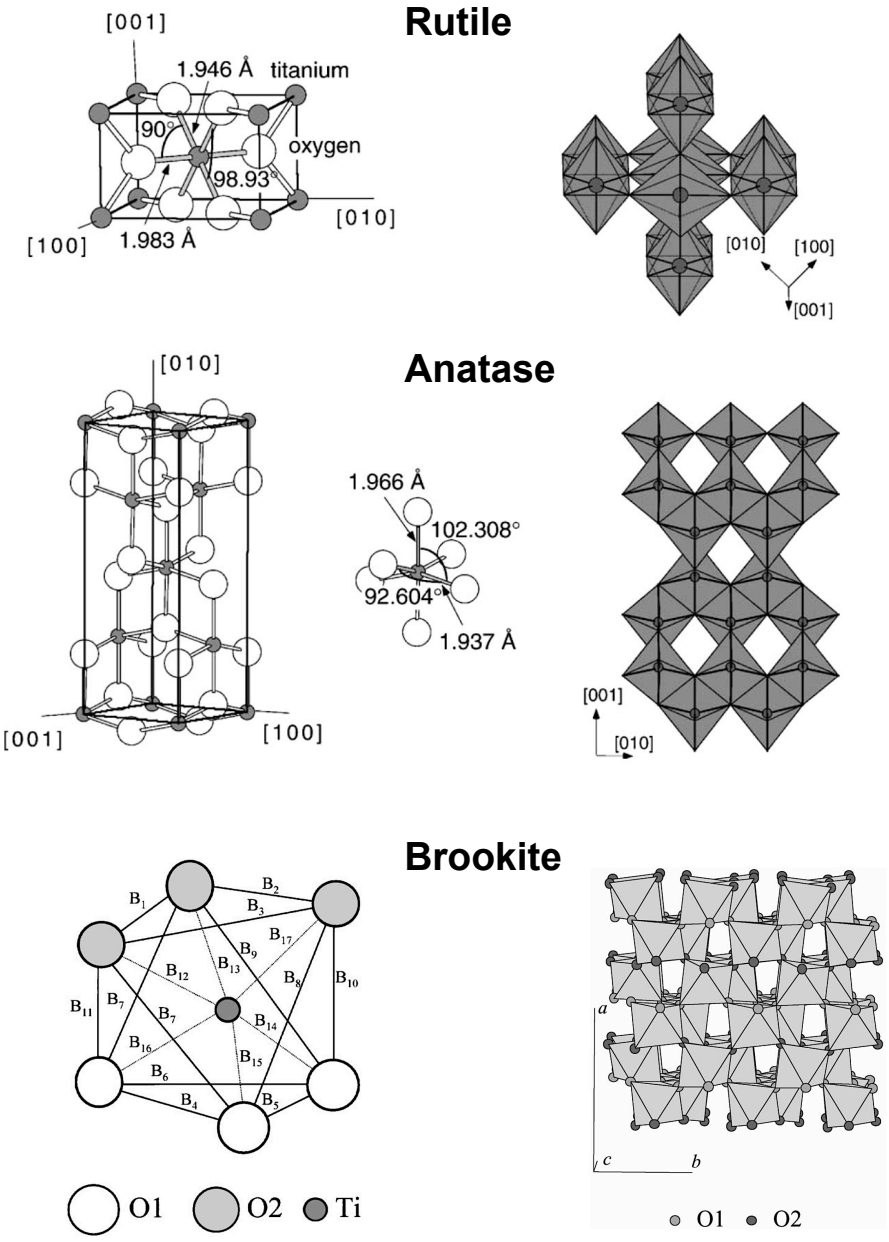


Figure 3.4: Bulk structure of rutile, anatase and brookite. For rutile and anatase structures, the small dark balls are Ti atoms, and the big white balls are O atoms. Slightly distorted octahedra is the basic building block for rutile and anatase structures; the bond lengths and angles of the octahedrally coordinated Ti atoms are indicated and the stacking of the octahedral in those two structures is shown on the right side. Images are adapted from reference [82]. For brookite structure, the left side is the representative octahedron of brookite's crystalline structure. Setting the crystallographic data for present analysis as $a = 9.182$ Å, $b = 5.456$ Å, $c = 5.143$ Å, using these lattice parameters and atom positions, the bond lengths in the figure have the following values: B_1 = 3.02 Å, B_2 = 2.84 Å, B_3 = 2.75 Å, B_4 = 2.77 Å, B_5 = 2.51 Å, B_6 = 2.83 Å, B_7 = 2.65 Å, B_8 = 2.99 Å, B_9 = 3.19 Å, B_{10} = 2.69 Å, B_{11} = 2.51 Å, B_{12} = 1.87 Å, B_{13} = 2.30 Å, B_{14} = 1.95 Å, B_{15} = 1.92 Å, B_{16} = 1,93 Å, B_{17} = 1.83 Å. The crystal structure of brookite is shown on the right side. Images are adapted from reference [83].

As the result of the crystallographic variety, different phases of TiO_2 exhibit distinct properties. Rutile shows unique applications in earth science. It is an economically important mineral as being applied in the manufacture of white TiO_2 pigment (a component in products including paint, paper and plastic) [84]. Rutile has a high refractive index, therefore it is widely used in interference applications like antireflective coatings [85-86]. The anatase phase has superior properties related to photoactivity, so it is favoured as a catalyst [87-89]. The pure brookite phase is comparatively hard to produce, which limits its applications for a long period. In recent years, with the increasing interest in the photocatalytic properties of brookite and the development of preparation methods (e.g. hydrothermal treatment), pure-phase brookite catalysts are now showing great potential [81, 90-92]. Apart from single-phase TiO_2, mixed-phase titanium oxides are commonly used, especially as commercial photocatalysts [93-97].

3.3.2 Defects and water dissociation on the rutile TiO_2(110) surface

The rutile TiO_2(110)-(1 × 1) surface has emerged as the prototypical metal oxide surface for fundamental studies on transition metal oxides. Numerous experimental and theoretical investigations of the rutile (110) face have been published [98-102]. Figure 3.5 shows a high-resolution STM image of a typical rutile TiO_2(110)-(1 × 1) surface. In the literature it has been argued that the bright lines running along the [001] direction are five-fold coordinated in-plane Ti atom rows under normal positive tunnelling condition [103-106]. Diebold et al. reported two kinds of point defects as labelled in Figure 3.6a: bright features centred on dark rows (type-A) and dark spots on bright rows (type-B). When exposing the sample to molecular oxygen at room temperature, the density of type-A defects drops while the density of type-B stays. So that the type-A defect was assigned as single oxygen vacancies (Figure 3.6b) [107]. However, Suzuki et al. argued that some of the type-A defects should be hydroxyl groups [108]. In 2001,

Schaub et al. identified both oxygen and hydroxyl defects through STM imaging and DFT calculation, and carried out the experiment of water dissociation on rutile TiO_2(110)-(1 × 1). Figure 3.7 shows the simulated STM images of individual defects based on the DFT calculation. Comparing Figure 3.7b against 3.7c, oxygen vacancies are clearly more extended than hydroxyl groups as the result of strong de-localisation of the two electrons. After exposing sample to sub-monolayer water through temperature programed deposition (TPD), they recorded the evidences of a doubling density of type-A defect, and the formed OH groups all situated at bridging oxygen sites. This phenomenon is explained as water molecules adsorb in oxygen vacancies and dissociate in-site; two hydroxyl groups are created per initial vacancy. Oxygen vacancies in the surface layer are identified as the active site for water dissociation through the transfer of one proton to a nearby oxygen atom, forming double-numbered hydroxyl groups [109]. A large number of following investigations confirmed this conclusion [106, 110-117]. Recent study also reported that water dissociation at oxygen vacancies quenches the dissociation on the defect-free area, which confirms the crucial role of defects in water dosing experiments of titanium oxides [118-121].

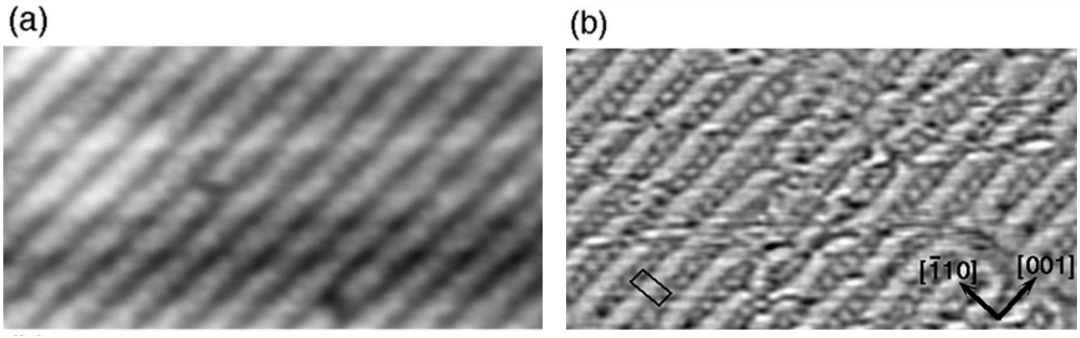


Figure 3.5: (a) Typical empty states STM image of the TiO_2(110)-(1 × 1) surface (image size: 95 Å × 50 Å; V_s = 4.0 V, I_t = 0.1 nA). The bright rows are thought to be due to titanium ions. (b) High resolution image of the (1 × 1) reconstruction recorded using a high tunneling current and low bias voltage which results in a very small tip-sample separation (image size: 95 Å × 50 Å; V_s = 0.75 V, I_t = 2.0 nA). A surface unit cell (6.5 Å × 3.0 Å) is indicated which contains contributions from both titanium and oxygen ions. To enhance the contrast in the image, low-level filtering was performed. Images are adapted from reference [104].

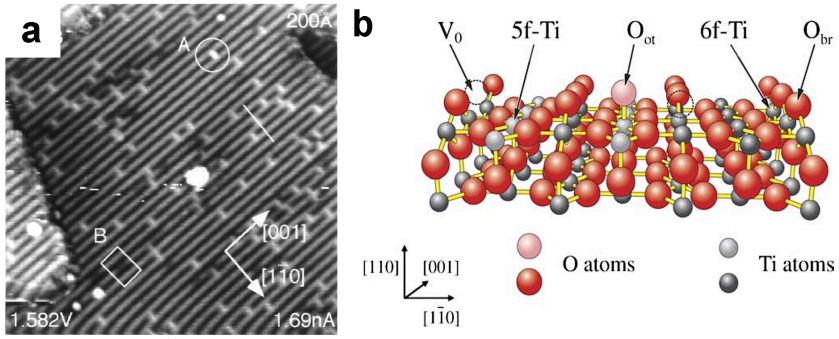


Figure 3.6: (a) STM image showing defects (labelled as 'A' and 'B'). Image is adapted from reference [107]. (b) Ball-and-stick model of rutile TiO_2(110)-(1 × 1) surface. Large red balls represent O atoms, and small grey balls represent Ti atoms (five-fold coordinated 5f-Ti and six-fold coordinated 6f-Ti). O atoms at bridging sites O_{br}, O atoms at on-top bonded site O_{ot} and a point defect V_o (missing O atom in the bridging oxygen rows) are indicated. Image is adapted from reference [116].

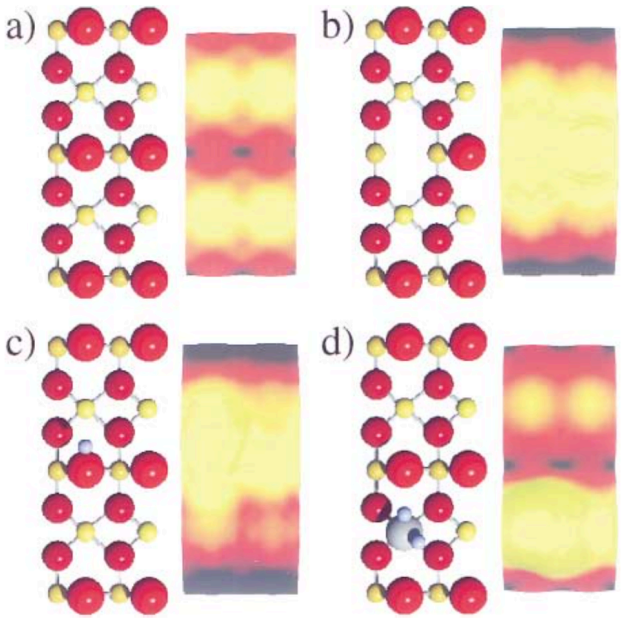


Figure 3.7: Ball-and-stick model and corresponding simulated STM image at 1 V showing the appearance of (a) vacancy-free surface, (b) bridging oxygen vacancy, (c) bridging OH group, and (d) water molecule on top of a five-fold coordinated Ti atom. Red atoms: O; yellow atoms: Ti; blue atoms: H. Images are adapted from reference [109].

As the investigations continued, the assignment of type-A defects has been reversed from what Schaub et al. reported [109]. In STM experiments, type-A defects could be removed by scanning the surface with a raised sample bias of +3 V. Diebold et al.

suggested this tip-induced defect removal was due to oxygen vacancies being refilled [107]. While Suzuki et al. believed that since type-A defects were unsaturated oxygen being absorbed on hydrogen adatoms and stabilised as hydroxyl, the high-bias scanning caused desorption of hydroxyl [108]. Bikondoa et al. carried out investigations combining the voltage-pulsing study and water dosing. Figure 3.8 shows that only brighter type-A defects could be removed by high-bias scanning. A surface area with only dark type-A defects was exposed to water and a replenishment of bright type-A defects was observed afterwards. This means the water dissociation happened and the dark type-A defects are oxygen vacancies, while the brighter type-A defects are hydroxyl groups [106, 122]. Evidences have been reported to support this conclusion [111, 114, 116, 123-125].

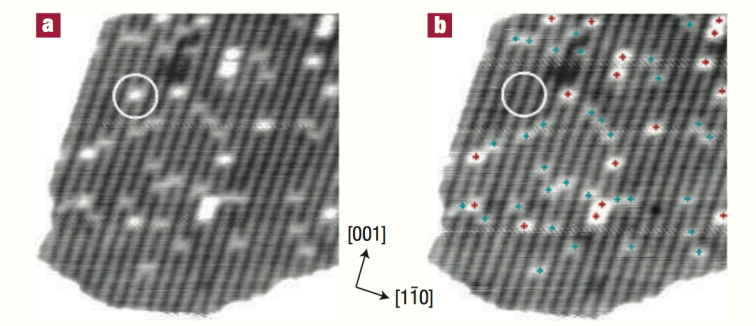


Figure 3.8: 15 × 15 nm^2 STM images of as-prepared TiO_2(110) (a) before and (b) after the voltage pulse (3 V, 0.35 nA, 300 ms) was applied to the bright defect in the circle. Brighter and dark type-A defects are labelled as red crosses and green crosses respectively. Images are adapted from reference [122].

Intensive studies about defects on rutile TiO_2(110) have been carried out [117, 126-145]. It is obvious that deeper insight of defects on titanium oxides will continue to be attractive because of its vital importance in the photochemical reactions. It is worth mentioning that various experimental methods of creating atomic defects on TiO_2 including annealing [82, 112, 146-147], Ar^+ ion bombardment [146, 148], electron bombardment [123, 146, 149-150], electron-stimulated deposition [151], and reactions with water/hydrogen [106, 108, 122, 146, 152-153] have been explored. However, most

experimental trials can only control the atomic defects at the macro-scale. In 2012, Minato et al. published a paper of creating single oxygen vacancy on TiO_2 via STM. As shown in Figure 3.9, a bridging oxygen vacancy could be created or moved through applying a high sample bias pulse for 1 s. Feedback loop was turned off to maintain the tip z-position during the process. Even though the mechanism of this STM-induced method of creating defects is still unclear, an electron field between STM tip and the sample surface was suggested to be responsible for the reactions [154-155]. This discovery provides a practical way to excite single defects in a well-controlled manner via STM. The diffusion of hydroxyl groups in rutile TiO_2(110) surfaces was reported by Schaub et al. in 2003 [156] and corrected by Wendt et al. in 2006 [111]. The diffusion proceeded exclusively perpendicular to the bridging oxygen rows direction of [001]. The adsorbed water molecules (situated at Ti rows) mediated the vacancy mobility by protons transfer. No diffusion of hydroxyl groups was observed in rutile TiO_2(110) surface before water exposure. Diffusion of oxygen vacancies was observed both along Ti rows and O rows with mediation of acetone [157].

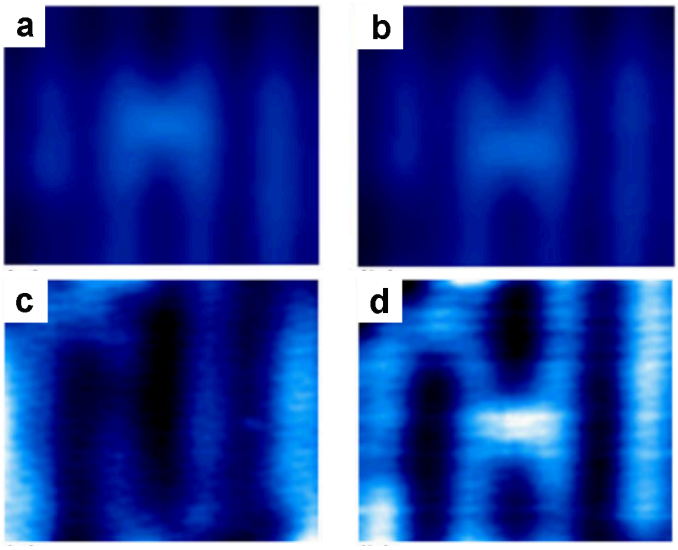


Figure 3.9: STM image of TiO_2(110) surface (a) before and (b) after the positive pulse injection (Image size: 3.5 nm × 3.0 nm; V_s = +1.5 V, I_t = 0.3 nA, T_s = -195 °C). The applied pulse was V_s = +3.5 V. Oxygen vacancy was moved to a lower position along [001] direction. STM image of TiO_2(110) surface (c) before and (d) after the negative pulse injection (Image size: 3.5 nm × 2.9 nm; V_s = +1.5 V, I_t = 0.3 nA, T_s = -195 °C). The applied pulse was V_s = -2.0 V. An oxygen vacancy was created. Images are adapted from reference [154].

3.3.3 TiO_x ultra-thin films

Titanium oxides ultra-thin films grown on substrates have been a hot topic over the past decade, driven by their distinctive structural, electronic and chemical properties that are not shown in bulk titanium terminations. Investigations have revealed new structures of titanium oxides that have been generated due to the strong influence of substrates. Experimental trials include both metal supports like Ru(0001) [158], Pt(111) [159-164], Pt_3Ti(111) [165-166], Mo(112) [167-170], Cu(001) [171-172], Au(111) [8, 46, 173], and oxide substrates like $SrTiO_3$ [174-177], $LaAlO_3$ [178-180], MgO [181-182], Al_2O_3 [183-185]. In this section, TiO_x ultra-thin films grown on metal substrates of Ru(0001), Pt(111) and Au(111) are reviewed.

TiO_x/Ru(0001)

A. Männig *et al.* reported TiO_x epitaxial films with a thickness ranging from sub-monolayer up to 3 ML grown on Ru(0001) in 2005 [158]. Samples were prepared by depositing Ti onto the clean Ru(0001) substrates in 10^{-5} Pa O_2 at 367 °C, then post-annealed in either an O_2 atmosphere or in UHV. Different structures were observed due to the variation in preparation conditions.

Firstly the post-annealing temperature was set at 527 °C for 60 s to study the difference made by post-annealing with or without oxygen. Film coverage varies from sub-monolayer to 1.4 MLs. Figure 3.10a illustrates that 0.5 ML coverage thin film being post-annealled in O_2. A surface being homogeneously covered by a large number of small equilateral-like triangle islands was formed. Triangle islands formed by post-annealing in UHV are significantly different in size, density and distribution (Figure 3.10b). In total, UHV annealing results in less ordered structures than O_2 annealing.

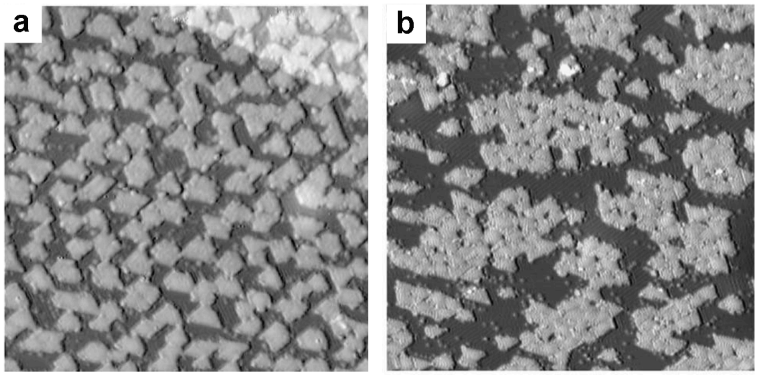


Figure 3.10: STM images of a 0.5 ML TiO_x covered Ru(0001) surface upon Ti deposition at 367 °C in 10^{-5} Pa O_2 and subsequent 60 s annealing at 527 °C in (a) 10^{-5} Pa O_2 (image size: 50 nm × 50 nm; V_t = 1.3 V, I_t = 178 pA); (b) UHV (image size: 46 nm × 46 nm; V_t = 1.15 V, I_t = 62 pA). Images are adapted from reference [158].

A comprehensive study of the structure and chemical composition of TiO_x ultra-thin film was carried out. 1 ML TiO_x was grown by annealing at 427 °C for 60 s with oxygen. A nearly closed film consisted of triangles in the first layer was observed. Addition triangle islands formed on the second layer. Flash annealing with oxygen helped to smooth the thin film and improved the order of periodic structure with triangle and occasionally rhombohedral elements (Figure 3.11a & b). The triangle structure was determined to be a non-rotated ($6\sqrt{3} \times 6\sqrt{3}$) superstructure with a periodicity of 2.85 nm by LEED, however it doesn't fit the STM images (Figure 3.11b). Further flash annealing induced two different surface structures (Figure 3.11c): majority well-ordered arrays of triangle islands and minority zig-zag structures.

A Moiré pattern was proposed to explain the ($6\sqrt{3} \times 6\sqrt{3}$) superstructure. The O-Ti-O tri-layer stacking could be viewed as TiO_2 octahedrons (Figure 3.12a) lying on Ru hexagonal substrate, which results in a pinwheel pattern with periodicity of about 2.7 nm (Figure 3.12c). This is a bit smaller than the result of LEED pattern (about 2.85 nm). However the STM images illustrate a surface containing coalesced triangle islands (Figure 3.11b). It was explained by the structural defects and irregularities in the O-Ti-O layer.

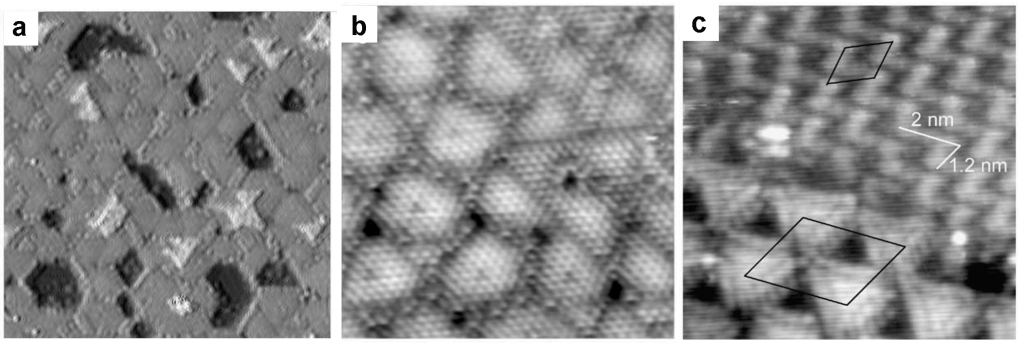


Figure 3.11: STM image of 1 ML TiO_x on Ru(0001) after different post-annealing procedures: (a) sample went through 427 °C annealing for 60 s in 10^{-5} Pa O_2 first, then annealed at 627 °C for 1 s in 10^{-5} Pa O_2 (image size: 21 nm × 21 nm; V_t = 1 V, I_t = 178 pA); (b) with additional annealing after (a) at 727 °C for 1 s in 10^{-5} Pa O_2 (10 nm × 10 nm; V_t = 0.9 V, I_t = 178 pA); (c) sample went through 427 °C annealing for 60 s in UHV first, then following with treatment of further annealing at 727 °C for 1 s in UHV (image size: 10 nm × 10 nm; V_t = 1 V, I_t = 450 pA). Images are adapted from reference [158].

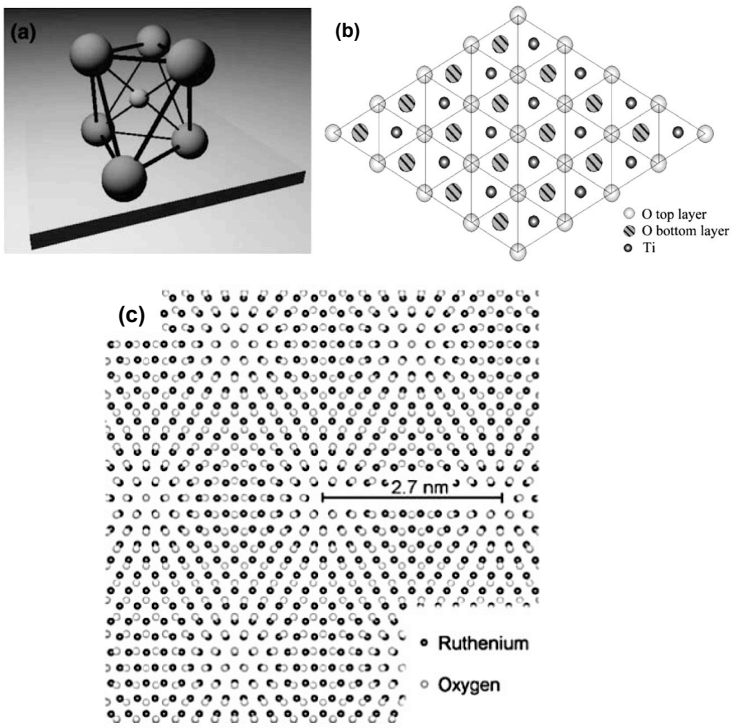


Figure 3.12: (a) Model for a TiO_2 monolayer, which shows an octahedron with one of its triangular faces parallel to the substrate. (b) Schematic top-view of the TiO_2 layer. The O atoms of the topmost layer have a distance of about 0.3 nm. (c) Moiré pattern which results from a superposition of the Ru(0001) surface lattice and an overlayer with a surface lattice constant of 0.3 nm. Images are adapted from reference [158].

TiO_x/Pt(111)

The idea of growing TiO_x thin films on Pt(111) comes from the strong metal support interaction (SMSI) in titania-supported Pt catalysts. The reversed system of TiO_x on the Pt metal is believed to have a similar synergistic effect between supports and thin films [161]. In 1995, Boffa et al. reported a ($\sqrt{43} \times \sqrt{43}$)R7.6° three-fold symmetric structure with a unit cell of 18.2 Å × 18.2 Å and stoichiometry of TiO_2 formed on Pt(111) at coverage between 1 and 5 MLs. A TiO_2(111) rutile surface plane of nearly close-packed O^- ions was suggested as the matching model. By heating up to 650 °C – 850 °C in UHV, an ordered overlayer with a unit cell of 18.2 Å × 13.9 Å and stoichiometry of Ti_4O_7 was generated at coverage of 1-1.5 MLs. The reduced surfaces of TiO_2(110) was recommended as a similar model. Due to the limitation of techniques at that time, resolution of STM images taken for those thin films was not high enough to define the accurate atomic models [159].

Sedona et al. reported a comprehensive study of six different structures of ultra-thin TiO_x films on Pt(111) in 2005 [160]. Deposition of Ti was performed in 10^{-4} Pa O_2 via an E-beam evaporator. Various TiO_x phases were observed as the function of the initial Ti dose and of the post-annealing conditions. Six structures with corresponding LEED patterns and high-resolution STM images are illustrated in Figure 3.13 & 3.14. In low coverage (0.4 ML), *Kagomé-Like phase* (*k*-TiO_x) formed. It shows a ((2.15 ± 0.05) × (2.15 ± 0.05)) hexagonal superstructure with respect to the Pt(111) substrate. As drawn on Figure 3.14a, a structural model with stoichiometry of Ti_2O_3 was built. According to the XPS results, an O-Ti stacking with Ti sitting at three-fold hollow sites of Pt(111) and O sitting at Ti bridging sites was suggested. When Ti coverage went up to 0.8 ML, two *Zigzag-Like phases* (*z*-TiO_x & *z'*-TiO_x) formed. Annealing in oxygen resulted in the *z*-TiO_x (Figure 3.14b) while annealing in UHV formed *z'*-TiO_x (Figure 3.14c). For *z*-TiO_x, an incommensurate superstructure with a rectangular unit cell of about (6.8 ± 0.1) Å × (8.6 ± 0.1) Å was analysed from LEED pattern, which has good agreement with the STM image. Even through the topography of *z'*-TiO_x is very similar to the *z*-TiO_x in the STM

images, LEED pattern illustrates a different unit cell of 16.6 Å × 14.4 Å. An O-Ti bilayer stacking exposing an oxygen terminal was proposed for *z*-TiO_x, while for the suggested bilayer structural model of *z'*-TiO_x, Ti occupied both the interface of Pt hollow sites and the outermost-layer as substitution of an O atom at kink sites of the zigzag. The *Rectangular Stoichiometric Phase* (*rect*-TiO_2) was best obtained by over 0.8 ML Ti deposition following with annealing at high temperature in rich oxygen (Figure 3.14d). A rectangular unit cell of (3.8 ± 0.1) Å × (3.0 ± 0.1) Å and the stoichiometry of TiO_2 was suggested. The structural model was believed to be octahedrally coordinated Ti atoms with O atoms on both sides of terminations. Figure 3.14e & f illustrate two *Wagon-Wheel-Like phases* (*w*-TiO_x and *w'*-TiO_x) at the coverage of 1.2 MLs. High quality *w*-TiO_x film was generated by annealing at 550 °C in oxygen, and *w'*-TiO_x was obtained by further annealing in UHV. The proposed hexagonal coincidence lattice of *w*-TiO_x was (√43 × √43)R7.6° with periodicity of 18.2 Å, and the pinwheel lattice of *w'*-TiO_x was (7 × 7)R21.8° with periodicity of 19.4 Å. Both structures were suggested to consist of O-Ti bilayer with Ti at the interface [160].

Following the study of TiO_x/Pt(111), comprehensive investigations of individual structures were carried out. For example, the complete structural characterisation and potential of using *Zigzag-Like* TiO_x as templates for growth of metal clusters [163, 186], the detailed structural and electronic properties of TiO_x thin films including *k*-TiO_x, *Zigzag-Like* TiO_x and *Wagon-Wheel-Like* TiO_x [162, 164, 187-188], the catalysis of reduced TiO_x thin films (*z'*-TiO_x, *w'*-TiO_x and *rect*-TiO_x) in the Au/TiO_x/Pt(111) model [189-190].

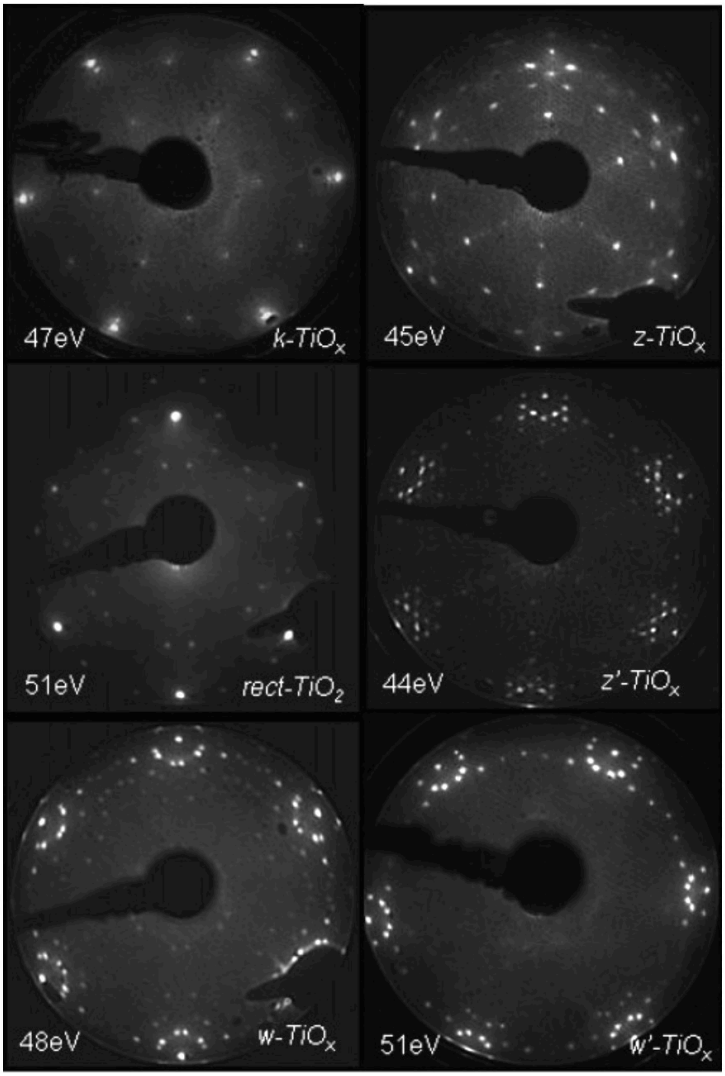


Figure 3.13: Summary of LEED patterns of the observed TiO_x films on Pt(111). Images are adapted from reference [160].

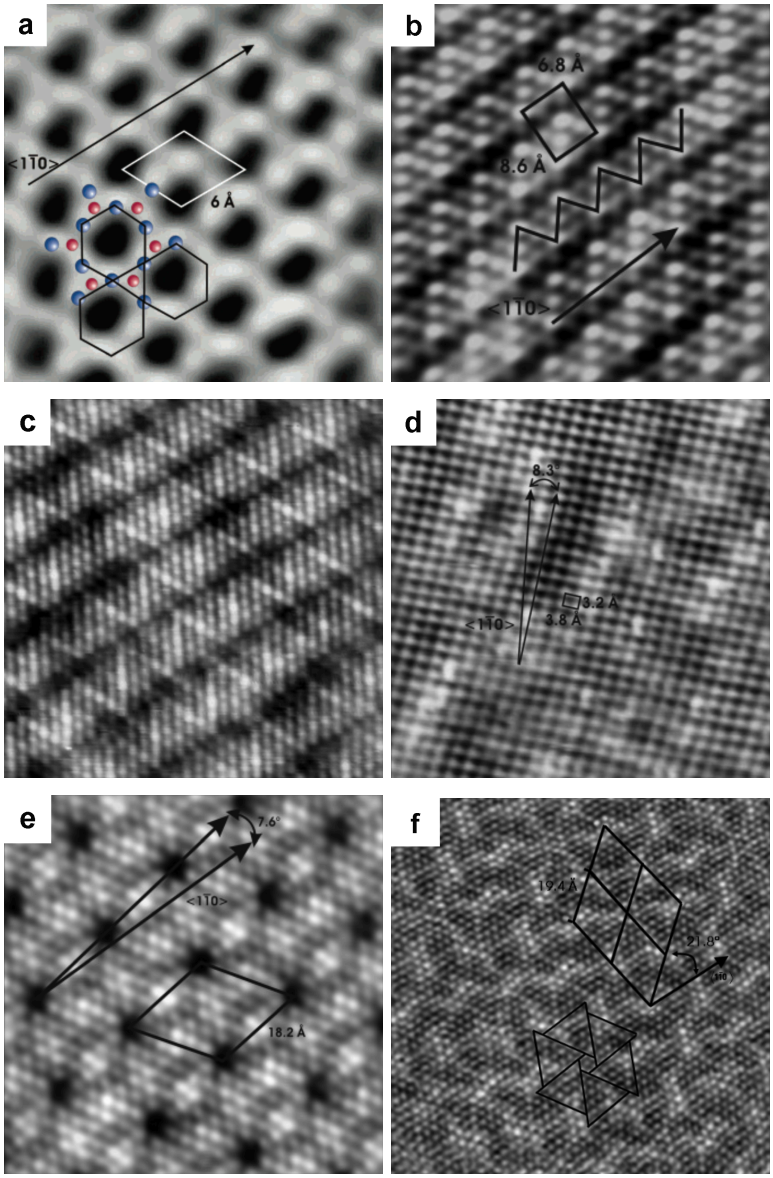


Figure 3.14: STM images of six different structures of TiO_x thin films grown on Pt(111). (a) *k*-TiO_x (Image size: 30 Å × 30 Å; V_s = -0.4 V, I_t = 1.06 nA). Blue balls drawn on the image present O atoms while red ones are Ti atoms. (b) *z*-TiO_x (Image size: 60 Å × 60 Å; V_s = 0.1 V, I_t = 1.5 nA). (c) *z*′-TiO_x (Image size: 90 Å × 90 Å; V_s = 0.8 V, I_t = 1.5 nA). (d) *rect*-TiO_x (Image size: 90 Å × 90 Å; V_s = 0.8 V, I_t = 1.8 nA). (e) *w*-TiO_x (Image size: 75 Å × 75 Å; V_s = 1.3 V, I_t = 1.9 nA). (f) *w*′-TiO_x (Image size: 126 Å × 126 Å; V_s = 0.2 V, I_t = 1.0 nA). Images are adapted from reference [160].

TiO_x/Au(111)

Since TiO_2 supported Au nanoclusters have shown high efficiency in multiple catalytic reactions [73, 191-199], the inverse TiO_x-on-Au catalyst models have been investigated with great expectations. Many experimental trials of titanium oxide nano-particles

deposited on Au(111) can been found [47, 200-209]. In most cases, structures of the formed titanium oxides can be found in the TiO_2 bulk terminations.

In recent years, a trend of growing TiO_x ultra-thin films with new structures on Au(111) substrates has been started. A comprehensive study of different ultra-thin TiO_x films grown on reconstructed (22 × √3)-Au(111) was firstly carried out by Wu et al. [8]. Ti was deposited at room temperature by an E-beam evaporator, followed by oxidising samples at 600°C in 10^{-6} Pa O_2 for half hour. Different ordered TiO_x structures formed with increasing Ti deposition. A hexagonal honeycomb structure was observed at low coverage. The high-resolution STM image in Figure 3.15 illustrates a (2 × 2) superstructure referring to the Au substrate. A structural model of honeycomb was suggested (Figure 3.16): Ti atoms occupy the three-fold hollow sites of Au lattice and form a hexagonal ring with (2 × 2) relationship to the Au substrate; O atoms locate at the bridging sites of Ti atoms. Therefore the stoichiometry is Ti_2O_3, which matches the Auger Electron Spectroscopy (AES) result. When the coverage of the thin films went up to about 1 ML, a pinwheel structure appeared. Figure 3.17a-c show the high-resolution STM images of the pinwheel structure: six interlocking triangles go around a central hub. A Moiré pattern with (√67 × √67)R12.2° reconstructed superstructure was developed in Figure 3.17d. A stoichiometry of TiO and Au-Ti-O stacking with O atoms sitting on the hollow sites or bridging sites of Ti atoms was suggested. The honeycomb phase can be converted into the pinwheel phase via UHV annealing, which demonstrates that the pinwheel is more reduced than the honeycomb. Triangle islands with multiple shapes and thicknesses dominated the surface structure when the thin film coverage went over 1 ML. AES result suggested a stoichiometry of $TiO_{1.30\pm0.04}$. When coverage went up to about 5 MLs, a row-like structure emerged along directions of $[\bar{1}01]$, $[1\bar{1}0]$ and $[01\bar{1}]$.

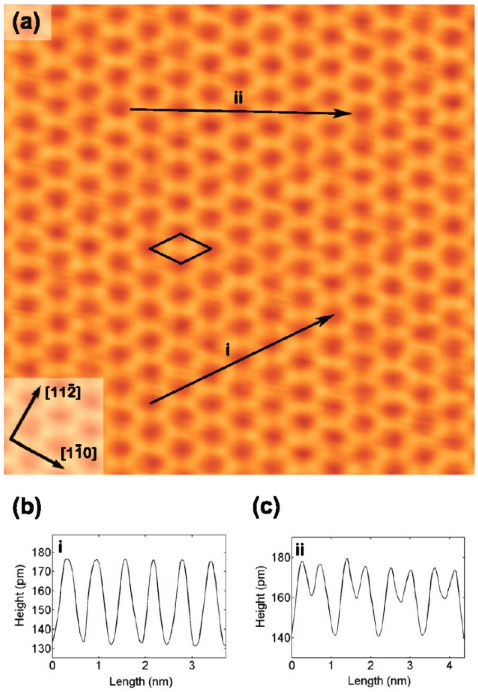


Figure 3.15: (a) High resolution STM image of the honeycomb structure with bright Ti atoms forming hexagonal rings. A (2 × 2) unit cell is indicated in the image (Image size: 8.5 × 8.5 nm^2, V_s = 0.98 V, I_t = 0.20 nA). (b), (c) Profiles taken along arrows marked as "i" and "ii" in (a), respectively. Images are adapted from reference [8].

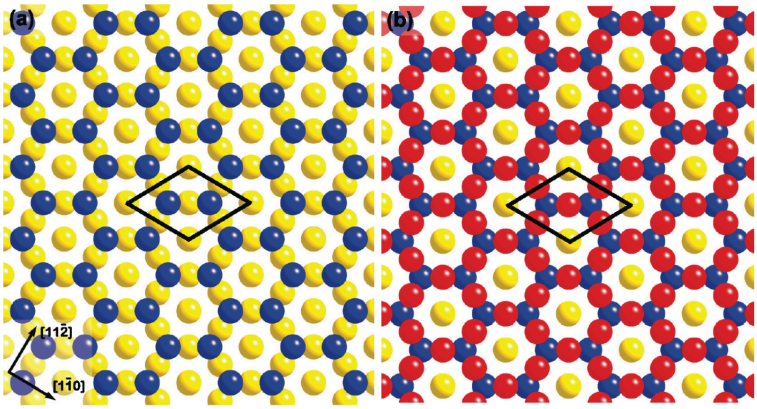


Figure 3.16: An atomic model for the hexagonal honeycomb structure with Ti atoms sitting in 3-fold hollow sites of the Au(111) substrate. Au atoms are yellow while Ti atoms are blue. (b) Same model with oxygen atoms (red) located at the bridging sites of the Ti atoms. The (2 × 2) unit cell is indicated on both images. Images are adapted from reference [8].

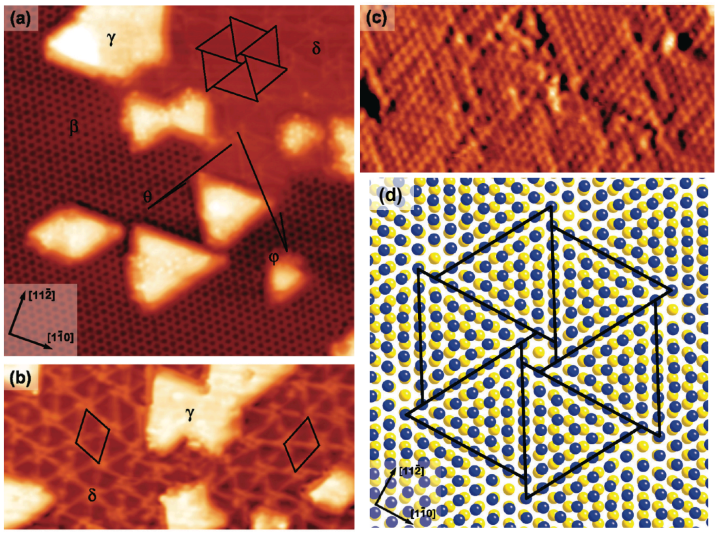


Figure 3.17: STM image of a TiO_x surface with coexisting honeycomb structure, pinwheel structure and triangle islands. An asymmetrical pinwheel is drawn with black lines as six triangles. Those spokes of the pinwheels are rotated by θ (2°) and φ (13°) with respect to the honeycomb structure (Image size: 24 × 24 nm^2, V_s = 0.98 V, I_t = 0.20 nA). (b) STM image showing two domains of the pinwheel structure (Image size: 31 × 14 nm^2, V_s = 1.41 V, I_t = 0.18 nA). (c) Constant height atomic resolution image of the pinwheel structure (Image size: 11 × 5 nm^2, V_s = -0.12 V, I_t = 0.50 nA). (d) The (√67 × √67)R12.2° reconstructed Moiré pattern model for the pinwheel structure where Ti atoms are arranged in a rotated lattice (blue, 3.27 Å periodicity) on the Au(111) surface (yellow, 2.89 Å periodicity). The position of the oxygen atoms is not shown. The six triangles that make up the pinwheel are drawn on the image. Images are adapted from reference [8].

Tumino et al. reported the 2D TiO_x ultra-thin films grown on Au(111) substrates through a very similar physical vapour deposition (PVD) technique [9]. Different from Wu et al.'s study, a Au(111) single crystal was used as the substrate in the experiments, which led to some changes in sample preparation processes. The honeycomb structure was generated in low coverage, and a (2 × 2) superstructure and stoichiometry of Ti_2O_3 was realised through measurements of STM profiles, LEED pattern, scanning tunnelling spectroscopy (STS) and density functional theory (DFT) calculation, which supports the conclusion of Wu et al. (Figure 3.18a & c). The pinwheel structure was observed as well in a wide range of surface coverage, however a (4√7 × 4√7)R19.1° superstructure with a periodicity of about 30 Å was proposed (Figure 3.18b-d). Triangle islands were found to grow on top of both honeycomb and pinwheel phases. High resolution STM image

(Figure 3.19a) confirms Wu et al.'s prediction that this structure is formed with a stacking of different layers. Row phase was reported at surface coverage of about 1-1.5 ML: rows orients along $[11\bar{2}]$ direction in Figure 3.19b; different domains could be observed with 120° to each other. The rectangular unit cell was suggested to be (5.7 ± 0.2) Å × (29 ± 0.5) Å (Figure 3.19c). This phase is similar to the star phase reported by Ragazzon et al., which was believed to be rutile-TiO_2(100) [10]. Another phase found at high coverage is needle-like structure (Figure 3.19d). The 'needle' typically has a width of about 5 nm and a length up to about 150 nm. Detailed study of this structure was not carried out.

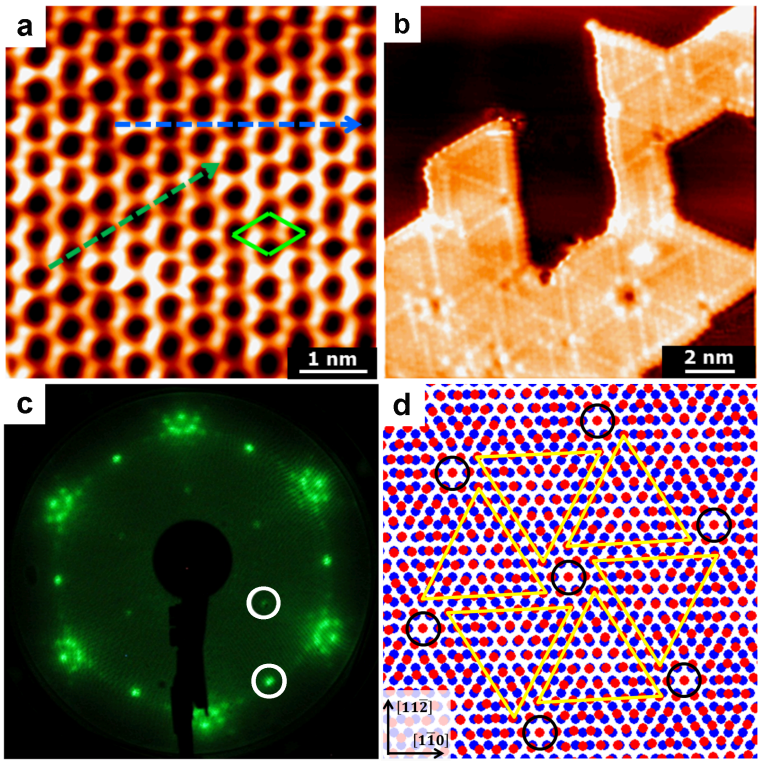


Figure 3.18: (a) STM image of the honeycomb phase at 1.5 ML coverage (V_s = 0.60 V, I_t = 0.20 nA). Unit cell is drawn in the picture. (b) STM image at 0.7 ML coverage showing the hexagonal pinwheel film (V_s = 1.50 V, I_t = 0.40 nA). (c) LEED pattern of surface with honeycomb and pinwheel structures at 1.5 ML coverage (50 eV). Bright spots being indicated by the white circle is the (2 × 2) honeycomb signal; the more complicated half-circle shaped signal comes from the pinwheel structure. (d) Atomic model of the Moiré coincidence pattern for pinwheel structure. Ti atoms are arranged in hexagonal lattice (red spots, 3.43 Å periodicity) rotated by 2.11° with respect to the Au lattice (blue dots, 2.89 Å periodicity). The resulting coincidence site (black circles) represented a (4√7 × 4√7)R19.1° superstructure. Yellow lines highlighted the triangular areas between the 'spokes' of the pinwheel. Images are adapted from reference [9].

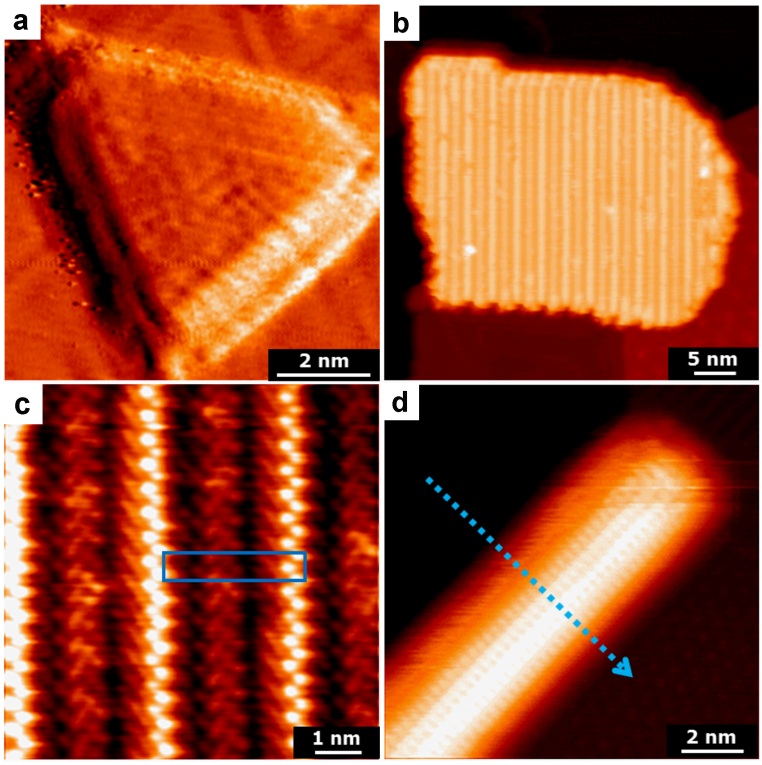


Figure 3.19: (a) Filtered STM image showing the layered structure of triangle islands (V_s = 0.80 V, I_t = 1.40 nA). (b) STM image of an island of the row phase at 1 ML coverage (V_s = 0.80 V, I_t = 0.20 nA). (c) Atomically resolved STM image of the row structure at 1 ML coverage (V_s = 0.30 V, I_t = 1.23 nA). The rectangular unit cell is drawn in the picture as a blue box. (d) Atomically resolved STM images of the needle structure at 1 ML coverage (V_s = 0.10 V, I_t = 3.10 nA). Topographic profile along the blue arrow direction is measured. Images are adapted from reference [9].

Ragazzon et al. investigated the growth of TiO_x ultra-thin films on reconstructed Au(111) substrates via chemical vapor deposition (CVD) [10, 210]. Titanium oxides nanostructures were grown by decomposition of titanium tetraisopropoxide (TTIP). Different dosing at various temperatures (200 °C – 500 °C) and post-deposition treatment created distinct phases. Figure 3.20 shows honeycomb structure at low coverage. The clear LEED pattern confirms the (2 × 2) structural model suggested by Wu et al. [8]. Figure 3.21 illustrates the star phase formed at higher coverage. High-resolution STM images of star phase exhibits parallel lines with zigzag look and another line pattern being broader but lower-height. The sides of the islands are preferentially

oriented along the ⟨1$\bar{1}$0⟩ directions of Au(111) substrate. The labeled unit cell was measured to be (24.5 ± 1.5) Å × (4.9 ± 0.14) Å, which is very close to the LEED result. They discussed that the star phase indicated an (8 × 1) reconstruction, which is similar to the (7 × 1) reconstruction of rutile TiO_2(100) on Pt(111) substrates [211]. Photoemission spectroscopy (PES) spectra suggested those two well-ordered structures being Ti_2O_3 and TiO_2 respectively [10]. In 2015, they reported the growth of TiO_2(B)(001)/Au(111) via the same technique [47]. The primitive oblique unit cell of TiO_2(B)(001) thin film is illustrated in Figure 3.22a (reference lattice parameters: b_1 = 3.75 Å, b_2 = 6.38 Å, and γ =107.1° [212]). This structure forms when the surface coverage is over 75%, and the atomic model induced from high-resolution STM images has a very good agreement with the reference model (Figure 3.22b) [47]. Apart from those three structures, a pinwheel-like phase was produced through annealing the honeycomb thin film at 500 °C [210].

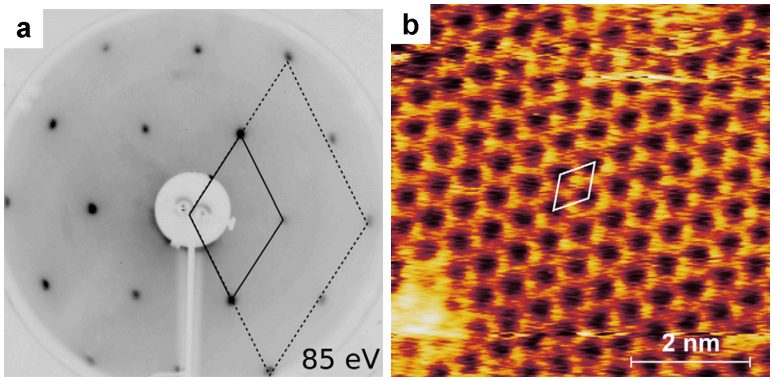


Figure 3.20: Honeycomb Ti_2O_3 on Au(111) (a) LEED pattern of the sample. The unit cell of Au(111) and the (2 × 2) unit cell of honeycomb are indicated with a dashed and a solid line respectively. (b) STM image of the sample. The unit cell is evidenced (V_s = 0.70 V, I_t = 0.23 nA). Images are adapted from reference [10].

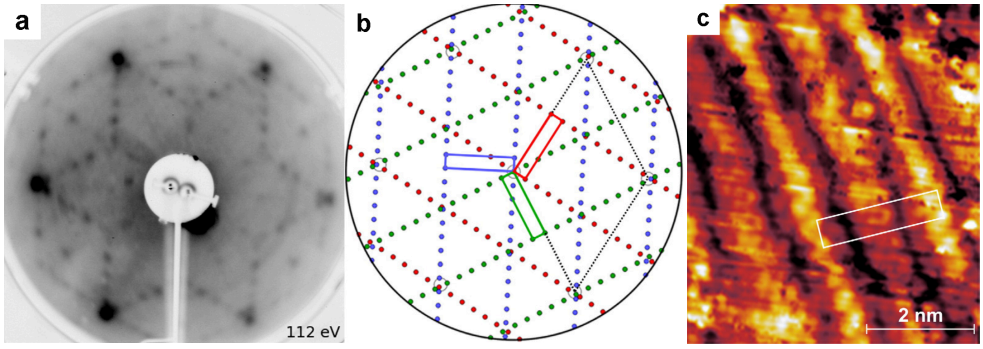


Figure 3.21: Star-TiO_2 on Au(111). (a) LEED pattern of the star phase. (b) Drawing illustrating the observed pattern in terms of three domains (red, green & blue) of a rectangular titania phase with the average lattice constants determined by LEED and STM. The surface structure appears as alternating bright zigzag lines and broader lines with a shorter apparent height. Images are adapted from reference [10].

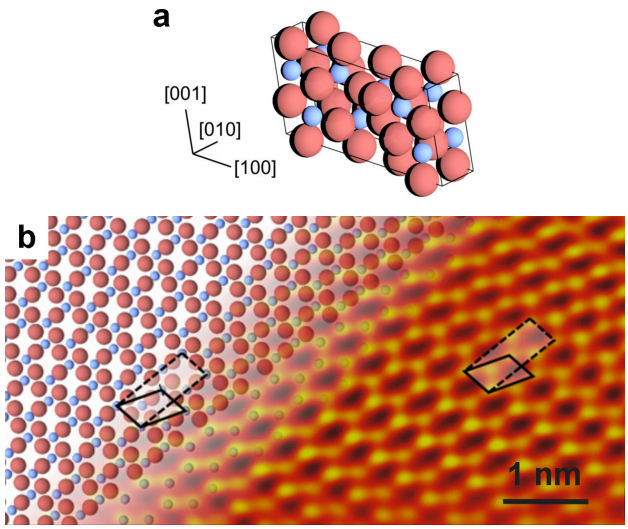


Figure 3.22: (a) Conventional unit cell of the TiO_2(B). O atoms are red and Ti atoms are blue. (b) TiO_2(B) atomic structure compared to STM images of TiO_2(B)/Au(111). Fourier-transform filtering was applied to highlight the atomic-scale periodicity. The rectangular unit cells are drawn. Images are adapted from reference [47].

Due to the high interest in the water-gas shift (WGS) reaction for TiO_x/Au(111) system, Farstad et al. studied the water adsorption and desorption of four TiO_x phases (honeycomb, star, TiO_2(B) and pinwheel) prepared by TTIP-mediated CVD [46]. In the experiment of honeycomb phase, very small amount of Ti sites were active for dissociation, and those sites were more related to the TiO_2 clusters. Therefore no water

adsorption was suggested for honeycomb phase. For star phase, the water adsorption behavior was consistent with that of rutile TiO_2(110) and (100). Only a small degree of water dissociation was observed for the TiO_2(B) phase. Defects at TiO_2(B) domain boundaries were suspected to be the dissociation sites. For the pinwheel structure, water dissociation was believed to be inherent to the oxidation of featured Ti species: about 20% of Ti sites were active for water desorption, which is about the amount of Ti sites of bright spokes and hubs in STM images [10]. They concluded that the dissociation propensity of TiO_x/Au(111) system resulted from the atomic structures of thin films and defects formed from preparation. All the discussion was based on the high-resolution photoelectron spectroscopy (HRPES) results, which makes it hard to identify the accurate sites of water adsorption.

Li et al. published their study of TiO pinwheel ultra-thin film grown on Au(111) substrate and its chemisorption of trimethyl acetic acid (TMAA) in 2014 [173]. A surface Moiré pattern was introduced to exhibit the 6-fold pinwheel pattern (Figure 3.23). Different from the literature reviewed in this section, a Ti/Au(111) alloy was first oxidised into rutile TiO_2(100) islands [202], then post-annealed in UHV to convert into a reduced pinwheel phase. The observed structure was very similar to that reported by Wu et al. [8], however a ($\sqrt{97} \times \sqrt{97}$)R15.3° reconstruction model with periodicity of 28.3 Å was suggested. This difference comes from two major modifications in this model: two atomic rows consist of triangle edges instead of one, and 10 Ti atoms form the shared triangle side instead of 8. Similar to Wu et al.'s result, Au-Ti-O stacking was argued to be preferred, and the ratio of Ti and O was about 1:1. With increasing deposition of TMAA onto the pinwheel thin film, the adsorption sequence was realised to be a consequence of a gradual shift in the relative atomic positions of TiO film with respect to the Au(111) substrates (Figure 3.24): the centre sites of pinwheel is most preferred due to the smallest Ti-O layer separation and surface dipole. This result demonstrates the suspicion of Farstad et al. that the bright spokes and hubs are responsible for water dissociation. A similar phenomenon was found in the FeO/Pt(111) system: a large in-

plane atomic spacing and a smaller Fe-O rumpling contribute to the adsorption of water monomers [213].

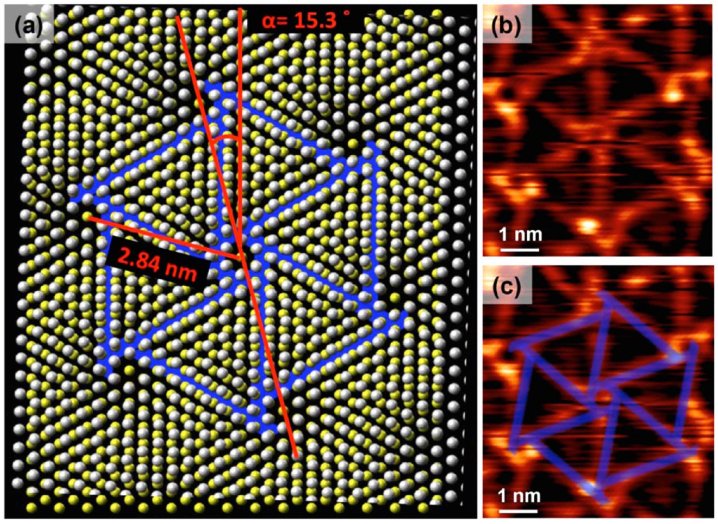


Figure 3.23: Atomic model of the pinwheel structure and a comparison with STM images. (a) Atomic model for the pinwheel structure, in which the hexagonal lattice of Ti atoms (silver), with 3.2 Å periodicity, is rotated 1.7° clockwise with respect to the Au(111) surface (gold balls, 2.89 Å periodicity). The overlap of those two layers result in a Moiré pattern which also described as a (√97 × √97)R15.3° reconstruction. Oxygen atoms are not shown for clarity. (b) Magnified STM image of one pinwheel structure. (c) The same STM image was overlapped with a half-transparent proposed atomic structure of a pinwheel for comparison. Images are adapted from reference [173].

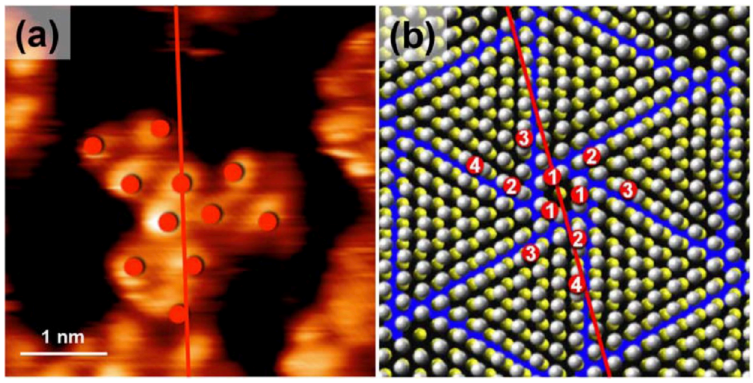


Figure 3.24: Adsorption sites of TMAA at 0.15 ML coverage. (a) STM image of TMA clusters adsorbed within the pinwheel. (b) The corresponding atomic model, which reproduces the adsorption geometry observed in (a). This image shows that the arrangement in (a) is a highly ordered arrangement of triads of TMA groups. The red balls represent TMA groups, and the numbers within the balls denote the sequence of site filling. The red lines show the orientation along the centres of pinwheels. Images are adapted from reference [173].

To sum up, the ultra-thin titanium oxide films growing on Au(111) commonly display a honeycomb structure, a pinwheel structure and triangle islands at monolayer coverage, and a row-like structure at high coverage. For the honeycomb structure, a (2 × 2) relationship to the Au substrate and stoichiometry of Ti_2O_3 has been confirmed by different research groups. Similar structure was reported in TiO_x/Pt(111) as kagomé phase (*k*-TiO_x) [160], and the proposed stoichiometry was Ti_2O_3 as well. The (2 × 2)-Ti_2O_3 honeycomb ultra-thin film grown on Au(111) is a very uniform structure. Domain boundaries rarely showed up in reported STM images. Experiments of using (2 × 2)-Ti_2O_3/Au(111) as substrate for metal deposition and growth of ultra-thin oxide films have been carried out [214]. However a comprehensive study of defects and domain boundaries of the honeycomb structure is still necessary. For the pinwheel structure, even though different superstructures and models were proposed, the similar characteristics in structure are undeniable. And it has been commonly agreed to be a more reduced oxide state than honeycomb phase. A wide variety of ultra-thin oxide films fabricated on Au(111) substrates with similarities in structural properties could be found. For example, V_2O_3(0001)/Au(111) shows a well-ordered hexagonal lattice [215]; FeO(111)/Au(111) [50], CoO(111)/Au(111) [216-217] and ZnO(0001)/Au(111) [218-219] all illustrate a hexagonal-shaped Moiré pattern.

It is worth mentioning that even though most studies of epitaxial growth of ultra-thin TiO_x films on metal substrates are for the purpose of building new structures, there are also investigations of growing epitaxial TiO_2 ultra-thin films on metal substrates that maintain the structures of bulk terminations. For example, Bennett et al. reported the epitaxial growth of stoichiometric rutile TiO_2(110) ultra-thin film on the W(100) substrate, which provides a possible way to produce technologically important rutile oxides that are not readily available (e.g. CrO_2 and MnO_2) [220-221]. After absorbing oxygen atoms, the W(100) surface shows a (2 × 1) reconstruction (6.32 × 3.16 Å), which has a good lattice match to the rutile TiO_2(110) (6.49 × 2.96 Å), and the researchers have achieved well-

oriented films. However, when the thickness of the film is less than 5 MLs, non-stoichiometric titanium oxide ultra-thin films formed due to band bending and charge transfer from the metal substrate [221-222]. Thornton et al. continued the investigation of TiO_2(110)/W(100)-O(2 × 1) ultra-thin films (less than 6 MLs) and found that the rutile TiO_2 grows as discrete islands aligned in either of the orthogonal principle directions of the W(100) substrates with (1 × 1) termination as well as (1 × 2) and (1 × 7) reconstructions [223-225].

3.4 NbO_x thin films

Similar to titanium, niobium is a transition element. The most common oxide phase is Nb_2O_5. Other oxide phases are NbO, Nb_2O_3 and NbO_2. Even though niobium oxides haven't been as commonly studied as titanium oxides, attention has been attracted due to their potentials as sensing materials [226-230], electrochromic materials [231-235] and semiconducting materials [236-239]. In recent years, research has focused on the NbO_x nanostructures with different morphologies that enable unique chemical/physical interactions at surface. In this section, the fundamental study of niobium oxides and the up-to-date fabrication and investigations of NbO_x ultra-thin films are reviewed.

3.4.1 Nb_2O_5 polymorphs

Nb_2O_5 is the main source for Nb-based materials. Naturally it is an unreactive transparent solid. Many Nb_2O_5 polymorphous phases have been reported (e.g. H-Nb_2O_5, T-Nb_2O_5, TT-Nb_2O_5) [240-246]. Generally they are based on the NbO_6 octahedral group. H-Nb_2O_5 (monoclinic) is the most stable structure, which can be produced through heating up other Nb_2O_5 phases to over 1000 °C. It has a monoclinic lattice contains (3 × 4) and (3 × 5) blocks that are formed by NbO_6 units. Within each block, NbO_6 links to

each other by sharing corners. Neighboring blocks are coupled by sharing edges with a half-unit-cell shift along *c*-axis. T-Nb_2O_5 (orthorhombic) is a metastable phase (form at 700-800 °C) that is built up with the orthorhombic unit cell. Six or seven oxygen atoms surround each Nb atom to form distorted octahedral or pentagonal bipyramids, and those polyhedras connect with each other by sharing edges/corners in *ab*-plane and corners in the *c*-axis [235, 242, 247]. Another common polymorph TT-Nb_2O_5 (pseudohexagonal) is even less stable (form at 300-500 °C). On the *ab*-plane, four, five or six oxygen atoms surround each Nb atom; and along the *c*-axis there exists an Nb-O-Nb-O chain structure [242]. This richness in structural isotropy contributes to the diverse physical and chemical properties, especially for the applications of nano-Nb_2O_5 [248-252].

3.4.2 NbO_x ultra-thin films

A lot of work on synthesis and characterisation of niobium oxide thin films has been done. Most studies concentrate on crystalline niobium oxide thin films with dozens of layers [232, 253-256], especially oxides-supported niobium thin films (e.g. NbO_x/Al_2O_3 [257-259], NbO_x/SiO_2 [260-262]). A few NbO_x ultra-thin films featuring distinctive structures and properties compared with bulk niobium oxides have been created. Based on the relevance to this work, experimental trials of growing ultra-thin film on Pt(111) [263-265] and Cu_3Au(100) [266-268], and oxidising surfaces of Nb(110)/(111)/(100) [269-275] are reviewed in this section.

NbO_x/Pt(111)

Xie et al. reported their work of epitaxial NbO_x ultra-thin film grown on Pt(111) single crystal substrate in 1994 [265]. Small amount of Nb was deposited onto the prepared Pt(111) substrate, followed by oxidation in 10^{-4} – 10^{-3} Pa O_2 and annealing at 530-630 °C to order the niobium oxide overlayer. Surface periodicities and crystal structures different from those of bulk oxides were created. Figure 3.25 shows the LEED patterns. Less oxidised NbO_x illustrates a hexagonal pattern rotated by 30° referring to Pt(111) and a

constant about 25% larger than Pt in real space. The electronic structure was suggested to be a composite of NbO, NbO_2 and Nb_2O_5. When the sample was fully oxidised, two hexagonal patterns appeared in different energy levels (Figure 3.25d), which indicates that two hexagonal lattices with different sizes coexist. Nb_2O_5 was proposed for the electronic structure. The unit cell for both structures were suspected to be highly distorted NbO_6 octahedra but with different arrangement and Nb=O surface sites. By sputtering Ar^+ on the fully oxidised Nb_2O_5 sample surface, oxygen anions were removed and oxygen vacancies were created. It was proposed in the further study that the oxygen vacancies of NbO_x surface play a key role on the adsorption of molecules [263]. In another paper, they argued that the NbO_x overlayer could segregate into Pt substrate and decompose at high temperature [264]. However, the lack of morphological studies weakens their conclusion.

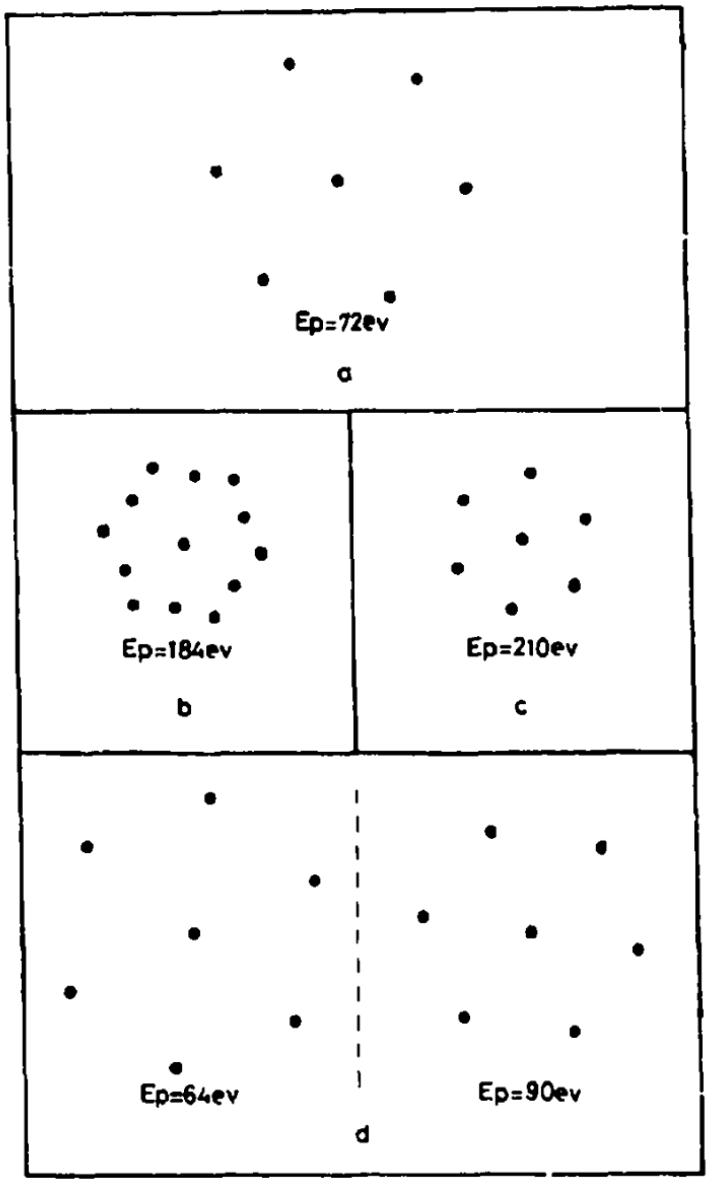


Figure 3.25: Schematic representation of LEED patterns observed with (a) the clean Pt(111)(1 × 1) substrate, and (b) a NbO_x overlayer of 0.2 ML coverage, (c) a NbO_x thin film of 2 layers thickness, and (d) a Nb_2O_5 thin film of 2 layers thickness on the Pt(111) substrate. The energy at which the patterns were observed is shown. Images are adapted from reference [265].

$NbO_x/Cu_3Au(100)$

Starr et al. tried to form a 2D NbO_x ultra-thin film on $Cu_3Au(100)$ substrates via vapor deposition [268]. Figure 3.26 shows the LEED pattern of a ($\sqrt{3} \times \sqrt{3}$)R30° structure and a coincidence (2 × 7) structure with respect to the hexagonal substrate layer. The

corresponding STM images are demonstrated in Figure 3.27. The same $NbO_x/Cu_3Au(100)$ was grown by Middeke et al. through E-beam evaporation [267]. High-resolution STM images of NbO_x thin film were obtained (Figure 3.28). Starr et al. suggested a O-Nb-O-$Cu_3Au(100)$ stacking, where Nb atoms sit on the close-packed oxygen atoms. A stoichiometry of Nb_2O_3 was expected without considering the oxygen atoms on top-layer. Four possible atomic structural models are illustrated in Figure 3.29, as well as the estimated stable structure calculated by DFT. A stoichiometry of Nb_2O_5 was detected by photoelectron spectroscopy (PES). The auger electron spectroscopy (AES) measurement done by Middeke et al. also indicated a stoichiometry of Nb_2O_5 for the 2D thin film. A further study of the catalysis activity of Pd–$Nb_2O_5/Cu_3Au(100)$ thin film was carried out [266]. Experiments showed 50% loss of the CO adsorption capacity and pronounced changes of the adsorption states when the sample was annealed above 27 °C. This phenomenon was explained by the alterations in the electronic structure as the result of Pd-Nb_2O_5 interactions.

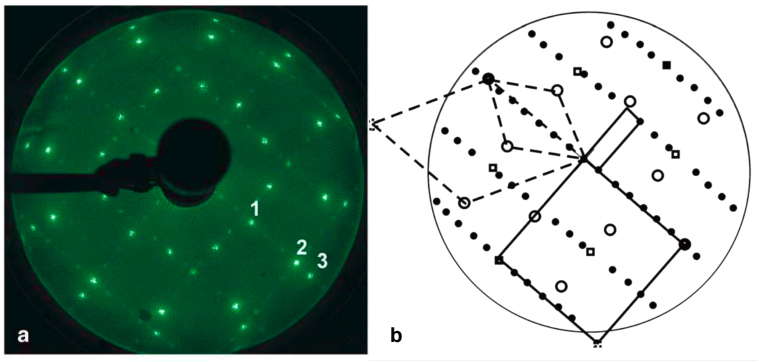


Figure 3.26: (a) The LEED pattern (Energy = 70 eV) of the niobium oxides thin film formed on $Cu_3Au(100)$-O by oxidation of a 1.6 Å-thick Nb layer at 500 °C in 10^{-4} Pa of O_2. The 12-spot rings (1-3) are observed due to the presence of two hexagonal domains rotated by 90°. (b) Schematic representation of the LEED pattern only showing spots from a single domain. Square symbols show spots from $Cu_3Au(100)$ substrate (unit cell is drawn as solid square). Open symbols are the most intense spots from the oxide film (unit cell is drawn by dash lines), and dots are the weak spots due to a coincidence (2 × 7) structure (unit cell is drawn as solid rectangle). Images are adapted from reference [268].

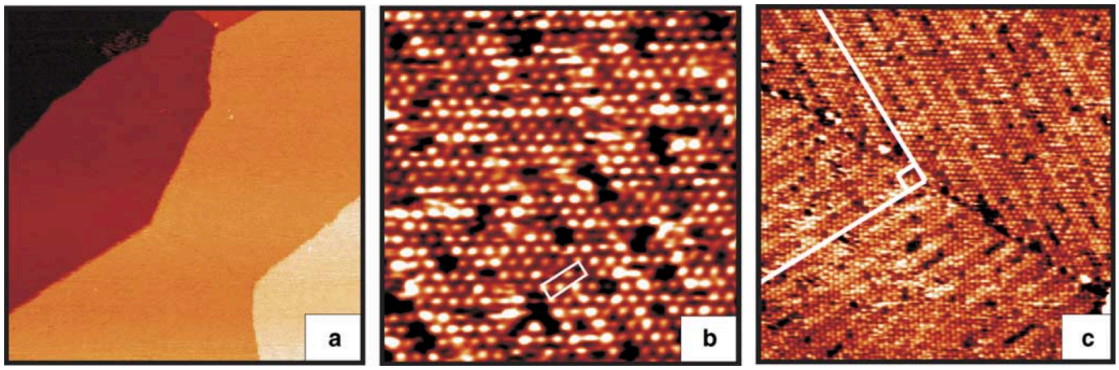


Figure 3.27: STM images of the niobia film grown on $Cu_3Au(100)$. (a) Large terraces separated by steps of about 2 Å in height (image size: 200 nm × 200 nm; V_s = 1.4 V, I_t = 1.0 nA). (b) Hexagonal structure of the niobia film with vacancy defects. The (2 × 7) superstructure cell is marked as a rectangle (image size: 15 nm × 15 nm; V_s = 1.4 V, I_t = 1.0 nA). (c) Two domains rotated by 90°, with each domain exhibiting characteristic surface modulation seen as strips (image size: 40 nm × 40 nm; V_s = 1.4 V, I_t = 1.0 nA). Images are adapted from reference [268].

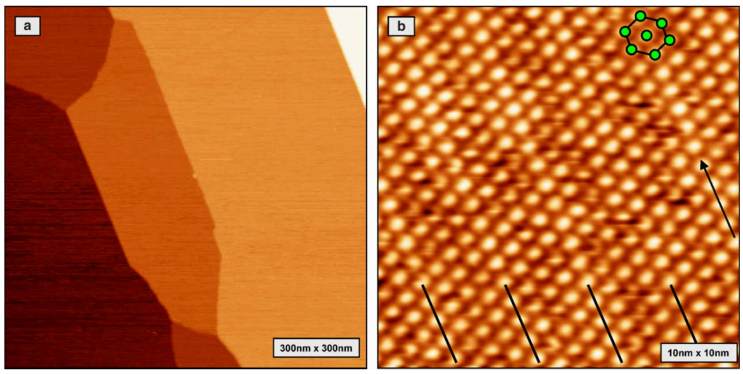


Figure 3.28: (a) Large area STM of the hexagonal NbO_x phase on $Cu_3Au(100)$-O. Clearly the two-dimensional character of the mono-phase oxide layer might be recognised (V_t = -1.0 V, I_t = 1 nA). (b) High resolution STM image of the hexagonal NbO_x phase exposed on all terraces visible in (a). Inserted black lines mark the weak superstructure formed by weak elevation of every fourth row schematically. Point distance: 0.53 nm. The arrow gives the ⟨011⟩ direction of $Cu_3Au(100)$ (V_t = -1.0 V, I_t = 1 nA). Images are adapted from reference [267].

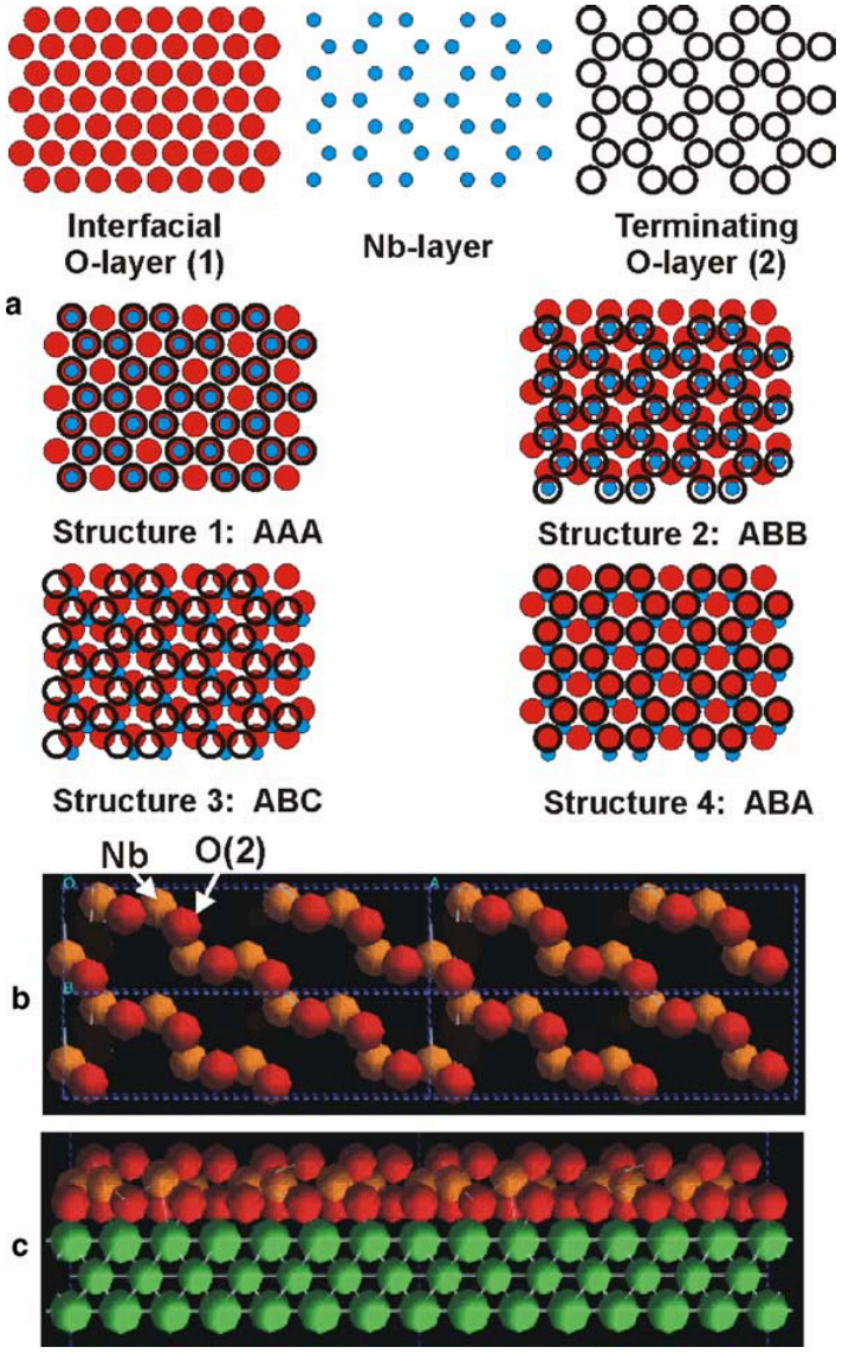


Figure 3.29: (a) Four potential structures considered for the Nb_2O_5 film formed on $Cu_3Au(100)$ consistent with LEED and PES results. The structures are formed through different registries in the stacking sequences of the two oxygen and niobium layers shown in the top of the figure. In all structures the stacking sequence is O(2)-Nb-O(1)-(Cu_3Au); the metal substrate is not shown for clarity. (b) The top and (c) the side views of the most stable structures determined by DFT. Only Nb and top O atoms are shown in the top view, for clarity. Images are adapted from reference [268].

NbO_x/Nb

Interactions of oxygen and Nb single crystal surfaces including (110), (111) and (100) forms passivating films in monolayer scale that are strongly influenced by the Nb substrates and oxidation conditions. Early studies mainly use indirect techniques like LEED, AES and XPS to charaterise the reconstructions of niobium oxides thin films [271, 273, 276-278]. Generally the formation of ordered NbO/NbO_2 ultra-thin films was discovered prior to the formation of fully oxidised Nb_2O_5. In 2001, STM was introduced in the study of oxygen-induced surface structures of Nb(110) [274]. Figure 3.30 illustrates a hexagonal symmetry superstructure consisting of regularly arranged network of finite chains rotated 5° with respect to Nb⟨111⟩ directions. It was obtained by Ar^+ sputtering and subsequent short annealing of the Nb(110) surface in UHV. RHEED and AES study confirmed this superstructure was induced by the segregation of oxygen from bulk to the surface. This superstructure was believed to be a precursor for the formation of an epitaxial FCC-NbO(111) layer on Nb(110) with in-plane orientation NbO$[10\bar{1}]$ ∥ Nb[001] and NbO$[1\bar{2}1]$ ∥ Nb$[1\bar{1}0]$. Li et al. reported the STM images of a formed NbO_2 overlayer on Nb(100) [279]. A ladder-like (3 × 10) structure was interpreted to be a modulated NbO_2(010) on the substrate (Figure 3.31). They identified this structure could change to a disordered structure upon exposure to oxygen at room temperature and restore through annealing in UHV [272]. Arfaoui et al. investigated a complex structure with several niobium oxides generated by segregation of oxygen dissolved in the Nb(110) [269-270]. A stoichiometry of $NbO_{x\approx1}$ was deduced from photoemission spectroscopy (PES), and the combination of LEED and STM results led to a quasi-periodic arranged parallel stick-like model. They proposed a side-to-side FCC-NbO nano-crystal for the NbO thin film. High density of defects and stacking faults were reported, which proved the self-organisation of the niobium oxides overlayer comes from the tilting of Nb(110) substrate. Wen et al. generated and determined the details of c(2 × 2)-O, (3 × 1)-O and (4 × 1)-O surface structures on Nb(100) by STM and DFT calculation [275]. DFT calculations have also been done on Nb(110) and (100) to understand the dynamics of

oxidation of Nb [280-282].

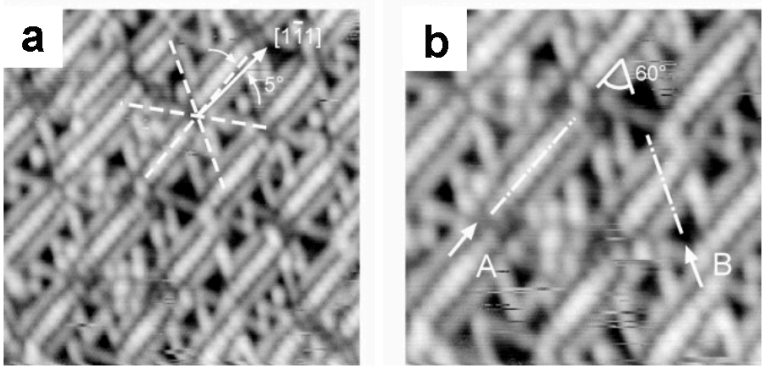


Figure 3.30: STM images of Nb surface after annealing at 1027 °C. Dash lines indicate a hexagonal symmetry of the surface structure. Dashed-dotted lines indicate height-profile scans. ((a) Image size: 10 × 10 nm^2, V_s = 0.20 V, I_t = 0.30 nA; (b) Image size: 7 × 7 nm^2, V_s = 0.20 V, I_t = 0.30 nA). Images are adapted from reference [274].

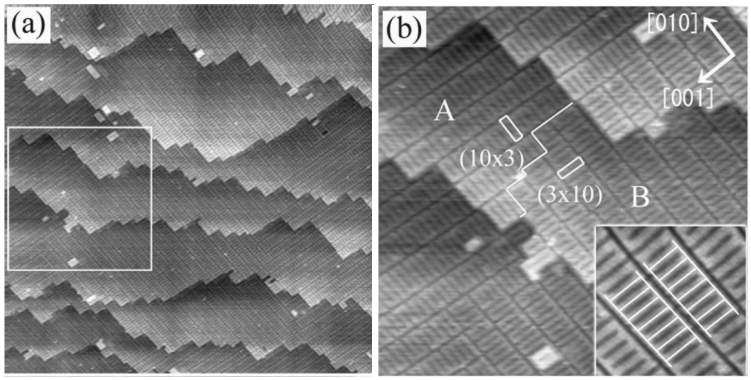


Figure 3.31: STM images of the surface of Nb(100) single crystal after numerous cycles of Ar-ion sputtering and flash annealing at 1700 °C. (a) Large-scale image, 100 × 100 nm^2; (b) Magnification of the square shown in (a), 40 × 40 nm^2. Images are adapted from reference [279].

To sum up, niobium oxides haven't been as widely studied as titanium oxides. Very limited work of ultra-thin NbO_x films grown on metal substrates could be found. However, reviews of those literatures exhibit great possibilities of fabricating structures different from bulk niobium oxides terminations. Substrates worked successfully for growing ultra-thin titanium oxides films like Au(111) could be considered.

3.5 Domain boundaries of 2D honeycomb-lattice films

In the review of TiO_x ultra-thin films grown on metal substrates (section 3.3.3), the honeycomb-lattice Ti_2O_3 2D films have been found in both TiO_x/Au(111) and TiO_x/Pt(111) systems which are described as (2 × 2)-Ti_2O_3 honeycomb structure and ((2.15 ± 0.05) × (2.15 ± 0.05))-Ti_2O_3 kagomé phase (*k*-TiO_x) respectively [8, 160]. Interestingly, even though the unit cells for both structures are the same, the STM images looks very different in large-scale view. When grown on the Au(111) substrate, the honeycomb structure was very uniform; domain boundaries (DBs) were rarely imaged in the literature. However, large amount of irregular DBs were observed in the film grown on the Pt(111) substrate. The reported honeycomb islands were about 60 Å in size and the boundaries of adjacent patches illustrated the black spots arranged in X-shaped features (Figure 3.32). This dramatic low apparent height was argued to be an electronic effect instead of reflection of topography. The variation of the density-of-states at the boundary was believed to cause this phenomenon: at the edges of hexagons, the kagomé mesh is less densely packed.

The Ti_2O_3 honeycomb ultra-thin film is not the only uniform 2D honeycomb lattice film. Graphene, for example, is an allotrope of carbon in the form of an atomic-scale 2D honeycomb lattice in which one atom forms each vertex. A (2 × 2) surface V_2O_3 honeycomb-lattice 2D structure grown on Pd(111) has been observed by Surnev et al. as well (Figure 3.32b) [283-284]. Generally speaking V_2O_3/Pd(111) honeycomb thin film is a flat sheet which is more similar to the HC-Ti_2O_3/Au(111) film, and a (√63 × √63)R19.1° Moiré-like VO_x structure was observed in Figure 3.32b which shows features that are close to TiO pinwheel structure in TiO_x/Au(111) system. However a lot of defects and domain boundaries are spotted in V_2O_3 honeycomb thin film in this STM image. Structural imperfections including domain/grain boundaries, edges, point defects and dislocations can strongly influence the performance of 2D films in terms of chemical, mechanical, optical and electronic properties. The impact could be positive such as providing controllable sites for chemical reactions and molecular absorption, or negative

like weakening the strength of the films. A review of the grain boundaries of graphene is carried out in section 3.5.1 as the model of the free-standing 2D honeycomb-lattice films. In section 3.5.2, DBs of silica honeycomb-lattice ultra-thin films grown on single crystal metal substrates are reviewed as the examples of DBs in metal-supported honeycomb-lattice oxides.

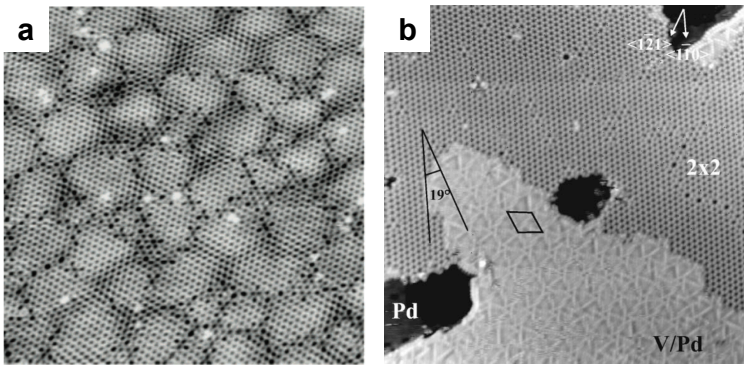


Figure 3.32: (a) Constant-current STM image of the *k*-TiO_x phase grown on Pt(111) substrate in large-scale (image size: 300 × 300 $Å^2$, V_s = 1.0 V, I_t = 1.0 nA). Image is adapted from reference [160]. (b) Large-scale STM image of 0.25 MLs V-oxide films growm on Pd(111) (image size: 300 × 300 $Å^2$, V_s = 2.0 V, I_t = 0.6 nA). Image is adapted from reference [284].

3.5.1 Grain boundaries (GBs) of graphene sheets

Graphene has been a high-profile material since being observed and characterised in 2004 [285]. It is a single layer of tightly packed carbon atoms that are bonded in a hexagonal lattice. It is also recognised as the basic structural element of other allotropes such as graphite, carbon nanotubes and fullerenes. Despite from being atomically thin, graphene is extremely strong, electrically and thermally conductive, and nearly transparent. Currently it has been used in a wide range of industries including energy, electronics, medicine and composites.

When the islands of isolated graphene nucleate from different sites, grain boundaries (GBs) will form when they continuously grow and run onto each other with a

misorientation. Unlike 3D graphite that permits a rich variety of GBs, the sheets of 2D graphene can only form limited types of GBs. Liu simulated the paired pentagon-heptagon (5-7) defects, which were argued to be energetically favourable [286]. By carefully arranging the constituent 5-7 cores, GBs with different tilts can be accommodated (Figure 3.33 a-c); it even works on the case when a zigzag domain edge meets an armchair-oriented domain edge via generating a defects line (Figure 3.33 d). Figure 3.33 e & f illustrated the simulative approach for constructing arbitrary GBs with pentagons and heptagons as large-angle GBs with low formation energies [287]. More possibilities of defects and GBs formed by pentagons and heptagons have been simulated [288-293]. Various types of polygons consisted of 4, 5, 6, 7, 8, 9 carbon atoms that form GBs in graphene sheets were predicted (Figure 3.33 g&h) [294]. A Stone-Wales (S-W) defect with 5-7-7-5 carbon atoms rings has been studied (Figure 3.33i) [295-296]. Similar to 5-7 units defects, an array of S-W defects could accommodate the tilting angles in graphene sheets (Figure 3.33j) [297]. In 2011, Huang et al. produced single-layer graphene on copper foils by CVD and imaged the GBs in atomic-resolution [298]. As shown in Figure 3.34a, by using aberration-corrected annular dark-field scanning transmission electron microscopy (ADF-STEM), they successfully captured two grains meeting with a relative misorientation of 27° and stitched together by a series of pentagons, heptagons and distorted hexagons. However the boundary is not straight and the 5-7 units are not periodic. A similar alternating pentagon-heptagon structure was revealed along the high-angle grain boundaries by Kim et al. (Figure 3.34b) [299]. Cockayne et al. studied a class of topological defects in graphene composed of a rotating sequence of dislocations that close on themselves [300]. Figure 3.34c shows one GB loop ‘flower’ consisting of repeating 5-7 units observed in an epitaxial graphene grown on SiC(0001), and this type of low-energy rotational GB loops have been discussed with schematic models [301]. Figure 3.34 d-f show three models of GB loops that are possible to form considering the formation energies and structural features: flower defect with C_6 symmetry; 555-777 defect with C_3 symmetry; Stone-Walse defect

with C_2 symmetry. Interestingly, the 555-777 defect was observed in the V_2O_3/Pd(111) system shown in Figure 3.32b. It's worth mentioning that graphene sheets with large-angle tilt boundaries that have a high density of defects are much stronger than those with low-angle boundaries. Grantab et al. explained that the 7-membered carbon rings were the critical bonds that initiated failure, and the large-angle boundaries were able to better accommodate these strained rings [302]. The investigations done by different research groups also proved that the existence of GBs only slightly reduced the strength of graphene films [288, 303-304], and the strength of tilt GBs would increase if the pentagon-heptagon defects were evenly spaced [305]. For individual grain grown from seed on Cu substrate, no epitaxial relationships were observed between graphene films and substrates; and the edges of most grains were predominantly parallel to zigzag directions [306-307]. However, when grown on Ni(111) substrates, a weak adsorption of graphene on Ni(111) existed. Graphene sits either on the FCC-hollow sites or on the HCP-hollow sites of Ni(111) substrates. When two different types of domains of graphene/Ni(111) met, the interface was separated by an identical ridge structure and the topological defects reconstructed naturally, which were recognised as extended line of defects (ELDs). Figure 3.35 a-c illustrated the models and STM image of the formed DB with a periodic structure consisting of one big octagon and two small pentagons [308]. On this basis, Botello-Méndez et al. investigated this 1D arrangement of topological defects within a density functional theory framework and revealed three types of ELDs listing as double-5 double-7 (d5d7), pentagon-octagon-pentagon (585) and triple-5 triple-7 (t5t7) structures (Figure 3.35d) [309].

This study of GBs and ELDs of graphene can be extended to other 2D honeycomb-lattice materials with weak bonding to substrates such as hexagonal boron nitride (h-BN) and transition metal dichalcogenides MX_2 (M = Mo, W; X = S, Se). For monolayer h-BN, when the GBs are polar (B-rich or N-rich), 5-7 defects containing homonuclear boron-boron or nitrogen-nitrogen bonds are energetically preferred (Figure 3.35e); when GBs are nonpolar, 4-8 defects form instead of the corresponding 5-7 defects (Figure 3.35f)

[310-311]. Unlike graphene and h-BN, the 2D metal dichalcogenides MX_2 films have the metal-ligand bonding and a sandwich structure with M atoms in between layers of X liagnds in a trigonal prismatic geometry, therefore the reported dislocations and GBs are qualitatively different [312-316].

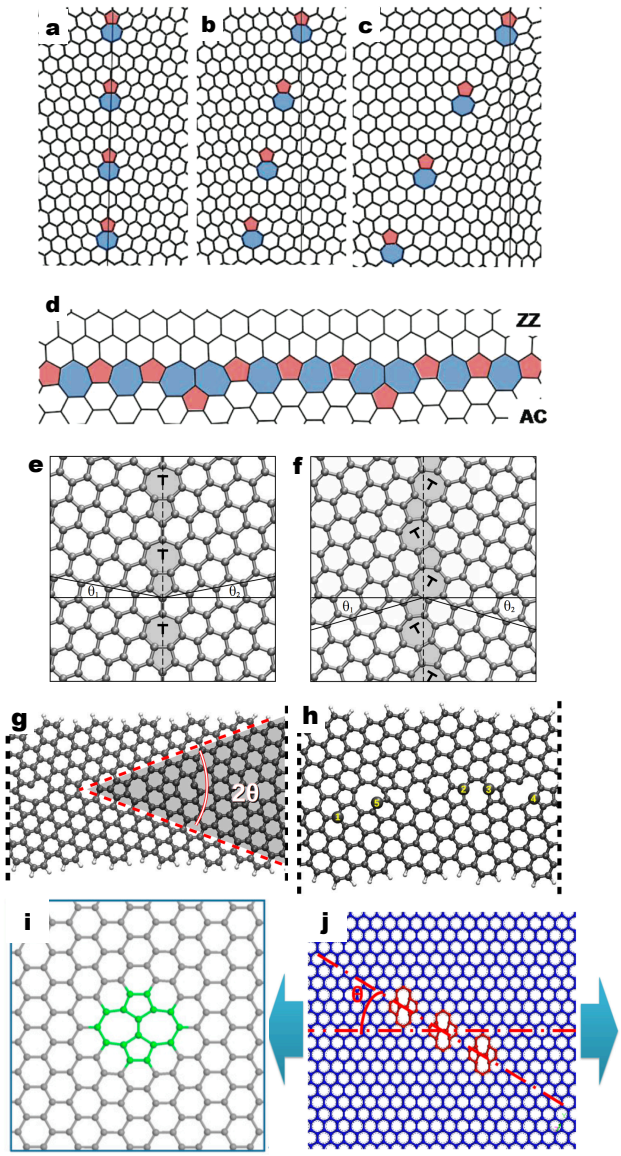


Figure 3.33: Simple grain boundary structures. Considering a GB separates the domain tilted to some angle α, typically it bisects the tilt at $\alpha/2$ angle relative to the crystal planes of the grains. Generally it may deviate by some angle β from the bisector, dividing the tilt angle into $\alpha/2 \pm \beta$. (a) GB in its generic bisector direction, (b) slanted by $\beta = \pm 12^{\circ}$, (c) and $\beta = \pm 24^{\circ}$. (d) An interface joining a zigzag edge and an armchair-oriented edge between the domains tilted to $\alpha = \pm 24^{\circ}$; the 'fly-head' pattern where the atomic rows removed is to reduce the interface mismatch strain. Atomic structures of (e) $\theta_1 = 21.8^{\circ}$ and (f) $\theta_2 = 32.2^{\circ}$ symmetric large-angle GBs. The dashed lines show the boundary lines and the slid lines define angles θ_1 and θ_2. (g) Grain boundary made by merging two graphene edges with the same chirality but different orientation and random translation along the boundary. Dashed vertical lines stand for periodicity across the horizontal direction; $\theta = 20.4^{\circ}$. (h) GB includes various polygons. (i) The computational model of graphene with a S-W defect in DFT calculations; (j) The defective graphene sheets with three S-W defects, the tilting angle θ is the angle between tensile direction (zigzag) and the axis of three S-W defects. Images (a)-(d) are adapted from reference [286]; (e) & (f) are from reference [287]; (g) & (h) are from [294]; (i) is from [295] and (j) is from [297].

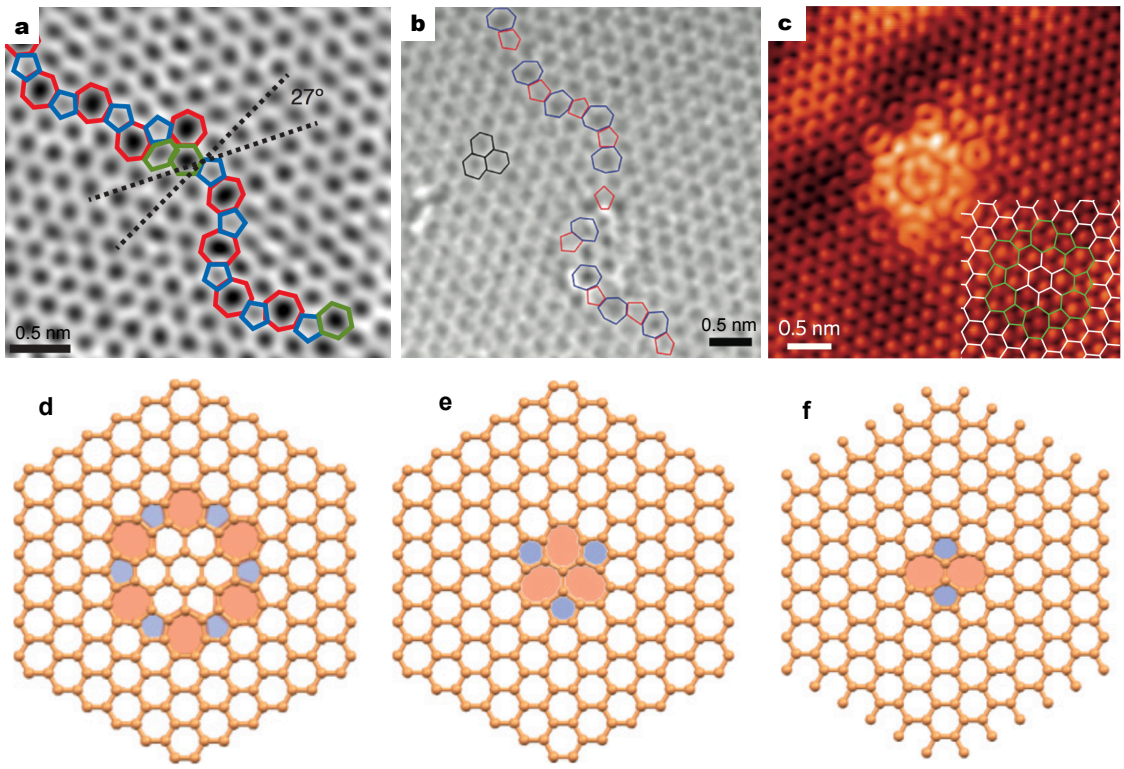


Figure 3.34: Atomic-resolution images and the schematic structural models of graphene crystals. (a) Two grains (bottom left, top right) intersect with a 27° relative rotation. An aperiodic line of defects stitches the two grains together. The pentagons (blue), heptagons (red) and distorted hexagons (green) of the grain boundary are outlined. Image is adapted from reference [298]. (b) Image of the high-angle tilt grain boundary of graphene. The pentagon, hexagon and heptagon are overlaid with red, black and blue polygons respectively. Image is adapted from reference [299]. (c) STM image of the flower-shaped point defect in epitaxial graphene grown on SiC(0001). Inset shows the structural model. Image is adapted from reference [301]. (d) Schematic structure of the flower defect with C_6 symmetry axis. (e) Schematic structure of the 555-777 defect with C_3 symmetry axis. (f) Schematic structure of the Stone-Wales defect with C_2 symmetry axis. Images d-f are adapted from [300].

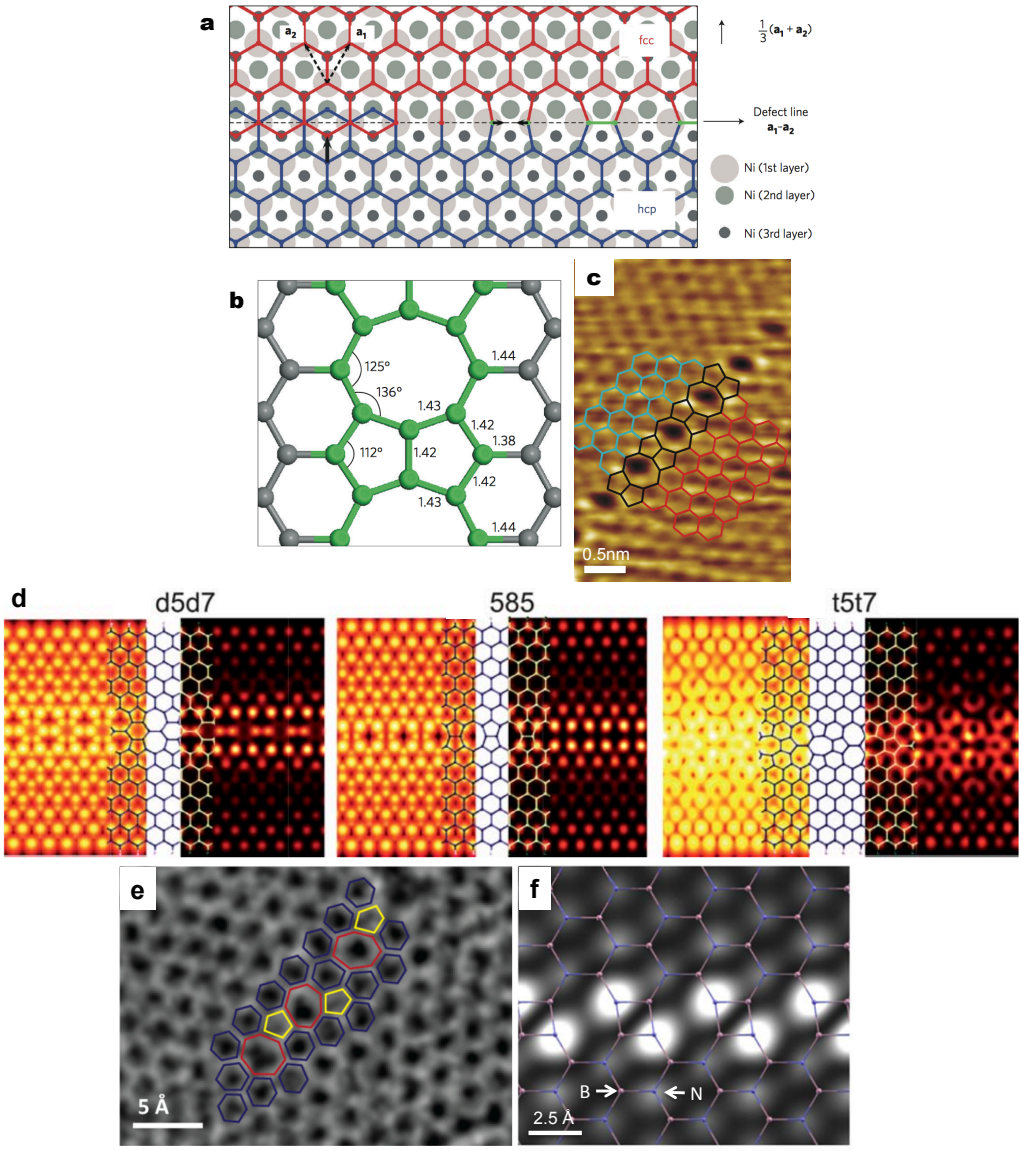


Figure 3.35: (a) Structural model and schematic formation of an extended one-dimensional defect in graphene. The unit cell vectors of two graphene half-lattice that sitting on FCC-hollow sites (red) and HCP-hollow sites (blue) of Ni(111) substrates respectively are $\mathbf{a_1}$ and $\mathbf{a_2}$ (dashed arrows), and those two graphene half-lattice are translated by a fractional unit cell vector 1/3($\mathbf{a_1}$ + $\mathbf{a_2}$) (solid arrow), joining along the $\mathbf{a_1}$ - $\mathbf{a_2}$ direction. The reconstructed domain boundary forms a periodic structure consisting of octagonal and pentagonal carbon rings. (b) The DFT relaxed geometry of the defect structure in (a). The labelled bond lengths are in Å. (c) STM image of extended one-dimensional defects in graphene with superimposed defect model. (d) *Ab initio* STM images of graphene simulated at (left) constant current ($6.7 \times 10^{-4} e/\text{Å}^3$) and (right) constant height (10.6 Å) for the d5d7, 585 and t5t7 ELDs. (e) HRTEM image of CVD-grown h-BN with inserted GB defects structure. Hexagon, heptagon and pentagon structures are depicted in blue, red and yellow respectively. (f) Simulated STM image of h-BN GB consisting of 4-8 membered rings (V_s = 0.5 V, constant height of 2 Å above BN); atomic structure is put in front. Images (a)-(c) are adapted from reference [308]; (d) is from [309]; (e) is adapted from reference [311]; (f) is from [310].

3.5.2 Domain boundaries of metal-supported 2D silica ultra-thin films

Silicon dioxide (SiO_2) has a number of distinct crystalline forms as well as amorphous forms, which lead to various properties. It is one of the most popular materials that have been applied to modern technological applications such as solar cells and microelectronics. Ultra-thin silica films grown on metal single crystal substrates have been used as model systems to investigate structures and properties of 2D materials in surface science area. A lot studies have shown that ordered silica epitaxial films tended to be constructed from hexagonal networks of corner-sharing SiO_4 tetrahedra. When grown on Mo(112) substrates, one of the oxygen atoms of each tetrahedron bonded to the substrates as a strong Si-O-Mo linkage while the other three form Si-O-Si bonded with neighbouring tetrahedra. The monolayer silica film formed a 2D honeycomb-lattice network that arranged in a *c*(2 × 2) structure with stoichiometry of $SiO_{2.5}$. As illustrated in Figure 3.36 a-d, an anti-phase domain boundary (APDB) propagated along the $[\bar{1}10]$ direction of Mo(112) was observed in a few high-resolution STM images, where the openings in the network were alternating eight- and four-membered rings instead of six-membered rings. This straight-line defects were the result of a half-lattice shift in the $[\bar{1}\bar{1}1]$ direction between two domains (Figure 3.36b) [317-320]. The existence of this APDB was predicted on the basis of the LEED results before being directly observed [321]. What's more, the eight-membered rings were argued to be the sites where deposited Au atoms chose to sit (Figure 3.36d). In contrast, for bilayer hexagonal crystalline silica films grown on Pd(100) and Ru(0001), there were no direct chemical bonds between silica and metal substrates: two layers of corner-sharing SiO_4 tetrahedra bonded together by a linking oxygen [322]. Figure 3.36 e&f illustrates the APDB with the unit cell of an elongated eight-membered ring formed to relieve the strain energy in SiO_2/Pd(100) [323]. When the preparation conditions changed, an amorphous bilayer of silica showing a 2D network of polygons could grow on Ru(0001) substrates (Figure

3.36g). The number (N) of members (Si atoms) forming each ring ranged from 4 to 9, with a maximum at N = 6 which corresponded to the crystalline structure [324]. The co-existence of crystalline and amorphous silica (Figure 3.36h) was reported at the coverage between monolayer and 2 MLs coverage [325]. For under monolayer coverage, silica bonded through the Si-O-Ru linkage and illustrated a (2 × 2) lattice structure corresponding to the Ru(0001) substrates, which is similar to monolayer silica grown on Mo(112). The APDBs that imaged as protruding lines were reported as the production of domains shifted by a half of the lattice with respect to each other (Figure 3.36i) [325]. When grown on Pt(111), only bilayer vitreous silica films were observed (Figure 3.36j) [326]. On one hand, when compared with Ru(0001) (lattice constant 2.71 Å), Pt(111) (lattice constant 2.77 Å) is less matched with free-standing bilayer crystalline SiO_2 (lattice constant 5.24-5.32 Å) to accommodate the (2 × 2) structure; On the other hand, the Si-O-Pt bond is much weaker than the Si-O-Mo bond, therefore no crystalline structure was formed in the silica/Pt(111) combination regardless of the coverage [327].

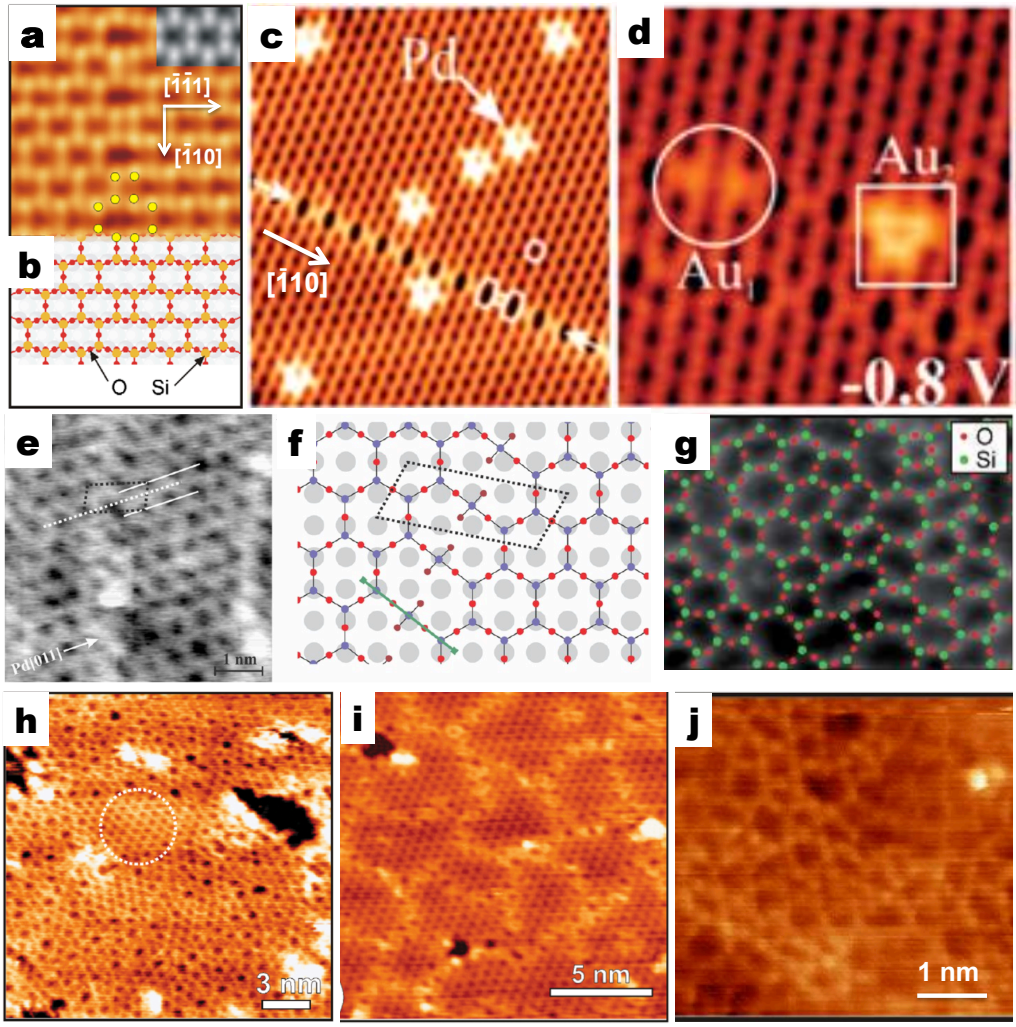


Figure 3.36: (a) STM image of the SiO_2/Mo(112) film with APDB. The superimposed Si atoms (yellow balls) indicate the observed Si atoms in the unit cell of APDB. The atomic protrusions seen in the up-right side are Si atoms (Image size: 3.2 nm × 3.2 nm, V_s = 1.2, I_t = 0.35 nA). (b) Structural model of the APDB shown in (a). (c) STM image of 0.1 ML Pd on SiO_2/Mo(112) thin film (Image size: 13 nm × 13 nm, V_s = 0.5 V). (d) STM image of Au deposits on SiO_2/Mo(112) thin film. (e) Close-up STM image of an APDB in SiO_2/Pb(100). The white lines highlight the offset between the rows across the APDB while the black parallelogram connects the first repeat units on each side of the APDB. (f) Structural model of the APDB in (d), gray balls are Pd atoms, red ones are O and blue balls are Si; the darker red balls highlight O atoms at a lower depth. The dotted parallelogram connects the centers of the six-membered rings on either side of the APB, which are assigned to the prominent dark spots in (d) (Image size: 4.5 nm × 4.5 nm). (g) Atomic resolution STM image of a vitreous silica film on Ru(0001) with complete model (Image size: 4 nm × 3 nm, V_s = 0.1 V, I_t = 0.1 nA). (h) High-resolution STM image of the 2 MLs silica film on Ru(0001). The dashed circle marks the ordered silica surface (V_s = 8 V, I_t = 0.1 nA). (i) STM image of the 1 ML silica film on Ru(0001) (V_s = 1.2 V, I_t = 0.1 nA). (j) STM image of the 2 MLs silica films on Pt(111) (V_s = 1.3 V, I_t = 0.13 nA). Image (a) & (b) are adapted from reference [320]; (c) & (d) are from [317]; (e) & (f) are from [323]; (g) is from [324]; (h) & (i) are from [325], (j) is from [326].

To sum up, the formation of grain/domain boundaries in 2D honeycomb-lattice ultra-thin films shows some regularity. When polygons that are not regular hexagons (6-membered rings) are observed, they often show up with certain combination such as pentagon-heptagon (5-7 units), quadrilateral-octagon (4-8 units), pentagon-pentagon-octagon (5-5-8 units), especially when the repeating units link into boundary lines. It is clear that there's a trend to maintain the average number of members forming each ring being 6 (same as hexagon). If thin films have no or only very weak bonding to substrates (e.g. graphene on Cu, SiO_2/Pt(111)), amorphous structures compete with the crystalline structures corresponding to the conditions, and the boundaries form in the energy-favourable way in the crystalline thin films – the 5-7 units are the most common defects to be observed. If thin films are strongly influenced by the substrates (e.g. graphene/Ni(111), $SiO_{2.5}$/Mo(112)), the epitaxial films have identified manner to bond to the substrates, therefore the domain boundaries will be crystallographically unique. On this basis, forces from both substrates and neighbouring film atoms will determine the specific structures of DBs. Back to the examples of Ti_2O_3 honeycomb ultra-thin films grown on Au(111) and Pt(111), the difference in terms of DBs comes from the lattice mismatch. Both Ti_2O_3/Au(111) and Ti_2O_3/Pt(111) follow the same manner of epitaxial growth: Ti atoms occupy the 3-fold hollow sites of substrates, and O atoms fulfill the bridging sites of Ti atoms. Ti_2O_3 honeycomb structure has a constant of about 6.0 Å, which matches better with close-packed Au(111) lattice along $[1\bar{1}0]$ direction (periodicity: 2.89 Å) than Pt(111) (periodicity: 2.77 Å). More strain needs to be relieved for Ti_2O_3/Pt(111), which ends up with the topography of islands separated by X-shape defects (Figure 3.32). However, even though Ti_2O_3/Au(111) has the potential of forming large-scale uniform monolayer thin film, DBs with long-repeating defect units could be predicted. A detailed study with STM and DFT modeling is needed, and this work will be presented in Chapter 5.

3.6 Summary and outlook

Intensive investigations of transition metal oxides thin films have been carried out. Through epitaxial growth of ultra-thin films on metal substrates, new structures apart from bulk terminations could be fabricated, which illustrate remarkable properties especially for applications of catalysts. Titanium oxides have been widely studied, and the recent publications of TiO_x/Au(111) show great potential of forming uniform structures (e.g. honeycomb) in large area. Those investigations are not only attractive for applications but also valuable for fundamental research. Expanding knowledge including structures, domain boundaries, defects and water dissociation of titanium oxides ultra-thin films are still required. Relevant reviews of well-studied rutile TiO_2 provide multiple ideas and methods for consideration.

Studies of other transition metal oxides including niobium oxide thin films have been carried out. Very few reported experiments could be found, especially for the early growth stage. Models and techniques successfully worked on titanium oxides ultra-thin films exhibit immeasurable possibilities for studies of niobium oxides ultra-thin films.

Chapter 4:

Structures of TiO_x Ultra-thin Films Grown on Au(111)

4.1 Background

4.1.1 Overview

TiO_x thin films have attracted great attention due to their remarkable properties in applications of photocatalysis [70-73], gas sensing [66-69] and as solar cells [62-65]. In the first studies of this field, the thicknesses of the titanium oxide films were in the range of a few hundreds of nanometers, and most thin films had the same terminations as have been found in bulk TiO_2. With the continuous development of technological innovation, the generation of thinner titanium oxide films became possible, and the ultra-thin titanium oxide films with new structures and properties have been created. The growth of TiO_x ultra-thin films on the (22 × √3)-reconstructed Au(111) substrate has been reported by Wu et al. [8], Tumino et al. [9] and Ragazzon et al. [10]. Different growth methods including PVD and CVD were applied, and various structures of TiO_x ultra-thin films have been recorded. A review that covers this subject forms part of Chapter 3 (section 3.3.3). However, a comprehensive study of the two most distinguishable structures, honeycomb (HC) and pinwheel, is still needed. In this chapter, an in-depth investigation using techniques including STM, LEED, XPS and DFT modelling is carried out. To obtain films with the best possible quality, ultra-thin films were produced by PVD, and experiments were conducted in two different UHV systems.

4.1.2 Experimental details

STM experiments were carried out in the JSTM-4500XT system. Mica-supported Au(111) single crystal films (Agilent Technologies, U.K.) were used as the substrates. To build up the reconstructed substrate surfaces, usually the original Au(111) thin films were sputtered by an Ar^+ with energy of 700 eV and operation current of 7.5 μA for 10 to 20 minutes depending on the surface cleanliness, and then annealed in UHV at 600 °C for about 1.5 hrs. A herringbone superstructure is regarded as the sign of successful

preparation of the (22 × √3) reconstructed Au(111) substrates. Ti deposition in UHV was achieved by e-beam evaporation of the 99.8% pure Ti rod (ADVENT Research Materials Ltd., U.K.). The sample was then oxidised in 10^{-6} Pa O_2 at 600 °C for about 30 minutes and then cooled down in the same atmosphere for another 30 minutes. Appropriate adjustment was applied to the sample preparation processes for the purpose of controlling the generated phases. To obtain pinwheel-dominated thin films, the annealing time was extended to 45 minutes; if a honeycomb structure was preferred, the annealing temperature could be lowered a bit (about 595 °C). STM imaging was performed in the constant current mode using electrochemically etched tungsten tips. Usually the applied sample voltage is positive, with the result that empty electronic states are imaged by the STM. The amount of deposited Ti is estimated in monolayer equivalents corresponding to the Au atom density of (1 × 1)-Au(111) substrate (1.4×10^{15} atoms per cm^2). Images were later processed with Image SXM, Fabviewer, Gwyddion and SmartAlign software. All the DFT models have been obtained with a plane wave DFT approach and gradient-corrected PW91 exchange-correlation functional implemented in VASP. The Ti_2O_3/Au(111) systems were represented by slabs composed of three atomic Au(111) layers (Au lattice parameter is 4.08 Å) with Ti_2O_3 structures adsorbed on one side only. Periodic slab images were separated by at least 11 Å of vacuum and dipole corrections were applied to eliminate the remaining spurious interaction. Atomic positions of Ti, O and surface Au atoms were fully relaxed until forces became smaller than 0.01 eV $Å^{-1}$. Positions of the remaining Au atoms were optimized in the direction normal to the surface only. The DFT calculations were carried out by Dr. Claudine Noguera and Dr. Jacek Goniakowski from the Institute of Nanosciences in Paris.

LEED and XPS experiments were carried out in the preparation chamber of customised SPECS ESCA system located at the Diamond Light Source synchrotron Beamline IO5. A 99.999% purity Au(111) single crystal (MaTeck GmbH, Germany) was used as the substrates. To form a clean reconstructed surface, the sample went through three sputtering & annealing cycles. In each cycle, the sample was sputtered by Ar^+ ions for

half hour with energy of 1 keV and operation current of 16 μA. The annealing temperature was set at 500 °C for half hour. A (22 × √3)-reconstructed Au(111) surface was then obtained as confirmed by LEED. After preparation of the substrates, Ti deposition was carried out at room temperature in UHV. A 99.8% pure Ti rod (ADVENT Research Materials Ltd., U.K.) was installed in a tungsten crucible for thermal evaporation. In the case of growing the honeycomb structure, the sample was oxidised in 1 × 10^{-6} Pa O_2 at 500 °C for an hour and then cooled down in O_2 atmosphere. If pinwheel structure was preferred, sample was oxidised in 1 × 10^{-4} Pa O_2 at room temperature for about 8 minutes to form fully oxidised TiO_2, then annealed in UHV at 500 °C for 30 minutes to obtain a pinwheel thin film. In LEED experiments, beam energy applied to the sample was in the range between 45 eV to 150 eV. In XPS experiments, Al K_α was used as the anode. It was applied with the voltage of 12.5 kV and the power of 250 W. The incident angle is 54°. LEED patterns were processed with Photoshop Elements while XPS spectra were processed with CasaXPS software. For the fitting of the core level photoemission data, a linear background was subtracted, and only Ti $2p_{3/2}$ components were fitted after removal of a Shirley background.

4.2 Results

4.2.1 STM and DFT of TiO_x ultra-thin films grown on Au(111)

Figure 4.1a illustrates a STM image of the (22 × √3)-reconstructed Au(111) surface. As reviewed in Chapter 3 (section 3.1.3), Au is a face centred cubic (FCC) crystal; the unreconstructed Au(111) plane consists of a hexagonal lattice. After sputtering and annealing processes, a reconstructed over-layer forms. In this reconstructed surface layer, a pairwise arrangement of the $\langle 11\bar{2} \rangle$-oriented bright line structure show up repeatedly along the $\langle 1\bar{1}0 \rangle$ direction, which is explained by alternating existence of both

regular FCC and faulted hexagonal close-packed (HCP) domains (indicated in Figure 4.1a) [40-41]. Those bright lines are identified as transition regions where Au atoms are packed closer together and raised up with respect to the surface plane, and a 120° bending of domain walls exists [40, 42]. A unit cell of (22 × √3) rectangle is deduced, which consists of two atomic rows aligned in the $\langle 11\bar{2} \rangle$ direction. 23 atoms are fitted into every 22 lattice spacings along the $\langle 1\bar{1}0 \rangle$ surface direction in each row, therefore the reconstructed layer is compressed by 4.55% in the $\langle 1\bar{1}0 \rangle$ directions [43-44, 328].

Figure 4.1b shows the TiO_x ultra-thin film grown on reconstructed Au(111) surface with multiple structures including honeycomb phase (labelled as **β**), pinwheel phase (labelled as **γ**) and triangle islands (labelled as **δ**). Au(111) substrate that was not covered by TiO_x thin films was labelled as **α**. The thin film was produced by depositing 0.4 ML Ti with subsequent oxidation. Similar observations have been reported by Wu et al. [8], Tumino et al. [9] and Ragazzon et al. [10]. Both honeycomb (HC) structure and pinwheel structure are distinguishable monolayer structures, while triangle islands are thicker in topography and appear much brighter in STM images. In experiments, HC structure is uniform in large area, and with carefully control of the deposition rate and oxidation process it can wet the surface with only a few domain boundaries/defects observed. Interests of studying HC structure is raised not only because it is a 2D thin film with regular structural feature but also because it has the potential to be used as substrates for further deposition. For the pinwheel structure, though structurally it is not as uniform as HC, it is still capable of occupying large surface area. A comprehensive study of those two structures is presented in the remainder of this chapter. Triangle islands are found with various shapes, irregular sizes and multiple layers, which make them difficult to study and control. From the literature, triangle islands were argued to be reduced titanium oxides with a stoichiometry of $TiO_{1.30\pm0.04}$ [8]; however, structurally they may be related to a termination of a bulk TiO_2 phase (rutile-TiO_2(100)) with a layer height of about 0.25 nm [9]. In fact, because it disturbs the formation of pure HC/pinwheel sheets and acts as the trigger point for the formation of defects, this phase is usually avoided

when generating 2D TiO_x thin films on Au(111). Triangle islands won't be discussed in detail in this thesis.

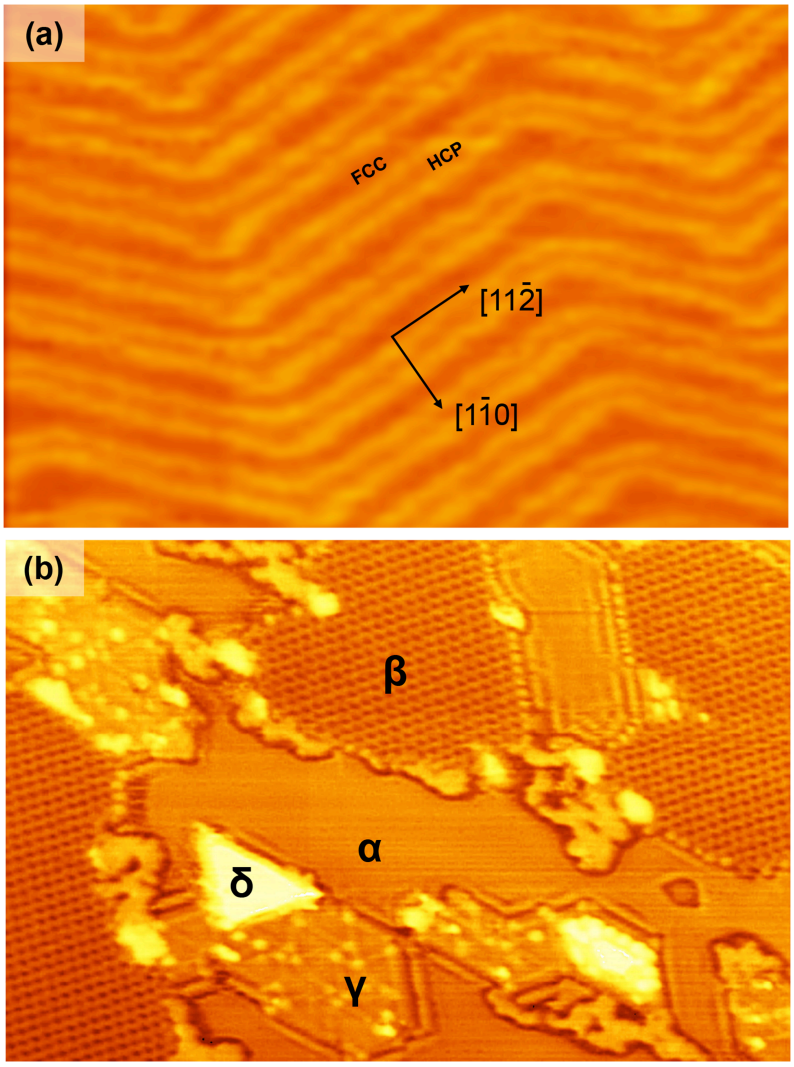


Figure 4.1: (a) STM image of the (22 × √3)-reconstructed Au(111) surface (image size: 75 × 50 nm^2, V_s = -1.0 V, I_t = 0.20 nA). (b) STM image of the TiO_x film grown on reconstructed Au(111) surface (image size: 30 × 20 nm^2, V_s = 0.94 V, I_t = 0.22 nA). 0.4 ML Ti was deposited at room temperature onto the reconstructed Au(111) surface, followed by annealing at 600 °C in 10^{-6} Pa of O_2 for 30 minutes. After cooling down, different structures including honeycomb (labelled as **β**), pinwheel (labelled as **γ**) and triangle islands (labelled as **δ**) were observed. Au(111) substrate that was not covered by TiO_x thin films was labelled as **α**.

Figure 4.2a shows an atomic-resolution STM image of the TiO_x HC structure. A hexagon unit with six bright atoms as vertexes is indicated. The white quadrilateral specifies a unit cell of this honeycomb structure. Figure 4.2b illustrates the density of states of the

Au(111) sample with a clean surface and a surface covered by HC structures. To obtain an STM image of the clean Au surface, the applied sample bias should be negative. Under the scanning condition that positive sample bias was applied to samples that covered by titanium oxide thin films in this chapter, bright spots are recognised as Ti atoms. If a negative sample bias is applied to the TiO_x/Au(111) surfaces, the signals of both Au and O would appear in STM images. Figure 4.2c & d are relaxed DFT models of HC structure. On the hexagonal lattice of Au(111) surface (yellow balls), Ti atoms (blue balls) sit on the three-fold hollow sites and form another layer of hexagonal lattice; the black quadrilateral indicates the unit cell of this Ti-layer having the (2 × 2) relationship to the substrates of Au lattice (Figure 4.2c). The FCC crystallographic unit cell of Au has dimensions of 4.08 Å, the close-packed $[1\bar{1}0]$ direction on the (111) surface has a (1 × 1) periodicity of 2.89 Å, therefore the (2 × 2) Ti-layer has a periodicity of 5.78 Å along $[1\bar{1}0]$. Compared with the hexagon lattice of Au, the hexagon lattice of Ti rotates by 30°, and the interatomic spacing is expanded to about 3.34 Å. This model matches the STM image of hexagons with bright vertex and a dark hole in the centre. Figure 4.2d is built on the basis of Ti-layer by adding the top-most layer of O atoms (red balls) at the bridging sites. This Au-Ti-O stacking sequence is energetically favourable due to charge transfer preference between Au and Ti (Au easily interacts with reduced Ti) [329]. The marked unit cell is the same with Ti-layer, and the stoichiometry is counted to be Ti_2O_3 in this black quadrilateral. Another way of calculating the stoichiometry is that each titanium oxide hexagon ring consists of 6 Ti atoms and 6 O atoms, and every Ti is shared by three neighbouring rings while O is shared by two, so the stoichiometry is Ti_2O_3. This structure is classified as the (2 × 2) HC Ti_2O_3 structure.

In former studies, regardless of the differences in preparation methods and experimental processes, titanium oxide thin films grown on Au(111) substrates showing HC structures were all argued to have a homogenous (2 × 2) superstructure, a stoichiometry of Ti_2O_3 and a Au-Ti-O stacking [8-10, 44]. The STM and DFT studies in this chapter confirm that the (2 × 2) HC Ti_2O_3 structure grown on Au(111) is generally applicable.

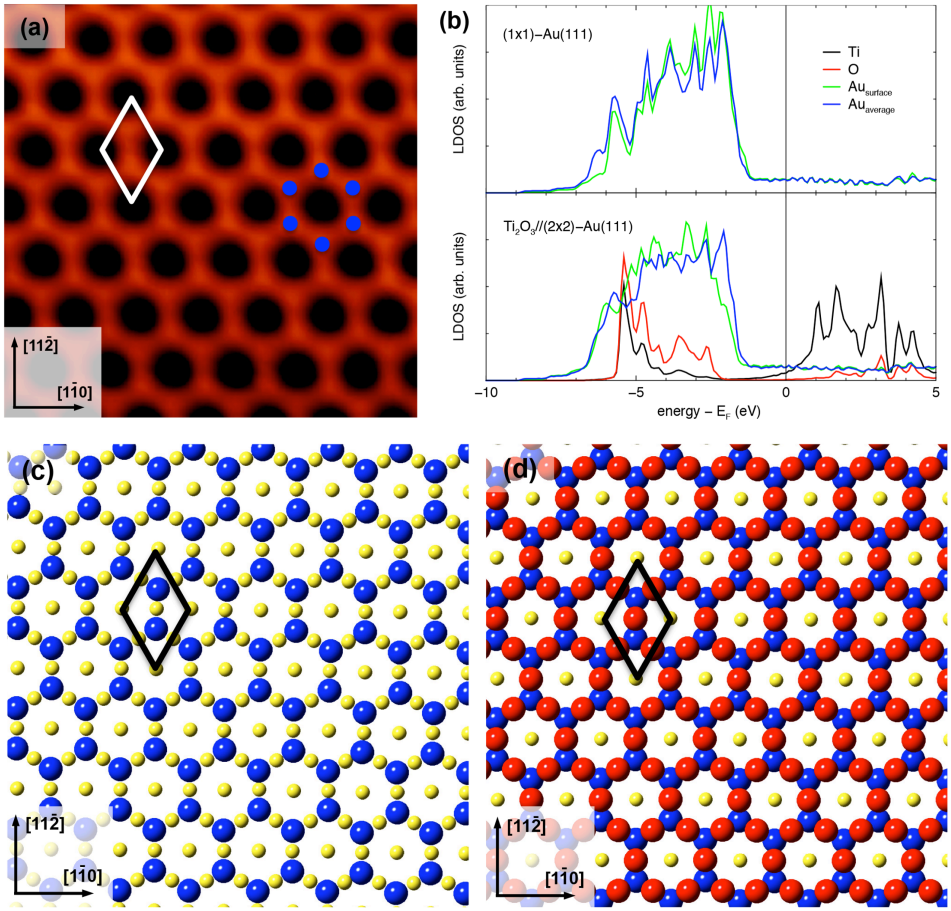


Figure 4.2: (a) Atomic-resolution STM image of the (2 × 2)-Ti_2O_3 honeycomb structure grown on Au(111) (image size: 3.8 × 3.8 nm^2, V_s = 0.90 V, I_t = 0.22 nA). Bright spots represent Ti atoms. A typical hexagonal ring formed by 6 Ti atoms (marked as blue balls) is indicated. This image is averaged from 11 STM images in the same area with the same resolution by SmartAlign. (b) Density of states (DOS) of the clean Au(111) sample and the one covered by Ti_2O_3 honeycomb thin film. Blue and green lines represent average and surface DOS of Au; black line represents DOS of Ti; red line represents DOS of O. This figure is calculated and drawn by Dr. Claudine Noguera and Dr. Jacek Goniakowski from the Institute of Nanosciences in Paris. (c) The relaxed DFT model for the Ti_2O_3 honeycomb structure with Ti atoms sitting in the three-fold hollow sites of the hexagonal Au(111) substrate. Au atoms are yellow while Ti atoms are blue. The Au-Au spacing of the Au(111) surface along $[1\bar{1}0]$ is 2.89 Å. (d) Same DFT model with oxygen atoms (red balls) locate at the bridging sites of Ti atoms. The (2 × 2) unit cell is indicated on all images by the white/black quadrilaterals.

Figure 4.3a shows an STM image of a sub-monolayer titanium oxide film which is composed with nearly pure pinwheel phase (labelled as **γ**) and a few triangle islands (labelled as **δ**) on the reconstructed Au(111) substrate (labelled as **α**). To obtain this pinwheel-dominated surface, 0.3 ML Ti was deposited onto the reconstructed Au(111)

surface, followed by annealing at 600 °C in 10^{-6} Pa O_2 for 45 minutes. An asymmetrical pinwheel-shaped unit is indicated which is formed by six interlocking triangles around a hub in the centre; spokes of the pinwheel appear to be brighter than other areas, so are the vertexes of triangles. In the atomic-resolution STM image (Figure 4.3b), detail of pinwheel structure is revealed: each triangle consists of Ti atoms rows aligned to the triangle's sides. The solid line in Figure 4.3b that links four neighbouring central hubs of pinwheels indicates a unit cell of the Ti-layer. Compared to the regular HC phase, pinwheel structure is complex. Triangles which form pinwheel units in Figure 4.3b are not exactly uniform: generally they are all likely to be equilateral triangles but have nuances in aspects including sizes and crystallographic directions; some triangle's sides are not as bright as others in appearance; a few sides of triangles (spokes of the pinwheel units) consist of double-line while others are single-line featured. The periodicity of Ti-layer is in the range of 26 – 30 Å through measurement in Figure 4.3b.

As reviewed in Chapter 3 (section 3.3.3), a few structural models have been proposed for the TiO_x pinwheel thin films grown on Au(111) in former studies. Wu et al. proposed a $(\sqrt{67} \times \sqrt{67})R12.2°$ reconstructed Moiré pattern model with a periodicity of 23 Å where Ti atoms are arranged in a rotated hexagonal lattice (3.27 Å periodicity) on the Au(111) surface (2.89 Å periodicity), which ended up with a pinwheel showing single-line spokes. Due to the complexity of the structure, positions of O atoms were hard to speculate but suggested to be at either the hollow or the bridging sites of Ti atoms, which lead to a stoichiometry of TiO. The Au-Ti-O stacking was argued to be preferred because that Au substrate was likely to bind with Ti due to charge transfer. The feature of bright spokes of pinwheels was the result of Ti atoms sitting at the bridging sites of Au lattice therefore being raised up topographically [8]. The pinwheel structure was observed in a wide range of surface coverage in Tumino et al.'s paper, however a $(4\sqrt{7} \times 4\sqrt{7})R19.1°$ superstructure with a periodicity of about 30 Å was derived. This model suggested pinwheels were with double-line spokes; the bright Ti atoms were the ones occupying the bridging and on-top sites, while others were sitting on the hollow or quasi-hollow

sites [9]. In Li et al.'s study, a (√97 × √97)R15.3° reconstruction with a periodicity of 28.3 Å was proposed for the pinwheel structure with double-line spokes [173]. In summary, all those proposed models derived from the similar pinwheel structure are close to each other – a slight misfit can result in a different Moiré pattern. Because a heterogonous surface is observed from the enlarged STM image (Figure 4.3b), it is difficult to define an accurate structural model for pinwheel structure. However, it is reasonable to propose that Ti atoms on the sides and vertexes of triangles occupy either the bridging or on-top sites of Au lattice, which leads to a brighter appearance in STM images. Even though the sites of O atoms cannot be seen from STM images, they are more likely to sit on top of the Ti layer as the result of a comparatively weaker interaction with Au. In experiments, pinwheel structure can be transferred to HC structure by oxidation, which suggests that Ti is more reduced in pinwheel phase than Ti^{3+} (Ti_2O_3 HC structure). This result agrees with the TiO stoichiometry of pinwheel in the literature.

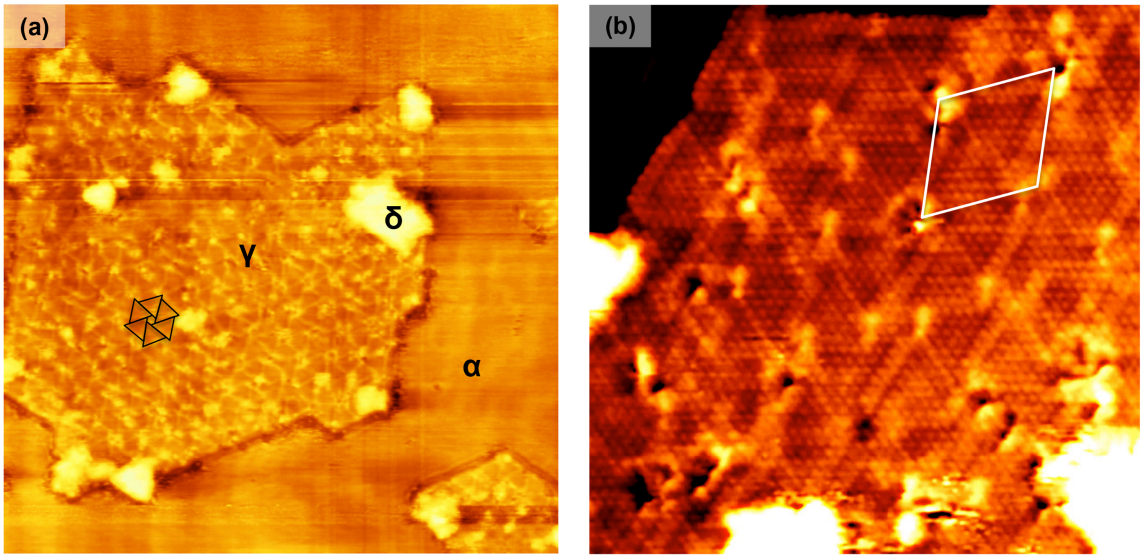


Figure 4.3: STM images of the TiO_x pinwheel structure grown on Au(111) substrates. (a) 0.3 ML Ti was deposited onto the reconstructed Au(111) surface at room temperature, followed by annealing at 600 °C in 10^{-6} Pa of O_2 for 45 minutes. Large area of pinwheel structures (labelled as **γ**) and a few triangle islands (labelled as **δ**) were observed. Au(111) substrate that was not covered by TiO_x thin films was labelled as **α.** A unit of pinwheel that consists of six triangles around a hub is indicated (Image size: 50 × 50 nm^2 , V_s = 0.83 V, I_t = 0.20 nA). (b) Atomic-scale STM image of pinwheel structure (Image size: 13 × 13 nm^2, V_s = 0.80 V, I_t = 0.25 nA). The white solid line that links four neighbouring hubs of pinwheels indicates a unit cell of pinwheel structure.

4.2.2 LEED of TiO_x ultra-thin films grown on Au(111)

Figure 4.4a-c show the LEED patterns of three surface structures taken at similar beam energies (about 100 eV). For a (22 × √3) reconstructed Au(111) surface, Figure 4.4a is observed under beam energy of 100 eV. LEED pattern of bulk Au(111) is a hexagon. When the reconstructed (22 × √3)-Au(111) surface layer forms, a hexagonal array shows up around each primary spot of bulk Au(111). In Figure 4.4a, the reconstructed Au arrays have alignment along the crystallographic $\langle 1\bar{1}0 \rangle$ directions of bulk Au(111) (indicated by dashed lines), and the measurement reveals that the spatial splitting between the additional hexagonal spots and the central spots (representing the bulk Au) is about 4% of the distance between two neighbouring primary spots of (1 × 1) Au(111), which can be explained by the structural model of (22 × √3) reconstructed Au(111) (the reconstructed Au(111) layer is slightly compressed by about 4% in the close-packed $\langle 1\bar{1}0 \rangle$ directions [328]). A number of sputtering & annealing cycles are required to obtain a sharp LEED pattern. Similar results have been shown in the literature [330-331].

Figure 4.4b illustrates the LEED pattern of (2 × 2) Ti_2O_3 honeycomb thin film grown on Au(111) substrates taken at beam energy of 96 eV. Compared to Figure 4.4a, the lifted superstructure of reconstructed Au(111) can't be observed any more. This result is similar to the LEED pattern of Ti_2O_3 honeycomb thin films grown on Au(111) that is reported in 2015 [9]. The disappearance of the hexagonal array of reconstructed Au(111) spots comes from two aspects: the reconstructed Au(111) surface has been covered by the TiO_x thin films that had been grown on it so the signal becomes weak; when the thin film is within monolayer thickness, the interaction between films and substrates is strong enough to lift the herringbone structures, and the formed oxide-Au interface releases the reconstruction of top-layer Au atoms. Therefore only the signal of the bulk terminated (1 × 1) Au(111) lattice is seen. However, extra spots appear in between primary hexagonal spots of (1 × 1) Au(111) lattice, as well as in between those hexagonal spots and the central point of LEED pattern. Those spots indicate the formation of a (2 × 2) superstructure, which is the Ti_2O_3 honeycomb structure.

Figure 4.4c shows the LEED pattern of thin film with pinwheel structure grown on reconstructed Au(111) substrate taken at beam energy of 97 eV. Similar to the LEED pattern of honeycomb structure (Figure 4.4b), pattern that represents reconstructed Au(111) disappears. Instead, two bright satellite spots emerge at the inner circle of initial (1 × 1) Au(111) pattern spots. LEED pattern of TiO_x pinwheel structure on Au(111) reported in the year of 2014 [210] and 2015 [9] also illustrated a close match.

From Figure 4.4a-c it can be concluded that LEED patterns of reconstructed Au(111) surface, honeycomb thin films and pinwheel thin films have significant difference from each other. In this way, structures of titanium oxide thin films grown on Au(111) are able to be estimated by simply examining the LEED pattern at an energy of about 100 eV instead of observing directly by STM.

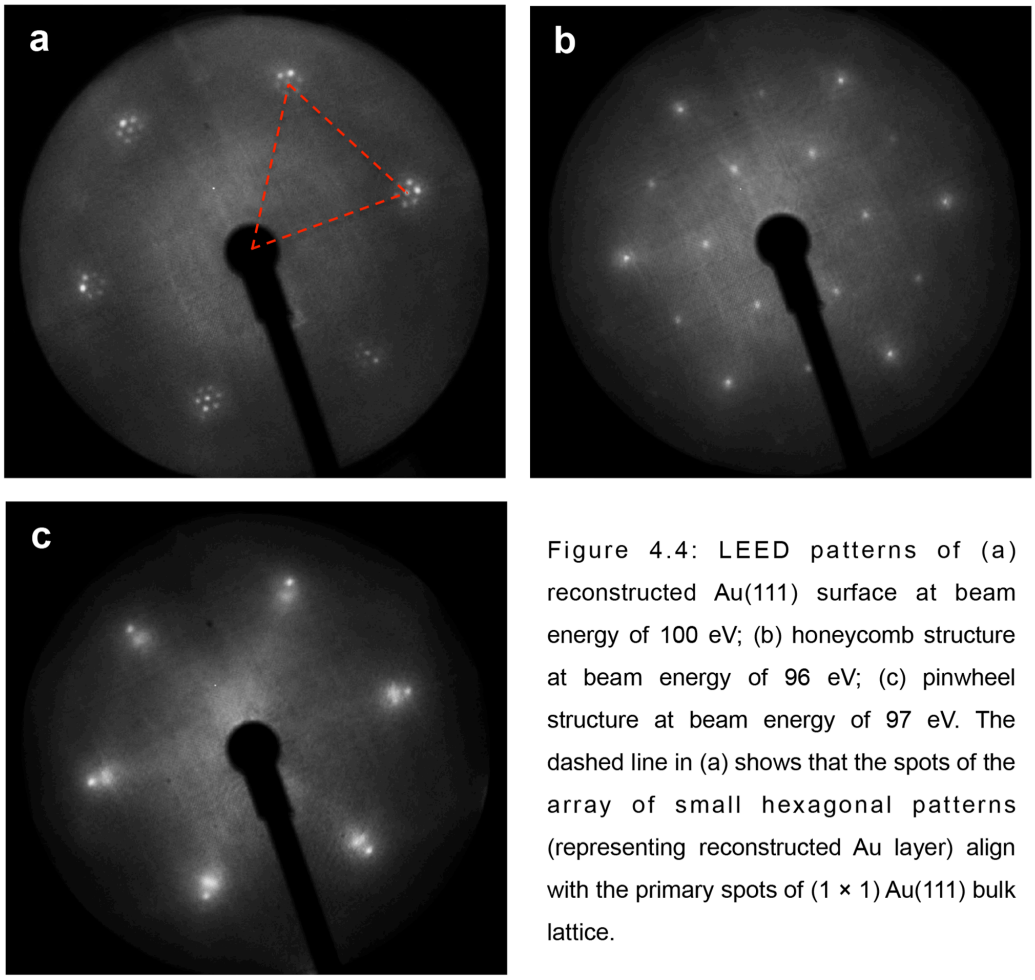


Figure 4.4: LEED patterns of (a) reconstructed Au(111) surface at beam energy of 100 eV; (b) honeycomb structure at beam energy of 96 eV; (c) pinwheel structure at beam energy of 97 eV. The dashed line in (a) shows that the spots of the array of small hexagonal patterns (representing reconstructed Au layer) align with the primary spots of (1 × 1) Au(111) bulk lattice.

Figure 4.5a-c illustrate LEED patterns of Ti_2O_3 honeycomb thin films grown on the reconstructed Au(111) substrates taken at beam energies increasing from 53 eV to 155 eV. Compared with the hexagonal pattern of the (1 × 1) Au(111), extra spots with lower brightness show up in Figure 4.5a. Spots appear in the middle positions of two nearest Au signals are easy to be seen, while spots in between each Au spot and the centre of LEED pattern are inconspicuous (pointed out by the blue arrows). Signals of the honeycomb superstructure become stronger when beam energy increases to 80 eV (Figure 4.5b). The unit cell of (2 × 2) HC lattice and (1 × 1) Au(111) lattice are indicated by dashed lines in blue and red respectively. Referring the relationship between LEED reciprocal space and the real space, this LEED pattern matches the DFT model of honeycomb structure, as well as the structural model in Wu's paper [8]. Figure 4.5c illustrates more spots appear; the pointed ones belong to the third order diffraction spots of the (2 × 2) reconstruction honeycomb lattice.

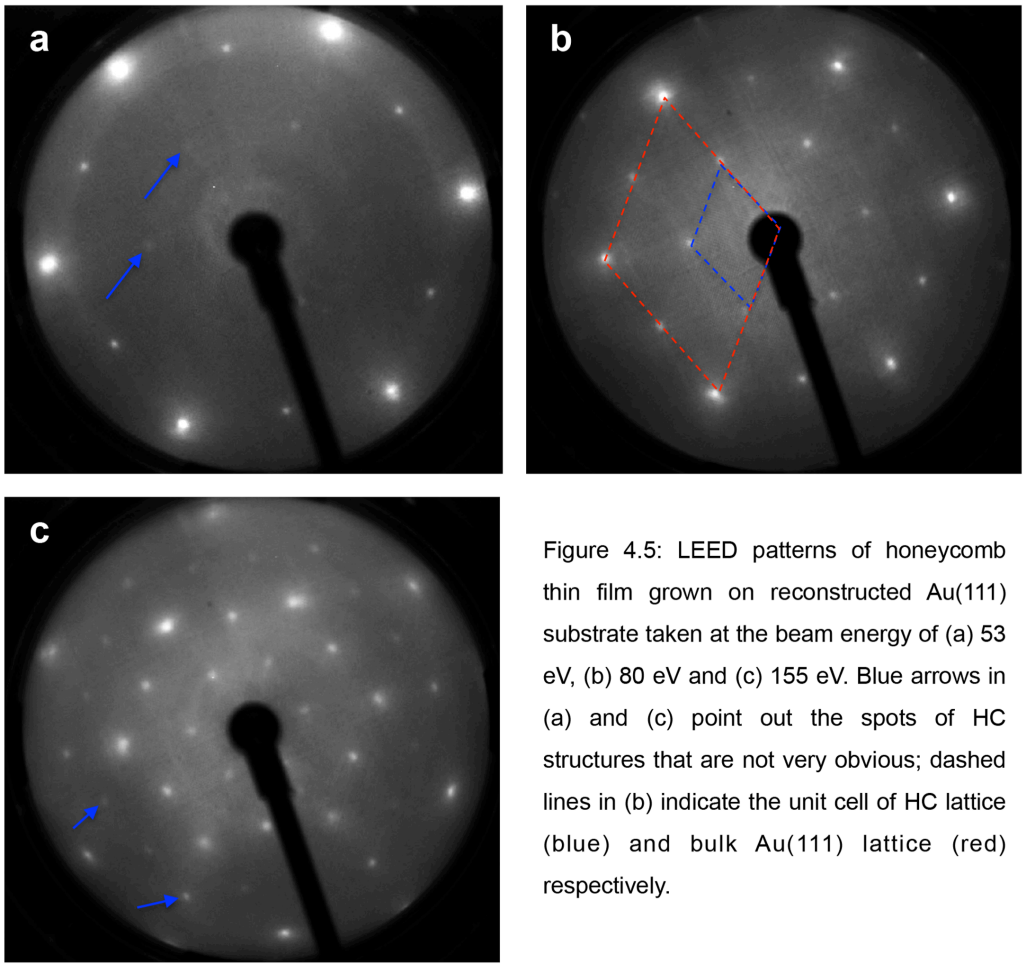


Figure 4.5: LEED patterns of honeycomb thin film grown on reconstructed Au(111) substrate taken at the beam energy of (a) 53 eV, (b) 80 eV and (c) 155 eV. Blue arrows in (a) and (c) point out the spots of HC structures that are not very obvious; dashed lines in (b) indicate the unit cell of HC lattice (blue) and bulk Au(111) lattice (red) respectively.

Figure 4.6 is the typical LEED patterns of titanium oxide pinwheel structures grown on reconstructed Au(111) substrates taken at beam energy of 51 eV and 87 eV. Figure 4.6a shows a few blurring spots appear around signals of (1 × 1) Au(111) lattice as hemisphere surrounding a central spot. When the beam energy is increased, the LEED pattern turns into Figure 4.6b – two recognisable spots show up instead of the hemisphere. The distance between the spots represents pinwheel structures and the central spot that comes from Au is about 10% of the distance between two neighbouring Au primary spots. Regarding to the relationship between LEED reciprocal space and the real space, the periodicity of pinwheel structure is estimated to be 10 times of that of (1 × 1) Au(111) lattice (known as 2.89 Å). This result makes sense considering the measurement from STM images (the periodicity of pinwheel structure is in the range of 26 – 30 Å). Regarding to the structural models proposed for pinwheel structures in the literature, where the periodicity was reported to be 23 Å (Wu et al. [8]), 30 Å (Tumino et al. [9]) and 28.3 Å (Li et al. [173]), the periodicity of pinwheel structure derived from LEED pattern is in a reasonable range. Due to the complexity and variety of pinwheel structures that are observed in STM images, the blurring signals in Figure 4.6a might originate from a mixture of structures depending on the slightly different coincidence sites. The limitation of the sharpness of LEED signals could contribute to the blurring as well. From the dashed lines indicated in Figure 4.6b, it is obvious that spots of pinwheel structures are not aligned in directions of $\langle 1\bar{1}0 \rangle$ – a rotation of about 15° exists in between the pinwheel structure thin film and the Au(111) lattice. Referring to the proposed structural models of pinwheel structures grown on Au(111), the pinwheel layer was argued to rotate in degree of 12.2° (Wu et al. [8]), 19.1° (Tumino et al. [9]) and 15.3° (Li et al. [173]). In terms of the periodicity and rotation of pinwheel structure, result obtained from LEED pattern is close to the proposed structural models in the literature.

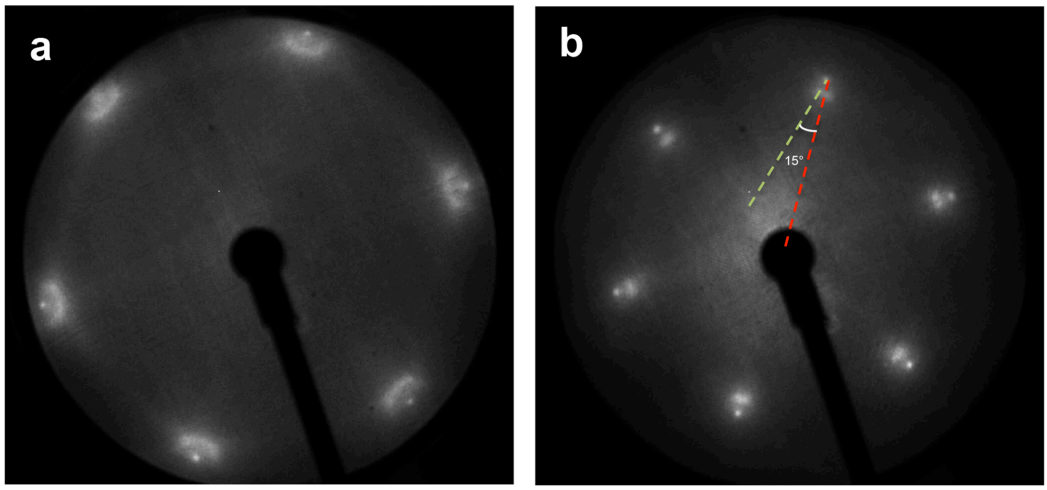


Figure 4.6: LEED patterns of pinwheel thin film grown on reconstructed Au(111) substrate taken at the beam energy of (a) 51 eV and (b) 87 eV. Dashed lines in (b) shows that the two satellite spots are not aligned with the spots of (1 × 1) Au(111) lattice in crystallographic directions of $\langle 1\bar{1}0 \rangle$ - a degree of about 15° exists.

As discussed in section 4.2.1, there is situation of generating thin films where honeycomb phase and pinwheel phase coexist on reconstructed Au(111) substrates. In this case, the LEED pattern should show signals of both. In Figure 4.7, a blurring semi-circle which comes from pinwheel structure appears around the (1 × 1) Au(111) spots (circled in red), and signals of (2 × 2) honeycomb are indicated by a blue arrow at the middle point of two neighbouring Au spots. A similar LEED pattern of thin films with a mixture of honeycomb and pinwheel structures on Au(111) was reported by Tumino et al. [9].

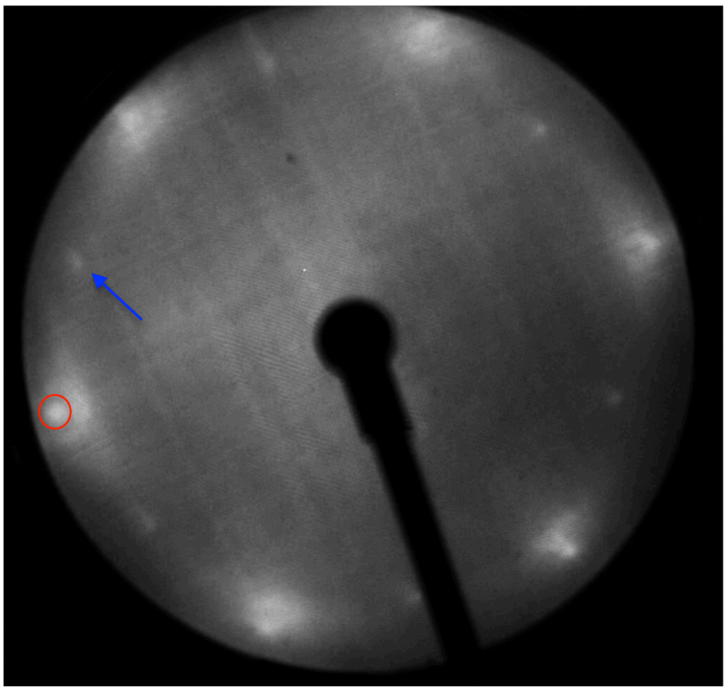


Figure 4.7: LEED patterns of TiO_X ultra-thin film grown on Au(111) substrate with coexistence of honeycomb and pinwheel structures. The LEED pattern was taken at a beam energy of 50 eV. Red circle indicates the spot of Au lattice; blue arrow points out the spot represents (2 × 2) HC structure.

4.2.3 XPS of TiO_x ultra-thin films grown on Au(111)

To investigate the chemical composition of TiO_x ultra-thin films grown on Au(111) substrates, samples examined by LEED that have been identified as honeycomb (HC)-dominated structure, pinwheel (PW)-dominated structure and mixed structures of HC and PW are studied by XPS. After Ti deposition, a HC-dominated thin film was generated by directly oxidising in 1 × 10^{-6} Pa O_2 at 500 °C for one hour, while a PW-dominated sample and sample with mixed structures were first oxidised in 1 × 10^{-4} Pa O_2 at room temperature for 8 minutes to form fully oxidised TiO_2. To obtain a PW-dominated surface, the sample was then annealed in UHV at 500 °C for 30 minutes to be sufficiently reduced. For the sample with mixed structures, it was annealed for 20 minutes instead; therefore TiO_2 was reduced into both HC and pinwheel structures. Figure 4.8 shows Ti $2p_{3/2}$ core level XPS spectra of selected samples. The Ti $2p_{3/2}$

spectra were fitted using three components: the first state appears at a binding energy (BE) of about 455.5 eV (green curve), which matches the spectroscopic signature in the literature for Ti^{2+}; the second state is at a BE of about 457.3 eV (blue curve) and is associated with Ti^{3+}; the third state (red curve) falls within the range of BE that have been reported for Ti^{4+} (about 458.7 eV). From the study of STM and DFT, those three components are related to pinwheel phase (TiO), HC phase (Ti_2O_3) and fully oxidised TiO_2 respectively. In Figure 4.8, the HC-dominated sample shows a strong Ti^{3+} peak with 54.7% concentration. Peaks of Ti^{2+} and Ti^{4+} are much weaker, which might come from titanium oxides that are partially less or over oxidised from deposited Ti atoms. The most significant spectroscopic signal for a PW-dominated sample is the Ti^{2+} peak, which has an atomic concentration of 55.5%; this result matches the proposed stoichiometry of pinwheel as TiO. Because the generation of pinwheel structure is via annealing the fully-oxidised TiO_2 in UHV, therefore signals of the non-reduced Ti^{4+} and less-reduced Ti^{3+} exist; however, their intensities are not comparable to the strength of Ti^{2+} peak. For the sample with mixed structures, intensities of Ti^{2+} and Ti^{3+} are in a similar range (36.5% and 39.9% concentration respectively), which indicates that the HC phase and pinwheel phase in the surface layer are nearly equal in amount. The procedure of preparing the mixed-structure sample and the PW-dominated sample is similar. Compared with the PW-dominated sample, the Ti^{4+} peak is stronger in the sample with mixed structures, which is because less fully-oxidised TiO_2 has been reduced in this sample. In summary, both HC and pinwheel are reduced titanium oxide phases, and pinwheel is more reduced than HC phase; a shift of the overlapped XPS spectra of Ti $2p_{3/2}$ from BE of about 459 eV towards 455.5 eV can be observed with the increasing amount of pinwheel phase formed in the surface. It's worth mentioning that for nano-structure grown on metal, XPS peaks refer to structural units rather than to oxidation states, therefore the peak shifts in Figure 4.8 reflect the change of surface structures as well as the difference of oxidation states.

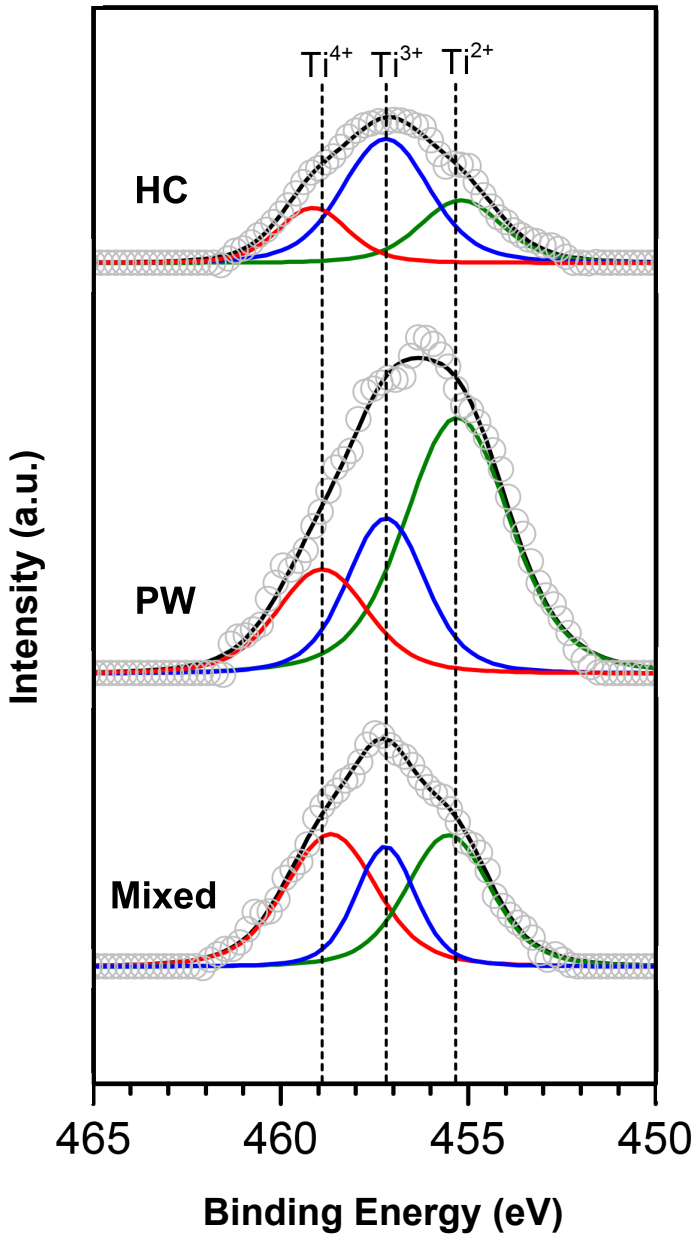


Figure 4.8: PES spectra of Ti $2p_{3/2}$ core level of TiO_x/Au(111). Three samples with honeycomb dominated structure (labelled 'HC'), pinwheel-dominated structure (labelled as 'PW') and mixed structures of honeycomb and pinwheel (labelled as 'Mixed') are examined. The Ti $2p_{3/2}$ spectra were deconvoluted into three components: Ti^{2+} (marked as green curves; standard binding energy: 455.5 ± 0.6 eV) is related to the TiO pinwheel structure; Ti^{3+} (marked as blue curves; standard binding energy: 457.3 ± 0.7 eV) is related to Ti_2O_3 honeycomb structure; Ti^{4+} (marked as red curves; standard binding energy: 458.7 ± 0.2 eV) is related to fully-oxidised titanium oxides including triangle islands. The standard binding energies of Ti $2p_{3/2}$ come form reference [332]. The grey bubbles represent the original collected data after background subtraction; the black curves are the fitted curves that overlap those three components.

4.3 Discussion

Experimental trials of growing TiO_x ultra-thin films have been carried out on a few metal substrates. A comparison between the two distinguishable structures (HC and pinwheel) found in TiO_X/Au(111) and similar structures reported in other systems is necessary. It has been mentioned that the (2 × 2) Ti_2O_3 honeycomb phase grown on Au(111) is the most notable structure. A similar hexagonal TiO_x lattice has been reported on Pt(111) by Sedona et al. as *Kagomé-Like phase* (*k*-TiO_x) [160]. The hexagonal over-layer observed via STM was argued to be a ((2.15 ± 0.05) × (2.15 ± 0.05)) superstructure with respect to the Pt(111) substrate; Pt-Ti-O stacking was suggested by XPS; the stoichiometry was estimated to be Ti_2O_3 with Ti occupying the 3-fold hollow sites of Pt(111) with O atoms sitting on the bridging sites of the Ti-layer. The LEED pattern of *k*-TiO_x is a close match to the result of our HC structure except that the second order spots of *k*-TiO_x are not coincident with the primary spots of Pt(111) lattice. In high-resolution STM images, *k*-TiO_x exhibited the same unit cell structure with HC-Ti_2O_3 despite the mismatch between Ti_2O_3 over-layer and Pt(111); however in large-scale STM image, significant amount of domain boundaries and defects separated the *k*-TiO_x hexagonal sheet into honeycomb islands with about 60 Å in size, which I believe to be the result of strain relief: a large amount of strain develops at the interface between the thin film and Pt(111) substrate, which is relieved through forming periodical boundaries so that the layer-by-layer epitaxial growth mode can continue. In contrast the experiments described in this thesis show that the HC-Ti_2O_3/Au(111) films are uniform; rare domain boundaries were observed due to a good match between HC structure and Au(111) substrate.

A (2 × 2) honeycomb sub-monolayer 2D structure was observed in VO_x/Pd(111) system which has a very similar appearance to the HC-Ti_2O_3 in STM images, and the *ab initio* total-energy DFT calculations suggested a stoichiometry of V_2O_3 and a Pd-V-O stacking: V atoms located at the hollow sites of Pd(111) and O atoms filled in the bridge sites of V-layer. In large-scale STM images of honeycomb structures, V_2O_3/Pd(111) showed more defects and domain boundaries than HC-Ti_2O_3/Au(111) but the V_2O_3 film still stayed as a

flat sheet; while in the *k*-TiO_x/Pt(111) system a structure of 'linked islands' was observed [283-284]. Other 2D honeycomb thin films with hexagonal lattice like graphene, metal-supported silica thin films are less relevant to HC-Ti_2O_3/Au(111) but are still useful in the study of the structural nature of domain boundaries.

As has been discussed, there is no standard structural model for titanium oxide pinwheel films grown on Au(111). Usually Pinwheel structures are attributed to Moiré patterns, which bring out a few similar examples. In the TiO_x/Ru(0001) system, a Moiré pattern was proposed to explain the non-rotated ($6\sqrt{3} \times 6\sqrt{3}$) superstructure deduced from LEED pattern. TiO_2 octahedrons (O-Ti-O tri-layer stacking) were suggested lying upon Ru hexagonal substrates, which resulted in a pinwheel structure. A strong Ti^{4+} signal from the XPS spectra supported this estimation. However the structural model had a slight deviation from the STM and LEED results, which was due to the structural defects and irregularities in the O-Ti-O layer. In the TiO_x/Pt(111) system, there are two Moiré-like models that show wagon-wheel structures – *w*-TiO_x and *w'*-TiO_x [160]. Different from the disunity in the structure of TiO_x/Au(111) pinwheel, *w*-TiO_x and *w'*-TiO_x exhibited uniform structures in STM images and LEED patterns: ($\sqrt{43} \times \sqrt{43}$)R7.6° pattern with periodicity of 18.2 Å for *w*-TiO_x, and (7 × 7)R21.8° pattern with periodicity of 19.4 Å for *w'*-TiO_x. A ($\sqrt{63} \times \sqrt{63}$)R19.1° Moiré-like VO_x ultra-thin film was reported in the VO_x/Pd(111) system, which was described to have a 'wagon wheel' superstructure as well [284]. Because of the tendency that Pt and Pd substrates are likely to form bulk alloys with Ti and V, the stacking sequence for both the TiO_x and VO_x wagon-wheel structures mentioned above were suggested to be Pt/Pd-Ti/V-O. And they were discussed to be results of Ti/V-oxide decomposition by analysis of XPS. This stacking sequence is similar to the pinwheel TiO_x/Au(111) films.

Ultra-thin TiO_x films illustrating regular structures more than honeycomb and pinwheel were observed grown on Au(111) substrates in the literature. A structure with row-like appearance was reported by Tumino et al. as row phase [9] and Ragazzon et al. as star phase [10] separately, and briefly described by Wu et al. as well [8]. This phase is a 3D

structure that showed up when Ti coverage was over 1 ML. In high-resolution STM images, those rows were alternatively being brighter and darker – the brighter rows showed a zigzag motif while the darker ones were broader. Rows were either oriented along three directions of crystallographic $\langle 11\bar{2} \rangle$ families or $\langle 1\bar{1}0 \rangle$ families in each island, and islands (with linear size of 20-50 nm) consisted of rows showed an orientation preference of along the $\langle 1\bar{1}0 \rangle$ directions. No exact structural models were defined but the rectangular unit cells in two papers were of similar sizes. This structure was suggested to be related to the rutile TiO_2(110). Other structures that were spotted in the ultra-thin TiO_x films grown on Au(111) substrates include a needle-like 'nanowire' with width of about 5 nm that was observed in samples made by PVD technique [9], and a metastable TiO_2(B)(001) phase developed by CVD showing three layers of Ti formed when Ti dosing was over 1.5 MLs [47]. Those structures were suggested to be associated with bulk terminations of TiO_2.

4.4 Conclusions

In summary, three phases are identified when growing sub-monolayer TiO_x films on the reconstructed Au(111) substrates – honeycomb, pinwheel and triangle islands. Among them, both HC and pinwheel are 2D films while triangle islands have multi-layer structures as well as irregular sizes and shapes. HC is a uniform structure which is able to wet the Au(111) surface with just a few defects/domain boundaries. A stoichiometry of Ti_2O_3 is proposed based on results of STM, DFT and XPS. Pinwheel is capable of forming films that cover large area of the Au(111) substrates, however structurally it is not as regular as HC. STM and LEED suggest a Moiré-like structure with periodicity in the range of 25 – 29 Å and a rotation of about 15° with respect to the Au substrate. The stacking sequence is believed to be Au-Ti-O for both phases due to the fact that the Au substrate has a priority to bond with Ti than O. Results of XPS indicate that HC is

associated with Ti^{3+}, and pinwheel is a more reduced titanium oxide phase. This is confirmed by the fact that pinwheel can be converted into HC phase by oxidation. Both HC and pinwheel structures have been developed experimentally in two UHV systems, and in the literature they were successfully generated by different methods, therefore it is reasonable to draw the conclusion that the formation of HC and pinwheel structures are repeatable.

Similar honeycomb structures have been reported in TiO_x/Pt(111) and VO_x/Pd(111) systems; the Moiré-like thin films showing a pinwheel/wagon-wheel structure were found in TiO_x/Ru(0001), TiO_x/Pt(111) and VO_x/Pd(111) systems. Combining all those studies, it seems that the multiple oxidation states of transition metals could be developed into ultra-thin films with novel structures on metal substrates. Regarding to the outstanding structural characters of Ti_2O_3 honeycomb thin films grown on Au(111), experimental trials of generating similar 2D honeycomb films via oxidation of other transition metals with oxidation state of +3 should be carried out. At the same time, a comprehensive study of defects and domain boundaries that have been observed in the HC-Ti_2O_3/Au(111) will be necessary.

Chapter 5:

Domain Boundaries in (2 × 2) Ti_2O_3 Honeycomb Ultra-thin Films Grown on Au(111)

5.1 Background

5.1.1 Overview

(2 × 2) Ti_2O_3 honeycomb (HC) ultra-thin films can be grown on (22 × √3)-reconstructed Au(111) substrates by physical vapour deposition (PVD) [8]. A comprehensive study of this structure has been carried out in Chapter 4, and a few domain boundaries (DBs) were observed in experiments. However, a thorough investigation of the DBs in HC Ti_2O_3/Au(111) hasn't so far been carried out by any research groups. Referring to the review of DBs in similar 2D hexagonal-lattice films in Chapter 3 (section 3.5), both linear and rotational DBs have been reported. Those studies are instructive to the research of the DBs in HC Ti_2O_3/Au(111). For linear DBs, structural models of the crystallographically unique DB gaps are simulated based on the crystallographic characters of the Ti_2O_3 HC structure and Au(111) surface. Atomic structures of DBs in honeycomb Ti_2O_3/Au(111) are affected by a variety of factors, an objective observation is essential; so scanning tunnelling microscopy (STM) is applied. Density functional theory (DFT) modelling is used to simulate the atomic structures of DBs and calculate their formation energies. Rotational DBs are rare but stand out when observed in STM experiments. This type of DB is studied with comparison to similar structures and models of boundary loops.

5.1.2 Experimental details

STM imaging was carried out in the JEOL JSTM 4500XT microscope system. Sample preparation was similar to what had been described in Chapter 4 (section 4.1.2) – mica-supported Au(111) single crystal plates (Agilent Technologies, U.K.) were used as substrates, Ti deposition was operated in room temperature via the Oxford Applied Research e-beam evaporator EGN4, and TiO_x thin films were obtained by annealing in 10^{-6} Pa oxygen at 600°C for 45 minutes. Imaging was carried out at a base pressure of

10^{-8} Pa in the constant current mode. STM images were processed with Image-SXM, FabViewer, Gwyddion, Smart-Align software; structural models of crystallographic DBs were produced with CrystalMaker software; DFT modelling and calculations were carried out by Dr. Claudine Noguera and Dr. Jacek Goniakowski from the Institute of Nanosciences in Paris, which have been obtained with a plane wave DFT approach and gradient-corrected PW91 exchange-correlation functional implemented in VASP. For the discussion of DBs, in addition to the HC structural model discussed in Chapter 4 (section 4.1.2), the distances between the periodic images of the simulated DBs were larger than 20 Å and 25 Å, respectively. The formation energy of the DB structures is a relative value compared to the perfect HC lattice.

5.2 Results

5.2.1 Structural models of the crystallographically unique linear domain boundaries in HC-Ti_2O_3/Au(111)

A single unit cell offset between two neighbouring domains results in a DB. For the (2 × 2) honeycomb Ti_2O_3/Au(111), due to the strong bonding between thin films and the substrates, the linear DBs have the energetically preferred directions: ⟨1 1 -2⟩ ($[11\bar{2}]$, $[1\bar{2}1]$, $[\bar{2}11]$) and ⟨1 -1 0⟩ ($[0\bar{1}1]$, $[1\bar{1}0]$, $[10\bar{1}]$). Figure 5.1a illustrates the structural model of the Ti_2O_3 HC thin film: Ti atoms occupy the 3-fold hollow sites of Au(111) substrates, while O atoms sit on the bridging sites of Ti-layer. A (2 × 2) superstructure is formed. To ease the procedure of modelling, the top-layer O atoms are removed – the Ti-layer is used to represent the HC thin films. Figure 5.1b shows that there are three more groups of 3-fold hollow sites of Au(111) that are crystallographically equivalent to the ones occupied by blue Ti atoms. Ti atoms that sit on those three

groups of featured sites are drawn as green, black and brown balls respectively. As illustrated in Figure 5.1c, when the HC film that nucleated from the black-featured Ti atoms grows and meets the HC film nucleated from the blue-featured Ti atoms, they are not able to bond with each other by forming the regular hexagon honeycomb. In this way, the gaps between two domains can be created in specific directions, which are identified as the crystallographically unique linear DBs.

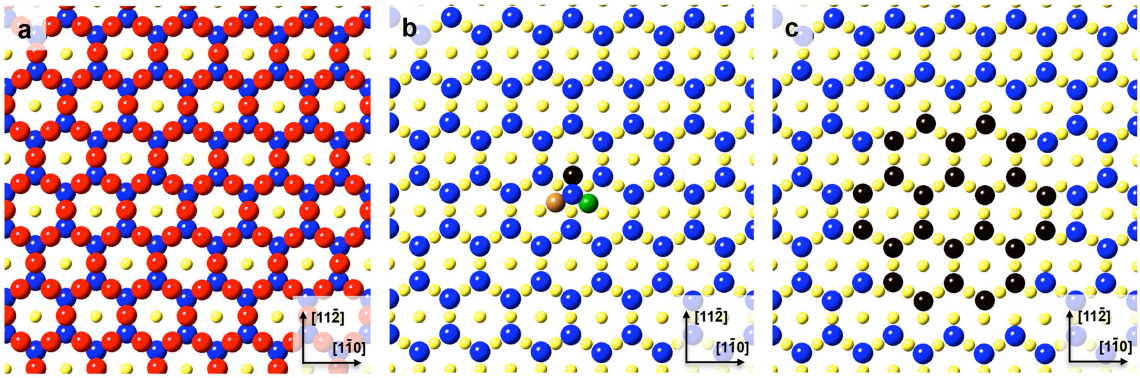


Figure 5.1: (a) Structural model of honeycomb Ti_2O_3/Au(111). Yellow balls are Au atoms, blue balls are Ti atoms and red balls are O atoms. (b) The HC sheet with the O atoms removed to aid the understanding of DB formation. Green, black and brown balls represent Ti atoms that sit on three other groups 3-fold hollow sites of the Au(111) substrates; (c) the HC sheet with a different domain in the center which nucleates from black-featured Ti atoms in (b). The Au-Au spacing of the Au(111) surface along $[1\bar{1}0]$ is 2.89 Å.

Because ⟨1 1 -2⟩ and ⟨1 -1 0⟩ are energetically preferred families of crystallographic directions in HC Ti_2O_3/Au(111), the linear DBs are more likely to be developed along them. Figure 5.2 illustrate the simulated structural models of crystallographically unique linear DBs along $[11\bar{2}]$. Figure 5.2 (a) & (d) have the same DB structures. The unit cell is formed by a narrow gap and a wide one along $[11\bar{2}]$. Referring to the literature [320], this DB can be explained by a half-lattice shift of HC along $[1\bar{1}0]$ (***a₁*** in Figure 5.2a); it is classified as A1. The boundaries shown in Figure 5.2 (b) & (e) are the same, as the ones in (c) & (f). The offsets in those two groups are labelled as ***a₂*** and ***a₃*** respectively,

and they are mirror-symmetric along $[1\bar{1}0]$. This makes those two groups of DBs crystallographically the same, and this DB is classified as A2. It can be explained by a $3/4$ –lattice shift of HC along $[1\bar{1}0]$ plus a $1/4$ –lattice shift along $[11\bar{2}]$.

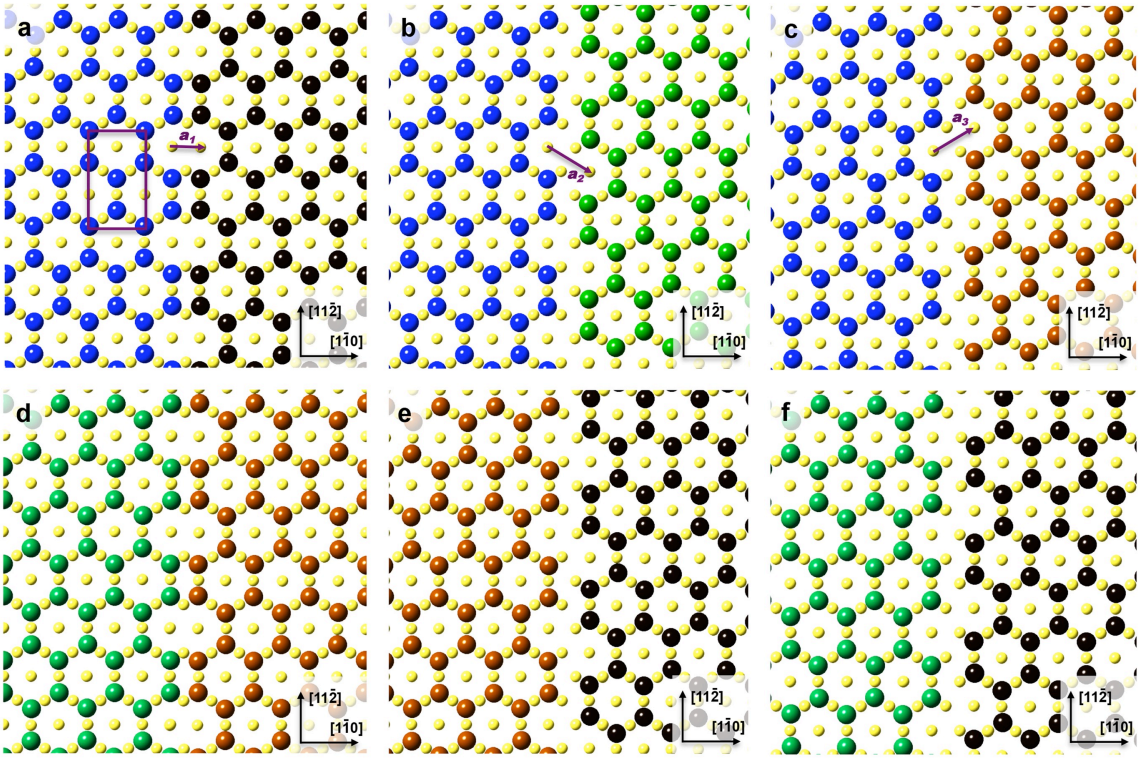


Figure 5.2: Building up structural models of crystallographic DBs of HC Ti_2O_3 (2 × 2)/Au(111) along $[11\bar{2}]$. Models are obtained by growing two different domains of HC from left and right side respectively, which meet in the middle and form a gap along $[11\bar{2}]$. Blue, green, black and brown balls represent four featured groups of Ti atoms. Images show the crystallographic DBs along $[11\bar{2}]$ when domains of (a) blue & black (b) blue & green (c) blue & brown (d) green & brown (e) brown & black (f) green & black grow into each other. The purple square in (a) is the unit cell lattice of HC thin film; $\boldsymbol{a_1}$, $\boldsymbol{a_2}$ and $\boldsymbol{a_3}$ indicate the shift of domains in (a), (b) and (c) respectively. The Au-Au spacing of the Au(111) surface along $[1\bar{1}0]$ is 2.89 Å.

Figure 5.3 illustrate the structural models of crystallographically unique linear DBs of HC Ti_2O_3/Au(111) along the $[1\bar{1}0]$ direction. Similar to the simulation that has been done along the $[11\bar{2}]$ direction (Figure 5.2), all the possible DBs developed from growing two

different domains can be grouped into three categories: Figure 5.3 (a) & (d), (b) & (e), (c) & (f). The DB in (a) & (d) is formed by a half-lattice shift of HC in $[11\bar{2}]$ direction ($\boldsymbol{b_1}$ in Figure 5.3a), and it is labelled as B1. The other two offsets show a mirror-symmetry along $[11\bar{2}]$ ($\boldsymbol{b_2}$ and $\boldsymbol{b_3}$ in Figure 5.3b&c), which results in the same type in crystallographic boundary. This type of DBs is classified as B2, and it has a $1/4$ −lattice shift of HC along $[1\bar{1}0]$ and a $1/4$ −lattice shift along $[11\bar{2}]$.

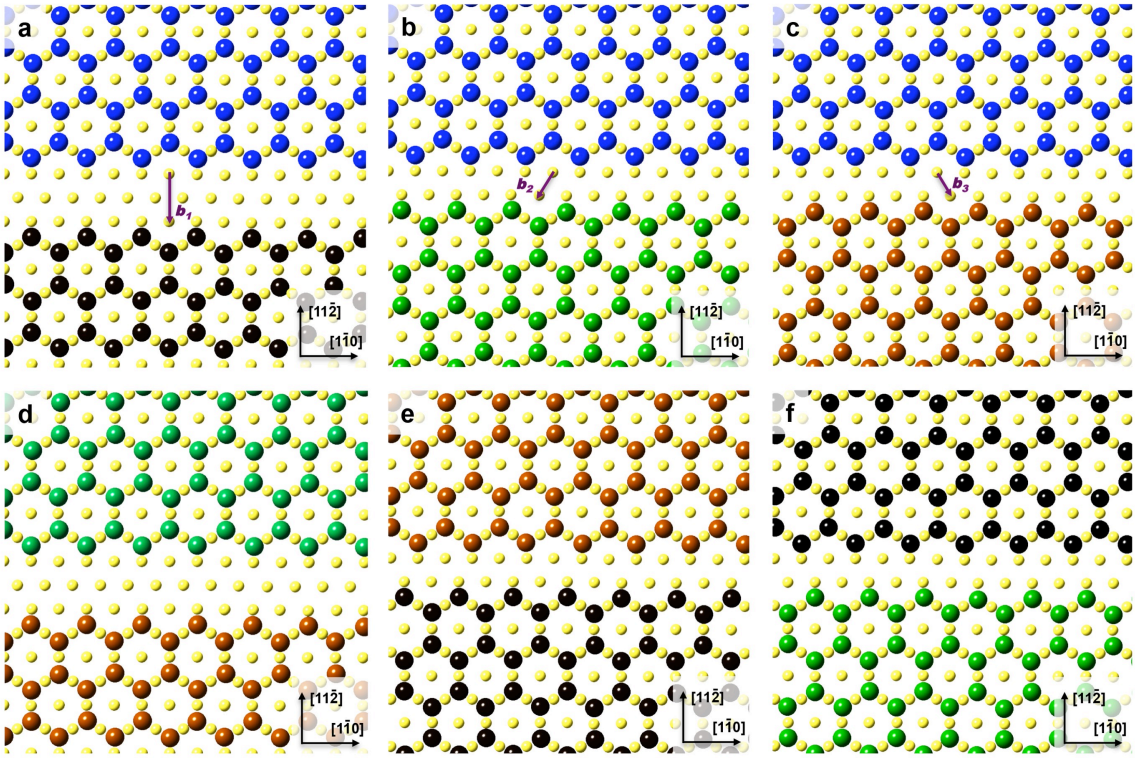


Figure 5.3: Building up structural models of crystallographically unique DBs of HC Ti_2O_3/Au(111) along the $[1\bar{1}0]$ direction. Models are obtained by growing two different groups of domains from the top and bottom sides, which meet in the middle and form a gap along $[1\bar{1}0]$. Blue, green, black and brown balls represent four featured groups of Ti atoms. Images show the crystallographic DBs along $[1\bar{1}0]$ when domains of (a) blue & black (b) blue & green (c) blue & brown (d) green & brown (e) brown & black (f) green & black grow into each other. $\boldsymbol{b_1}$, $\boldsymbol{b_2}$ and $\boldsymbol{b_3}$ indicate the shift of domains in (a), (b) and (c) respectively. The Au-Au spacing of the Au(111) surface along $[1\bar{1}0]$ is 2.89 Å.

Figure 5.4 shows how a domain is isolated from a uniform HC sheet with a different

domain by generating a closed loop. This loop consists of various types of crystallographically unique linear DBs, and all the DBs are along either ⟨1 1 -2⟩ or ⟨1 -1 0⟩ groups of crystallographic directions. However, the atomic structures of each DB cannot be revealed from the structural models. This is because factors that influence the atomic structures are complex. Referring to the literature of DBs in Chapter 3 (section 3.5), the bond angles of three neighbouring Ti atoms change in the DBs to release the energy raised from the offsets between two domains, and polygons more than the regular hexagons generate. There are multiple combinations of polygons that are able to work as the repeat unit cell in the DBs (e.g. 5,7 unit, 5,5,8 unit, 4,8 unit); the identical crystallographically unique DB may be able to form different atomic structures. At the same time, in order to form the atomic DB structures that are energetically preferred, one line of hexagons can be removed along the DB directions to expand the width of a specific crystallographically unique DB gap. This adds to the variety of the atomic structures of linear DBs. What's more, different from the free-standing HC 2D thin films like graphene – only forces come from neighbouring atoms in the thin films matter to atomic structures of DBs, forces from substrates need to be counted as well when it goes to the HC-Ti_2O_3/Au(111) system due to the strong bonding between epitaxial thin films and substrates. Therefore the direct experimental observation of the atomic structures is needed to obtain a comprehensive understanding of DB structures.

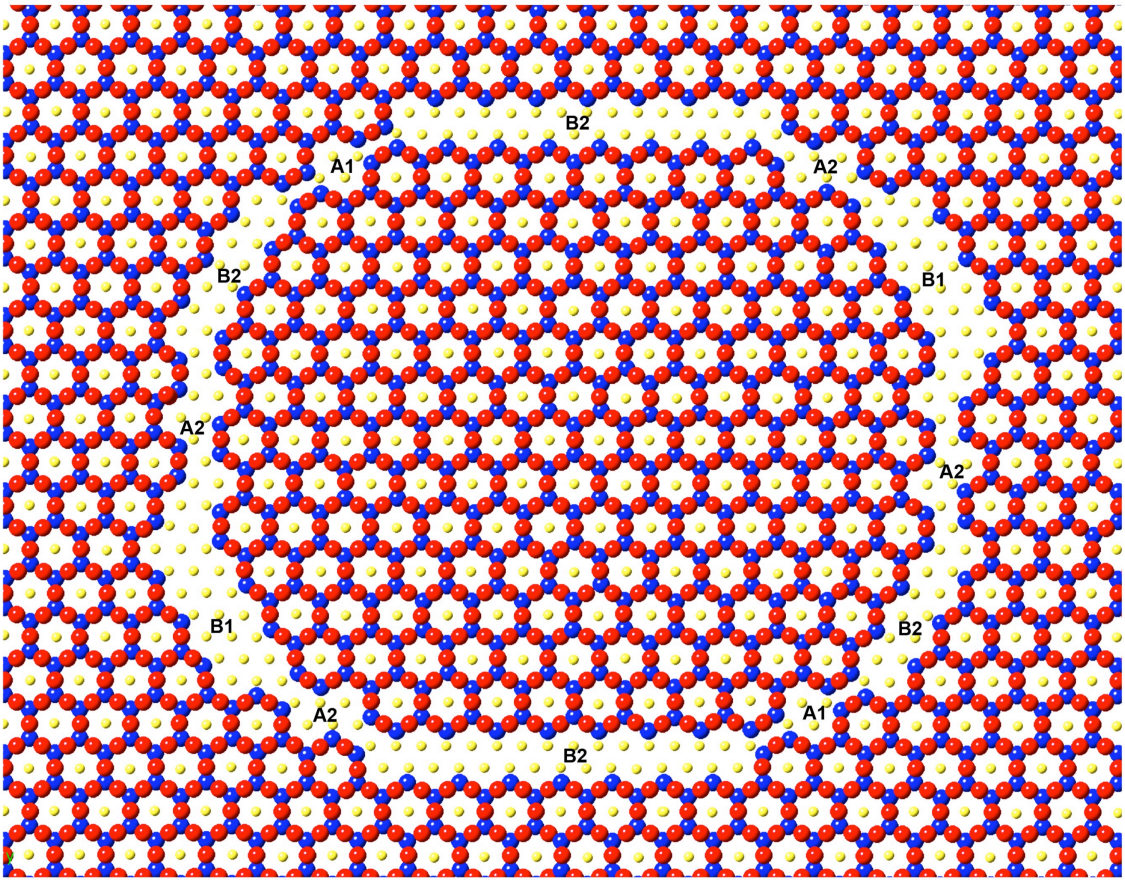


Figure 5.4: The structural model of the Ti_2O_3 HC thin film grown on Au(111) with two domains. A closed-circle gap with different types of crystallographically unique DBs labelled on it isolates the domain inside from the rest of the uniform HC sheet. Yellow balls represent Au atoms, blue balls are Ti atoms and red balls are O atoms. The Au-Au spacing of the Au(111) surface is 2.89 Å.

5.2.2 STM and DFT of linear domain boundaries in HC-Ti_2O_3/Au(111)

STM is an essential technique to investigate domain boundaries in honeycomb-Ti_2O_3/Au(111) structure. Very high-resolution STM images can directly show the atomic structures of DBs, and guide the DFT modelling of atomic DB structures. Figure 5.5a is an STM image of the most common DB to be observed in experiments. As illustrated in the large-scale image, it is able to generate a continuous DB line consisting of the same repeat unit without changing direction. The enlarged picture shows a unit cell of quadrilateral-octagon unit (4-8 unit) along the $[11\bar{2}]$ direction, which consists of a small 4-fold ring and a large 8-fold ring sharing one edge. A very similar anti-phase DB has been reported in the SiO_2/Mo(112) system [317, 319-320]. Considering the imaging conditions in this chapter (constant current mode with positive sample bias), the bright spots in the STM images are Ti atoms. The two different domains only have an offset along the $[1\bar{1}0]$ direction. The profile taken along the blue arrow indicates that the big ring has a width of about 0.9 nm along $[1\bar{1}0]$ (Figure 5.5b), which is about 1.5 times the periodicity of the HC lattice along the same direction. The FCC crystallographic unit cell of Au has dimensions of 4.08 Å, the close-packed $[1\bar{1}0]$ direction on the (111) surface has a (1 × 1) periodicity of 2.89 Å, therefore the periodicity of (2 × 2) HC-Ti_2O_3 is about 5.78 Å along the $[1\bar{1}0]$ direction. Comparing with the crystallographic structures of DBs that have been discussed in section 5.2.1, this result matches the width of the larger gap in the crystallographic A1 DB model. This DB is named A1 4,8. Figure 5.5c shows the relaxed DFT model: the 4-8 units of Ti atoms are the reflection of the bright spots observed in the STM image; O atoms are located at the bridging sites on the top-most layer. The formation energy of this DB is 0.145 eV $Å^{-1}$. This low formation energy and the uniform atomic structure of DB reveal that A1 4,8 DB suits the HC sheet very well: it is not only easy to be generated but also being very stable. The formation of A1 4,8 DB doesn't change the stoichiometry of Ti_2O_3 HC structure. From the DFT model, the

average number of Ti/O atoms in each ring is $\frac{4+8}{2} = 6$, and each Ti atom is shared by three neighbouring rings while each O atom is shared by two rings, therefore the stoichiometry is retained.

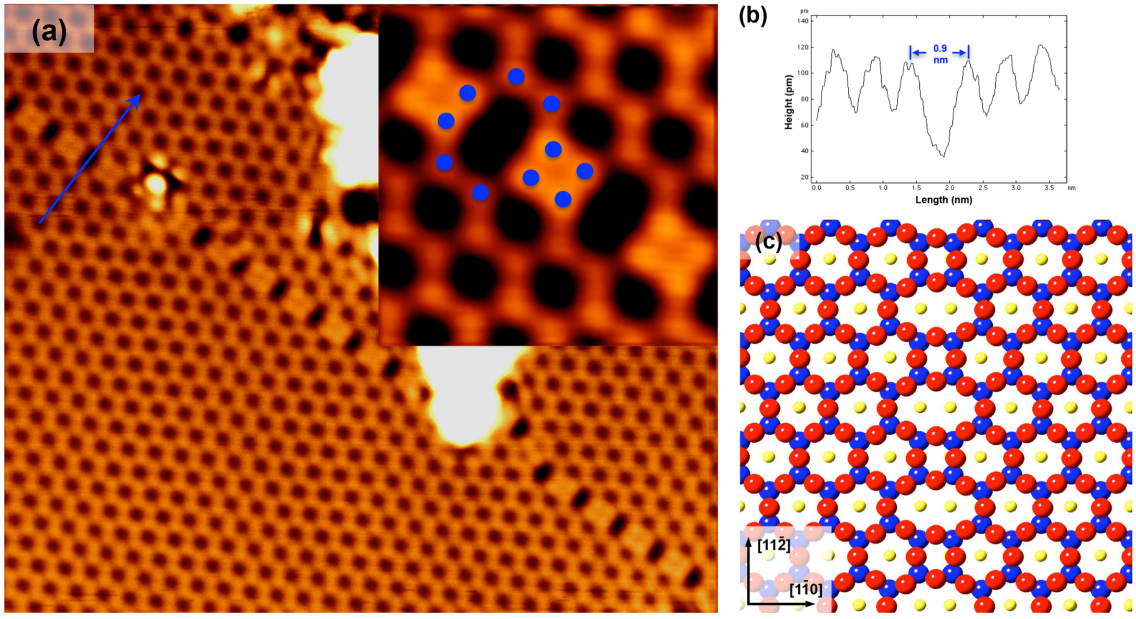


Figure 5.5: (a) STM image of the Ti_2O_3 HC thin film grown on Au(111) with a continuous long 4, 8 DBs (image size: 15.5 × 13.2 nm^2, V_s = 0.95 V, I_t = 0.22 nA). Image inserted at the top right corner shows the detailed structure of the DB (image size 2.5 × 2.5 nm^2); a repeat unit of a 4-membered small ring and an 8-membered big ring is indicated. This image is averaged from 11 STM images in the same area with the same resolution by SmartAlign. (b) Profile taken along the marked blue arrow in (a). (c) Relaxed DFT model of the A1 4, 8 DB. Au atoms are yellow; Ti atoms are blue; O atoms are red. The Au-Au spacing of the Au(111) surface along $[1\bar{1}0]$ is 2.89 Å. The formation energy of this DB is 0.145 eV $Å^{-1}$.

Figure 5.6a shows the STM image of the other type of linear DB that goes along the $[11\bar{2}]$ direction. In contrast with the A1 4,8 DB, it does not form a continuous DB line with many repeat units. Usually it turns into other types of DBs by shifting the direction along the ⟨1 -1 0⟩ families of crystallographic directions; defects are sometimes generated at the junction. In the high-resolution STM image, a DB unit cell is drawn out: two small 5-membered rings sharing two atoms fit into the narrower part of the DB gap, and two

large 7-membered rings fit into the wider part. The offset between those two domains are in both the $[1\bar{1}0]$ and $[11\bar{2}]$ directions, and each 5-7 unit that goes along $[11\bar{2}]$ is distorted towards the center of the DB gap. Crystallographically this DB belongs to the A2 type; it is named A2 5,5,7,7 DB. Figure 5.6b illustrates the relaxed DFT model in the case of generating a continuous DB, which has a formation energy of 0.244 eV $Å^{-1}$. Compared with A1 4,8 DB, more atoms are displaced from their ideal positions in A2 5,5,7,7 DB, therefore it is not surprising that the formation energy is higher. When it comes to the stoichiometry, this DB maintains the average Ti/O atoms in each ring to be 6 ($\frac{5+5+7+7}{4} = 6$) and has the same atom sharing rules as the regular HC structure (each Ti atom is shared by three rings while each O atom is shared by two), so the stoichiometry is still Ti_2O_3.

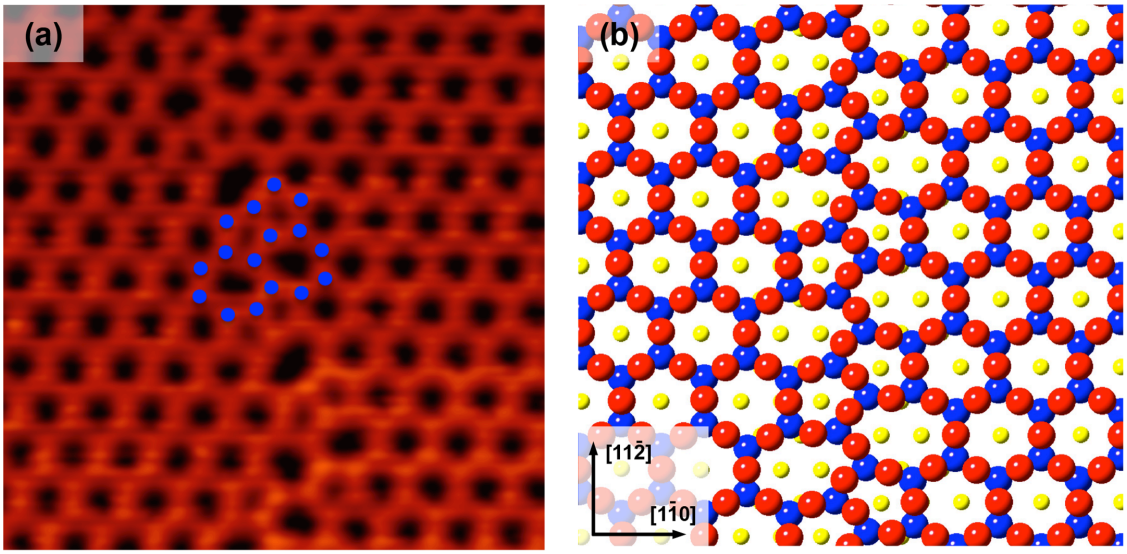


Figure 5.6: (a) STM Image showing the detailed structure of a mixture of DBs (image size: 6 × 6 nm^2, V_s = 0.9 V, I_t = 0.22 nA). A unit cell of two 5-membered small rings and two 7-membered big rings is indicated on the image. Crystallographically it belongs to the A2 DB. (b) Relaxed DFT model for the A2 5,5,7,7 DB. Au atoms are yellow; Ti atoms are blue; O atoms are red. The Au-Au spacing of the Au(111) surface along $[1\bar{1}0]$ is 2.89 Å. The formation energy of this DB is 0.244 eV $Å^{-1}$.

Figure 5.7a illustrates a continuous DB line along the $[1\bar{1}0]$ direction. Clearly this DB has a double-line atomic structure, and the enlarged STM image shows that the unit cell consists of two 5-7 units linked with each other with a rotation of 180° by sharing the edge along $[1\bar{1}0]$. Because the size of pentagon is smaller than heptagon, so the sharing edge has a 'snake' shape instead of being a straight line that equally divides the DB gap along $[1\bar{1}0]$. According to the profile taken along $[11\bar{2}]$ that crosses the DB perpendicularly (blue arrow in Figure 5.7a), those two domains are offset only along $[11\bar{2}]$, and the nearest 'holes' of HC between them has a distance of approximately 1.5 nm (Figure 5.7b). All these features reveal that crystallographically this is a B1 DB. Figure 5.7 c & d are the two relaxed DFT structural models that are most energetically favoured. Figure 5.7c is named B1a 5,5,8 DB (B1a in short), and the unit cell is composed of two small 5-fold rings and a large 8-fold ring. The two pentagons are aligned with each other along $[11\bar{2}]$ by sharing an edge in the middle of the DB gap, while the 8-fold rings sit on both sides of the double-pentagon units along $[1\bar{1}0]$ and share Ti atoms with neighbouring pentagons. The formation energy of B1a is 0.269 eV $Å^{-1}$. The other DFT model for B1 crystallographic DB is illustrated in Figure 5.7d. It is called B1b 5,7 DB (B1b in short) and it's the model that reflects the linear DB observed in Figure 5.7a. As described above, a 'snake'-like line in the middle of the DB gap separates the DB into two paths that go along $[1\bar{1}0]$, and each path is filled with 5-7 units. Every pentagon meets a heptagon from the other path across the 'snake'-like line, and is surrounded by two additional heptagons from both the left and right sides in the same path along $[1\bar{1}0]$. The marked bar in Figure 5.7c indicates the distance of nearest honeycomb 'holes' in two domains to be 1.5 times of the periodicity of (2 × 2) Ti_2O_3 HC lattice in the $[11\bar{2}]$ direction (whose periodicity is about 10.01 Å), which fits the value measured in Figure 5.7b. The formation energy of B1b DB is 0.283 eV $Å^{-1}$. For the stoichiometry of DBs, both B1a and B1b retain the stoichiometry of Ti_2O_3 HC structure: the average number of Ti/O atoms in each ring is the same to the number in regular

hexagon ring (B1a: $\frac{5+5+8}{3}$ = 6; B1b: $\frac{5+7+5+7}{4}$ = 6), and each Ti atom is shared by three neighbouring rings while each O atom is shared by two. Compared with the formation energy of B1a, the value of B1b is a little bit higher. However, only B1b DB was observed experimentally. It suggests that the experimental circumstance is different from the ideal condition that the DFT modelling was based on. Generally speaking, the conditions in experiments are complex, and it is difficult to accurately control and monitor factors that influence the formation of HC thin films as well as DBs. Those include annealing temperature, pressure and purity of O_2 inside the STM chamber, and the deposition rate of Ti. What's more, the precision of calculations in DFT modelling needs to be taken into account. Therefore even though the calculation demonstrates B1a is slightly more stable when compared with B1b, the fact that only B1b DB has been observed in STM experiments is more persuasive, and suggests that under the experimental conditions in the UHV chamber at room temperature it is the more stable DB structure.

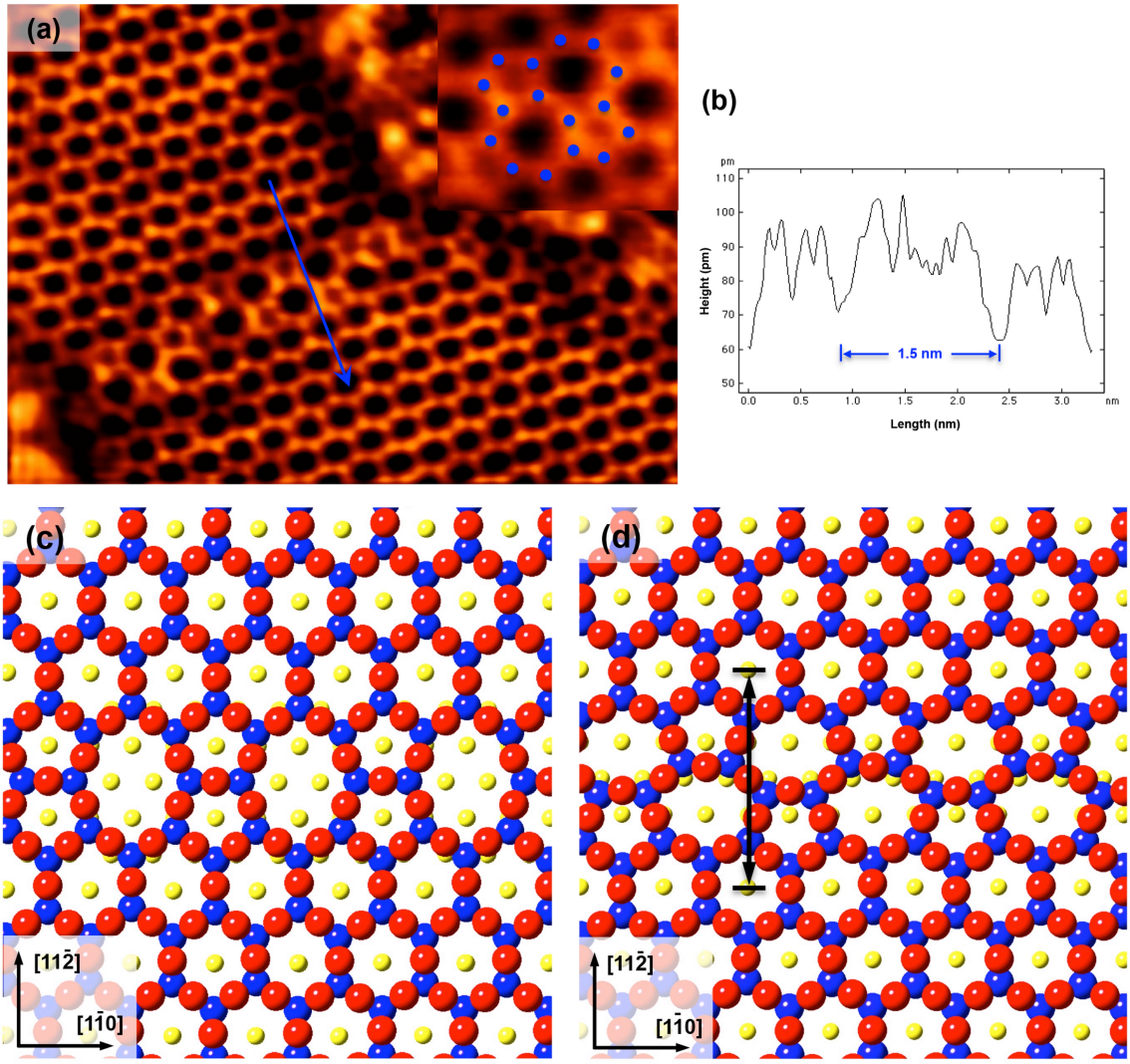


Figure 5.7: (a) Large-scale image showing a continuous double-line DB (image size: 10.5 × 7.5 nm^2, V_s = 1 V, I_t = 0.22 nA). Image at the top right corner is the detailed structure of the DB (image size 2.3 × 2 nm^2); the repeat unit consists of two 5-membered small ring and two 7-membered large rings as indicated on the image. This image is averaged from 4 STM images in the same area with the same resolution by SmartAlign. (b) Profile taken along the marked blue arrow in (a). (c) & (d) Two relaxed DFT models of the B1 DB. Au atoms are yellow; Ti atoms are blue; O atoms are red. The Au-Au spacing of the Au(111) surface along $[1\bar{1}0]$ is 2.89 Å. The unit cell of (c) is an 8-membered large ring with two aligned 5-membered small rings; it is classified as B1a 5,5,8 DB and the formation energy of this DB is 0.269 eV $Å^{-1}$. The unit cell of (d) is formed by a pair of 5-7 units reversely linked with each other; it is classified as B1b 5,7 DB. (d) is the model that reflects the STM image (a), and the double-headed arrow specifies the distance between two hexagon 'holes' across the DB along $[11\bar{2}]$. The formation energy of this DB is 0.283 eV $Å^{-1}$.

Figure 5.8a shows the other type of linear DB that forms along $[1\bar{1}0]$ with three repeat units (indicated by the white square). The enlarged STM image illustrates the unit cell of this DB is a distorted 5,5,8 unit. The profile taken along $[11\bar{2}]$ (blue arrow in Figure 5.8b) reveals that the offset between two domains is the result of displacements in both the $[1\bar{1}0]$ and $[11\bar{2}]$ directions. Crystallographically this DB belongs to the B2 type. Figure 5.8 c & d are two DFT atomic models that are energetically favoured for B2. The model illustrated in Figure 5.8c reflects the STM image shown in Figure 5.8a. The width of this DB is about 3/4 of the periodicity of the (2 × 2) Ti_2O_3 HC lattice in the $[11\bar{2}]$ direction (marked as 'i'). As labelled in Figure 5.8b, the distance between two 'peaks' across the large ring of DB along $[11\bar{2}]$ is approximately 0.8 nm, which is supposed to be a bit bigger than the width of DB. This measurement matches the assumption (width of this DB is about 0.75nm). Similar to B1a DB (Figure 5.7c), the unit cell consists of a 5,5,8 unit, however a distortion along $[1\bar{1}0]$ is observed as the result of fitting in a narrower DB gap. This DB is named B2a 5,5,8 (B2a in short), and the formation energy is 0.326 eV $Å^{-1}$. The other DFT model for crystallographic B2 DB has a similar unit cell to B1b (Figure 5.7d), which is a double-line structure filled up with staggered 5-7 units, and it is named B2b 5,7 DB (B2b in short). In contrast to B2a, the width of B2b DB is expanded to about 5/4 of the periodicity of the HC lattice in the $[11\bar{2}]$ direction (marked 'ii' in Figure 5.8d). To obtain this wider DB gap, one line of hexagons along $[1\bar{1}0]$ in the structural model of B2 is removed. The formation energy of B2b DB is 0.329 eV $Å^{-1}$, which is very similar to the formation energy of B2a. It is worth mentioning that two other DFT models have been tried for the B2 crystallographic DB. One fits the 5,5,8 units into the wider B2 DB gap. It failed because the gap was too wide to be closed by a single 8-membered ring. The value of the formation energy is 0.625 eV $Å^{-1}$, which is not competitive with the B2a and B2b models. The other attempt was to squeeze the double-line 5-7 pairs into a narrower B2 DB gap. It caused an extremely strong distortion; the formation energy for this DB is 0.595 eV $Å^{-1}$, which is also much higher than the value of the B2a and B2b

models. Therefore only the formation of B2a and B2b makes sense from the point of view of DFT modelling. For the stoichiometry of DBs, both B2a and B2b retain Ti_2O_3, which follow the principle of calculating stoichiometry of B1a and B1b DB structures. However, B2b 5,7 DB structure has not appeared in STM experiments, regardless of the fact that the formation energy of this DB is very close to B2a 5,5,8, and B2a has been observed experimentally. The explanation of the absence of B2b DB structure is more or less the same as the absence of B1a DB: the real circumstances of experiments are much more complex than the conditions of what DFT modelling was based on, and the calculation itself has a certain degree of error. Considering that the STM images are still the most convincible evidence, B2a DB is the only DB structure that has been observed experimentally for B2 type of crystallographically unique DBs, and the formation energy of it has been argued to be energetically preferred.

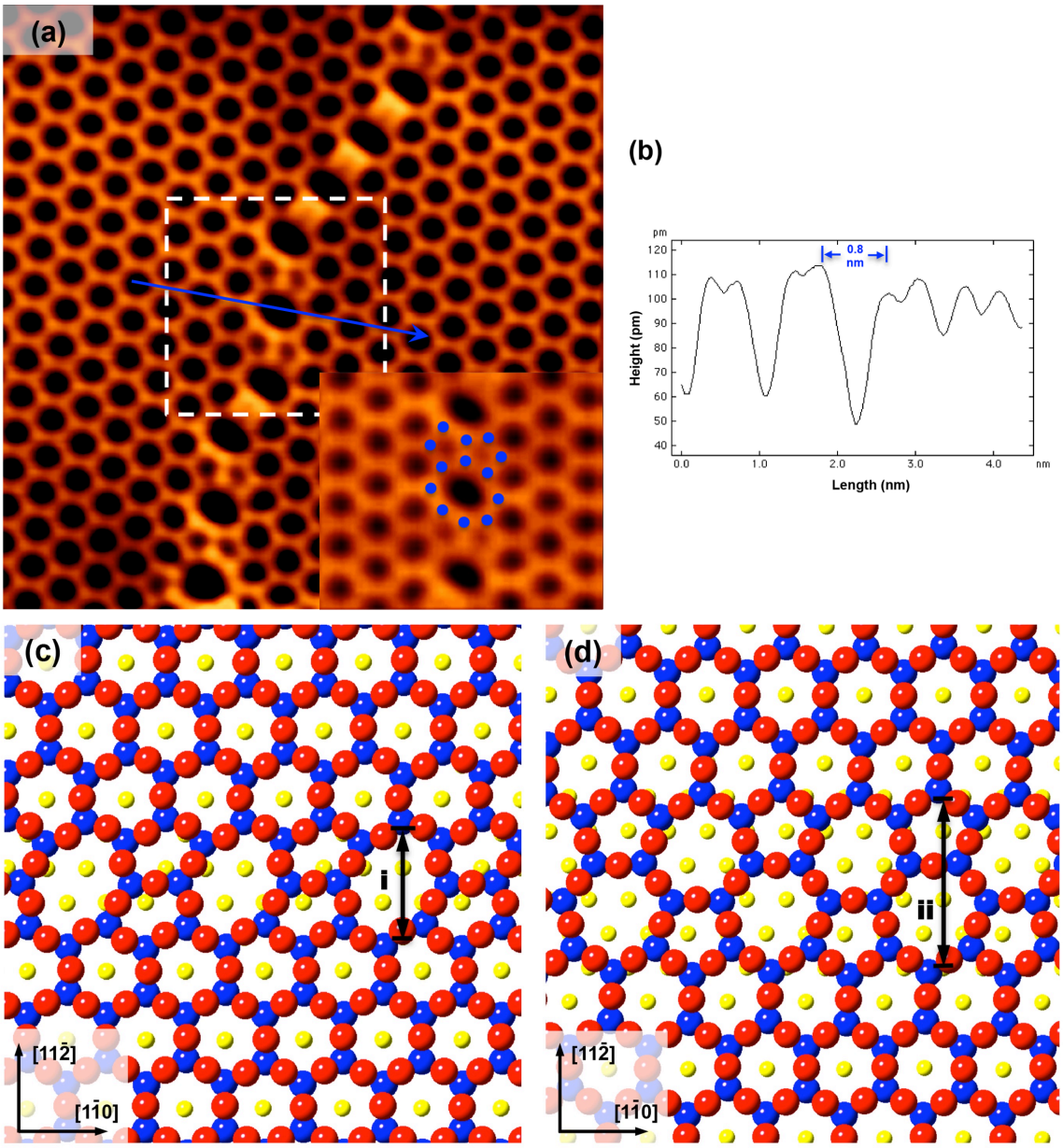


Figure 5.8: (a) Large-scale STM image shows mixed DBs (image size: 9 × 9 nm^2, V_s = 1 V, I_t = 0.25 nA). Image at the bottom right corner illustrates the detailed structure of the DB highlighted by the dashed box (image size 4 × 3.5 nm^2); a repeat unit cell consisting of two 5-membered small rings and an 8-membered large ring is indicated. This image is averaged from 88 STM images in the same area with the same resolution by SmartAlign. (b) Profile taken along the blue arrow marked in (a). (c) & (d) Two relaxed DFT models of the B2 DB. Au atoms are yellow; Ti atoms are blue; O atoms are red. The Au-Au spacing of the Au(111) surface along $[1\bar{1}0]$ is 2.89 Å. The black bar marked i and ii are the width of the DB in those two models respectively. (c) is the narrowed version of B2 DB, the unit cell consists of a distorted 5,5,8 unit. This DB is classified as B2a 5,5,8 and it matches the STM image (a). The formation energy of this DB is 0.326 eV $Å^{-1}$. (d) is expanded crystallographic B2 DB (obtained by removing one line of hexagons in the gap of the crystallographic B2 DB). The unit cell consists of a pair of 5-7 units aligned with distortion. This DB is classified as B2b 5,7. The formation energy of this DB is 0.329 eV $Å^{-1}$.

Table 5.1 sums up the classification of the linear DBs of HC Ti_2O_3/Au(111). Among all the DBs, A1 4,8 is the most common one to be observed, and it usually develops a continuous line with many repeat units. The low formation energy confirms that A1 4,8 is the easiest to be generated compared with the other DBs. The A2 5,5,7,7 DB is not likely to form a continuous line in practice but turns into other DBs or defects after only one or two repeat units. B1b 5,7 and B2a 5,5,8 are both able to develop a continuous DB line, but the range and stability are not comparable to A1 4,8. Even though B1a and B2b DBs have a fair chance to form according to the results of the DFT modelling and the values of their formation energies, they were not observed in STM images. Figure 5.9 illustrates a STM image with the three types of linear DBs that can be found in long-range: A1 4,8, B1b 5,7 and B2a 5,5,8. Either defects or a mixture of short-range DBs (including single unit cell) connects those DBs.

Domain Boundaries (DBs) in (2 × 2) honeycomb Ti_2O_3/Au(111)						
Directions of DB	**< 1 1 -2 >**		**< 1 -1 0 >**			
Crystallographic DB	A1	A2	B1		B2	
Atomic DB* (DFT models)	A1 4,8	A2 5,5,7,7	B1a 5,5,8	B1b 5,7	B2a 5,5,8	B2b 5,7
Formation Energy (eV Å^{-1})	0.145	0.244	0.269	0.283	0.326	0.329

* DBs that are underlined have been observed in STM images

Table 5.1: A summary of the classification of the DBs of the (2 × 2) honeycomb Ti_2O_3/Au(111) and the formation energy of each type.

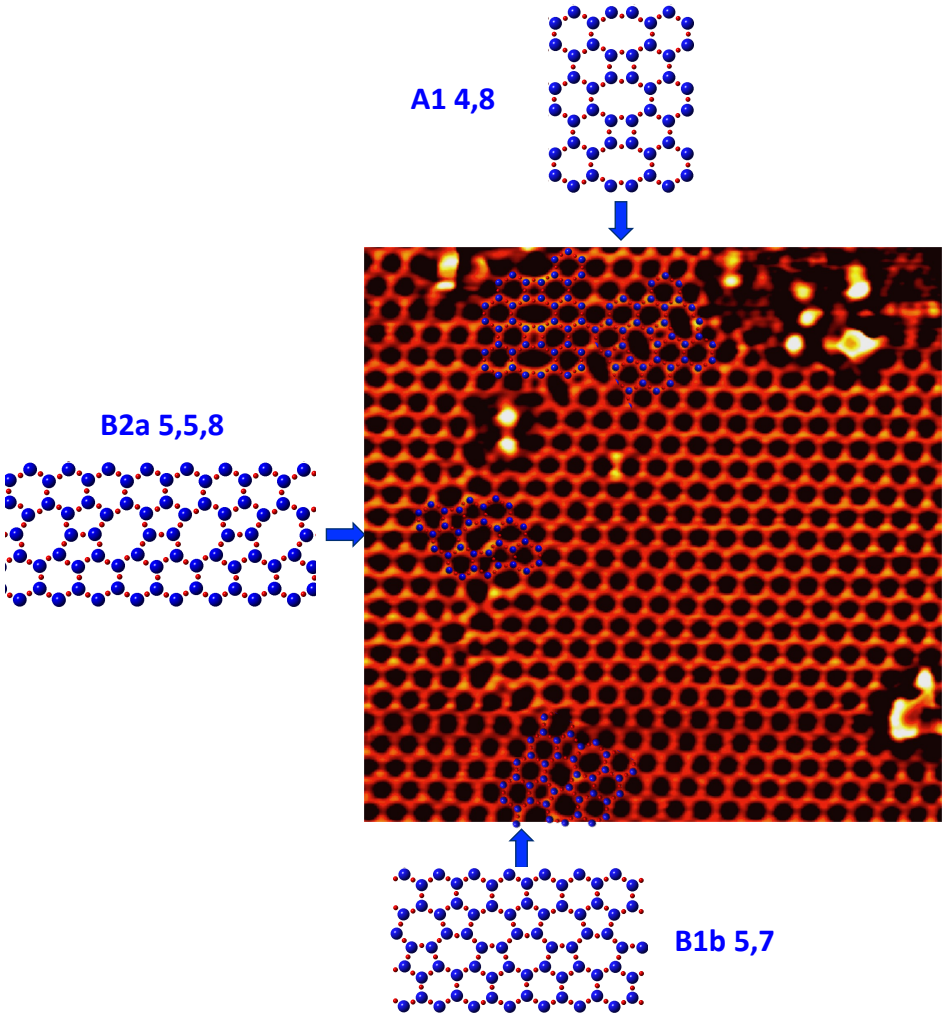


Figure 5.9: A large scale STM image of a honeycomb Ti_2O_3/Au(111) thin film with multiple types of DBs boundaries (image size: 14 × 14 nm^2, V_s = 0.9 V, I_t = 0.22 nA). Three types of long-range linear DBs (A1 4,8; B1b 5,7; B2a 5,5,8) are labelled with corresponding structural models drawn on the image. The blue balls are Ti atoms and the red small balls are bridging O atoms. This image is averaged from 10 STM images in the same area with the same resolution by SmartAlign.

5.2.3 STM of rotational domain boundaries in HC-Ti_2O_3/Au(111)

Figure 5.10a illustrates an interesting 'snowflake' domain that is isolated from the uniform honeycomb Ti_2O_3/Au(111) thin film by a closed DB loop. This DB consists of six end-to-end 5-7 units with rotational directions and different degrees of distortions (Figure 5.10b). Ignoring the distortions of pentagons and heptagons, the 'snowflake' domain closes in on itself with six-fold symmetry (C_6): the 7-fold rings are all elongated along the ⟨1 -1 0⟩ families of crystallographic directions in the view of the large HC sheet domain, while the 5-fold rings are aligned in directions of ⟨1 1 -2⟩. For stoichiometry of this DB loop, since the average number of Ti/O atoms in each ring ($\frac{5+7}{2} = 6$) and the rules of atom sharing (each Ti atom is shared by three rings while each O atom is shared by two rings) are the same with regular HC structure, so the stoichiometry stays as Ti_2O_3. In the year 2011, a similar closed-circle boundary loop was reported in epitaxial graphene grown on SiC(0001), which was called 'flower'-shaped grain boundary loop [300].

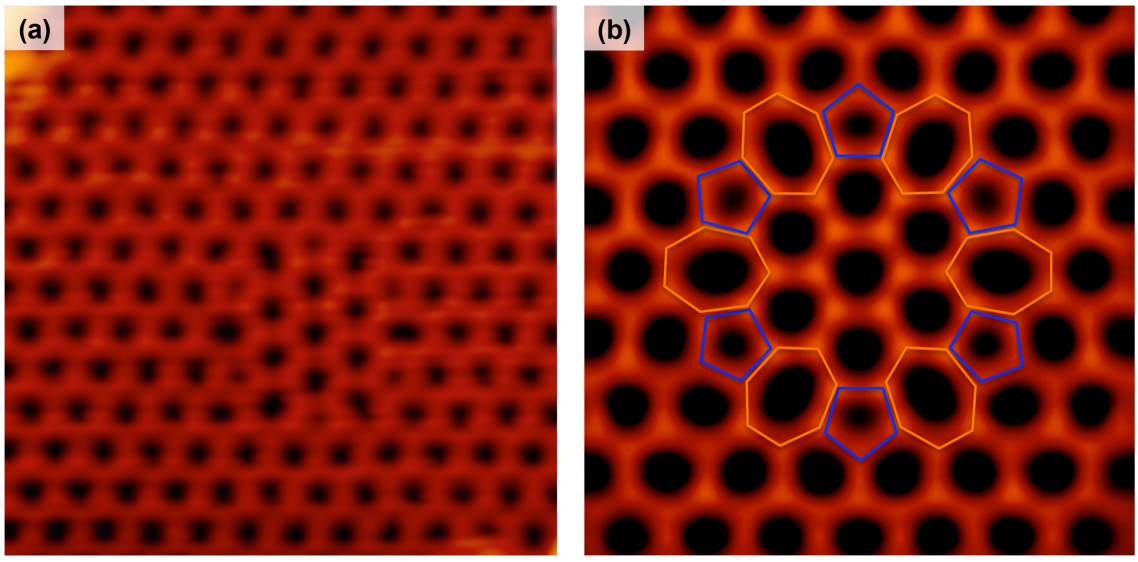


Figure 5.10: STM images of the honeycomb Ti_2O_3/Au(111) thin film with a 'snowflake' shape domain. (a) The large-scale STM image (image size: 6.5 × 6.5 nm^2, V_s = 0.9 V, I_t = 0.22 nA). (b) The detailed 'snowflake' domain (image size: 4.2 × 4.2 nm^2). Fourier-transform filtering was applied. The rotating 5-7 units with different degree of distortions form the closed domain boundary by sharing one edge. The pentagons and heptagons are drawn in blue and orange respectively.

Figure 5.11 illustrates another rotational defect observed in honeycomb Ti_2O_3/Au(111). It has an 'X' shape and is smaller than the ''snowflake' DB. Comparatively this structure is easier to be generated as it has been found in a few STM images. Figure 5.11a shows a regular X-shaped unit that is formed by four elongated large rings surrounded a hexagon; the spaces between those large rings are filled with four small rings. Figure 5.11c is the detailed STM image. The four large rings are heptagons with different degree of distortion, and the small rings are pentagons. It can be seen as four 5-7 units link end-to-end surrounding a hexagon in the centre. The X-shaped defect has C_2 symmetry axis (180° rotation), and it stretches along ⟨1 -1 0⟩. The stoichiometry of the X-shaped unit retains Ti_2O_3: the average number of Ti/O atoms in each ring is $\frac{5+7}{2} = 6$, and each Ti atom belongs to three neighbouring rings while every bridging O atom is shared by two rings. When the distortion is strong enough to break the regular 'X' shape, a unit with an irregular structure would be generated. As seen in Figure 5.11b, the large ring in the upper left side of the 'X' shape consists of 8 Ti atoms instead of 7.

The similar X-shaped defect have been found in *k*-TiO_x phase (Ti_2O_3) grown on Pt(111) [160] and (2 × 2) V oxide honeycomb film (V_2O_3) grown on Pd(111) [284]. In both systems, the X-shaped units link with each other and form a DB line instead of appearing by itself as a single unit in HC Ti_2O_3/Au(111). As discussed in Chapter 3 (section 3.5), more strain needs to be relieved for the Ti_2O_3/Pt(111) system, therefore the topography of islands separated by X-shape defects was observed in STM images. In the HC Ti_2O_3/Au(111) system, a better match between epitaxial film and substrate is achieved, so only single X-shaped unit was generated. Compared with *k*-TiO_x phase/Pt(111) and (2 × 2) HC V-oxides/Pd(111), the frequency of observing this rotational defect is very low in HC Ti_2O_3/Au(111).

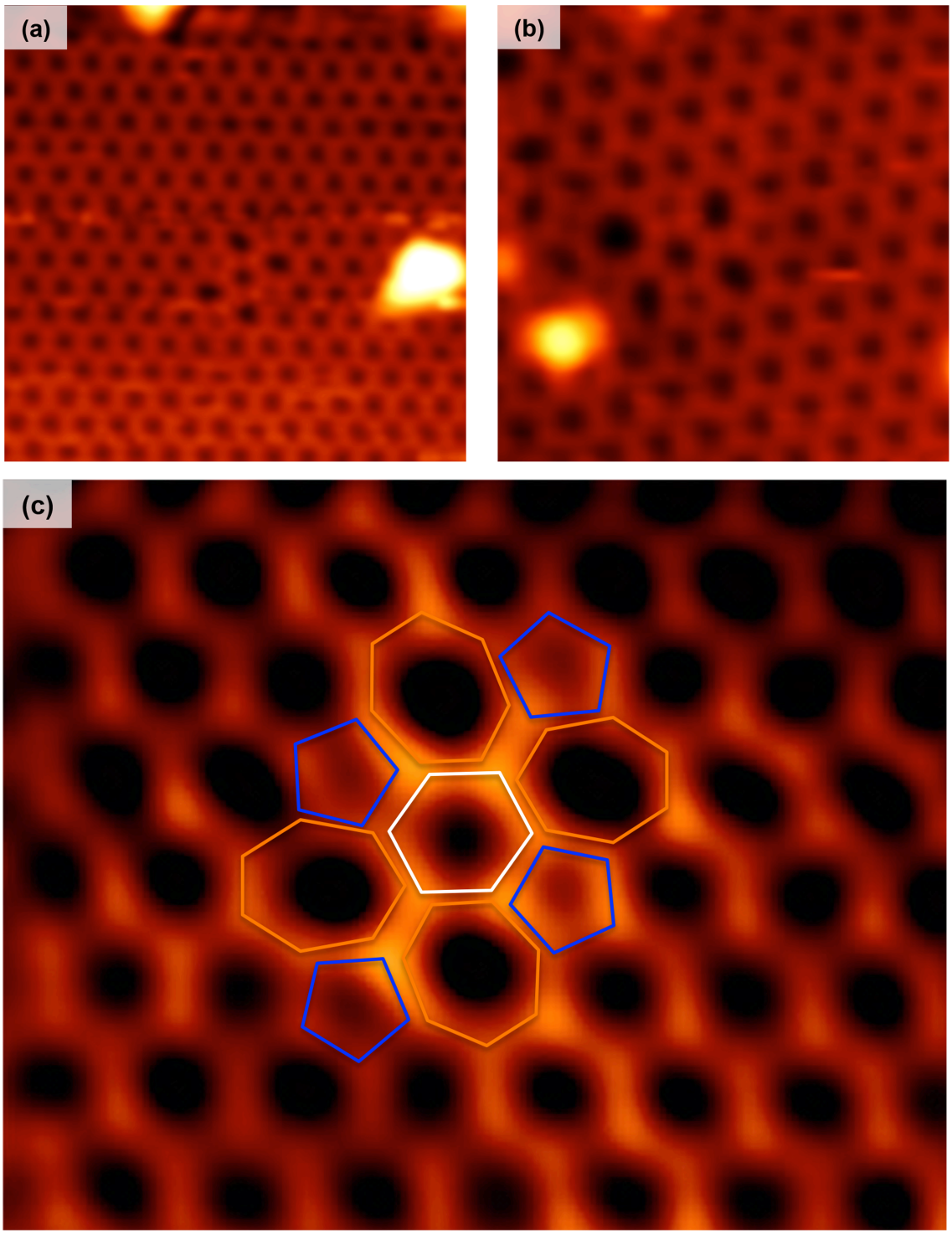


Figure 5.11: STM images of the HC Ti_2O_3/Au(111) thin film with X-shaped rotational defect. (a) Regular X-shaped unit (image size: 8 × 8 nm^2, V_s = 0.9 V, I_t = 0.22 nA). (b) Irregular X-shaped unit (image size: 5 × 5 nm^2, V_s = 0.95 V, I_t = 0.22 nA). (c) Details of the X-shaped unit (image size: 4.5 × 4.5 nm^2, V_s = 0.9 V, I_t = 0.22 nA). Fourier-transform filtering was applied. Pentagons are drawn in blue, heptagons are drawn in orange and the hexagon is drawn in white.

Figure 5.12 illustrates another type of small rotational defect in HC Ti_2O_3/Au(111). Figure 5.12a shows two units next to each other with a rotation. At first glance this rotational defect has a triangle-like structure, therefore it is called triangle-shaped unit. It has a C_3 symmetry axis and it is formed by three 5-7 units rotated by 120° from each other; all the 7-membered rings are elongated in ⟨1 -1 0⟩ families of the crystallographic directions (Figure 5.12b). Similar to the 'snowflake' DB structure and X-shaped defect, the stoichiometry of the triangle-shaped unit is Ti_2O_3: the average number of Ti/O atoms in each ring is $\frac{5+7}{2} = 6$, and each Ti atom belongs to three neighbouring rings while every bridging O atom is shared by two rings. Similar to the X-shaped defect, this triangle-shaped rotational defect has been very commonly observed in the (2 × 2) HC V_2O_3/Pd(111) system [284], and appeared in *k*-phase Ti_2O_3/Pt(111) as well [160]. What's more, a schematic model of this rotational structure was brought up in the study of grain boundary loops in graphene, which was named 555-777 defect [300]. The argument of the infrequent observation of the X-shaped defect works on the triangle-shaped defect as well – a good matching of HC Ti_2O_3 thin film and Au(111) substrate makes it harder to be developed for the purpose of relieving strains.

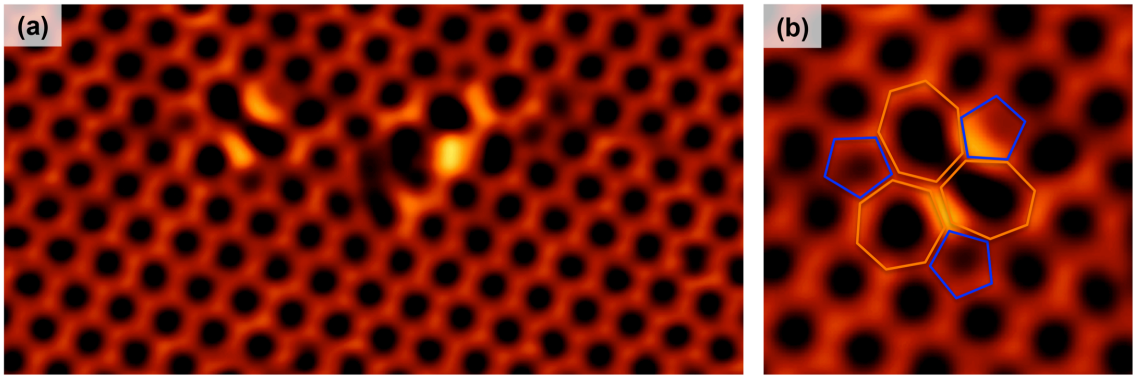


Figure 5.12: STM images of the triangle-shaped defect in HC Ti_2O_3/Au(111) thin film. (a) Two triangle-shaped defects rotated to each other (image size: 8 × 4 nm^2, V_s = 0.9 V, I_t = 0.22 nA). (b) Enlarged triangle-shaped unit with pentagons (drawn in blue) and heptagons (drawn in orange) indicated in the image (image size: 3 × 3 nm^2, V_s = 0.9 V, I_t = 0.22 nA). Fourier-transform filtering was applied.

Figure 5.13a shows a small defect unit with a 'cross' feature in HC Ti_2O_3/Au(111). In detail, it consists of two large 7-membered rings (marked as orange heptagons) elongated along the ⟨1 1 -2⟩ crystallographic directions and two small 5-embered rings (marked as pentagons) going along ⟨1 -1 0⟩ in Figure 5.13b. This unit has C_2 symmetry axis (180° rotation), which makes it a rotational structure. The same structure has been reported in HC graphene sheets as well as other 2D hexagonal films including monolayer boron nitride (BN), and it was called Stone-Wales (S-W) defect [295, 300, 333-334], therefore the name of S-W defect is used for this structure in the HC Ti_2O_3/Au(111) system. The stoichiometry of S-W defect is the same as Ti_2O_3 HC sheet as well as other rotational structures listed above: the average number of Ti/O atoms in each ring is 6 ($\frac{5+7+5+7}{4} = 6$), and the atom sharing rules are the same. Again, due to the good matching of over-layer thin films and substrates in the Ti_2O_3/Au(111) system, S-W defect haven't been observed frequently, and it showed up as a single unit when it was seen in experiments.

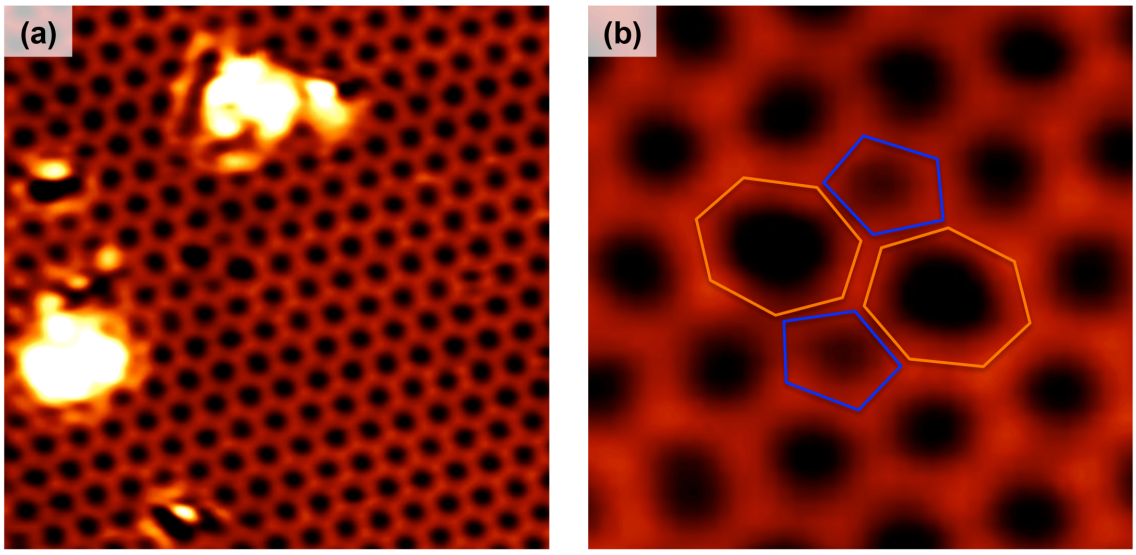


Figure 5.13: STM images of the S-W DB structure in HC Ti_2O_3/Au(111) thin film. (a) An S-W unit (image size: 10 × 10 nm^2, V_s = 0.95 V, I_t = 0.22 nA). (b) Enlarged S-W unit with pentagons (drawn in blue) and heptagons (drawn in orange) indicated in the image (image size: 2 × 2 nm^2, V_s = 0.95 V, I_t = 0.22 nA). Fourier-transform filtering was applied.

5.3 Discussion

It is instructive to compare the DBs of HC Ti_2O_3/Au(111) with those reported in other ultra-thin 2D films with a HC structure (e.g. graphene and metal-supported silica). For the linear DBs, the one with the unit cell of a 4-8 unit is comparatively the most stable as well as energetically the most favourable: it was observed in the longest range in both Ti_2O_3/Au(111) and SiO_2/Mo(112) films compared with other linear DBs [317, 320]. Similar grain boundary structure was reported in the hexagonal boron nitride thin film (h-BN), however the 4-8 units are distorted in this system [310]. The linear DBs with unit cell of 5,5,8 unit have also been found in various other 2D HC thin films including graphene [308-309]. Because graphene is either a free-standing film or only has very weak bonding with substrates, so the 5,5,8 units are relaxed within the film with very little distortion. However, for the DBs with 5,5,8 units in Ti_2O_3/Au(111) (B1a & B1b), the forces come from substrates cannot be ignored – a distortion of 5,5,8 units was observed in B2a DB structure. In the literature, most DBs with unit cells that based on the 5-7 unit have single-line structures [298-299], which is different from the double-line structures reported in the Ti_2O_3/Au(111) thin films (B1b 5,7 DB and B2b 5,7 DB). The multi-line DBs based on 5-7 units have been observed in graphene as double 5 double 7 (d5d7) and trible 5 trible 7 (t5t7) – neither of which is similar to the DBs shown in the Ti_2O_3/Au(111) thin films [309]. For the rotational structures in 2D honeycomb films, very limited literature could be found. The ‘flower’-shape grain loop reported by Cockayne et al. in epitaxial graphene on SiC(0001) matches the ‘snowflake’ DB in Ti_2O_3/Au(111) [300]. A group of rotational structures with symmetry axis ranging from C_2 to C_6 were simulated in their paper, however only the ‘flower’-shape grain boundary loop and S-W defect were observed experimentally in graphene. Even so, the schematic models of the rotational boundary loops have been found in other 2D HC thin films. For example, the triangle-shaped defect was seen in HC Ti_2O_3/Au(111), Ti_2O_3/Pt(111) [160] and V_2O_3/Pd(111) [284] thin films, and the S-W defect was observed in the HC Ti_2O_3/Au(111) system as well. For X-shaped defect, it was treated more likely as a unit cell of linear DBs in HC thin films of

Ti_2O_3/Pt(111) [160] and V_2O_3/Pd(111) [284], which showed up quite often. However, due to the good matching between thin films and substrates in the HC Ti_2O_3/Au(111) system, it is rare to be observed and only shows up as a single unit in experiments. This also works on other types of rotational DB structures discussed in the HC Ti_2O_3/Au(111) system in this chapter. Interestingly, all the linear and rotational DB structures/defects retain the stoichiometry of Ti_2O_3, which is the same as the HC structure of Ti_2O_3/Au(111). This result reveals that there's a trend of maintaining the stoichiometry of original 2D HC thin films being Ti_2O_3 for the DB structures that are generated in HC Ti_2O_3/Au(111) thin films.

5.4 Conclusions

In summary, there are two kinds of DBs with repeat units in the Ti_2O_3/Au(111) honeycomb thin films – linear DBs and rotational DBs/defects. For linear DBs, a comprehensive study was carried out theoretically and experimentally. Considering the strong influence of the Au(111) substrates, two families of crystallographic directions stand out for the formation of DBs: ⟨1 1 -2⟩ and ⟨1 -1 0⟩. Four types of crystallographically unique DB structures were simulated: A1 and A2 along ⟨1 1 -2⟩; B1 and B2 along ⟨1 -1 0⟩. Further study based on STM imaging and DFT modelling revealed six atomically unique DB structures under the classification of crystallographic DBs: A1 4,8; A2 5,5,7,7; B1a 5,5,8 and B1b 5,7; B2a 5,5,8 and B2b 5,7. Even though they are all possible to form from the point of view of DFT modelling, only A1 4,8, B1b 5,7 and B2a 5,5,8 have been observed in experiments that developed linear DBs in long-range; the short-range A2 5,5,7,7 DB existed with only one or two repeat units; neither B1a 5,5,8 nor B2b 5,7 were found in STM images. Due to the difficulty of obtaining atomic-resolution STM images of DBs, the possibility of forming those two types of linear DBs cannot be ruled out; however the objective evidence of STM images

is still most convincing. At this stage, it is reasonable to draw the conclusion that A1 4,8, B1b 5,7 and B2a 5,5,8 are the three types of linear DBs that exist over a long-range in the Ti_2O_3/Au(111) honeycomb thin films; A1 4,8 DB structure is the easiest to form in theory and is most commonly to be observed in experiments.

Rotational DBs/defects are comparatively rare to be found in experiments: only one STM image of the 'snowflake' DB loop consisting of distorted 5-7 units was seen; a few X-shaped defects were observed; very limited STM images of triangle-shaped defects and S-W defects were found. All those rotational structures showed up as a single unit in the HC Ti_2O_3/Au(111) system. Since the atomic-resolution STM images have been obtained, a further study with DFT modelling is going to be carried out.

Chapter 6:

Point Defects in Honeycomb Ti_2O_3 Thin Films Grown on Au(111) Substrates

6.1 Background

6.1.1 Overview

The rutile TiO_2(110) surface has been widely researched due to its outstanding physical and chemical properties that can be utilised in fields such as solar cells, photocatalysts and gas sensors [106, 335-337]. Since the photo-assisted splitting of water on a TiO_2(110) electrode was reported in 1972 [75], water dissociation on rutile TiO_2(110) surfaces has attracted a lot attention because this phenomenon plays a key role in photocatalysis [98-102]. It has been reviewed that oxygen vacancies are the active site for water dissociation in Chapter 3 (section 3.3.2) [106, 109-117]. In recent years, successful synthesis of ultrathin TiO_x films with remarkable structures (that are not found in bulk titanium oxides terminations) on metal substrates has been reported; two notable TiO_x structures – honeycomb (HC) and pinwheel – have been grown on Au(111) substrates in this thesis (Chapter 4). Farstad et al. studied the water adsorption and desorption of ultrathin TiO_x films on Au(111) out of the interest in the water-gas shift (WGS) reaction [46]. They drew conclusions that no water adsorption was suggested for perfect Ti_2O_3 HC films; the small percentage of active Ti sites were believed to be contribution of defects. In pinwheel films the bright spokes and hubs were believed to be responsible for water dissociation. In the year of 2014, Li et al. published their study which argued that adsorption sequence for pinwheel structure was a consequence of a gradual shift in the relative atomic positions of pinwheel film with respect to the Au(111) substrates [173]. This result emphasises the crucial role of imperfections in TiO_x ultrathin films for water adsorption and desorption. To reveal the nature of water adsorption and desorption in Ti_2O_3 HC thin films, an in-depth study of the imperfections of the thin films is necessary.

In the uniform Ti_2O_3 HC thin films grown on reconstructed Au(111) substrates, only a few defects and domain boundaries were observed. A comprehensive investigation of

domain boundaries has been reported in Chapter 5. In this chapter, point defects in the HC-Ti_2O_3/Au(111) are discussed. Because point defects are rarely found experimentally, the idea of creating defects on purpose emerges. In the year of 2012, Minato et al. published a well-controlled method to excite single oxygen vacancies on TiO_2 in STM by applying a high sample bias pulse for 1 s [154-155]. This technique is used in my experiments to create point defects in HC-Ti_2O_3/Au(111) thin films.

6.1.2 Experimental details

STM experiments were carried out in the JSTM-4500XT system. Mica-supported Au(111) single crystal films (Agilent Technologies, U.K.) were used as the substrates. The sample preparation processes were the same as described in Chapter 4 (section 4.1.2). STM scanning was performed in the constant current mode with positive sample voltage at room temperature, so that empty electronic states were imaged by the STM. To create single defects in a regular Ti_2O_3 HC thin film, a high sample bias pulse was applied for about 1 second via tip cleaning action. The pulsed voltage was set up at about 3 V. After this process the standard STM scan continued to image the same surface area. All the STM images were processed with Image SXM, SmartAlign and Gwyddion software. Structural models of point defects were generated with CrystalMaker.

6.2 Results

6.2.1 Titanium vacancies in HC-Ti_2O_3/Au(111) thin films

Figure 6.1a-h illustrates STM images that record the diffusion of a heart-shaped hole in

a HC-Ti_2O_3/Au(111) ultra-thin film for about 5 minutes. From the calculation of Density of States (DOS) in Chapter 4 it is clear that bright spots in Ti_2O_3 HC STM images are Ti atoms as a positive sample bias is applied during scanning. The DFT model of the HC-Ti_2O_3 film discussed in Chapter 4 shows a (2 × 2) hexagonal lattice with respect to the (1 × 1) Au(111) lattice. Ti-layer is in-between the Au substrate and the O-layer, which sits at the three-fold hollow sites of (1 × 1) Au hexagonal lattice. O atoms locate at the bridging sites of Ti-layer. Three neighbouring Ti hexagons around the heart-shaped hole are drawn in Figure 6.1a-h. The observed Ti atoms are indicated by filled blue balls; the missing Ti atoms which are supposed to compose the (2 × 2) hexagonal lattice are marked as unfilled blue balls. Figure 6.1a-h reveals that the heart-shaped hole comes from three missing Ti atoms, and the locations of those Ti vacancies change through the continuous imaging. However these Ti vacancies stick with each other as a group and keep the heart shape of the ‘hole’. Movements of these defects are more like turning around than diffusing in a straight line (average diffusion speed: 0.16 nm/min). The depth of this Ti vacancy ‘hole’ is measured to be about 80 pm (Figure 6.1i). Comparing to the thickness of regular HC film (about 40 pm), this dark point defect hole seems to be deeper in STM images. However the local electron density of regular HC thin film is higher than the area with the Ti vacancy ‘hole’, the difference in depth could be an effect of STM imaging mechanism than the actual topography.

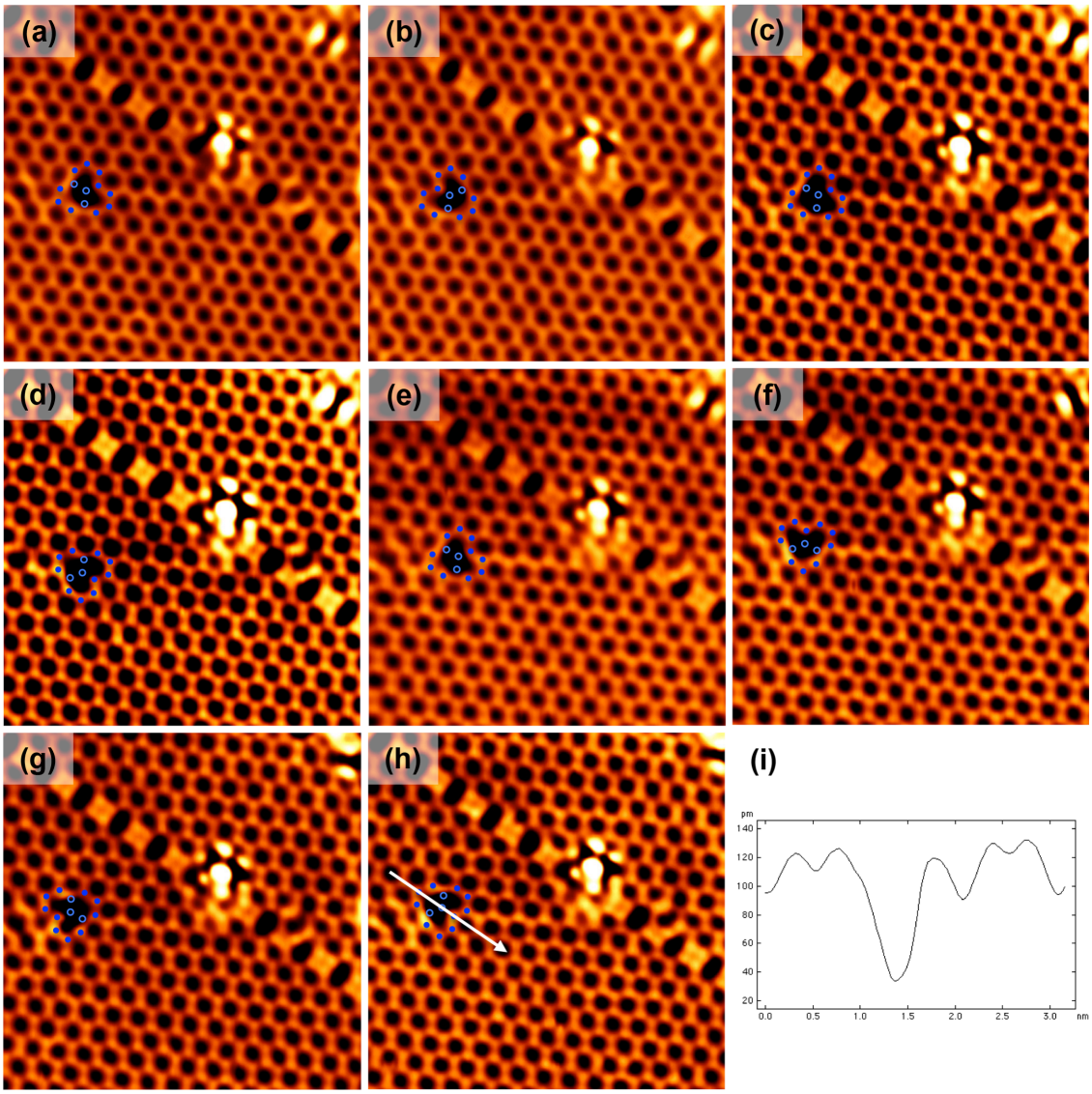


Figure 6.1: (a)-(h) STM images of diffusion of a heart-shaped hole. A linear domain boundary is observed and used to determine the relative position of defects. Image size: 8 × 8 nm^2; V_s = 0.95 V; I_t = 0.22 nA. Three Ti hexagons are indicated. The filled blue balls are observed Ti atoms while the unfilled blue balls are the missing Ti atoms. (i) A profile taken along the white arrow marked in (h) which crosses the defect. The depth of the point defect hole is about 80 pm.

The STM images in Figure 6.2 illustrate diffusion of a triangle-shaped defect in a slightly shorter period of time (about 4.5 minutes). Compared with the heart-shaped hole, this triangle hole is smaller in size as it comes from missing only one Ti atom in the Ti-layer (indicated in Figure 6.2b). Moreover, diffusion of a single Ti vacancy is faster (average diffusion speed: 0.53 nm/min) and shows a larger active area. This triangle-shaped defect ends up being at the upper right corner of the STM image (Figure 6.2f). The mechanism of diffusion of Ti vacancy can be seen as that when two locations in the HC lattice have very similar thermodynamic potential, the choice of which site to occupy would be arbitrary for the Ti atoms. Therefore if a neighbouring Ti atom takes the vacancy site instead of its original location, a diffusion of Ti vacancy would be observed. A movie shows diffusion of both the triple Ti vacancy (Figure 6.1) and the single Ti vacancy (Figure 6.2) has been created. The single Ti vacancy defect is more commonly observed in experiments.

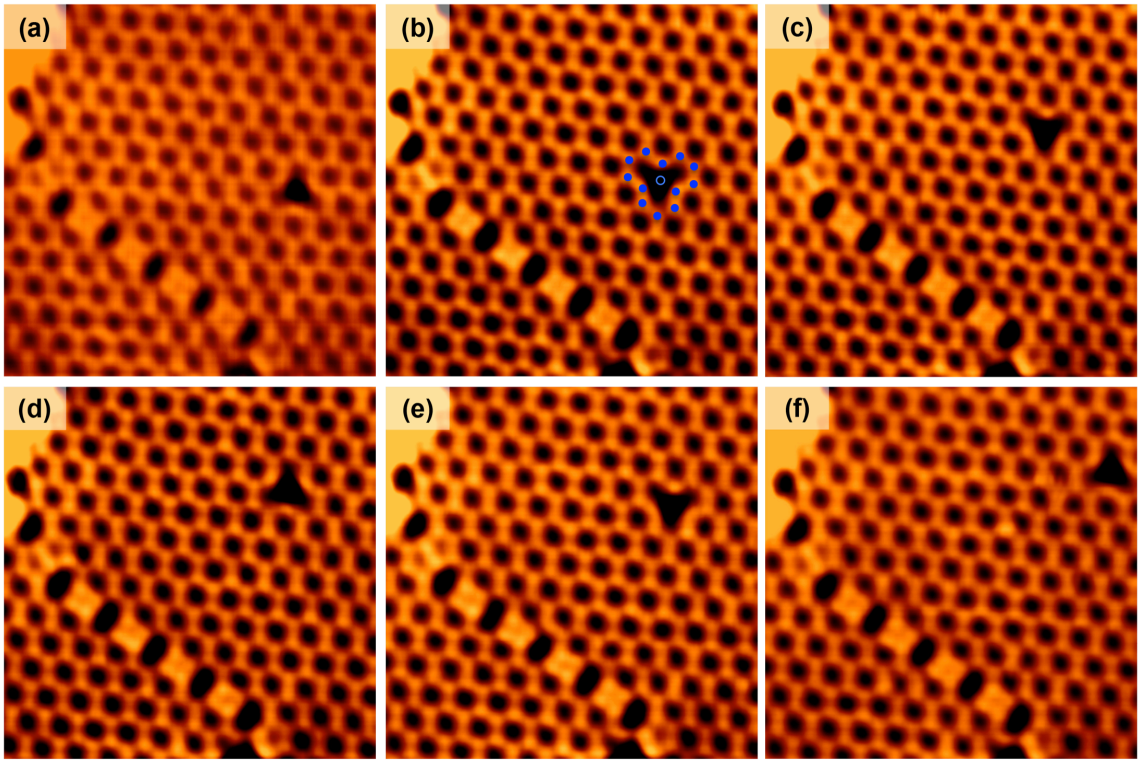


Figure 6.2: STM images of diffusion of a triangle-shaped defect on the upper right side. A linear domain boundary is observed and used to determine the relative position of the triangle-shaped defect. Image size: 6.5 × 6.5 nm^2, V_s = 0.95 V; I_t = 0.22 nA. Three neighbouring Ti hexagons around the defect are indicated in (b). The filled blue balls are Ti atoms while the unfilled blue ball is the missing Ti atom that composes the honeycomb lattice.

Figure 6.3 shows structural models of HC-Ti_2O_3/Au(111) thin films with Ti vacancies increasing from one to four. Unfilled blue and red balls indicate Ti vacancies and the corresponding O atoms that are missing from the regular HC hexagonal lattice. In the case of generating a single Ti vacancy, three O atoms are removed (Figure 6.3a); the stoichiometry of the missing unit is TiO_3. Considering the stoichiometry of the regular HC structure is Ti_2O_3 ($TiO_{1.5}$), generation of the single Ti vacancy makes the oxidation state of HC thin film reduced. In Figure 6.3b, the vacancy 'hole' consists of two missing Ti atoms and five O atoms has a stoichiometry of $TiO_{2.5}$ (Ti_2O_5). If the two Ti vacancies are not bonded together, then two single Ti vacancy units (as shown in Figure 6.3a) will form, which ends up with six O atoms being removed instead of five; the HC sheet will

be more reduced than what is shown in Figure 6.3b. Similarly, for three linked Ti vacancies, seven corresponding O atoms are missing from the perfect HC lattice; the stoichiometry of this vacancy 'hole' is $TiO_{2.33}$ (Ti_3O_7) (Figure 6.3c). However if this vacancy block is separated into three single Ti-vacancy units or one single Ti-vacancy unit (Figure 6,3a) plus a vacancy block consists of two linked Ti vacancies (Figure 6.3b), the HC thin film will be more reduced from Ti_2O_3. And so on, when four Ti vacancies are bonded as a block (Figure 6.3d), the stoichiometry of the 'hole' is $TiO_{2.25}$ (Ti_4O_9), which is closer to the stoichiometry of original HC islands ($TiO_{1.5}$) than generating four Ti vacancies in other ways. To reduce the influence of Ti vacancies formed in HC-Ti_2O_3/Au(111), Ti vacancies are more likely to bond with each other as a block. This result matches the experimental observation of three Ti vacancies moving together as one unit as discussed previously.

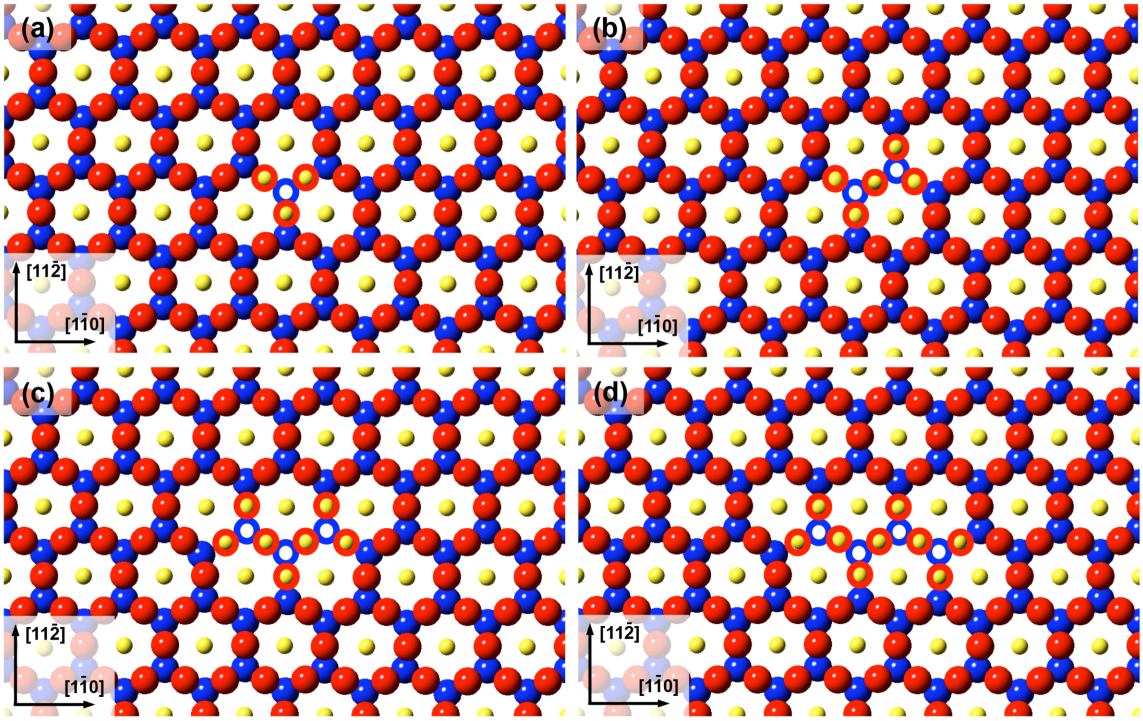


Figure 6.3: Structural models for HC-Ti_2O_3/Au(111) thin films with (a) one Ti vacancy; (b) two linked Ti vacancies; (c) three linked Ti vacancies; (d) four linked Ti vacancies. The filled blue balls are Ti atoms; the unfilled blue balls are the missing Ti atoms; the filled red balls are O atoms; the unfilled red balls are the missing O atoms. The Au-Au spacing of the Au(111) surface along $[1\bar{1}0]$ is 2.89 Å.

6.2.2 Oxygen vacancies/hydroxyl groups in HC-Ti_2O_3/Au(111) thin films

Figure 6.4a-f illustrates a different type of point defect observed in HC-Ti_2O_3/Au(111) thin films. Instead of showing a dark hole (discussed in section 6.2.1), these point defects look like bright balls attached on the HC sheet. Three bright-featured point defects are activated by applying a +3 V pulse for one second via the tip cleaning process. During continuous STM scanning, these bright balls diffuse independently: the one located lowest diffuses in a comparatively higher speed than other two, while the one located upmost hardly moves. The two less mobile point defects still appear as a pair when their distance is about 0.8 nm (since Figure 6.4c). In the mean time, the more active point defect keeps diffusing towards the downright side. The location of this type of point defects (unfilled white circles) are marked as in-between two neighbouring Ti atoms (filled blue balls) in Figure 6.4c. From the proposed DFT model of Ti_2O_3 HC thin films in Chapter 4, those bridging sites of Ti-layer are supposed to be occupied by O atoms. Therefore this type of point defect is likely to be an oxygen vacancy or a hydroxyl group. Profiles taken along arrows marked as '**i**' (along $\langle 11\bar{2} \rangle$ of Au(111) lattice) and '**ii**' (along $\langle 1\bar{1}0 \rangle$ of Au(111) lattice) in Figure 6.4c confirm that the locations of these two point defects are both at the O bridging sites of the HC lattice (Figure 6.4g). The measured height of the bright point defect is about 35 ± 3 pm.

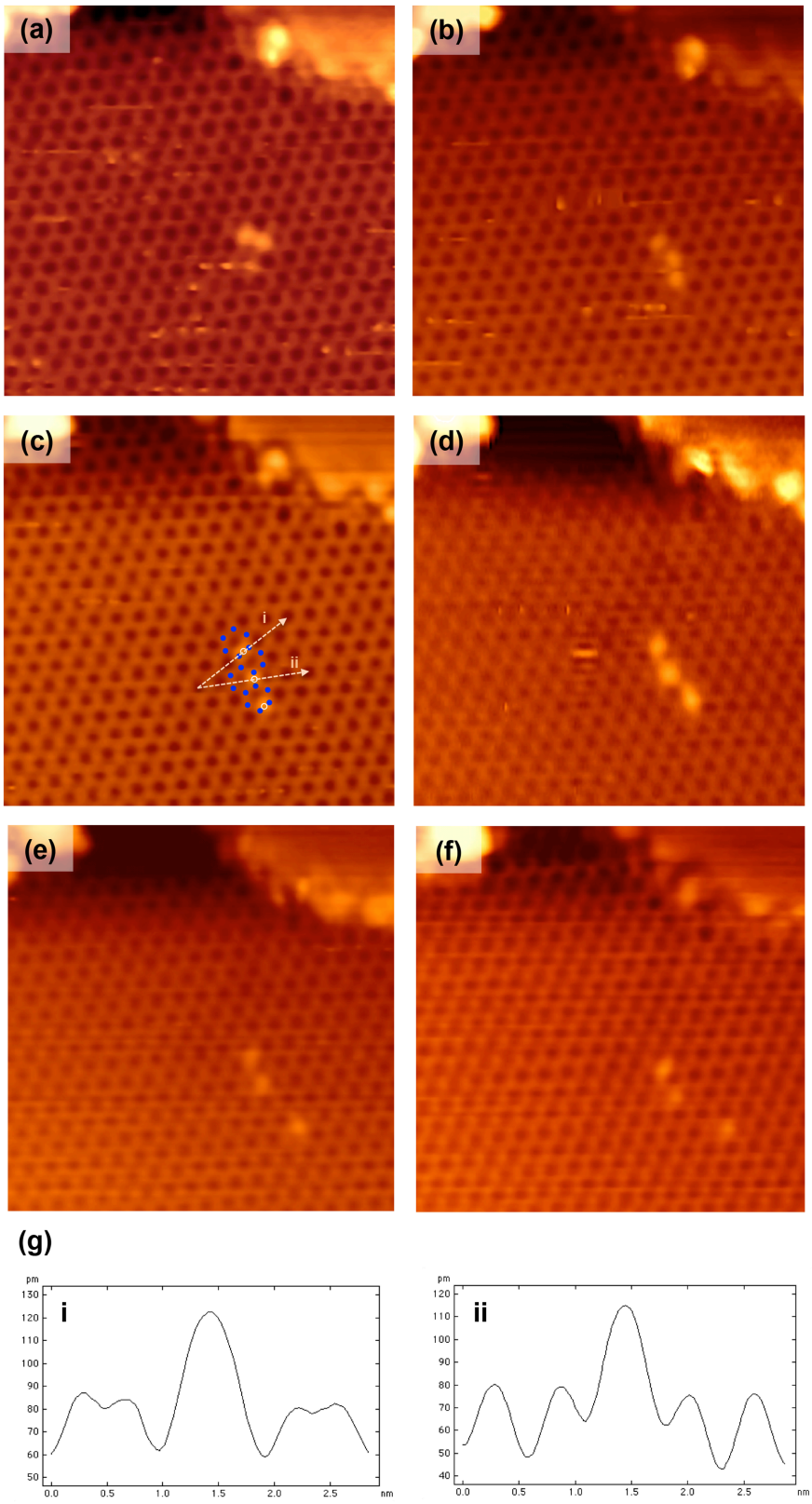


Figure 6.4: (a)-(f) STM images of diffusion of three bright point defects that are created by a +3 V voltage pulse. Image size: 10 × 10 nm^2, V_s = 0.9 V; I_t = 0.24 nA. Four Ti hexagons are indicated in (c). Ti atoms are marked as blue balls. Three bright spots that are located at the bridging sites are marked as unfilled white circles. (g) Profiles that are taken along the arrows marked '**i**' and '**ii**' drawn in (c) which cross the bright spots. The height of the bright point defect is about 35 ± 3 pm.

6.2.3 Point defect pairs in HC-Ti_2O_3/Au(111) thin films

In Figure 6.5a, a pair of bright point defects is shown (marked as unfilled white balls). Instead of sitting in the O bridging sites of HC lattice, they are located at the Ti apex sites. A profile taken along $\langle 11\bar{2} \rangle$ which crosses the bright point defects confirms their positions (Figure 6.5b). In this case the bright point defects are likely to be hydroxyl groups adsorbed on Ti atoms. During the continuous STM scanning, no diffusion of these point defects was observed. The height of the bright point defect in Figure 6.5a is about 35 pm, which matches the measurement done in Figure 6.4.

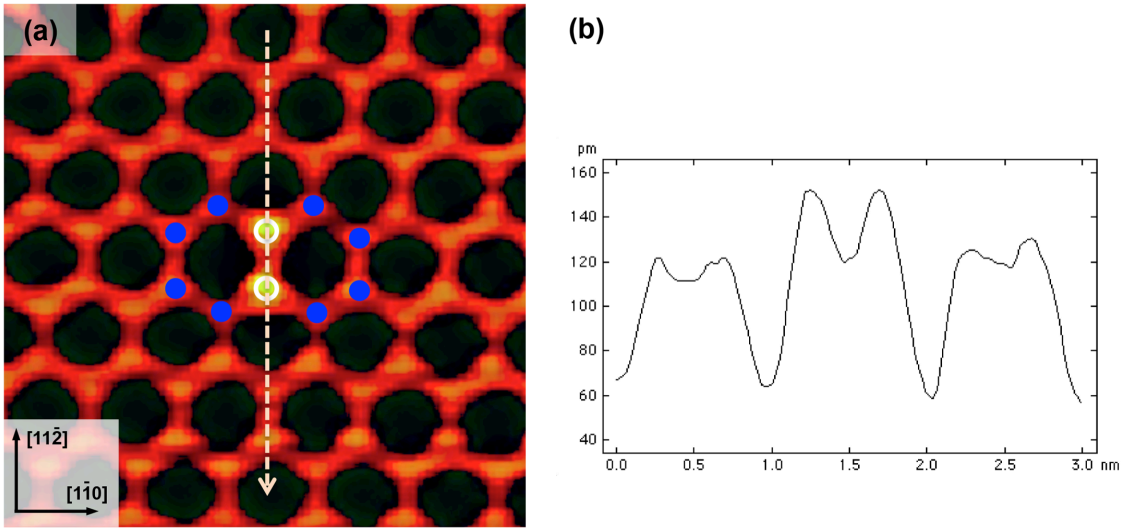


Figure 6.5: (a) High-resolution STM image of the HC-Ti_2O_3/Au(111) thin film with two bright point defects (image size: 3.5 × 3.5 nm^2, V_s = 0.9 V; I_t = 0.22 nA). Two hexagons of Ti are indicated. The filled blue balls are Ti atoms while the unfilled white balls are the bright point defects. This image is averaged from 10 STM images in the same area with the same resolution by SmartAlign. (b) Profile taken along the arrow drawn in (a).

Figure 6.6a shows two dark-bright point defect pairs observed in a high-resolution STM image. Those defect pairs are activated by applying +3 V voltage pulses in the regular HC-Ti_2O_3/Au(111) thin film. The hexagons of Ti atoms (filled blue balls) which surround one dark-bright point defect pair are marked as well as the dark point defect (unfilled blue ball) and the bright one (unfilled white ball). Profiles taken along arrows labelled as

'**i**' and '**ii**' indicate that the bright point defect is located at a Ti apex site with a height of approximately 35 pm; the dark point defect is similar to the Ti vacancy (discussed in section 6.2.1) that shows up as a hole around the Ti apex site next to the bright point defect (Figure 6.6b). Therefore the dark point defect is assigned as a Ti vacancy while the bright point defect is likely to be a hydroxyl group attached on the Ti atom. Diffusion of point defects happens in this case, however the dark-bright point defect pair moves as a unit.

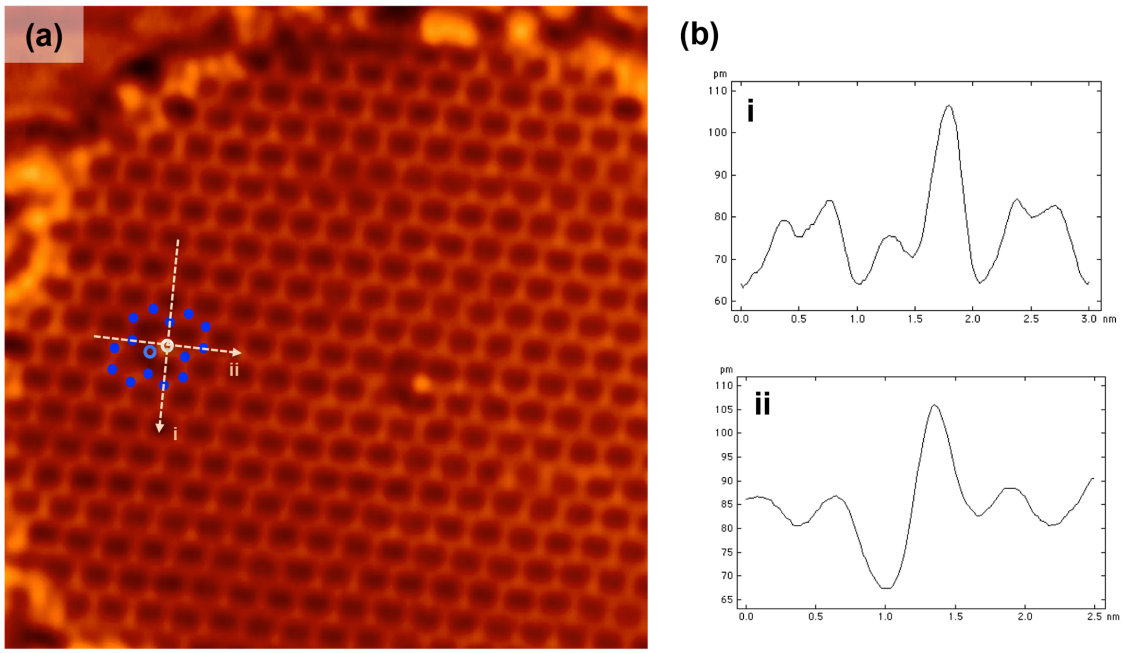


Figure 6.6: (a) High-resolution STM image of the HC-Ti_2O_3/Au(111) thin film with two dark-bright pair of point defects (image size: 10 × 10 nm^2, V_s = 1.0 V; I_t = 0.21 nA). Four hexagons of Ti around one dark-bright pair of point defect are indicated. The filled blue balls are Ti atoms; the unfilled blue ball is the dark point defect (Ti vacancy); the unfilled white ball is the bright point defect. (b) Profiles taken along arrows labelled '**i**' and '**ii**' in (a).

6.3 Discussion

No study of point defects in HC-Ti_2O_3/Au(111) was found in the literature. However point defects in rutile TiO_2(110) (1 × 1) have been studied intensively. A comparison between point defects reported in rutile TiO_2(110) surfaces and what is found in HC-Ti_2O_3/Au(111)

thin films is instructive. Even though the bright point defects (type-A defects) were generally agreed to be related to water dissociation (Chapter 3, section 3.3.2), only the darker ones were assigned as oxygen vacancies; the brighter type-A defects were demonstrated to be hydroxyl groups [107-109, 122]. The dark features (type-B defects) in rutile TiO_2(110) surfaces were suspected to be missing oxygen atoms below the surface [82]. In HC-Ti_2O_3/Au(111) thin films, bright point defects which sit at the bridging oxygen sites of the (2 × 2) HC hexagonal lattice are suggested to be oxygen vacancies/hydroxyl groups; similar bright point defects sitting in the Ti-apex sites of the HC lattice are possibly hydroxyl groups bonded to Ti atoms. The measured height of the bright point defects is about 35 pm, which is very close to the height of type-A defects [107] and hydroxyl groups adsorbed on the five-fold Ti atoms in the rutile TiO_2(110) surfaces [138, 338]. Since both perfect rutile TiO_2(110) surfaces and HC-Ti_2O_3/Au(111) thin films show no water dissociation, oxygen vacancies in the HC-Ti_2O_3/Au(111) thin films have the chance to be the crucial factor in water dissociation reactions as well as confirmed in rutile TiO_2(110) surfaces. However, the method used to create oxygen vacancies/hydroxyl groups in this thesis (discovered by Minato et al. [154]) is only able to form a very limited number of defects; methods of creating sufficient amount of oxygen vacancies in HC-Ti_2O_3/Au(111) need to be explored before carrying out the water dissociation experiments in the HC-Ti_2O_3/Au(111) thin films. The correct identification of the oxygen vacancies is needed as well.

Diffusion of hydroxyl groups occupying the O bridging sites in rutile TiO_2(110) surfaces was suggested to be mediated by the adsorbed water molecules [111, 156]. For oxygen vacancies in rutile TiO_2(110) surfaces, they were reported to diffuse with assistance of acetone [157] and positive pulse [154]. In this chapter, diffusion of point defects (oxygen vacancies/hydroxyl groups and Ti vacancies) in HC-Ti_2O_3/Au(111) surfaces are mobile at room temperature – no mediation is required. However when there are more than one Ti vacancies bonded together, they are more likely to diffuse as a block. Oxygen vacancies/hydroxyl groups in bridging oxygen sites diffuse more independently, while a

force balance might steady the oxygen vacancies/hydroxyl groups as pairs. Similar paired bridging hydroxyls were observed in the rutile TiO_2(110) surfaces as a very stable configuration [111]. For the Ti-bonded hydroxyl groups in rutile TiO_2(110) surfaces, they were reported to be quite stable and immobile [338]. In experiments, no diffusion is observed for the bright point defects pair occupying the Ti-apex sites; the pairing of single Ti vacancy and Ti-bonded hydroxyl group next to each other is very stable as well.

6.4 Conclusions

In summary, two types of point defects are found in HC-Ti_2O_3/Au(111) thin films, which are proposed as Ti vacancies and oxygen vacancies/hydroxyl groups separately. Ti vacancies have the appearance of a dark 'hole' due to the lack of Ti atoms that compose the HC lattice. When a single Ti vacancy is observed, it usually shows up as a triangle-shaped hole with good mobility at room temperature. However, when a bigger 'hole' that consists of a few bonded Ti vacancies forms, the mobility under room temperature is limited due to that a bonded group of vacancies is stoichiometrically preferred than the same number of independent Ti vacancies. On the contrary, oxygen vacancies/hydroxyl groups are observed as bright-featured spots attached at either the oxygen bridging sites or the Ti-apex sites of HC lattice. Diffusion of the bright point defects occupying the O bridging sites of HC lattice is more independent in experiments, however two oxygen vacancies/hydroxyl groups could pair together with a fixed distance. Compared with point defects reported in rutile TiO_2(110) (1 × 1) surfaces, no mediation is needed for diffusion of point defects in HC-Ti_2O_3/Au(111) thin films at room temperature. Paired Ti-bonded hydroxyl groups are noticed, so as the dark-bright point defect pairs (recognised as Ti-vacancy and Ti-bonded hydroxyl group pairs). The bonding of point defect pairs is very steady in experiments – the paired bright point defect unit is not moving, while the dark-bright point defect pair diffuses as a unit.

Because of the complexity in generating point defects in STM images, more

investigation is needed to confirm the identities of point defects illustrated in HC-Ti_2O_3/Au(111) thin films. For example, the bright point defect pair shown in Figure 6.5 could be a result of defects in Au(111) substrate surface underneath the HC film. In future studies, DFT calculating and STM image simulations are considered to be involved, which can help by predicting the stability of the defect and how rapidly it will diffuse. Also, if considering carrying out the water dissociation experiments similar to what have been done in rutile TiO_2(110) (1 × 1) surfaces, finding out methods of creating sufficient amount of point defects will be necessary. Due to the fact that the ultra-thin Ti_2O_3 HC film is very fragile compared to the bulk terminations of crystals, techniques used in creating oxygen vacancies in rutile TiO_2(110) such as ion/electron bombardment cannot be applied to HC ultra-thin film. It will be a big challenge to obtain plenty of oxygen vacancies in the Ti_2O_3 HC sheet without damaging the structure of the thin film.

Chapter 7:

NbO_x Ultra-thin Films Grown on Au(111) Substrates

7.1 Background

7.1.1 Overview

Titanium oxide thin films have been emphatically discussed in the previous chapters. Structures that do not belong to the bulk terminations of TiO_2 have been generated in forms of ultra-thin films via epitaxial growth on the metal substrates. For example, honeycomb and pinwheel phases in the TiO_x/Au(111) system [8-10]; *Kagomé-Like phase* (*k*-TiO_x), *Zigzag-Like phases* (*z*-TiO_x & *z'*-TiO_x) and *Wagon-Wheel-Like phases* (*w*-TiO_x and *w'*-TiO_x) in the TiO_x/Pt(111) system [160]. Among all those structures, the (2 × 2) Ti_2O_3 honeycomb (HC) ultra-thin film grown on reconstructed Au(111) substrate has attracted a lot of attention due to its outstanding uniformity. A similar structure which is grown on Pt(111) is *k*-TiO_x, however misfit between thin films and substrates leads to the formation of extensive domain boundaries and defects. This (2 × 2) hexagonal lattice was reported in the experiments of growing ultra-thin VO_x films on Pd(111) substrates as well [283-284]. The V_2O_3 HC ultra-thin film shows the potential of developing into substrates for deposition as well as Ti_2O_3 HC ultra-thin film. Given the facts above, it is worth trying to grow the honeycomb-like epitaxial thin films by oxidising transition metals that can readily adopt a +3 oxidation state on three-fold symmetrical metal substrate.

Niobium locates nearby titanium in the periodic table as a transition metal and they have similar atomic radii (Ti: 147 pm; Nb: 146 pm). The most commonly encountered oxidation state of niobium is +5, which exists in various polymorphic forms based on the octahedrally coordinated NbO_6 structure [339]; however a +3 oxidation state also exists. Similar to titanium oxides, niobium oxides show a wide rage of properties suitable for catalysis [340-342], in solar cells [343-345] and as materials in gas sensors [346-347]. Most studies of niobium oxide thin films have concentrated on the crystalline phases with a thickness of tens of atomic layers, and the substrates used were mostly oxides (e.g. Al_2O_3, SiO_2). Very limited work of growing NbO_x ultra-thin films on metal substrates

has been done; studies including using Pt(111) and $Cu_3Au(100)$ as substrates have been reviewed in Chapter 3 (section 3.4.2). Considering that the honeycomb Ti_2O_3 ultra-thin films illustrate impressive quality when grown on reconstructed Au(111) surface via PVD, and the reversed system of Au/Nb_2O_5 shows high photoactivity [348] as well as good catalytic activity [349-350], so the reconstructed Au(111) can be considered to be a promising choice as a substrate. Experimental trials of growing ultra-thin NbO_x films on reconstructed Au(111) following a similar PVD process to that are used for the growth of TiO_x ultra-thin films was carried out, and the results are reported in the remainder of this chapter.

7.1.2 Experimental details

STM imaging was carried out in the JEOL JSTM 4500XT microscope system. The same mica-supported Au(111) single crystal plates (Agilent Technologies, U.K.) that have been used in experiments of generating TiO_x thin films (Chapter 4-6) were applied. The deposition and oxidation processes were the same as growing TiO_x thin films by replacing Ti rod with a 99.9% pure Nb rod (Goodfellow Cambridge Ltd., U.K.). STM images were processed with Image-SXM, FabViewer and Gwyddion software; possible structural models of NbO_x nanostructures were produced with CrystalMaker software.

7.2 Results

7.2.1 STM of NbO_x ultra-thin films grown on Au(111)

STM images shown in Figure 7.1 illustrate the evolution of ultra-thin NbO_x films grown on reconstructed Au(111) substrates with increasing Nb coverage up to 3 MLs. Two

distinct structures can be identified and named as the honeycomb phase and the hollow triangle phase related to their appearance. An irregular bright feature is observed as the result of further layers. Different structures are labelled as **α** (reconstructed Au), **β** (honeycomb structure), **γ** (hollow triangles) and **δ** (multi-layer bright features).

Figure 7.1a shows an STM image of the reconstructed Au(111) surface. As reviewed in Chapter 3 (section 3.1.3), the unreconstructed Au(111) surface should have a hexagonal lattice as being a face centred cubic (FCC) crystal. After annealing, the formed reconstructed surface layer illustrates a bright paired-lines structure called the herringbone reconstruction. Figure 7.1 b-d show the NbO_x ultra-thin films that grow on reconstructed Au(111) surfaces within monolayer coverage after oxidation. When the Nb dosing is small (0.2 ML, Figure 7.1b), a triangle-featured phase shows up in large amounts, accompanied by a few small islands that have a hexagonal lattice. The size of the triangles varies, however they all look like equilateral triangles; only the sides of the triangles are bright, the inner 'body' of the triangles retain the same brightness as the Au surface, therefore these structures are named the hollow triangle phase. When the deposition amount of Nb increases (0.5 ML, Figure 7.1c), large areas of honeycomb islands form, which has a very similar appearance to the Ti_2O_3 honeycomb thin films grown on Au(111); a few defects and linear domain boundaries are observed as well (as discussed for the Ti_2O_3 honeycomb thin films in Chapter 5). In the case of still having considerable area of bare Au surface available, hollow triangles may grow as single units, or next to each other by sharing sides, or link to the edge of honeycomb islands; but they rarely grow upon each other or onto the honeycomb thin films. However when the exposed Au(111) area is limited (0.9 ML Nb coverage, Figure 7.1d), large numbers of hollow triangles conjoined into irregular islands consist of mixtures of dots and vague triangles; some very bright spots are observed, which indicate multiple layers; a few triangles start growing upon honeycomb thin films. Figure 7.1e & f illustrate STM images of the over-monolayer NbO_x thin films grown on the reconstructed Au(111) surface. When the coverage is in between a monolayer and 2 MLs (1.6 MLs, Figure 7.1e), thin

film is dominated by multi-layer bright features that show no crystalline structures. Only a few triangle-featured units are observed on the exposed monolayer honeycomb islands; very limited bare Au surface is identified as being dark in the images. When the second layer of NbO_x thin films is completed (2.3 MLs, Figure 7.1f), the third layer shows no identifiable structural features but randomly located multi-layer spots. In this stage, the influence of Au(111) substrates is considered to be negligible.

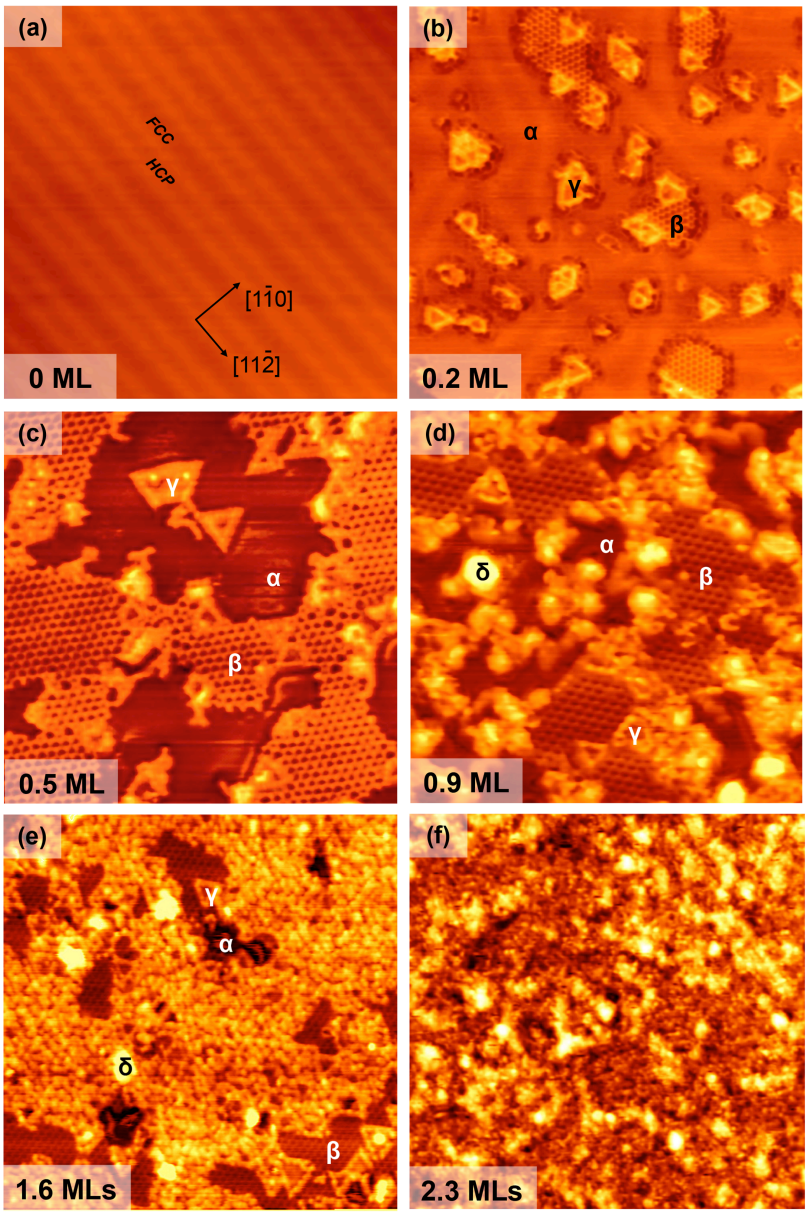


Figure 7.1: Increasing amounts of Nb were deposited onto the reconstructed Au(111) substrates, followed by annealling at 600 °C in 10^{-6} Pa of O_2 for 30 minutes. The Nb dosing is labelled in each image. Different structures are marked as **α** (reconstructed Au), **β** (honeycomb-like structure), **γ** (hollow triangles) and **δ** (multi-layer bright features). (a) (22 × √3)-reconstructed Au(111) surface (Image size: 35 × 35 nm^2, V_s = -2.0 V, I_t = 0.1 nA); (b) 0.2 ML: hollow triangles with small honeycomb islands on Au (Image size: 32 × 32 nm^2, V_s = 0.8 V, I_t = 0.22 nA); (c) 0.5 ML: hollow triangles and large area of honeycomb islands with a few domain boundaries/defects on Au (Image size: 22 × 22 nm^2, V_s = 0.5 V, I_t = 0.22 nA); (d) 0.9 ML: Au surface nearly fully-covered by hollow triangles and honeycomb islands, and some bright-featured spots show up (Image size: 20 × 20 nm^2, V_s = 1.0 V, I_t = 0.25 nA); (e) 1.6 MLs: multi-layer bright features dominate the surface; hollow triangles growing on top of first-layer thin film with small area of honeycomb exposed and very limited Au substrate being observed (Image size: 28 × 28 nm^2, V_s = 1.0 V, I_t = 0.25 nA); (f) 2.3 MLs: bright features grow upon the completed second-layer thin film; no identifiable structures observed (Image size: 40 × 40 nm^2, V_s = 0.9 V, I_t = 0.20 nA).

Figure 7.2a shows an atomic-resolution STM image of the NbO_x honeycomb structure. Considering that a positive voltage was applied during STM imaging, similar to the TiO_x/Au(111) system, the bright atoms illustrated in the STM images are Nb. Figure 7.2b & c are the profiles taken along marked arrows '**i**' & '**ii**' respectively. Along the $[1\bar{1}0]$ direction of Au, the periodicity of honeycomb structure is about 6 Å (Figure 7.2b); while along the $[11\bar{2}]$ direction the periodicity is approximately 10 Å (Figure 7.2c). Referring to the FCC crystallographic unit cell of Au which has dimensions of 4.08 Å, on the (111) surface the close-packed $[1\bar{1}0]$ direction has a periodicity of 2.89 Å, and the perpendicular $[11\bar{2}]$ direction has a periodicity of 5.01 Å; therefore the Nb-layer shows a (2 × 2) reconstruction with respect to the (1 × 1) Au(111) substrate. Oxygen atoms cannot be observed directly from Figure 7.2a so their locations are not determined at this stage. However the height and periodicity of NbO_x honeycomb thin film are very close to the Ti_2O_3 honeycomb thin film grown on Au(111), and the STM images of them look very similar to each other, so the NbO_x honeycomb thin film is likely to have the same structure as the Ti_2O_3 honeycomb thin films discussed previously.

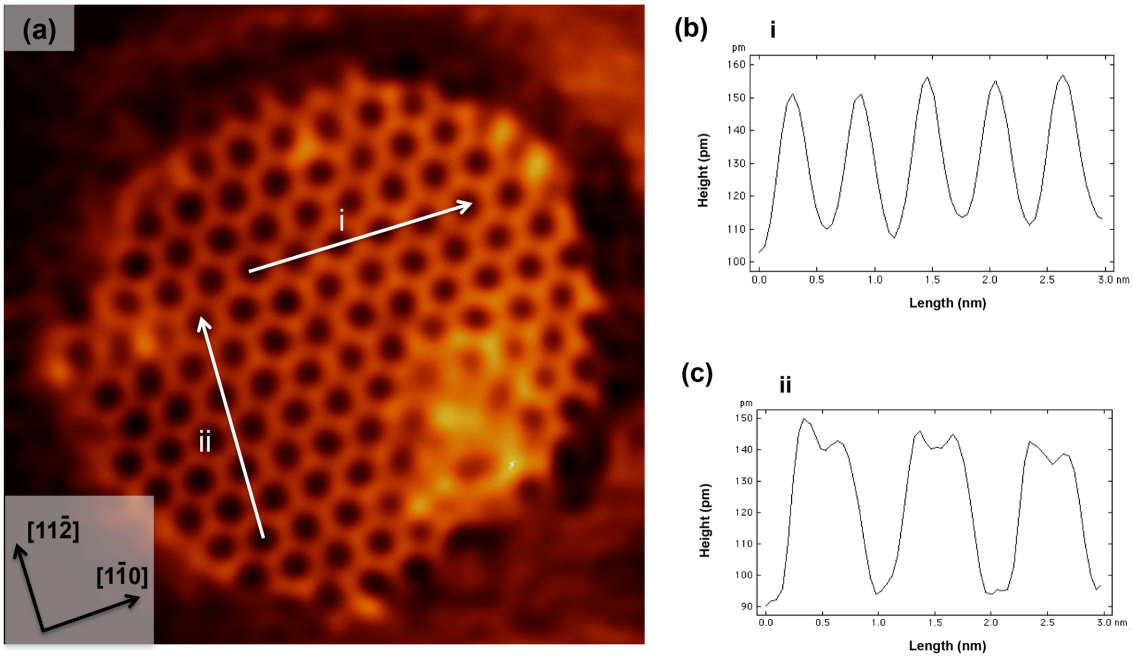


Figure 7.2: (a) High-resolution STM image of NbO_x thin film showing hexagonal lattice, which is identified as honeycomb structure (Image size: 8 × 8 nm^2, V_s = 0.85 V, I_t = 0.25 nA). The bright spots are Nb atoms. (b) & (c) Profiles taken along arrows marked as '**i**' and '**ii**' in (a).

Figure 7.3a illustrates a surface with coexistence of NbO_x honeycomb and hollow triangle structures. The crystallographic $[1\bar{1}0]$ direction of the Au(111) substrate is marked out by a white arrow that is identified by the honeycomb structure. Interestingly the triangle unit linked to this honeycomb island has one side that goes along $[1\bar{1}0]$, similar to other triangle units that are not attached to honeycomb islands (marked by white arrows). Even though the sizes of hollow triangles differ from each other (most sides are in the range of 1-3 nm), it seems that their sides have a preference of growing along the $\langle 1\bar{1}0 \rangle$ families of crystallographic directions on Au(111). Hollow triangles also show a trend to link with each other by sharing edges. Figure 7.3b illustrates a high-resolution image of two attached hollow triangles. In the 3D profile (Figure 7.3c), it is clear that the edge of the triangle unit is a double-line structure that is formed by Nb atoms, and the inner sides of triangles look a bit higher than the outer sides. The height of center area of triangles is much lower than the edges, which confirms the suspicion of it being hollow in the centre. Triangle units that share edge of outer triangles are in similar sizes in this case; in experiments, edge-sharing between hollow triangles with different sizes is common as well. Figure 7.3d is an atomic-resolution single unit of a hollow triangle. Figure 7.3e & f show profiles taken along dashed arrows marked as 'i' (black) and 'ii' (yellow) that are parallel to the outer side and inner side of a hollow triangle in Figure 7.3d. It can be counted that the outer side of the triangle consists of 9 Nb atoms while the inner side have 6 Nb atoms. Generally speaking the hollow triangle structure is higher than the honeycomb structure, and the inner sides of triangles are comparatively even higher than the outer sides of the triangles. However, information of STM images shows the total density of electrons on the surface as a function of positions; the observed height could come from the topography of real surfaces, or just be a result of congregation of local electrons. The distance between neighbouring Nb atoms in the same side of a triangle is about 3.33 Å; two neighbouring Nb atoms located at the linked inner side and the outer side of a triangle unit have a similar spacing.

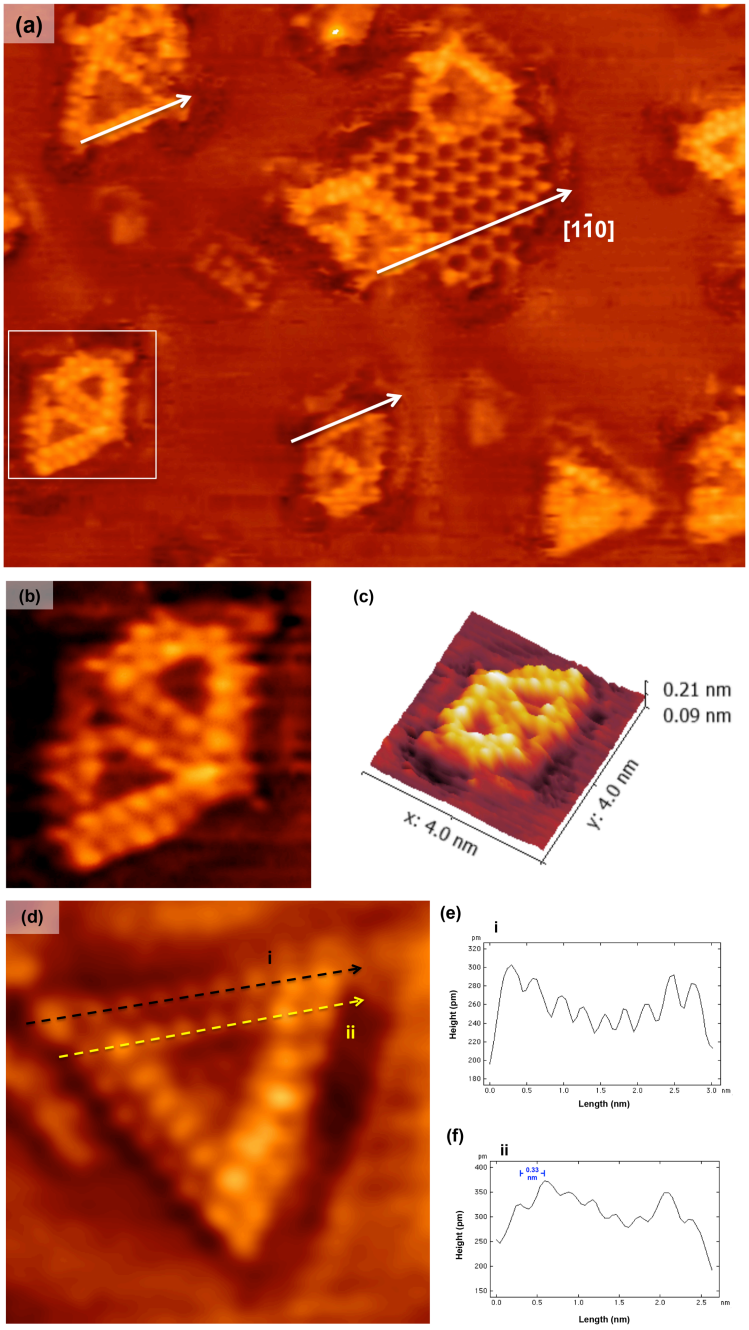


Figure 7.3: (a) STM image of NbO_x thin films grown on Au(111) with both honeycomb and hollow triangle structures (Image size: 17 × 13 nm^2, V_s = 0.8 V, I_t = 0.22 nA). The crystallographic direction of $[1\bar{1}0]$ is marked by a white arrow in the honeycomb thin film and the linked hollow triangle; other two hollow triangles' sides which are parallel to the $[1\bar{1}0]$ direction are marked out as well. (b) High-resolution STM image and (c) 3D profile image of a double-triangle unit that is marked by a 4 × 4 nm^2 square in (a). Hollow triangles show a double-edge feature and those two hollow triangles linked by sharing one outer edge. (d) High-resolution STM image of a hollow triangle unit (Image size: 3.7 × 3.7 nm^2, V_s = 0.45 V, I_t = 0.25 nA). (e) & (f) Profiles taken along dashed arrows marked as 'i' and 'ii' in (d), which are the paralleled outer and inner sides of the triangle. The labelled distance of 0.33 nm in (f) represents the distance between two neighbouring Nb atoms that belong to outer and inner sides of the hollow triangle.

7.2.2 Structural models of NbO_x thin films grown on Au(111)

Based on the atomic-resolution STM images, structural models of NbO_x honeycomb and hollow triangle phases are proposed. Figure 7.4a & b illustrate the atomic models for the NbO_x honeycomb structure. Because the oxygen atoms cannot be directly observed from STM images in experiments, firstly a structural model is built that represents the relationship between the Nb-layer and the reconstructed Au(111) substrate (Figure 7.4a). Nb atoms (green balls) consistently sit in the three-fold hollow sites of the hexagonal Au(111) lattice (yellow balls) with one Au atom located midway between two neighbouring Nb atoms; a (2 × 2) hexagonal lattice is formed (a unit cell of the Nb-layer is drawn in Figure 7.4a). Compared with the Au hexagonal lattice, the Nb hexagonal lattice is rotated by 30°, and the spacing is expanded to about 3.34 Å (lattice spacing of Au(111) is 2.89 Å). Considering that the Au-Nb interaction is strong (the presentation of Nb can decrease Au agglomeration [351]), O atoms are more likely to sit upon the Nb-layer than in-between Au and Nb layers. Figure 7.4b illustrates a proposed model of O atoms taking over the bridging sites of Nb-layer. Two Nb atoms and three O atoms are counted in one unit cell (drawn in Figure 7.4b), therefore the stoichiometry of this honeycomb model is Nb_2O_3. However no experimental measurement of the chemical composition has been done, this proposed structural model could be different from the actual honeycomb structures.

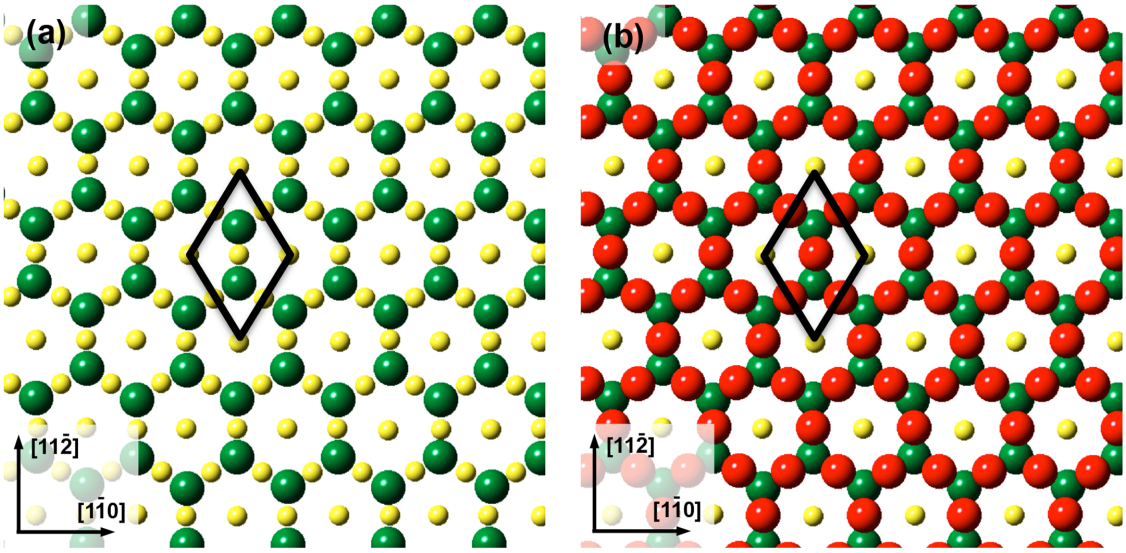


Figure 7.4: (a) Structural model for the NbO_x honeycomb phase with Nb atoms sitting in the three-fold hollow sites of the hexagonal Au(111) surface. (b) The same model with O atoms added on the top of Nb-layer in (a) by occupying the bridging sites of Nb-layer. Yellow balls represent Au atoms, green balls are Nb atoms and red balls are O atoms. The unit cells of Nb-layer and the honeycomb thin film are drawn with the black lines. The Au-Au spacing of the Au(111) surface along $[1\bar{1}0]$ is 2.89 Å.

In Figure 7.5, structural models for the single hollow triangle unit observed in Figure 7.3d are proposed. The analysis of STM images suggests that hollow triangle units are equilateral triangles whose sides run along $\langle 1\bar{1}0\rangle$, and their sides show a double-line structure. The number of Nb atoms compose sides of the specific triangle observed in Figure 7.3d is 9 for the sides of outer triangle and 6 for the sides of inner triangle. The measured spacing of the neighbouring Nb atoms in the rows of triangle sides is about 0.33 ± 0.03 nm, which is similar to the Au(111) lattice spacing in the $\langle 1\bar{1}0\rangle$ directions. Two possible models of the Nb-layer are built: Nb atoms either sit in the three-fold hollow sites of Au(111) (Figure 7.5a), or occupy the bridging sites (Figure 7.5d). In the triangle sides shown in Figure 7.5a, the nearest three-fold hollow sites of each Nb atom along $\langle 1\bar{1}0\rangle$ are vacant while the second nearest vacancies are occupied. In Figure 7.5d, Nb atoms choose the nearest bridging sites along $\langle 1\bar{1}0\rangle$ to sit in the triangle sides. O atoms are added on top of Nb-layer regarding to the strong bonding between Au and

Nb. In Figure 7.5b, the O atoms occupy the three-fold HCP hollow sites; the O-layer ends up with a regular double-line hollow triangle that has 8 atoms in each side of the outer triangle and 5 atoms in each side of the inner triangle. O-layer in Figure 7.5e has the same fitting but shifts along with the Nb-layer. The stoichiometry is $NbO_{0.85}$ for models shown in Figure 7.5b & e. Another fitting of O atoms is shown in Figure 7.5c & f: O atoms sit on the three-fold FCC hollow sites of Nb-layer in Figure 7.5c; O-layer in Figure 7.5f follows the fitting manner of Figure 7.5c but with a shift that accompany the Nb-layer. More O atoms are adsorbed in these two structural models; the stoichiometry is $NbO_{1.13}$. Generally speaking the structural models with Nb atoms sitting in the three-fold hollow sites of Au(111) (Figure 7.5a-c) are energetically preferred than models whose Nb-layer occupies bridging sites of Au(111) (Figure 7.5d-f). Comparing STM images of honeycomb phase and hollow triangle phase (Figure 7.2 & Figure 7.3), the sides of hollow triangles are much higher than the honeycomb islands. This result can be a real height difference in sample surface or because of different densities of local electrons in two phases. All the proposed structural models for triangle hollow phase have a higher density of electrons in the double-line sides of the triangles than honeycomb structure. If it is the topography of real structures that causes the height difference in STM images, hollow triangle models with Nb atoms sit at the bridging sites of Au lattice (Figure 7.5d-f) are more likely to be correct. However different stacking sequence than proposed in Figure 7.5 can also be the reason of the height difference. For example, a sandwiched O-layer exists in-between Au substrate and Nb-layer. The height of inner triangle is also considered to be higher than then outer triangle from STM images; this might simply be a result of a higher local density of electrons.

Because the proposed models in Figure 7.5 all show a hollowed-centre structure, it seems that the hollow triangle phase doesn't require a large amount of Nb dosing to be generated, which fits the fact that a lot of hollow triangles form when the coverage of NbO_x thin film is small. Also the space inside the triangles allows growth of overlapping hollow triangles, which explains the diversity in morphology observed in STM images.

The stoichiometry is suggested to be approximately $NbO_{x\approx1}$, which indicates that the oxidation state of Nb is +2 in hollow triangle phase; hollow triangle is a more reduced phase than honeycomb. However, without the directly characterisation of chemical composition (e.g. XPS), it is hard to confirm the accurate structural model for NbO_x hollow triangles.

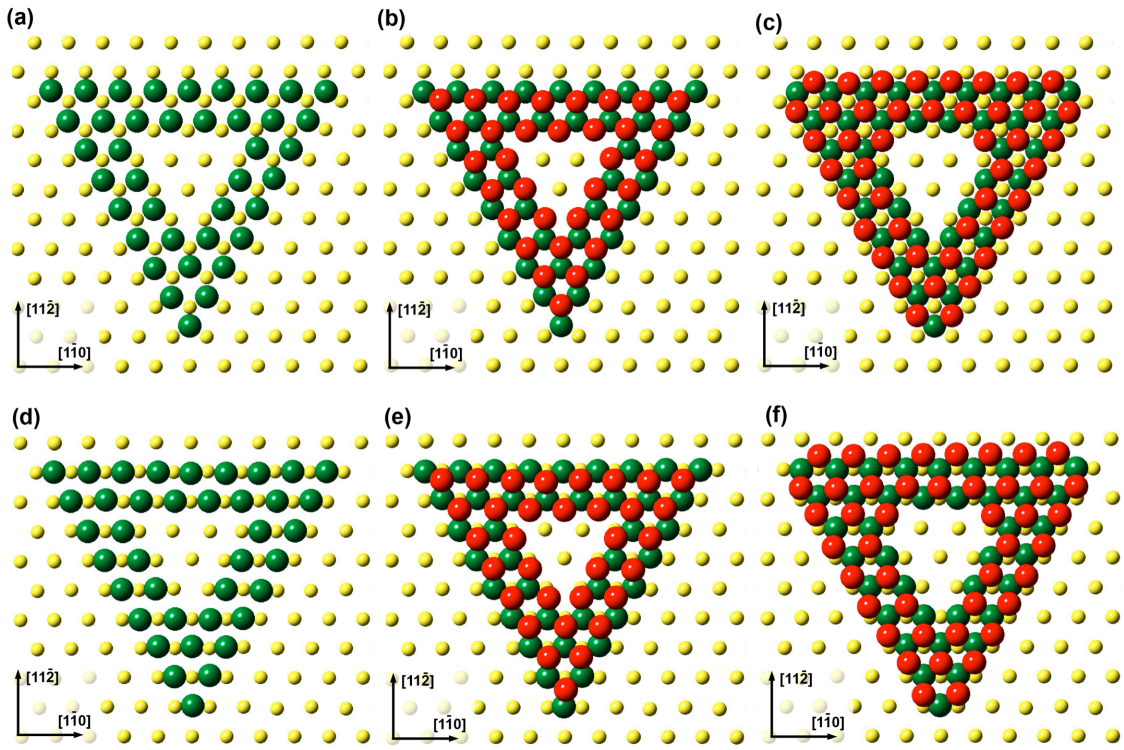


Figure 7.5: Two proposed structural models for the hollow triangle structure showed in Figure 7.3d. (a) Nb atoms sit in the three-fold hollow sites of Au(111) surface as sides of the double-line hollow triangle. The outer side of the triangle consists of 9 atoms while the inner side has 6 atoms. (b) O atoms are added on top of the Nb-layer in (a) by choosing the three-fold HCP hollow sites to occupy. (c) O atoms are added on top of (a) by sitting on the FCC hollow sites instead. (d) Nb atoms sit in the bridging sits of Au(111) hexagonal lattice as sides of the double-line hollow triangle. (e) O atoms following the fitting manner in (b) are added onto Nb-layer shown in (d). (f) O atoms are added on top of the Nb-layer shown in (d) with the same fitting of (c). The Au-Au spacing of the Au(111) surface along $[1\bar{1}0]$ is 2.89 Å.

7.3 Discussion

Although the study presented in this thesis of NbO_x ultra-thin films grown on Au(111) is relatively limited, a comparison between NbO_x/Au(111) and TiO_x/Au(111) is instructive. The Nb_2O_3 honeycomb structure has been successfully generated, which is very similar to the Ti_2O_3 honeycomb structure. Even the observed domain boundaries in the Nb_2O_3 honeycomb thin film are in full accord with what have been reported in Ti_2O_3 honeycomb thin films (Chapter 5). Though lacking the chemical composition characterisation, it is likely that the honeycomb NbO_x thin films follow the stacking and structure of the Ti_2O_3 honeycomb thin films. Combined with other close relative honeycomb ultra-thin films that have been discussed in Chapter 4 including *k*-TiO_x grown on Pt(111) [160] and (2 × 2) V_2O_3 thin film grown on Pd(111) [283-284], synthesis of Nb_2O_3 honeycomb films on Au(111) inspires more experimental ideas of building up the M_2O_3 (M: transition metals) honeycomb thin films on the three-fold symmetrical metal substrates. For the NbO_x hollow triangle phase, no matching structures were reported in the TiO_x/Au(111) system, however the TiO_x pinwheel phase can be seen as consisting of six interlocking regular triangles. Those TiO_x solid triangle units have similarities with the NbO_x hollow triangles: the rows of TiO_x solid triangles run nearly along the $\langle 1\bar{1}0 \rangle$ families of crystallographic directions (the rotation of Ti-layer is only about 2° referring to the Au lattice), and the spacing of neighboured Ti atoms is close to the Au-Au spacing in Au(111) lattice. In experiments of growing TiO_x ultra-thin films on Au(111), some single solid triangle units or two linked triangles that share the edge were observed. However, the diversity of morphology is limited in TiO_x solid triangles as it is a condensed structure, and they have a strong trend to be closed-packed into pinwheel units that grow into a flat film. For NbO_x hollow triangles, in addition to the basic linked triangles that share one edge and grow next to each other, cases including sharing part of the edge and triangles growing into each other were observed in STM images. When large amounts of Nb are deposited and grow into hollow triangles, the hollowed-centre areas are filled up with overlapping hollow triangles; shapes of triangle units are no longer easy to identify.

What's more, from the structural models proposed in this chapter it seems that Nb atoms that sit at the outer sides of triangles are not tightly bonded; STM images showing the movement and irregularity of those Nb atoms were spotted. In contrast, the solid triangles in TiO_x pinwheel thin films work more like close-packed units. When the coverage of thin films goes over 2 MLs, structures that with specific features were reported in the TiO_x/Au(111) system (e.g. row structure [8]), however in the NbO_x/Au(111) system regular structures were rarely observed when the thin films grow over 1 ML.

Though only limited research has been done of growing ultra-thin NbO_x films on metal substrates, a comparison between different systems is necessary. As reviewed in Chapter 3 (section 3.4), epitaxial NbO_x thin films were grown on Pt(111) single crystal substrates and different hexagonal structures were detected by LEED [264-265]. When the coverage was sub-monolayer, a hexagonal lattice which expanded 25% compared to Pt(111) and rotated by 30° was formed, and it was suggested to be a reduced oxide of Nb_2O_5. When the coverage of thin film was increased to 2 MLs, fully-oxidised Nb_2O_5 films with hexagon lattices were generated. However the lack of direct observation of the morphology weaken the accuracy of this study. Another system of ultra-thin NbO_x films was built up on Cu_3Au(111) substrates [267-268]. A ($\sqrt{3} \times \sqrt{3}$)R30° hexagon structure and a coincidence (2 × 7) structure with respect to the hexagonal substrate layer was deduced from the LEED pattern, and research using STM, PES, AES and DFT proposed a few structural models with O-Nb-O-(Cu_3Au) stacking and the stoichiometry of Nb_2O_5. The NbO_x ultra-thin films grown on hexagonal lattice substrates including Pt(111), Cu_3Au(111) and Au(111) all result in forming a hexagonal lattice layer, which confirmed that structures of epitaxial NbO_x thin films are strongly influenced by the substrates. However no reports of NbO_x hollow triangles were found in the literature of growing NbO_x thin films on metal substrates. A few interesting NbO_x structures in monolayer scale were generated through oxidising the Nb single crystal surfaces including (110), (111) and (100) [269-270, 272, 275, 280-282]. For example, a regularly

arranged network of finite chains showing hexagonal symmetry was reported on Nb(110) [274], and a ladder-like (3 × 10) structure was found on Nb(100) [279].

7.4 Conclusions

Nb has been deposited onto the reconstructed Au(111) substrates and oxidised following a similar process of growing TiO_x ultra-thin films on Au(111) in Chapter 4. Two distinguishable structures have been formed under monolayer coverage: honeycomb structure and hollow triangles. STM images of NbO_x honeycomb are very similar to Ti_2O_3 honeycomb thin films grown on Au(111), therefore it is likely that NbO_x honeycomb structure has a stoichiometry of Nb_2O_3 and a Au-Nb-O stacking sequence. For NbO_x hollow triangles, they show a variety in sizes but the sides of triangles all run along $\langle 1\bar{1}0 \rangle$, and they are all double-lined equilateral triangles. Due to the fact that hollow triangle is not a close-packed dense structure, multiply ways of bonding triangle units have been observed, and the hollow sites are filled up when Nb dosing increases. Structural models have been proposed for NbO_x hollow triangle phase, and it is suggested to be more reduced than the honeycomb phase. Further studies are necessary to better understand the NbO_x/Au(111) system, especially the characterisation of chemical composition is needed. Based on this successful trial of generating 2D honeycomb ultra-thin films, growing M_2O_3 (M: transition metals) honeycomb thin films on three-fold symmetrical metal substrates could be promoted to more systems. This will be meaningful for the potential applications of honeycomb ultra-thin films.

Chapter 8:

Conclusions

8.1 Overview

This thesis presents original work on the initial stage of epitaxial growth of ultra-thin oxide films including TiO_x and NbO_x. The substrate applied in the experiments is (22 × √3) reconstructed Au(111) which shows repeatedly parallel pairs of bright rows as a result of surface compression. However the three-fold symmetrical hexagonal lattice of normal Au(111) surface is used in discussion because the generation of oxide thin film forms a strong film-substrate bonding that releases the compression of the substrate. Recognisable thin film structures that don't belong to bulk crystal terminations have been observed. Characterisation techniques such as STM, LEED and XPS have been used to study the chemical composition and structures of the novel reconstructions. Results that have been reported in Chapter 4-7 are summarised in section 8.2 and 8.3 based on the type of oxides; an outline for the future work is shown in section 8.4.

8.2 TiO_x ultra-thin films grown on Au(111)

TiO_x ultra-thin films have been generated in two different UHV systems on Au(111) substrates. Two notable 2D reconstructions have been developed in sub-monolayer coverage: a regular honeycomb (HC) phase which has a (2 × 2) superstructure with respect to the (1 × 1) Au(111) lattice; a pinwheel phase which shows a Moiré-like pattern with periodicity in the range of 25 – 29 Å and a rotation of about 15° with respect to the Au substrate. The stoichiometry of HC structure is Ti_2O_3, while the pinwheel phase is more reduced and has a stoichiometry of TiO. Another phase called triangle islands was observed as a multi-layer structure with various shapes and sizes.

Among all the reconstructions observed in ultra-thin TiO_x films, the (2 × 2) HC structure raises a lot attention due to its uniformity and potential of being used as a substrate template. Only a few domain boundaries (DBs) and defects have been found in HC

films; however they still show regular patterns – repeat units are exhibited in either linear or rotational arrangement. Because of the strong bonding to the Au(111) substrate, the linear DBs in HC sheets form along two families of crystallographic directions that are energetically preferred by the Au(111) lattice: ⟨1 1 -2⟩ and ⟨1 -1 0⟩. Six atomically unique DB structural models have been proposed (A1 4,8; A2 5,5,7,7; B1a 5,5,8 and B1b 5,7; B2a 5,5,8 and B2b 5,7), and three of them have been confirmed in STM experiments that could be developed into long-range DBs (A1 4,8, B1b 5,7 and B2a 5,5,8). Rotational DBs show up far less frequently. However their appearance is very unique, especially for a six-fold symmetrical 'snowflake' DB loop.

Another type of imperfection discovered in HC-Ti_2O_3/Au(111) thin films are point defects. Generally speaking there are two kinds of point defects. The dark ones that exhibit as a hole in the Ti-apex sites of HC sheets are assigned as Ti vacancies. The bright ones show up like spots attached on the HC sheet are either oxygen vacancies (bright point defects sitting on the oxygen bridging sites) or hydroxyl groups (bright point defects that bonded on oxygen bridging sites or Ti-apex sites). In the case of having more than one Ti vacancies, due to the trend of reducing the impact to the stoichiometry of HC sheet, they preferred to link into a big hole, therefore the mobility of each vacancy in this bonded group is limited through diffusion. For bright point defects, diffusion is more independent. Pairing of oxygen vacancies/hydroxyl groups steadies defects. A stable point defect pair consists of a Ti vacancy and a hydroxyl group that is bonded to the neighbouring Ti-apex atom has also been found in experiments.

In summary, Au(111) substrate strongly influences the structures of ultra-thin TiO_x films that are grown on it. In the monolayer coverage, a variety of well-ordered ultra-thin films form and show unique structures. Even the imperfections discovered in the new structures reveal a strong interaction between substrate and thin film. The impact of the substrate structures has to be considered when studying the elemental growth of these ultra-thin films.

8.3 NbO_x ultra-thin films grown on Au(111)

For the purpose of developing regular HC ultra-thin films like Ti_2O_3/Au(111), Nb was selected because of its similarity to Ti (e.g. atomic radii, oxidation state, properties of oxides). Following the same procedure of growing ultra-thin TiO_x films on Au(111), two identifiable NbO_x reconstructions have been generated in sub-monolayer coverage. One is the (2 × 2) honeycomb phase that is nearly identical with the Ti_2O_3 HC structure; the other one is the hollow triangle phase that shows double-line sides and various sizes. Structural models based on the STM images have suggested the stoichiometry of the HC phase being Nb_2O_3 while the hollow triangle being $NbO_{x\approx1}$. When the Nb coverage increases, the hollowed centre of triangle is filled up; after the first layer of NbO_x is completed, large amounts of multi-layer bright features with no crystalline structure form. The success of building up the Nb_2O_3 HC structure is meaningful. It proves that growing M_2O_3 (M: transition metal has oxidation state of +3) honeycomb ultra-thin films on three-fold symmetrical metal substrates is feasible, which pushes forward the idea of developing uniform HC structure into applications (e.g. substrate templates). However the lack of characterisation of the chemical composition of NbO_x films leads to the uncertainty of atomic structures. The follow-up study is still needed to resolve this issue.

8.4 Future work

A lot work of TiO_x ultra-thin films grown on Au(111) within monolayer coverage has been done in this thesis. For the Ti_2O_3 HC structure, a comprehensive understanding has been achieved which covers both the regular structure and the observed imperfections including domain boundaries and point defects. Domain boundaries that have linear structural forms have been studied in details, while the rotational DBs/defects still need

to be analysed by DFT modelling. This part of work will be carried out in collaboration with the Paris group. For point defects, the identification of specific point defects is still uncertain; DFT calculation and STM image simulations will need to be applied to the continue this research, which could also be helpful in the study of stability and diffusion of point defects. Based on the similarity between the rutile TiO_2(110) surface and Ti_2O_3 HC thin film, water dissociation experiments are considered to be valuable for the investigation of photocatalytic property of the HC structure. In addition to verifying the oxygen vacancies in HC thin films, methods of preparing the HC thin film with plenty of oxygen vacancies to take part in the reaction are yet to be explored.

For the work of developing NbO_x ultra-thin films on Au(111), even though an identical HC structure has been observed, characterisation of its chemical composition is still needed to confirm the atomic structure of the NbO_x HC thin film. In the mean time, differences between the HC structures of Ti_2O_3 and NbO_x thin films should be discussed; DFT calculations would be helpful. The other notable structure found in NbO_x/Au(111) – hollow triangles – is also worth exploring. The same as mentioned previously for the future study of NbO_x HC structure, chemical composition characterisation and DFT modelling should be applied to determine the structure of hollow triangle phase as well as investigating its formation mechanism. Interesting phenomenon like lacking of a single Ti atom in the vertex of outer-triangle and movement of the neighbouring Nb atom was noticed; further observation and explanation is required. What's more, experimental trials of generating more well-ordered reconstructions of NbO_x/Au(111) by changing the conditions of forming ultra-thin films will be carried out.

Due to the fact that the HC structure of Ti_2O_3 ultra-thin film has been reproduced by depositing and oxidising transition metal with a +3 oxidation state (Nb) on metal substrate with three-fold symmetrical lattice (Au(111)), it is natural to keep trying to develop the identical HC structure by following the same procedures. Transition metals like Mn, Cr and Fe that have oxidation state of +3 are promising to form M_2O_3 (M: metal) HC thin films by growing epitaxially on three-fold symmetrical metal substrates such as

Au(111) and Pt(111). Novel structures other than reported in the literature or discussed in this thesis might be revealed. On the other hand, since the technique of generating regular HC Ti_2O_3/Au(111) ultra-thin film has been well practiced, experiments of using it as a template for molecular assembly could start being planned.

References:

[1] U. H. Frank, *Transparent Conductive Oxides in Thin Film Photovoltaics*. JPCS **559**, 012016 (2014).

[2] J. Quiñonero, T. Lana-Villarreal, and R. Gómez, *Improving the Photoactivity of Bismuth Vanadate Thin Film Photoanodes through Doping and Surface Modification Strategies*. Appl. Catal., B **194**, 141 (2016).

[3] V. C. Anitha, A. N. Banerjee, and S. W. Joo, *Recent Developments in TiO2 as n- and p-type Transparent Semiconductors: Synthesis, Modification, Properties, and Energy-related Applications*. J. Mater. Sci. **50**, 7495 (2015).

[4] M. Beidaghi and Y. Gogotsi, *Capacitive Energy Storage in Micro-scale Devices: Recent Advances in Design and Fabrication of Micro-supercapacitors*. Energ. Environ. Sci. **7**, 867 (2014).

[5] S. Bagheri, Z. A. Mohd Hir, A. T. Yousefi, and S. B. Abdul Hamid, *Progress on Mesoporous Titanium Dioxide: Synthesis, Modification and Applications*. Micropor. Mesopor. Mat. **218**, 206 (2015).

[6] M. S. Chen and D. W. Goodman, *The Structure of Catalytically Active Gold on Titania*. Science **306**, 252 (2004).

[7] I. X. Green, W. Tang, M. Neurock, and J. T. Yates, *Observation of Dual Catalytic Sites During Oxidation of CO on a Au/TiO2 Catalyst*. Science **333**, 736 (2011).

[8] C. Wu, M. S. J. Marshall, and M. R. Castell, *Surface Structures of Ultrathin TiOx Films on Au(111)*. J. Phys. Chem. C **115**, 8643 (2011).

[9] F. Tumino, P. Carrozzo, L. Mascaretti, C. S. Casari, M. Passoni, S. Tosoni, C. E. Bottani, and A. L. Bassi, *Two-Dimensional TiOx Nanostructures on Au(111): A Scanning Tunneling Microscopy and Spectroscopy Investigation*. 2D Mater. **2**, 045011 (2015).

[10] D. Ragazzon, A. Schaefer, M. H. Farstad, L. E. Walle, P. Palmgren, A. Borg, P. Uvdal, and A. Sandell, *Chemical Vapor Deposition of Ordered TiOx Nanostructures on Au(111)*. Surf. Sci. **617**, 211 (2013).

[11] C. J. Davisson and L. H. Germer, *Reflection and Refraction of Electrons by a Crystal of Nickel*. Proc. Natl. Acad. Sci. U.S.A. **14**, 619 (1928).

[12] E. J. Scheibner, L. H. Germer, and C. D. Hartman, *Apparatus for Direct Observation of Low-Energy Electron Diffraction Patterns*. Rev. Sci. Instrum. **31**, 112 (1960).

[13] J. J. Lander, J. Morrison, and F. Unterwald, *Improved Design and Method of Operation of Low Energy Electron Diffraction Equipment*. Rev. Sci. Instrum. **33**, 782 (1962).

[14] G. Binnig and H. Rohrer, *Scanning Tunnelling Microscopy*. Physica B & C **127**, 37 (1984).

[15] G. Binnig and H. Rohrer, *Scanning Tunnelling Microscopy*. Surf. Sci. **152**, 17 (1985).

[16] C. J. Chen, *Introduction to Scanning Tunneling Microscopy*. OUP Oxford, (2008).

[17] B. D. Ratner and D. G. Castner, in *Surface Analysis - The Principal Techniques*. John Wiley & Sons, U.K., (2009).

[18] K. Siegbahn *et al.*, *ESCA (Atomic, Molecular and Solid State Structure Studied by Means of Electron Spectroscopy)*. Almqvist & Wiksells Sweden, (1967).

[19] G. W. Gobeli, F. G. Allen, and E. O. Kane, *Polarization Evidence for Momentum Conservation in Photoelectric Emission from Germanium and Silicon*. Phys. Rev. Lett. **12**, 94 (1964).

[20] C. N. Berglund and W. E. Spicer, *Photoemission Studies of Copper and Silver: Theory*. Phys. Rev. **136**, A1030 (1964).

[21] C. N. Berglund and W. E. Spicer, *Photoemission Studies of Copper and Silver: Experiment*. Phys. Rev. **136**, A1044 (1964).

[22] N. V. Smith, M. M. Traum, and F. J. Di Salvo, *Mapping Energy Bands in Layer Compounds from the Angular Dependence of Ultraviolet Photoemission*. Sol. State. Comm. **15**, 211 (1974).

[23] C. A. Gerken and G. A. Somorjai, *Low-Energy Electron Diffraction. Characterization of Materials.* John Wiley & Sons, U.S.A., (2002).

[24] C. A. Lucas, in *Surface Analysis - the Principal Techniques*, edited by John C. Vickerman, and I. S. Gilmore. John Wiley and Sons, U.K., (2009).

[25] K. Oura, V. G. Lifshits, A. Saranin, A. V. Zotov, and M. Katayama, *Surface Science - An Introduction*. Springer-Verlag Berlin Heidelberg, Germany, (2003).

[26] S. I. Park and C. F. Quate, *Scanning Tunneling Microscope*. Rev. Sci. Instrum. **58**, 2010 (1987).

[27] M. S. J. Marshall and M. R. Castell, *Scanning Tunnelling Microscopy of Epitaxial Nanostructures*. Chem. Soc. Rev. **43**, 2226 (2014).

[28] J. Tersoff and D. R. Hamann, *Theory of the Scanning Tunneling Microscope*. Phys. Rev. B. **31**, 805 (1985).

[29] J. Tersoff and D. R. Hamann, *Theory and Application for the Scanning Tunneling Microscope*. Phys. Rev. Lett. **50**, 1998 (1983).

[30] D. T. Newell, *The Surface Structure and Reconstructions of SrTiO3(001)*. for the degree of Doctor of Philosophy, University of Oxford, (2007).

[31] N. D. Lang, *Spectroscopy of single atoms in the scanning tunneling microscope*. Phys. Rev. B. **34**, 5947 (1986).

[32] N. J. DiNardo, *Nanoscale Characterization of Surface and Interfaces*. Wiley-VCH Verlag GmbH, Germany, (1994).

[33] M. R. Castell, in *Nanocharacterisation: 2nd edition*, edited by A. I. Kirkland, and S. J. Haigh. Royal Society of Chemistry Publishing, Cambridge, (2015).

[34] P. Sutter, in *Science of Microscopy*, edited by P. W. Hawkes, and J. C. H. Spence.

Springer, U.S.A., (2008).

[35] P. van der Heide, *X-Ray Photoelectron Spectroscopy: An Introduction to Principles and Practices*. John Wiley & Sons, Canada, (2012).

[36] V. I. Nefedov, *X-Ray Photoelectron Spectroscopy of Solid Surfaces*. VSP BV, Netherlands, (1988).

[37] M. S. J. Marshall, D. T. Newell, D. J. Payne, R. G. Egdell, and M. R. Castell, *Atomic and Electronic Surface Structures of Dopants in Oxides: STM and XPS of Nb- and La-Doped SrTiO3(001)*. Phys. Rev. B **83**, 035410 (2011).

[38] K. Oura, V. G. Lifshits, A. A. Saranin, A. V. Zotov, and M. Katayama, *Surface Science: An Introduction*. Springer-Verlag Berlin Heidelberg New York, Germany, (2003).

[39] G. A. Somorjai and Y. Li, *Introduction to Surface Chemistry and Catalysis*. John Wiley & Sons, Inc., U.S.A., (2010).

[40] J. V. Barth, H. Brune, G. Ertl, and R. J. Behm, *Scanning Tunneling Microscopy Observations on the Reconstructed Au(111) Surface: Atomic Structure, Long-range Superstructure, Rotational Domains, and Surface Defects*. Phys. Rev. B **42**, 9307 (1990).

[41] Y. Wang, N. S. Hush, and J. R. Reimers, *Simulation of the Au(111)-(22 $\times$ $\sqrt{3}$) Surface Reconstruction*. Phys. Rev. B **75**, 233416 (2007).

[42] H. Brune and K. Kern, in *The Chemical Physics of Solid Surfaces*, edited by D. A. King, and D. P. Woodruff. Elsevier, Switzerland, (1997).

[43] M. A. Van Hove, R. J. Koestner, P. C. Stair, J. P. Bibérian, L. L. Kesmodel, I. BartoŠ, and G. A. Somorjai, *The Surface Reconstructions of the (100) Crystal Faces of Iridium, Platinum and Gold: I. Experimental Observations and Possible Structural Models*. Surf. Sci. **103**, 189 (1981).

[44] C. Wu and M. R. Castell, in *Oxide Materials at the Two-Dimensional Limit*, edited by P. F. Netzer, and A. Fortunelli. Springer International Publishing, Switzerland, (2016).

[45] C. H. Shue, S. L. Yau, and K. Itaya, *In Situ Scanning Tunneling Microscopy of Au(111) in Acidic and Alkaline Potassium Cyanide*. J. Phys. Chem. B **108**, 17433 (2004).

[46] M. H. Farstad, D. Ragazzon, L. E. Walle, A. Schaefer, A. Sandell, and A. Borg, *Water Adsorption on TiOx Thin Films Grown on Au(111)*. J. Phys. Chem. C **119**, 6660 (2015).

[47] D. Ragazzon, M. H. Farstad, A. Schaefer, L. E. Walle, P. Uvdal, A. Borg, and A. Sandell, *Growth of TiO2(B)(001) on Au(111) by Chemical Vapor Deposition*. Surf. Sci. **633**, 102 (2015).

[48] C. Wu and M. R. Castell, *Ba and BaOx Surface Structures on Au(111)*. Surf. Sci. **606**, 181 (2012).

[49] X. Deng and C. Matranga, *Selective Growth of Fe2O3 Nanoparticles and Islands on Au(111)*. J. Phys. Chem. C **113**, 11104 (2009).

[50] N. A. Khan and C. Matranga, *Nucleation and Growth of Fe and FeO*

Nanoparticles and Films on Au(111). Surf. Sci. **602**, 932 (2008).

[51] A. J. Window *et al.*, *The Structure of Epitaxial V2O3 Films and Their Surfaces: A Medium Energy Ion Scattering Study*. Surf. Sci. **606**, 1716 (2012).

[52] J. Seifert, E. Meyer, H. Winter, and H. Kuhlenbeck, *Surface Termination of an Ultrathin V2O3-Film on Au(111) Studied via Ion Beam Triangulation*. Surf. Sci. **606**, L41 (2012).

[53] A. C. Dupuis, M. Abu Haija, B. Richter, H. Kuhlenbeck, and H. J. Freund, *V2O3(0001) on Au(111) and W(110): Growth, Termination and Electronic Structure*. Surf. Sci. **539**, 99 (2003).

[54] S. Ma, J. Rodriguez, and J. Hrbek, *STM Study of the Growth of Cerium Oxide Nanoparticles on Au(111)*. Surf. Sci. **602**, 3272 (2008).

[55] J. A. Venables and G. L. Price, in *Epitaxial Growth Part B*, edited by J. W. Matthews. Academic Press, U.K., (1975).

[56] S. Kowarik, K. Broch, A. Hinderhofer, A. Schwartzberg, J. O. Ossó, D. Kilcoyne, F. Schreiber, and S. R. Leone, *Crystal Grain Orientation in Organic Homo- and Heteroepitaxy of Pentacene and Perfluoropentacene Studied with X-Ray Spectromicroscopy*. J. Phys. Chem. C **114**, 13061 (2010).

[57] M. A. Herman, W. Richter, and H. Sitter, in *Epitaxy: Physical Principles and Technical Implementation*. Springer Berlin Heidelberg, Germany, (2004).

[58] M. J. Stowell, in *Epitaxial Growth*, edited by J. W. Matthews. Academic Press, (1975).

[59] M. Liu, Z. Ji, and L. Shang, *Nanotechnology: Nanostructured Surface*. Wiley VCH, Germany, Vol. 8, (2010).

[60] H. Brune, in *Surface and Interface Science*, edited by K. Wandelt. Wiley-VCH Verlag GmbH & Co. KGaA, Germany, (2013).

[61] S. K. Srivastava, *Epitaxial Growth and Characterization of Multifunctional Heterostructures: Integrating Ferromagnets, Ferroelectrics, Insulators and III-V Semiconductors*. For the Degree of Doctor of Philosophy, University of Minnesota, (2008).

[62] Y. Bai, I. Mora-Seró, F. De Angelis, J. Bisquert, and P. Wang, *Titanium Dioxide Nanomaterials for Photovoltaic Applications*. Chem. Rev. **114**, 10095 (2014).

[63] S. Hu, M. R. Shaner, J. A. Beardslee, M. Lichterman, B. S. Brunschwig, and N. S. Lewis, *Amorphous TiO2 Coatings Stabilize Si, GaAs, and GaP Photoanodes for Efficient Water Oxidation*. Science **344**, 1005 (2014).

[64] L. Yang, C. McCue, Q. Zhang, E. Uchaker, Y. Mai, and G. Cao, *Highly Efficient Quantum Dot-Sensitized TiO2 Solar Cells Based on Multilayered Semiconductors (ZnSe/CdS/CdSe)*. Nanoscale **7**, 3173 (2015).

[65] J. Liu, X. Fu, D. Cao, L. Mao, J. Wang, D. Mu, B. Mi, B. Zhao, and Z. Gao, *Stacked graphene–TiO2 photoanode via electrospray deposition for highly efficient dye-sensitized solar cells*. Org. Electron. **23**, 158 (2015).

[66] J. Bai and B. Zhou, *Titanium Dioxide Nanomaterials for Sensor Applications*.

Chem. Rev. **114**, 10131 (2014).

[67] S. Nasirian and H. Milani Moghaddam, *Effect of Different Titania Phases on the Hydrogen Gas Sensing Features of Polyaniline/TiO2 Nanocomposite*. Polymer **55**, 1866 (2014).

[68] E. Comini, V. Galstyan, G. Faglia, E. Bontempi, and G. Sberveglieri, *Highly Conductive Titanium Oxide Nanotubes Chemical Sensors*. Micropor. Mesopor. Mat. **208**, 165 (2015).

[69] Z. Zhu, J. Chang, and R. Wu, *Fast ozone Detection by Using a Core–shell Au@TiO2 Sensor at Room Temperature*. Sensor. Actuat. B: Chem. **214**, 56 (2015).

[70] J. Chen, F. Qiu, W. Xu, S. Cao, and H. Zhu, *Recent Progress in Enhancing Photocatalytic Efficiency of TiO2-based Materials*. Appl. Catal. A: Gen. **495**, 131 (2015).

[71] F. Dufour, S. Pigeot-Remy, O. Durupthy, S. Cassaignon, V. Ruaux, S. Torelli, L. Mariey, F. Maugé, and C. Chanéac, *Morphological Control of TiO2 Anatase Nanoparticles: What is the Good Surface Property to Obtain Efficient Photocatalysts?* Appl. Catal. B: Environ. **174-175**, 350 (2015).

[72] J. Schneider, M. Matsuoka, M. Takeuchi, J. Zhang, Y. Horiuchi, M. Anpo, and D. W. Bahnemann, *Understanding TiO2 Photocatalysis: Mechanisms and Materials*. Chem. Rev. **114**, 9919 (2014).

[73] Z. Bian, T. Tachikawa, P. Zhang, M. Fujitsuka, and T. Majima, *Au/TiO2 Superstructure-Based Plasmonic Photocatalysts Exhibiting Efficient Charge Separation and Unprecedented Activity*. J. Am. Chem. Soc. **136**, 458 (2014).

[74] H. Perron, C. Domain, J. Roques, R. Drot, E. Simoni, and H. Catalette, *Optimisation of Accurate Rutile TiO2 (110), (100), (101) and (001) Surface Models from Periodic DFT Calculations*. Theor. Chem. Acc. **117**, 565 (2007).

[75] A. Fujishima and K. Honda, *Electrochemical Photolysis of Water at a Semiconductor Electrode*. Nature **238**, 37 (1972).

[76] D. A. H. Hanaor and C. C. Sorrell, *Review of the Anatase to Rutile Phase Transformation*. J. Mater. Sci. **46**, 855 (2010).

[77] K. Sabyrov, N. D. Burrows, and R. L. Penn, *Size-Dependent Anatase to Rutile Phase Transformation and Particle Growth*. Chem. Mater. **25**, 1408 (2013).

[78] N. Satoh, T. Nakashima, and K. Yamamoto, *Metastability of Anatase: Size Dependent and Irreversible Anatase-Rutile Phase Transition in Atomic-Level Precise Titania*. Sci. Rep. **3**, 1959 (2013).

[79] J. G. Li and T. Ishigaki, *Brookite → Rutile Phase Transformation of TiO2 Studied with Monodispersed Particles*. Acta Mater. **52**, 5143 (2004).

[80] J. Huberty and H. Xu, *Kinetics Study on Phase Transformation from Titania Polymorph Brookite to Rutile*. J. Solid State Chem. **181**, 508 (2008).

[81] A. Di Paola, M. Bellardita, and L. Palmisano, *Brookite, the Least Known TiO2 Photocatalyst*. Catalysts **3**, 36 (2013).

[82] U. Diebold, *The Surface Science of Titanium Dioxide*. Surf. Sci. Rep. **48**, 53

(2003).

[83] X. Bokhimi, A. Morales, M. Aguilar, J. A. Toledo-Antonio, and F. Pedraza, *Local Order in Titania Polymorphs*. Int. J. Hydrogen. Energy. **26**, 1279 (2001).

[84] G. Meinhold, *Rutile and Its Applications in Earth Sciences*. Earth-Sci. Rev. **102**, 1 (2010).

[85] S. Matsushita *et al.*, *Calculation and Fabrication of Two-Dimensional Complete Photonic Bandgap Structures Composed of Rutile TiO2 Single Crystals in Air/Liquid*. J. Mater. Sci. **51**, 1066 (2015).

[86] J. Cai, J. Ye, S. Chen, X. Zhao, D. Zhang, S. Chen, Y. Ma, S. Jin, and L. Qi, *Self-Cleaning, Broadband and Quasi-Omnidirectional Antireflective Structures Based on Mesocrystalline Rutile TiO2 Nanorod Arrays*. Energy Environ. Sci. **5**, 7575 (2012).

[87] K. O. Awitor, A. Rivaton, J. L. Gardette, A. J. Down, and M. B. Johnson, *Photo-Protection and Photo-Catalytic Activity of Crystalline Anatase Titanium Dioxide Sputter-Coated on Polymer Films*. Thin. Solid. Films. **516**, 2286 (2008).

[88] J. Zhang, P. Zhou, J. Liu, and J. Yu, *New Understanding of the Difference of Photocatalytic Activity Among Anatase, Rutile and Brookite TiO2*. Phys. Chem. Chem. Phys. **16**, 20382 (2014).

[89] H. Eskandarloo, M. Hashempour, A. Vicenzo, S. Franz, A. Badiei, M. A. Behnajady, and M. Bestetti, *High-Temperature Stable Anatase-Type TiO2 Nanotube Arrays: A Study of the Structure-Activity Relationship*. Appl. Catal. B Environ. **185**, 119 (2016).

[90] J. Xie, X. Lü, J. Liu, and H. Shu, *Brookite Titania Photocatalytic Nanomaterials: Synthesis, Properties, and Applications*. Pure. Appl. Chem. **81**, 2407 (2009).

[91] S. Thennarasu, K. Rajasekar, and K. Balkis Ameen, *Hydrothermal Temperature as a Morphological Control Factor: Preparation, Characterization and Photocatalytic Activity of Titanate Nanotubes and Nanoribbons*. J. Mol. Struct. **1049**, 446 (2013).

[92] Y. Zou, X. Tan, T. Yu, Y. Li, Q. Shang, and W. Wang, *Synthesis and Photocatalytic Activity of Chrysanthemum-like Brookite TiO2 Nanostructures*. Mater. Lett. **132**, 182 (2014).

[93] Z. Rui, S. Wu, C. Peng, and H. Ji, *Comparison of TiO2 Degussa P25 with Anatase and Rutile Crystalline Phases for Methane Combustion*. Chem. Eng. J. **243**, 254 (2014).

[94] K. S. Lin, H. W. Cheng, W. R. Chen, and J. F. Wu, *Synthesis, Characterization and Application of Anatase-Type Titania Nanoparticles*. J. Environ. Eng. Manage. **20**, 69 (2010).

[95] H. Li, B. Xu, and Y. Fan, *Dramatic Activity of Mixed-Phase TiO2 Photocatalyst Synthesized by Hydrothermal Method*. Chem. Phys. Lett. **558**, 66 (2013).

[96] P. Apopei, C. Catrinescu, C. Teodosiu, and S. Royer, *Mixed-Phase TiO2 Photocatalysts: Crystalline Phase Isolation and Reconstruction, Characterization and Photocatalytic Activity in the Oxidation of 4-Chlorophenol from Aqueous Effluents*. Appl. Catal. B Environ. **160–161**, 374 (2014).

[97] S. Wai Ruu, O. L. Hendrik, S. Mustaffa, and Y. Leny, *High Photocatalytic Activity of Mixed Anatase-Rutile Phases on Commercial TiO2 Nanoparticles*. IOP Conf. Ser.: Mater. Sci. Eng. **107**, 012005 (2016).

[98] Y. Du, J. Li, Y. Liu, X. Niu, F. Guo, and Q. Feng, *Synthesis of {110}-faceted Rutile TiO2 Nanocrystals from Tetratitanate Nanoribbons for Improving Dye-Sensitized Solar Cell Performance*. RSC Adv. **6**, 9717 (2016).

[99] Y. Y. Yu, U. Diebold, and X. Gong, *NO Adsorption and Diffusion on Hydroxylated Rutile TiO2(110)*. Phys. Chem. Chem. Phys. **17**, 26594 (2015).

[100] A. Argondizzo, X. Cui, C. Wang, H. Sun, H. Shang, J. Zhao, and H. Petek, *Ultrafast Multiphoton Pump-Probe Photoemission Excitation Pathways in RutileTiO2 (110)*. Phys. Rev. B **91**, 155429 (2015).

[101] D. Fernández-Torre, A. Yurtsever, J. Onoda, M. Abe, S. Morita, Y. Sugimoto, and R. Pérez, *Pt Atoms Adsorbed on TiO2(110)-(1x1) Studied with Noncontact Atomic Force Microscopy and First-Principles Simulations*. Phys. Rev. B **91**, 075401 (2015).

[102] H. Feng *et al.*, *Temperature- and Coverage-Dependent Kinetics of Photocatalytic Reaction of Methanol on TiO2(110)-(1 × 1) Surface*. J. Phys. Chem. C **120**, 5503 (2016).

[103] C. Sánchez-Sánchez, C. González, P. Jelinek, J. Méndez, P. L. d. Andres, J. A. Martín-Gago, and M. F. López, *Understanding Atomic-Resolved STM Images on TiO2 (110)-(1 × 1) Surface by DFT Calculations*. Nanotechnology **21**, 405702 (2010).

[104] R. E. Tanner, M. R. Castell, and G. A. D. Briggs, *High Resolution Scanning Tunnelling Microscopy of the Rutile TiO2(110) Surface*. Surf. Sci. **412–413**, 672 (1998).

[105] C. Xu, X. Lai, G. W. Zajac, and D. W. Goodman, *Scanning Tunneling Microscopy Studies of the TiO2(110) Surface: Structure and the Nucleation Growth of Pd*. Phys. Rev. B **56**, 13464 (1997).

[106] C. L. Pang, R. Lindsay, and G. Thornton, *Chemical Reactions on Rutile TiO2(110)*. Chem. Soc. Rev. **37**, 2328 (2008).

[107] U. Diebold, J. Lehman, T. Mahmoud, M. Kuhn, G. Leonardelli, W. Hebenstreit, M. Schmid, and P. Varga, *Intrinsic Defects on a TiO2(110)(1×1) Surface and Their Reaction with Oxygen: A Scanning Tunneling Microscopy Study*. Surf. Sci. **411**, 137 (1998).

[108] S. Suzuki, K. I. Fukui, H. Onishi, and Y. Iwasawa, *Hydrogen Adatoms on TiO2(110)-(1x1) Characterized by Scanning Tunneling Microscopy and Electron Stimulated Desorption*. Phys. Rev. Lett. **84**, 2156 (2000).

[109] R. Schaub, P. Thostrup, N. Lopez, E. Lægsgaard, I. Stensgaard, J. K. Nørskov, and F. Besenbacher, *Oxygen Vacancies as Active Sites for Water Dissociation on Rutile TiO2(110)*. Phys. Rev. Lett. **87**, 266104 (2001).

[110] I. M. Brookes, C. A. Muryn, and G. Thornton, *Imaging Water Dissociation on TiO2(110)*. Phys. Rev. Lett. **87**, 266103 (2001).

[111] S. Wendt, J. Matthiesen, R. Schaub, E. K. Vestergaard, E. Lægsgaard, F. Besenbacher, and B. Hammer, *Formation and Splitting of Paired Hydroxyl Groups on Reduced TiO2(110)*. Phys. Rev. Lett. **96**, 066107 (2006).

[112] Z. Dohnálek, I. Lyubinetsky, and R. Rousseau, *Thermally-Driven Processes on*

Rutile TiO2(110)-(1 × 1): A Direct View at the Atomic Scale. Prog. Surf. Sci. **85**, 161 (2010).

[113] L. A. Harris and A. A. Quong, *Molecular Chemisorption as the Theoretically Preferred Pathway for Water Adsorption on Ideal Rutile TiO2(110)*. Phys. Rev. Lett. **93**, 086105 (2004).

[114] Z. Zhang, O. Bondarchuk, B. D. Kay, J. M. White, and Z. Dohnálek, *Imaging Water Dissociation on TiO2(110): Evidence for Inequivalent Geminate OH Groups*. J. Phys. Chem. B **110**, 21840 (2006).

[115] N. G. Petrik and G. A. Kimmel, *Reaction Kinetics of Water Molecules with Oxygen Vacancies on Rutile TiO2(110)*. J. Phys. Chem. C **119**, 23059 (2015).

[116] S. Wendt *et al.*, *Oxygen Vacancies on TiO2(110) and Their Interaction with H2O and O2: A Combined High-resolution STM and DFT Study*. Surf. Sci. **598**, 226 (2005).

[117] M. A. Henderson, *A Surface Science Perspective on Photocatalysis*. Surf. Sci. Rep. **66**, 185 (2011).

[118] L. E. Walle, D. Ragazzon, A. Borg, P. Uvdal, and A. Sandell, *Competing Water Dissociation Channels on Rutile TiO2(110)*. Surf. Sci. **621**, 77 (2014).

[119] D. A. Duncan, F. Allegretti, and D. P. Woodruff, *Water Does Partially Dissociate on the Perfect TiO2(110) Surface: A Quantitative Structure Determination*. Phys. Rev. B **86**, 045411 (2012).

[120] D. J. Wesolowski *et al.*, *Comment on "Structure and Dynamics of Liquid Water on Rutile TiO2(110)"*. Phys. Rev. B **85**, 167401 (2012).

[121] L. M. Liu, C. J. Zhang, G. Thornton, and A. Michaelides, *Structure and Dynamics of Liquid Water on Rutile TiO2(110)*. Phys. Rev. B **82**, 161415 (2010).

[122] O. Bikondoa, C. L. Pang, R. Ithnin, C. A. Muryn, H. Onishi, and G. Thornton, *Direct Visualization of Defect-Mediated Dissociation of Water on TiO2(110)*. Nat. Mater. **5**, 189 (2006).

[123] C. L. Pang *et al.*, *Tailored TiO2(110) Surfaces and Their Reactivity*. Nanotechnology **17**, 5397 (2006).

[124] G. Teobaldi, W. A. Hofer, O. Bikondoa, C. L. Pang, G. Cabailh, and G. Thornton, *Modelling STM Images of TiO2(110) from First-Principles: Defects, Water Adsorption and Dissociation Products*. Chem. Phys. Lett. **437**, 73 (2007).

[125] X. Cui, B. Wang, Z. Wang, T. Huang, Y. Zhao, J. Yang, and J. G. Hou, *Formation and Diffusion of Oxygen-Vacancy Pairs on TiO2(110)-(1×1)*. J. Chem. Phys. **129**, 044703 (2008).

[126] M. Z. Baykara, H. Mönig, T. C. Schwendemann, Ö. Ünverdi, E. I. Altman, and U. D. Schwarz, *Three-Dimensional Interaction Force and Tunneling Current Spectroscopy of Point Defects on Rutile TiO2(110)*. Appl. Phys. Lett. **108**, 071601 (2016).

[127] C. L. Pang, A. Sasahara, H. Onishi, Q. Chen, and G. Thornton, *Noncontact Atomic Force Microscopy Imaging of Water Dissociation Products on TiO2(110)*. Phys. Rev. B **74**, 073411 (2006).

[128] C. A. Walenta, S. L. Kollmannsberger, J. Kiermaier, A. Winbauer, M. Tschurl, and

U. Heiz, *Ethanol Photocatalysis on Rutile TiO2(110): The Role of Defects and Water*. Phys. Chem. Chem. Phys. **17**, 22809 (2015).

[129] Y. Y. Yu and X. Q. Gong, *CO Oxidation at Rutile TiO2(110): Role of Oxygen Vacancies and Titanium Interstitials*. ACS Catal. **5**, 2042 (2015).

[130] Y. Yoon *et al.*, *Anticorrelation Between Surface and Subsurface Point Defects and the Impact on the Redox Chemistry of TiO2(110)*. Chem. Phys. Chem. **16**, 313 (2015).

[131] K. Matsunaga, Y. Tanaka, K. Toyoura, A. Nakamura, Y. Ikuhara, and N. Shibata, *Existence of Basal Oxygen Vacancies on the Rutile TiO2(110) surface*. Phys. Rev. B **90**, 195303 (2014).

[132] H. Shi, Y. C. Liu, Z. J. Zhao, M. Miao, T. Wu, and Q. Wang, *Reactivity of the Defective Rutile TiO2 (110) Surfaces with Two Bridging-Oxygen Vacancies: Water Molecule as a Probe*. J. Phys. Chem. C **118**, 20257 (2014).

[133] S. C. Jensen and C. M. Friend, *The Dynamic Roles of Interstitial and Surface Defects on Oxidation and Reduction Reactions on Titania*. Top. Catal. **56**, 1377 (2013).

[134] Z. T. Wang, N. A. Deskins, M. A. Henderson, and I. Lyubinetsky, *Inhibitive Influence of Oxygen Vacancies for Photoactivity on TiO2(110)*. Phys. Rev. Lett. **109**, 266103 (2012).

[135] H. Y. Lee, S. J. Clark, and J. Robertson, *Calculation of Point Defects in Rutile TiO2 by the Screened-Exchange Hybrid Functional*. Phys. Rev. B **86**, 075209 (2012).

[136] T. S. Bjørheim, A. Kuwabara, C. E. Mohn, and T. Norby, *Defects at the (110) Surface of Rutile TiO2 from ab Initio Calculations*. Int. J. Hydrogen Energy **37**, 8110 (2012).

[137] S. Chrétien and H. Metiu, *Electronic Structure of Partially Reduced Rutile TiO2(110) Surface: Where are the Unpaired Electrons Located?* J. Phys. Chem. C **115**, 4696 (2011).

[138] S. Tan, Y. Ji, Y. Zhao, A. Zhao, B. Wang, J. Yang, and J. G. Hou, *Molecular Oxygen Adsorption Behaviors on the Rutile TiO2(110)-1×1 Surface: An in Situ Study with Low-Temperature Scanning Tunneling Microscopy*. J. Am. Chem. Soc. **133**, 2002 (2011).

[139] P. Scheiber, A. Riss, M. Schmid, P. Varga, and U. Diebold, *Observation and Destruction of an Elusive Adsorbate with STM: O2/TiO2(110)*. Phys. Rev. Lett. **105**, 216101 (2010).

[140] C. Sánchez-Sánchez, C. González, P. Jelinek, J. Méndez, P. L. d. Andres, J. A. Martín-Gago, and M. F. López, *Understanding Atomic-Resolved STM images on TiO 2(110)-(1 × 1) Surface by DFT Calculations*. Nanotechnology **21**, 405702 (2010).

[141] E. Lira, J. Ø. Hansen, P. Huo, R. Bechstein, P. Galliker, E. Lægsgaard, B. Hammer, S. Wendt, and F. Besenbacher, *Dissociative and Molecular Oxygen Chemisorption Channels on Reduced Rutile TiO2(110): An STM and TPD Study*. Surf. Sci. **604**, 1945 (2010).

[142] A. C. Papageorgiou, N. S. Beglitis, C. L. Pang, G. Teobaldi, G. Cabailh, Q. Chen, A. J. Fisher, W. A. Hofer, and G. Thornton, *Electron Traps and Their Effect on the*

Surface Chemistry of TiO2(110). Proc. Natl. Acad. Sci. **107**, 2391 (2010).

[143] A. Janotti, J. B. Varley, P. Rinke, N. Umezawa, G. Kresse, and C. G. Van de Walle, *Hybrid Functional Studies of the Oxygen Vacancy in TiO2*. Phys. Rev. B **81**, 085212 (2010).

[144] C. M. Yim, C. L. Pang, and G. Thornton, *Oxygen Vacancy Origin of the Surface Band-Gap State of TiO2(110)*. Phys. Rev. Lett. **104**, 036806 (2010).

[145] N. G. Petrik, Z. Zhang, Y. Du, Z. Dohnálek, I. Lyubinetsky, and G. A. Kimmel, *Chemical Reactivity of Reduced TiO2(110): The Dominant Role of Surface Defects in Oxygen Chemisorption*. J. Phys. Chem. C **113**, 12407 (2009).

[146] K. Onda, B. Li, and H. Petek, *Two-Photon Photoemission Spectroscopy of TiO2(110) Surfaces Modified by Defects and O2 or H2O Adsorbates*. Phys. Rev. B **70**, 045415 (2004).

[147] E. Lira *et al.*, *The Importance of Bulk Ti3+ Defects in the Oxygen Chemistry on Titania Surfaces*. J. Am. Chem. Soc. **133**, 6529 (2011).

[148] V. E. Henrich, G. Dresselhaus, and H. J. Zeiger, *Observation of Two-Dimensional Phases Associated with Defect States on the Surface of TiO2*. Phys. Rev. Lett. **36**, 1335 (1976).

[149] C. L. Pang and G. Thornton, *Manipulation of Oxide Surfaces*. Surf. Sci. **603**, 3255 (2009).

[150] L. Q. Wang, D. R. Baer, and M. H. Engelhard, *Creation of Variable Concentrations of Defects on TiO2(110) Using Low-Density Electron Beams*. Surf. Sci. **320**, 295 (1994).

[151] M. L. Knotek and P. J. Feibelman, *Ion Desorption by Core-Hole Auger Decay*. Phys. Rev. Lett. **40**, 964 (1978).

[152] S. Kajita, T. Minato, H. S. Kato, M. Kawai, and T. Nakayama, *First-Principles Calculations of Hydrogen Diffusion on Rutile TiO2(110) Surfaces*. J. Chem. Phys. **127**, 104709 (2007).

[153] A. Borodin and M. Reichling, *Characterizing TiO2(110) Surface States by Their Work Function*. Phys. Chem. Chem. Phys. **13**, 15442 (2011).

[154] T. Minato, M. Kawai, and Y. Kim, *Creation of Single Oxygen Vacancy on Titanium Dioxide Surface*. J. Mater. Res. **27**, 2237 (2012).

[155] T. Minato, S. Kajita, C. L. Pang, N. Asao, Y. Yamamoto, T. Nakayama, M. Kawai, and Y. Kim, *Tunneling Desorption of Single Hydrogen on the Surface of Titanium Dioxide*. ACS Nano. **9**, 6837 (2015).

[156] R. Schaub, E. Wahlström, A. Rønnau, E. Lægsgaard, I. Stensgaard, and F. Besenbacher, *Oxygen-Mediated Diffusion of Oxygen Vacancies on the TiO2(110) Surface*. Science **299**, 377 (2003).

[157] Y. Xia, B. Zhang, J. Ye, Q. Ge, and Z. Zhang, *Acetone-Assisted Oxygen Vacancy Diffusion on TiO2(110)*. J. Phys. Chem. Lett. **3**, 2970 (2012).

[158] A. Männig, Z. Zhao, D. Rosenthal, K. Christmann, H. Hoster, H. Rauscher, and R. J. Behm, *Structure and Growth of Ultrathin Titanium Oxide Films on Ru(0001)*. Surf.

Sci. **576**, 29 (2005).

[159] A. B. Boffa, H. C. Galloway, P. W. Jacobs, J. J. Benítez, J. D. Batteas, M. Salmeron, A. T. Bell, and G. A. Somorjai, *The Growth and Structure of Titanium Oxide Films on Pt(111) Investigated by LEED, XPS, ISS, and STM*. Surf. Sci. **326**, 80 (1995).

[160] F. Sedona *et al.*, *Ultrathin TiOx Films on Pt(111): A LEED, XPS, and STM Investigation*. J. Phys. Chem. B **109**, 24411 (2005).

[161] M. C. Asensio, M. Kerkar, D. P. Woodruff, A. V. de Carvalho, A. Fernández, A. R. González-Elipe, M. Fernández-Garcia, and J. C. Conesa, *The Growth of Thin Ti and TiOx Films on Pt(111): Morphology and Oxidation States*. Surf. Sci. **273**, 31 (1992).

[162] G. Barcaro, S. Agnoli, F. Sedona, G. A. Rizzi, A. Fortunelli, and G. Granozzi, *Structure of Reduced Ultrathin TiOx Polar Films on Pt(111)*. J. Phys. Chem. C **113**, 5721 (2009).

[163] G. Barcaro, F. Sedona, A. Fortunelli, and G. Granozzi, *Structure of a TiOx Zigzag-Like Monolayer on Pt(111)*. J. Phys. Chem. C **111**, 6095 (2007).

[164] F. Sedona, S. Agnoli, and G. Granozzi, *Ultrathin Wagon-Wheel-Like TiOx Phases on Pt(111): A Combined Low-Energy Electron Diffraction and Scanning Tunneling Microscopy Investigation*. J. Phys. Chem. B **110**, 15359 (2006).

[165] C. Breinlich, M. Buchholz, M. Moors, S. Le Moal, C. Becker, and K. Wandelt, *Scanning Tunneling Microscopy Investigation of Ultrathin Titanium Oxide Films Grown on Pt3Ti(111)*. J. Phys. Chem. C **118**, 6186 (2014).

[166] M. Séverine Le, M. Marco, E. Jan Markus, B. Christian, B. Conrad, and W. Klaus, *Structural and Compositional Characterization of Ultrathin Titanium Oxide Films Grown on Pt3Ti(111)*. J. Phys. Condens. Matter **25**, 045013 (2013).

[167] M. S. Chen, W. T. Wallace, D. Kumar, Z. Yan, K. K. Gath, Y. Cai, Y. Kuroda, and D. W. Goodman, *Synthesis of Well-Ordered Ultra-Thin Titanium Oxide Films on Mo(1 1 2)*. Surf. Sci. **581**, 115 (2005).

[168] D. Kumar, M. S. Chen, and D. W. Goodman, *Characterization of Ultra-Thin TiO2 Films Grown on Mo(112)*. Thin Solid Films **515**, 1475 (2006).

[169] Y. Zhang, L. Giordano, and G. Pacchioni, *Structure, Composition and Electronic Properties of TiOx/Mo(112) Thin Films*. J. Phys. Chem. C **111**, 7437 (2007).

[170] J. Seifert and H. Winter, *Surface Symmetry of Monolayer Titanium Oxide on Mo(112) Studied via Fast Atom Diffraction*. Nucl. Instrum. Meth. B **315**, 9 (2013).

[171] P. Finetti, M. Caffio, B. Cortigiani, A. Atrei, and G. Rovida, *Mechanism of Growth and Structure of Titanium Oxide Ultrathin Films Deposited on Cu(0 0 1)*. Surf. Sci. **602**, 1101 (2008).

[172] A. Atrei, A. M. Ferrari, P. Finetti, A. Beni, and G. Rovida, *LEED and DFT Study of the Quasihexagonal TiO2 Structure on Cu(001)*. J. Phys. Chem. C **113**, 19578 (2009).

[173] Z. Li, D. V. Potapenko, and R. M. Osgood, *Using Moiré Patterning to Map Surface Reactivity versus Atom Registration: Chemisorbed Trimethyl Acetic Acid on TiO/Au(111)*. J. Phys. Chem. C **118**, 29999 (2014).

[174] C. Wu, K. Kruska, and M. R. Castell, *Initial Growth Stages of Titanium and*

Barium Oxide Films on SrTiO3(001). Surf. Sci. **618**, 94 (2013).

[175] S. H. Phark, Y. J. Chang, and T. Won Noh, *Selective Growth of Perovskite Oxides on SrTiO3 (001) by Control of Surface Reconstructions*. Appl. Phys. Lett. **98**, 161908 (2011).

[176] Y. Du, D. J. Kim, T. C. Kaspar, S. E. Chamberlin, I. Lyubinetsky, and S. A. Chambers, *In-Situ Imaging of the Nucleation and Growth of Epitaxial Anatase TiO2(001) Films on SrTiO3(001)*. Surf. Sci. **606**, 1443 (2012).

[177] Q. Shang, T. Yu, X. Tan, Z. Zhang, Y. Zou, L. Zhang, Y. Zhang, and S. Wang, *Enhanced Photoelectrochemical Performance of {001}TiO2/{001}SrTiO3 Epitaxial Heterostructures*. J. Solid State Chem. **20**, 123 (2015).

[178] B. S. Jeong, D. P. Norton, J. D. Budai, and G. E. Jellison, *Epitaxial Growth of Anatase by Reactive Sputter Deposition Using Water Vapor as the Oxidant*. Thin Solid Films **446**, 18 (2004).

[179] S. Zheng, C. A. J. Fisher, T. Kato, Y. Nagao, H. Ohta, and Y. Ikuhara, *Domain Formation in Anatase TiO2 Thin Films on LaAlO3 Substrates*. Appl. Phys. Sci. **101**, 191602 (2012).

[180] L. Yuan *et al.*, *Nucleation Dynamics of Nanostructural TiO2 Films with Controllable Phases on (001) LaAlO3*. Nanotechnology **25**, 014014 (2014).

[181] M. Schuisky, A. Hårsta, A. Aidla, K. Kukli, A. A. Kiisler, and J. Aarik, *Atomic Layer Chemical Vapor Deposition of TiO2 Low Temperature Epitaxy of Rutile and Anatase*. J. Electrochem. Soc. **147**, 3319 (2000).

[182] V. F. Silva *et al.*, *Substrate-Controlled Allotropic Phases and Growth Orientation of TiO2 Epitaxial Thin Films*. J. Appl. Cryst. **43**, 1502 (2010).

[183] K. Vasu, M. B. Sreedhara, J. Ghatak, and C. N. R. Rao, *Atomic Layer Deposition of p-Type Epitaxial Thin Films of Undoped and N-Doped Anatase TiO2*. ACS Appl. Mater. Interfaces **8**, 7897 (2016).

[184] K. Möldre, L. Aarik, H. Mändar, A. Niilisk, R. Rammula, A. Tarre, and J. Aarik, *Atomic Layer Deposition of Rutile and TiO2-II from TiCl4 and O3 on Sapphire: Influence of Substrate Orientation on Thin Film Structure*. J. Cryst. Growth **428**, 86 (2015).

[185] T. Luttrell, S. Halpegamage, E. Sutter, and M. Batzill, *Photocatalytic Activity of Anatase and Rutile TiO2 Epitaxial Thin Film Grown by Pulsed Laser Deposition*. Thin Solid Films **564**, 146 (2014).

[186] Francesco Sedona and G. Granozzi., *Defect Evolution in Oxide Nanophases: The Case of a Zigzag-Like TiOx Phase on Pt(111)*. Phys. Rev. B **77** (2008).

[187] P. Finetti, F. Sedona, G. A. Rizzi, U. Mick, F. Sutara, M. Svec, V. Matolin, K. Schierbaum, and G. Granozzi, *Core and Valence Band Photoemission Spectroscopy of Well-Ordered Ultrathin TiOx Films on Pt(111)*. J. Phys. Chem. C **111**, 869 (2007).

[188] F. Sedona, M. Eusebio, G. Andrea Rizzi, G. Granozzi, D. Ostermann, and K. Schierbaum, *Epitaxial TiO2 Nanoparticles on Pt(111): A Structural Study by Photoelectron Diffraction and Scanning Tunneling Microscopy*. Phys. Chem. Chem. Phys. **7**, 697 (2005).

[189] L. Artiglia, T. Diemant, H. Hartmann, J. Bansmann, R. J. Behm, L. Gavioli, E. Cavaliere, and G. Granozzi, *Stability and Chemisorption Properties of Ultrathin TiOx/Pt(111) Films and Au/TiOx/Pt(111) Model Catalysts in Reactive Atmospheres*. Phys. Chem. Chem. Phys. **12**, 6864 (2010).

[190] G. A. Rizzi, F. Sedona, L. Artiglia, S. Agnoli, G. Barcaro, A. Fortunelli, E. Cavaliere, L. Gavioli, and G. Granozzi, *Au Nanoparticles on a Templating TiOx/Pt(111) Ultrathin Polar Film: A Photoemission and Photoelectron Diffraction Study*. Phys. Chem. Chem. Phys. **11**, 2177 (2009).

[191] R. Burch, *Gold Catalysts for Pure Hydrogen Production in the Water-Gas Shift Reaction: Activity, Structure and Reaction Mechanism*. Phys. Chem. Chem. Phys. **8**, 5483 (2006).

[192] P. Kast, G. Kučerová, and R. J. Behm, *On the Nature of the Active Au Species: CO Oxidation on Cyanide Leached Au/TiO2 Catalysts*. Catal. Today **244**, 146 (2015).

[193] K. Christmann, S. Schwede, S. Schubert, and W. Kudernatsch, *Model Studies on CO Oxidation Catalyst Systems: Titania and Gold Nanoparticles*. Chem. Phys. Chem. **11**, 1344 (2010).

[194] M. Valden, X. Lai, and D. W. Goodman, *Onset of Catalytic Activity of Gold Clusters on Titania with the Appearance of Nonmetallic Properties*. Science **281**, 1647 (1998).

[195] M. S. Chen and D. W. Goodman, *The Structure of Catalytically Active Gold on Titania*. Science **306**, 252 (2004).

[196] X. Z. Li and F. B. Li, *Study of Au/Au3+-TiO2 Photocatalysts toward Visible Photooxidation for Water and Wastewater Treatment*. Environ. Sci. Technol. **35**, 2381 (2001).

[197] M. Murdoch, G. I. N. Waterhouse, M. A. Nadeem, J. B. Metson, M. A. Keane, R. F. Howe, J. Llorca, and H. Idriss, *The Effect of Gold Loading and Particle Size on Photocatalytic Hydrogen Production from Ethanol over Au/TiO2 Nanoparticles*. Nat. Chem. **3**, 489 (2011).

[198] Y. C. Pu *et al.*, *Au Nanostructure-Decorated TiO2 Nanowires Exhibiting Photoactivity Across Entire UV-visible Region for Photoelectrochemical Water Splitting*. Nano Lett. **13**, 3817 (2013).

[199] T. Jiang, C. Jia, L. Zhang, S. He, Y. Sang, H. Li, Y. Li, X. Xu, and H. Liu, *Gold and Gold-Palladium Alloy Nanoparticles on Heterostructured TiO2 Nanobelts as Plasmonic Photocatalysts for Benzyl Alcohol Oxidation*. Nanoscale **7**, 209 (2015).

[200] Z. Song, J. Hrbek, and R. Osgood, *Formation of TiO2 Nanoparticles by Reactive-Layer-Assisted Deposition and Characterization by XPS and STM*. Nano Lett. **5**, 1327 (2005).

[201] D. V. Potapenko, J. Hrbek, and R. M. Osgood, *Scanning Tunneling Microscopy Study of Titanium Oxide Nanocrystals Prepared on Au(111) by Reactive-Layer-Assisted Deposition*. ACS Nano. **2**, 1353 (2008).

[202] D. V. Potapenko and R. M. Osgood, *Preparation of TiO2 Nanocrystallites by Oxidation of Ti−Au(111) Surface Alloy*. Nano Lett. **9**, 2378 (2009).

[203] K. Lauwaet, K. Schouteden, E. Janssens, C. Van Haesendonck, and P. Lievens, *Morphology and Electronic Properties of Thermally Stable TiOx Nanoclusters on Au(111)*. Phys. Rev. B **83**, 155433 (2011).

[204] J. A. Rodriguez, S. Ma, P. Liu, J. Hrbek, J. Evans, and M. Pérez, *Activity of CeOx and TiOx Nanoparticles Grown on Au(111) in the Water-Gas Shift Reaction*. Science **318**, 1757 (2007).

[205] J. Biener, E. Farfan-Arribas, M. Biener, C. M. Friend, and R. J. Madix, *Synthesis of TiO2 Nanoparticles on the Au(111) surface*. J. Chem. Phys. **123**, 094705 (2005).

[206] I. Nakamura, H. Mantoku, T. Furukawa, and T. Fujitani, *Active Sites for Hydrogen Dissociation over TiOx/Au(111) Surfaces*. J. Phys. Chem. C **115**, 16074 (2011).

[207] J. D. Grunwaldt, U. Göbel, and A. Baiker, *Preparation and Characterization of Thin TiO2-Films on Gold/Mica*. Fresenius J. Anal. Chem. **358**, 96 (1997).

[208] S. Datar, P. M. Kumar, M. Sastry, and C. V. Dharmadhikari, *Scanning Tunneling Microscopy/Spectroscopy of Titanium Dioxide Nanoparticulate Film on Au(111) Surface*. Colloids Surf. **232**, 11 (2004).

[209] E. Farfan-Arribas, J. Biener, C. M. Friend, and R. J. Madix, *Reactivity of Methanol on TiO2 Nanoparticles Supported on the Au(111) Surface*. Surf. Sci. **591**, 1 (2005).

[210] D. Ragazzon, *Titania Nnaoscale Films and Surfaces. Surface Science Investigation of Structure and Properties*. Digital Comprehensive Summaries of Uppsala Dissertations from the Faculty of Science and Technology, Uppsala University, (2014).

[211] E. Cavaliere, L. Artiglia, G. A. Rizzi, L. Gavioli, and G. Granozzi, *Structure and Thermal Stability of Fully Oxidized TiO2/Pt(111) Polymorphs*. Surf. Sci. **608**, 173 (2013).

[212] A. Vittadini, M. Casarin, and A. Selloni, *Structure and Stability of TiO2-B Surfaces: A Density Functional Study*. J. Phys. Chem. C **113**, 18973 (2009).

[213] L. R. Merte *et al.*, *Water Clustering on Nanostructured Iron Oxide Films*. Nat. Commun. **5** (2014).

[214] C. Wu, M. R. Castell, J. Goniakowski, and C. Noguera, *Stoichiometry Engineering of Ternary Oxide Ultrathin Films: BaxTi2O3 on Au(111)*. Phys. Rev. B **91**, 155424 (2015).

[215] V. Simic-Milosevic, N. Nilius, H. P. Rust, and H. J. Freund, *Local Band Gap Modulations in Non-Stoichiometric V2O3 Films Probed by Scanning Tunneling Spectroscopy*. Phys. Rev. B **77**, 125112 (2008).

[216] M. Li and E. I. Altman, *Cluster-Size Dependent Phase Transition of Co Oxides on Au(111)*. Surf. Sci. **619**, L6 (2014).

[217] M. Li and E. I. Altman, *Shape, Morphology, and Phase Transitions During Co Oxide Growth on Au(111)*. J. Phys. Chem. C **118**, 12706 (2014).

[218] F. Stavale, L. Pascua, N. Nilius, and H. J. Freund, *Morphology and Luminescence of ZnO Films Grown on a Au(111) Support*. J. Phys. Chem. C **117**, 10552 (2013).

[219] X. Deng, K. Yao, K. Sun, W.-X. Li, J. Lee, and C. Matranga, *Growth of Single-*

and Bilayer ZnO on Au(111) and Interaction with Copper. J. Phys. Chem. C **117**, 11211 (2013).

[220] N. D. McCavish and R. A. Bennett, *Ultra-thin Film Growth of Titanium Dioxide on W(1 0 0)*. Surf. Sci. **546**, 47 (2003).

[221] R. A. Bennett, J. S. Mulley, M. A. Newton, and M. Surman, *Spectroscopy of Ultrathin Epitaxial Rutile TiO2(110) Films Grown on W(100)*. J. Chem. Phys. **127**, 084707 (2007).

[222] R. A. Bennett and N. D. McCavish, *Non-Stoichiometric Oxide Surfaces and Ultra-thin Films: Characterisation of TiO2*. Top. Catal. **36**, 11 (2005).

[223] J. Matharu, G. Cabailh, and G. Thornton, *Synthesis of TiO2(110) Ultra-thin Films on W(100) and Their Reactions with H2O*. Surf. Sci. **616**, 198 (2013).

[224] C. L. Pang, D. C. Grinter, J. Matharu, and G. Thornton, *A Scanning Tunneling Microscopy Study of Ultrathin Film Rutile TiO2(110) Supported on W(100)-O(2 × 1)*. J. Phys. Chem. C **117**, 25622 (2013).

[225] G. T. Harrison, M. C. Spadaro, C. L. Pang, D. C. Grinter, C. M. Yim, P. Luches, and G. Thornton, *Lepidocrocite-like TiO2 and TiO2(110)–(1 × 2) Supported on W(100)*. Mater. Sci. Tech. **32**, 203 (2016).

[226] R. Ab Kadir, R. A. Rani, M. M. Y. A. Alsaif, J. Z. Ou, W. Wlodarski, A. P. O'Mullane, and K. Kalantar-Zadeh, *Optical Gas Sensing Properties of Nanoporous Nb2O5 Films*. ACS Appl. Mater. Interfaces **7**, 4751 (2015).

[227] A. Mozalev, M. Bendova, R. M. Vazquez, Z. Pytlicek, E. Llobet, and J. Hubalek, *Formation and Gas-sensing Properties of a Porous-Alumina-Assisted 3-D Niobium-Oxide Nanofilm*. Sens. Actuator B-Chem. **229**, 587 (2016).

[228] Z. Dai, H. Dai, Y. Zhou, D. Liu, G. Duan, W. Cai, and Y. Li, *Monodispersed Nb2O5 Microspheres: Facile Synthesis, Air/Water Interfacial Self-Assembly, Nb2O5-Based Composite Films, and Their Selective NO2 Sensing*. Adv. Mater. Interf. **2**, 1500167 (2015).

[229] G. Z. Li, H. P. Tang, W. Y. Zhang, G. Li, L. L. Yu, and Y. N. Li, *Fabrication of Multilayer Nb2O5 Nanoporous Film by Anodization of Niobium Foils*. Rare Metals **34**, 77 (2013).

[230] Y. C. Wu, S. J. Wu, and C. H. Lin, *High Performance EGFET-Based PH Sensor Utilizing Low-Cost Industrial-Grade Touch Panel Film as the Gate Structure*. IEEE Sens. J. **15**, 6279 (2015).

[231] E. Pehlivan, K. Koc, F. Z. Tepehan, and G. G. Tepehan, *Structural, Optical and Electrochromic Properties of Tantalum Pentoxide-Doped Niobium Pentoxide Thin Films*. J. Sol-Gel Sci. Technol. **77**, 172 (2015).

[232] Ö. D. Coşkun, S. Demirel, and G. Atak, *The Effects of Heat Treatment on Optical, Structural, Electrochromic and Bonding Properties of Nb2O5 Thin Films*. J. Alloy. Comp. **648**, 994 (2015).

[233] J. Kim, G. K. Ong, Y. Wang, G. LeBlanc, T. E. Williams, T. M. Mattox, B. A. Helms, and D. J. Milliron, *Nanocomposite Architecture for Rapid, Spectrally-Selective Electrochromic Modulation of Solar Transmittance*. J. Am. Chem. Soc **15**, 5574 (2015).

[234] N. Usha, R. Sivakumar, and C. Sanjeeviraja, *Electrochromic Properties of Radio Frequency Magnetron Sputter Deposited Mixed Nb2O5:MoO3 (95:5) Thin Films Cycled in H+ and Li+ Ions*. Mat. Sci. Semicon. Proc. **30**, 31 (2015).

[235] R. A. Rani, A. S. Zoolfakar, A. P. O'Mullane, M. W. Austin, and K. Kalantar-Zadeh, *Thin Films and Nanostructures of Niobium Pentoxide: Fundamental Properties, Synthesis Methods and Applications*. J. Mater. Chem. A **2**, 15683 (2014).

[236] S. Zhuiykov, E. Kats, K. Kalantar-Zadeh, and Y. Li, *Synthesis and Nanoscale Investigation of the Electrical Properties of Quasi-2D Semiconductor Nb2O5 Nanosheets*. IEEE Trans. Nanotechnol. **12**, 641 (2013).

[237] C. Y. Han, W. M. Tang, C. H. Leung, C. M. Che, and P. T. Lai, *A Study on La Incorporation in Transition-Metal (Y, Zr, and Nb) Oxides as Gate Dielectric of Pentacene Organic Thin-Film Transistor*. IEEE Trans. Electron Dev. **62**, 2313 (2015).

[238] N. A. Tulina, A. N. Rossolenko, I. Y. Borisenko, I. M. Shmytko, A. M. Ionov, and A. A. Ivanov, *Resistive Switching and Diode Properties of Mesoscopic Niobium Oxide-Based Structures*. Bull. Russ. Acad. Sci., Phys. **79**, 759 (2015).

[239] A. Mozalev, R. M. Vazquez, C. Bittencourt, D. Cossement, F. Gispert-Guirado, E. Llobet, and H. Habazaki, *Formation, Structure, Properties of Niobium-Oxide Nanocolumn Arrays via Self-Organized Anodization of Sputter-Deposited Aluminum-on-Niobium Layers*. J. Phys. Chem. C **2**, 4847 (2014).

[240] S. Li, Q. Xu, E. Uchaker, X. Cao, and G. Cao, *Comparison of Amorphous, Pseudohexagonal and Prthorhombic Nb2O5 for High-Rate Lithium Ion Insertion*. Cryst. Eng. Comm. **18**, 2532 (2016).

[241] W. Li, R. Gao, M. Chen, S. Zhou, and L. Wu, *Facile Synthesis and Unique Photocatalytic Property of Niobium Pentoxide Hollow Spheres and the High Optoelectronic Performance of Their Nanofilm*. J. Colloid. Interface Sci. **411**, 220 (2013).

[242] E. Tsang, X. Zhou, L. Ye, and S. C. Edman Tsang, *Nanostructured Nb2O5 Catalysts*. Nano Rev. **3**, 17631 (2012).

[243] Y. Narendar and G. L. Messing, *Synthesis, Decomposition and Crystallization Characteristics of Peroxo-Citrato-Niobium: An Aqueous Niobium Precursor*. Chem. Mater. **9**, 580 (1997).

[244] K. Saito and A. Kudo, *Controlled Synthesis of TT Phase Niobium Pentoxide Nanowires Showing Enhanced Photocatalytic Properties*. Bull. Chem. Soc. Jpn. **82**, 1030 (2009).

[245] C. Zhang *et al.*, *Synthesis and Electrochemical Properties of Niobium Pentoxide Deposited on Layered Carbide-Derived Carbon*. J. Power Sources **274**, 121 (2015).

[246] K. Kato, *Structure Refinement of H-Nb2O5*. Acta Cryst. **B32**, 764 (1976).

[247] T. Ikeya and M. Senna, *Change in the Structure of Niobium Pentoxide due to Mechanical and Thermal Treatments*. J. Non-Cryst. Solids **105**, 243 (1988).

[248] J. Liu, D. Xue, and K. Li, *Single-Crystalline Nanoporous Nb2O5 Nanotubes*. Nanoscale Res. Lett. **6**, 1 (2011).

[249] S. G. Chen, S. Chappel, Y. Diamant, and A. Zaban, *Preparation of Nb2O5*

Coated TiO2 Nanoporous Electrodes and Their Application in Dye-Sensitized Solar Cells. Chem. Mater. **13**, 4629 (2001).

[250] X. Chen, T. Yu, X. Fan, H. Zhang, Z. Li, J. Ye, and Z. Zou, *Enhanced Activity of Mesoporous Nb2O5 for Photocatalytic Hydrogen Production*. Appl. Surf. Sci. **253**, 8500 (2007).

[251] S. Park, S. Park, S. Kim, S. K. Hyun, and C. Lee, *Room Temperature Hydrogen Sensing Properties of Multiple-Networked Nb2O5-Nanorod Sensors Decorated with Pd Nanoparticles*. J. Korean Phys. Soc. **65**, 1414 (2014).

[252] M. Qamar, M. Abdalwadoud, M. I. Ahmed, A. M. Azad, B. Merzougui, S. Bukola, Z. H. Yamani, and M. N. Siddiqui, *Single-Pot Synthesis of ⟨001⟩-Faceted N-Doped Nb2O5/Reduced Graphene Oxide Nanocomposite for Efficient Photoelectrochemical Water Splitting*. ACS Appl. Mater. Interfaces **7**, 17954 (2015).

[253] B. Ohtani, K. Iwai, S. I. Nishimoto, and T. Inui, *Electrochromism of Niobium Oxide Thin Films Prepared by the Sol‐Gel Process*. J. Electrochem. Soc. **141**, 2439 (1994).

[254] M. A. Aegerter, *Sol-Gel Niobium Pentoxide: A Promising Material for Electrochromic Coatings, Batteries, Nanocrystalline Solar Cells and Catalysis*. Sol. Energ. Mat. Sol. Cells **68**, 401 (2001).

[255] G. Ramírez, S. E. Rodil, S. Muhl, D. Turcio-Ortega, J. J. Olaya, M. Rivera, E. Camps, and L. Escobar-Alarcón, *Amorphous Niobium Oxide Thin Films*. J. Non-Cryst. Solids **356**, 2714 (2010).

[256] F. B. Destro, M. Cilense, M. P. Nascimento, F. G. Garcia, L. R. O. Hein, and A. Z. Simões, *Corrosion Behaviour of Polycrystalline Nb2O5 Thin Films and Its Size Effects*. Prot. Met. Phys. Chem. Surf. **52**, 104 (2016).

[257] T. Kitano, T. Shishido, K. Teramura, and T. Tanaka, *Acid Property of Nb2O5/Al2O3 Prepared by Impregnation Method by Using Niobium Oxalate Solution: Effect of PH on the Structure and Acid Property*. Catal. Today **226**, 97 (2014).

[258] Y. Wang, R. B. Comes, S. Kittiwatanakul, S. A. Wolf, and J. Lu, *Epitaxial Niobium Dioxide Thin Films by Reactive-Biased Target Ion Beam Deposition*. J. Vac. Sci. Technol. A **33**, 021516 (2015).

[259] Y. Li, S. Yan, L. Qian, W. Yang, Z. Xie, Q. Chen, B. Yue, and H. He, *Effect of Tin on Nb2O5/α-Al2O3 Catalyst for Ethylene Oxide Hydration*. J. Catal. **241**, 173 (2006).

[260] M. S. P. Francisco, R. Landers, and Y. Gushikem, *Local Order Structure and Surface Acidity Properties of a Nb2O5/SiO2 Mixed Oxide Prepared by the Sol–Gel Processing Method*. J. Solid State Chem. **177**, 2432 (2004).

[261] M. Anilkumar and W. F. Hoelderich, *Gas Phase Beckmann Rearrangement of Cyclohexanone Oxime to ε-Caprolactam over Mesoporous, Microporous and Amorphous Nb2O5/Silica Catalysts: A Comparative Study*. Catal. Today **198**, 289 (2012).

[262] M. Massa, A. Andersson, E. Finocchio, and G. Busca, *Gas-Phase Dehydration of Glycerol to Acrolein over Al2O3-, SiO2-, and TiO2-Supported Nb- and W-Oxide Catalysts*. J. Catal. **307**, 170 (2013).

[263] T. Ushikubo, Y. Koike, K. Wada, L. Xie, D. Wang, and X. Guo, *Study of the Structure of Niobium Oxide by X-ray Absorption Fine Structure and Surface Science Techniques*. Catal. Today **28**, 59 (1996).

[264] L. Xie, D. Wang, X. Wei, Y. Cao, X. Guo, T. Ushikubo, and K. Wada, *The Preparation of a Vertical Bar Model Nb Oxide Catalyst Epitaxially Grown*. Acta Phys. Chim. **11**, 234 (1995).

[265] L. Xie, D. Wang, C. Zhong, X. Guo, T. Ushikubo, and K. Wada, *The Preparation of and Water Adsorption on Thin Films of Niobium Oxide on Pt(111)*. Surf. Sci. **320**, 62 (1994).

[266] F. Höbel, A. Bandara, G. Rupprechter, and H. J. Freund, *Deactivation of Pd Particles Supported on Nb2O5/Cu3Au(1 0 0): SFG and TPD Studies from UHV to 100 mbar*. Surf. Sci. **600**, 963 (2006).

[267] J. Middeke, R. P. Blum, M. Hafemeister, and H. Niehus, *Controlled Preparation of Well-Ordered Transition Metal Oxide Layers on a Metallic Surface*. Surf. Sci. **587**, 219 (2005).

[268] D. E. Starr *et al.*, *Preparation and Characterization of Well-Ordered, Thin Niobia Films on a Metal Substrate*. Surf. Sci. **599**, 14 (2005).

[269] I. Arfaoui, J. Cousty, and C. Guillot, *A Model of the NbOx ≈ 1 Nanocrystals Tiling a Nb(110) Surface Annealed in UHV*. Surf. Sci. **557**, 119 (2004).

[270] I. Arfaoui, J. Cousty, and H. Safa, *Tiling of a Nb(110) Surface with NbO Crystals Nanosized by the NbO/Nb Misfit*. Phys. Rev. B **65**, 115413 (2002).

[271] R. Franchy, T. U. Bartke, and P. Gassmann, *The Interaction of Oxygen with Nb(110) at 300, 80 and 20 K*. Surf. Sci. **366**, 60 (1996).

[272] Y. Li, B. An, S. Fukuyama, K. Yokogawa, and M. Yoshimura, *Surface Oxidation of a Nb(100) Single Crystal by Scanning Tunneling Microscopy*. Mater. Charact. **48**, 163 (2002).

[273] R. Pantel, M. Bujor, and J. Bardolle, *Continuous Measurement of Surface Potential Variations During Oxygen Adsorption on the (100), (110) and (111) Faces of Niobium Using Mirror Electron Microscope*. Surf. Sci. **62**, 589 (1977).

[274] C. Sürgers, M. Schöck, and H. v. Löhneysen, *Oxygen-Induced Surface Structure of Nb(110)*. Surf. Sci. **471**, 209 (2001).

[275] M. Wen, B. An, S. Fukuyama, and K. Yokogawa, *First-Principles Study of Oxidized Nb(100) Surface Structures*. Surf. Sci. **603**, 216 (2009).

[276] K. H. Rieder, *On the Interaction of Oxygen with Nb(110) and Nb(750)*. Appl. Surf. Sci. **4**, 183 (1980).

[277] J. M. Sanz and S. Hofmann, *Auger Electron Spectroscopy and X-ray Photoelectron Spectroscopy Studies of the Oxidation of Polycrystalline Tantalum and Niobium at Room Temperature and Low Oxygen Pressures*. J. Less Common Metals **92**, 317 (1983).

[278] Y. S. Wang, X. M. Wei, Z. J. Tian, Y. M. Cao, R. S. Zhai, T. Ushikubo, K. Sato, and S. X. Zhuang, *An AES, UPS and HREELS Study of the Oxidation and Reaction of*

Nb(110). Surf. Sci. **372**, L285 (1997).

[279] Y. Li, B. An, X. Xu, S. Fukuyama, K. Yokogawa, and M. Yoshimura, *Surface Structure of Niobium-Dioxide Overlayer on Niobium(100) Identified by Scanning Tunneling Microscopy*. J. Appl. Phys. **89**, 4772 (2001).

[280] D. N. Tafen and M. C. Gao, *Oxygen Atom Adsorption on and Diffusion into Nb(110) and Nb(100) from First Principles*. JOM **65**, 1473 (2013).

[281] Q. Wang, J. Shang, and Z. Yang, *First-Principles Study on the Initial Oxidization of a Nb(100) Surface*. J. Phys. Chem. C **116**, 23371 (2012).

[282] Q. Wang and J. Shang, *First-Principles Study on the Incipient Oxidization of Nb(110)*. J. Phys. Condens. Matter **24**, 225005 (2012).

[283] S. Surnev, G. Kresse, M. Sock, M. G. Ramsey, and F. P. Netzer, *Surface Structures of Ultrathin Vanadium Oxide Films on Pd(111)*. Surf. Sci. **495**, 91 (2001).

[284] S. Surnev, L. Vitali, M. G. Ramsey, F. P. Netzer, G. Kresse, and J. Hafner, *Growth and Structure of Ultrathin Vanadium Oxide Layers on Pd(111)*. Phys. Rev. B **61**, 13945 (2000).

[285] K. S. Novoselov, A. K. Geim, S. V. Morozov, D. Jiang, Y. Zhang, S. V. Dubonos, I. V. Grigorieva, and A. A. Firsov, *Electric Field Effect in Atomically Thin Carbon Films*. Science **306**, 666 (2004).

[286] Y. Liu and B. I. Yakobson, *Cones, Pringles, and Grain Boundary Landscapes in Graphene Topology*. Nano Lett. **10**, 2178 (2010).

[287] O. V. Yazyev and S. G. Louie, *Topological Defects in Graphene: Dislocations and Grain Boundaries*. Phys. Rev. B **81**, 195420 (2010).

[288] J. Zhang, J. Zhao, and J. Lu, *Intrinsic Strength and Failure Behaviors of Graphene Grain Boundaries*. ACS Nano **6**, 2704 (2012).

[289] L. Liu, J. Zhang, H. Gao, L. Wang, X. Jiang, and J. Zhao, *Tailoring Physical Properties of Graphene: Effects of Hydrogenation, Oxidation, and Grain Boundaries by Atomistic Simulations*. Comput. Mater. Sci. **112, Part B**, 527 (2016).

[290] J. Zhuang, R. Zhao, J. Dong, T. Yan, and F. Ding, *Evolution of Domains and Grain Boundaries in Graphene: A Kinetic Monte Carlo Simulation*. Phys. Chem. Chem. Phys. **18**, 2932 (2016).

[291] F. Meng, D. Hu, and J. Song, *Impurity-Induced Grain Boundary Strengthening in Polycrystalline Graphene*. J. Phys. Chem. C **120**, 1952 (2016).

[292] J. Sun, N. Lin, Z. Li, H. Ren, C. Tang, and X. Zhao, *Electronic and Transport Properties of Graphene with Grain Boundaries*. RSC Adv. **6**, 1090 (2016).

[293] X. Zhang, Z. Xu, Q. Yuan, J. Xin, and F. Ding, *The Favourable Large Misorientation Angle Grain Boundaries in Graphene*. Nanoscale **7**, 20082 (2015).

[294] S. Malola, H. Häkkinen, and P. Koskinen, *Structural, Chemical, and Dynamical Trends in Graphene Grain Boundaries*. Phys. Rev. B **81**, 165447 (2010).

[295] Y. Ren and G. Cao, *Effect of Geometrical Defects on the Tensile Properties of Graphene*. Carbon **103**, 125 (2016).

[296] J. Lu, Y. Bao, C. L. Su, and K. P. Loh, *Properties of Strained Structures and Topological Defects in Graphene*. ACS Nano **7**, 8350 (2013).

[297] L. He, S. Guo, J. Lei, Z. Sha, and Z. Liu, *The Effect of Stone–Thrower–Wales Defects on Mechanical Properties of Graphene Sheets – A Molecular Dynamics Study*. Carbon **75**, 124 (2014).

[298] P. Y. Huang *et al.*, *Grains and Grain Boundaries in Single-Layer Graphene Atomic Patchwork Quilts*. Nature **469**, 389 (2011).

[299] K. Kim, Z. Lee, W. Regan, C. Kisielowski, M. F. Crommie, and A. Zettl, *Grain Boundary Mapping in Polycrystalline Graphene*. ACS Nano. **5**, 2142 (2011).

[300] E. Cockayne, G. M. Rutter, N. P. Guisinger, J. N. Crain, P. N. First, and J. A. Stroscio, *Grain Boundary Loops in Graphene*. Phys. Rev. B **83**, 195425 (2011).

[301] O. V. Yazyev and Y. P. Chen, *Polycrystalline Graphene and Other Two-Dimensional Materials*. Nat. Nano **9**, 755 (2014).

[302] R. Grantab, V. B. Shenoy, and R. S. Ruoff, *Anomalous Strength Characteristics of Tilt Grain Boundaries in Graphene*. Science **330**, 946 (2010).

[303] G.-H. Lee *et al.*, *High-Strength Chemical-Vapor–Deposited Graphene and Grain Boundaries*. Science **340**, 1073 (2013).

[304] G. Yong, S. Hong Xiang, G. Yi Jun, and Z. Gan He, *Finite Temperature Effect on Mechanical Properties of Graphene Sheets with Various Grain Boundaries*. Chin. Phys. B **25**, 066104 (2016).

[305] Y. Wei, J. Wu, H. Yin, X. Shi, R. Yang, and M. Dresselhaus, *The Nature of Strength Enhancement and Weakening by Pentagon–Heptagon Defects in Graphene*. Nat. Mater. **11**, 759 (2012).

[306] Q. Yu *et al.*, *Control and Characterization of Individual Grains and Grain Boundaries in Graphene Grown by Chemical Vapour Deposition*. Nat. Mater. **10**, 443 (2011).

[307] J. Tian, H. Cao, W. Wu, Q. Yu, and Y. P. Chen, *Direct Imaging of Graphene Edges: Atomic Structure and Electronic Scattering*. Nano Lett. **11**, 3663 (2011).

[308] J. Lahiri, Y. Lin, P. Bozkurt, I. I. Oleynik, and M. Batzill, *An Extended Defect in Graphene as a Metallic Wire*. Nat. Nano **5**, 326 (2010).

[309] A. R. Botello-Mendez, X. Declerck, M. Terrones, H. Terrones, and J. C. Charlier, *One-Dimensional Extended Lines of Divacancy Defects in Graphene*. Nanoscale **3**, 2868 (2011).

[310] Y. Liu, X. Zou, and B. I. Yakobson, *Dislocations and Grain Boundaries in Two-Dimensional Boron Nitride*. ACS Nano **6**, 7053 (2012).

[311] A. L. Gibb, N. Alem, J. H. Chen, K. J. Erickson, J. Ciston, A. Gautam, M. Linck, and A. Zettl, *Atomic Resolution Imaging of Grain Boundary Defects in Monolayer Chemical Vapor Deposition-Grown Hexagonal Boron Nitride*. J. Am. Chem. Soc. **135**, 6758 (2013).

[312] Z. Zhang, X. Zou, V. H. Crespi, and B. I. Yakobson, *Intrinsic Magnetism of Grain Boundaries in Two-Dimensional Metal Dichalcogenides*. ACS Nano **7**, 10475 (2013).

[313] A. M. van der Zande *et al.*, *Grains and Grain Boundaries in Highly Crystalline Monolayer Molybdenum Disulphide*. Nat. Mater. **12**, 554 (2013).

[314] A. N. Enyashin, M. Bar Sadan, L. Houben, and G. Seifert, *Line Defects in Molybdenum Disulfide Layers*. J. Phys. Chem. C **117**, 10842 (2013).

[315] Y. C. Lin *et al.*, *Three-Fold Rotational Defects in Two-Dimensional Transition Metal Dichalcogenides*. Nat. Commun. **6** (2015).

[316] S. Wang, G. D. Lee, S. Lee, E. Yoon, and J. H. Warner, *Detailed Atomic Reconstruction of Extended Line Defects in Monolayer MoS2*. ACS Nano **10**, 5419 (2016).

[317] S. Ulrich, N. Nilius, H. J. Freund, U. Martinez, L. Giordano, and G. Pacchioni, *Evidence for a Size-Selective Adsorption Mechanism on Oxide Surfaces: Pd and Au atoms on SiO2/Mo(112)*. Chem. Phys. Chem. **9**, 1367 (2008).

[318] H. J. Freund and G. Pacchioni, *Oxide Ultra-thin Films on Metals: New Materials for the Design of Supported Metal Catalysts*. Chem. Soc. Rev. **37**, 2224 (2008).

[319] J. Weissenrieder, S. Kaya, J. L. Lu, H. J. Gao, S. Shaikhutdinov, H. J. Freund, M. Sierka, T. K. Todorova, and J. Sauer, *Atomic Structure of a Thin Silica Film on a Mo(112) Substrate: A Two-Dimensional Network of SiO4 Tetrahedra*. Phys. Rev. Lett. **95**, 076103 (2005).

[320] S. Kaya, M. Baron, D. Stacchiola, J. Weissenrieder, S. Shaikhutdinov, T. K. Todorova, M. Sierka, J. Sauer, and H. J. Freund, *On the Geometrical and Electronic Structure of an Ultra-Thin Crystalline Silica Film Grown on Mo(112)*. Surf. Sci. **601**, 4849 (2007).

[321] T. Schroeder, M. Adelt, B. Richer, M. Naschitzki, M. Baumer, and H. J. Freund, *Epitaxy Growth of SiO2 on Mo(112)*. Surf. Rev. Lett. **07**, 7 (2000).

[322] D. Löffler *et al.*, *Growth and Structure of Crystalline Silica Sheet on Ru(0001)*. Phys. Rev. Lett. **105**, 146104 (2010).

[323] E. I. Altman, J. Götzen, N. Samudrala, and U. D. Schwarz, *Growth and Characterization of Crystalline Silica Films on Pd(100)*. J. Phys. Chem. C **117**, 26144 (2013).

[324] L. Lichtenstein, C. Büchner, B. Yang, S. Shaikhutdinov, M. Heyde, M. Sierka, R. Włodarczyk, J. Sauer, and H. J. Freund, *The Atomic Structure of a Metal-Supported Vitreous Thin Silica Film*. Angew. Chem. Int. Ed. **51**, 404 (2012).

[325] B. Yang *et al.*, *Thin Silica Films on Ru(0001): Monolayer, Bilayer and Three-Dimensional Networks of [SiO4] Tetrahedra*. Phys. Chem. Chem. Phys. **14**, 11344 (2012).

[326] X. Yu, B. Yang, J. Anibal Boscoboinik, S. Shaikhutdinov, and H. J. Freund, *Support Effects on the Atomic Structure of Ultrathin Silica Films on Metals*. Appl. Phys. Lett. **100**, 151608 (2012).

[327] S. Shaikhutdinov and H. J. Freund, *Ultrathin Silica Films on Metals: The Long and Winding Road to Understanding the Atomic Structure*. Adv. Mater. **25**, 49 (2013).

[328] F. Hanke and J. Björk, *Structure and Local Reactivity of the Au(111) Surface*

Reconstruction. Phys. Rev. B **87**, 235422 (2013).

[329] K. Okazaki-Maeda, Y. Morikawa, S. Ichikawa, S. Tanaka, and M. Kohyama, *Electronic Structures of Ag and Au Adsorbed on TiO2(110) Surfaces by First-Principles Calculations*. Materials Transactions **47**, 2669 (2006).

[330] D. M. Zehner and J. F. Wendelken, *Anomalous Au(111) Surfaces Studied by LEED, AES and Oxygen Chemisorption.* in *Proc. 7th Intern. Congr. & 3rd Int. Conf. on Solid. Surf.* Vienna p.^pp. 517. (1977)

[331] A. T. D'Agostino and P. N. Ross Jr, *LEED/Electrochemical Analysis of Au Single Crystals: Stability of the UHV Prepared Surfaces of Au(111) and Au(100) in Aqueous Electrolyte*. Surf. Sci. **185**, 88 (1987).

[332] NIST Standard Reference Database 20, Version 3.4 (web version) (http:/srdata.nist.gov/xps/) 2003.

[333] R. Wang, J. Yang, X. Wu, and S. Wang, *Local Charge States in Hexagonal Boron Nitride with Stone-Wales Defects*. Nanoscale **8**, 8210 (2016).

[334] A. J. Stone and D. J. Wales, *Theoretical Studies of Icosahedral C60 and Some Related Species*. Chem. Phys. Lett. **128**, 501 (1986).

[335] M. Gratzel, *Photoelectrochemical Cells*. Nature **414**, 338 (2001).

[336] R. Wang, K. Hashimoto, A. Fujishima, M. Chikuni, E. Kojima, A. Kitamura, M. Shimohigoshi, and T. Watanabe, *Light-induced Amphiphilic Surfaces*. Nature **388**, 431 (1997).

[337] D. Zhang, M. Yang, and S. Dong, *Hydroxylation of the Rutile TiO2(110) Surface Enhancing Its Reducing Power for Photocatalysis*. J. Phys. Chem. C **119**, 1451 (2015).

[338] Y. Du, N. A. Deskins, Z. Zhang, Z. Dohnálek, M. Dupuis, and I. Lyubinetsky, *Imaging Consecutive Steps of O2 Reaction with Hydroxylated TiO2(110): Identification of HO2 and Terminal OH Intermediates*. J. Phys. Chem. C **113**, 666 (2009).

[339] I. Nowak and M. Ziolek, *Niobium Compounds: Preparation, Characterization, and Application in Heterogeneous Catalysis*. Chem. Rev. **99**, 3603 (1999).

[340] S. C. Ghosh, C. C. Li, H. C. Zeng, J. S. Y. Ngiam, A. M. Seayad, and A. Chen, *Mesoporous Niobium Oxide Spheres as an Effective Catalyst for the Transamidation of Primary Amides with Amines*. Adv. Synth. Catal. **356**, 475 (2014).

[341] B. Li, M. Gu, Z. Nie, X. Wei, C. Wang, V. Sprenkle, and W. Wang, *Nanorod Niobium Oxide as Powerful Catalysts for an All Vanadium Redox Flow Battery*. Nano Lett. **14**, 158 (2014).

[342] Y. Zhao, X. Zhou, L. Ye, and S. C. E. Tsang, *Nanostructred Nb2O5 Catalysts*. Nano Rev. **3**, 1 (2012).

[343] D. D. Yao, R. A. Rani, A. P. O'Mullane, K. Kalantar-zadeh, and J. Z. Ou, *High Performance Electrochromic Devices Based on Anodized Nanoporous Nb2O5*. J. Phys. Chem. C **118**, 476 (2014).

[344] A. Sacco, M. S. Di Bella, M. Gerosa, A. Chiodoni, S. Bianco, M. Mosca, R. Macaluso, C. Calì, and C. F. Pirri, *Enhancement of Photoconversion Efficiency in Dye-sensitized Solar Cells Exploiting Pulsed Laser Deposited Niobium Pentoxide Blocking*

Layers. Thin Solid Films **574**, 38 (2015).

[345] A. Llordes, G. Garcia, J. Gazquez, and D. J. Milliron, *Tunable Near-infrared and Visible-light Transmittance in Nanocrystal-in-glass Composites*. Nature **500**, 323 (2013).

[346] S. Park, S. Park, S. Lee, H. W. Kim, and C. Lee, *Hydrogen Sensing Properties of Multiple Networked Nb2O5/ZnO Core–Shell Nanorod Sensors*. Sens. Actuator B-Chem. **202**, 840 (2014).

[347] R. A. Rani, A. S. Zoolfakar, J. Z. Ou, M. R. Field, M. Austin, and K. Kalantar-zadeh, *Nanoporous Nb2O5 Hydrogen Gas Sensor*. Sens. Actuator B-Chem. **176**, 149 (2013).

[348] H. Y. Lin, H. C. Yang, and W. L. Wang, *Synthesis of Mesoporous Nb2O5 Photocatalysts with Pt, Au, Cu and NiO Cocatalyst for Water Splitting*. Catal. Today **174**, 106 (2011).

[349] U. Guth and J. Zosel, *Electrochemical Solid Electrolyte Gas Sensors — Hydrocarbon and NOx Analysis in Exhaust Gases*. Ionics **10**, 366 (2004).

[350] I. Sobczak, K. Jagodzinska, and M. Ziolek, *Glycerol Oxidation on Gold Catalysts Supported on Group Five Metal Oxides—A Comparative Study with Other Metal Oxides and Carbon Based Catalysts*. Catal. Today **158**, 121 (2010).

[351] I. Sobczak, J. Florek, K. Jagodzinska, and M. Ziolek, in *Scientific Bases for the Preparation of Heterogeneous Catalysts*, edited by E. Gaigneaux *et al.* Elsevier, Belgium, (2010).